AD 701203

AD _____

TECHNICAL REPORT

70-7-GP

WIND TUNNEL TESTS AND ANALYSES FOR GROUND-MOUNTED, AIR-SUPPORTED STRUCTURES (REVISED)

by

A. E. Dietz, R. B. Proffitt, R. S. Chabot, and E. L. Moak

Hayes International Corporation
Birmingham, Alabama

and

C. J. Monego
U. S. Army Natick Laboratories

Contract No. DA19-129-AMC-953(N)

Project Reference:
1M62410D503

July 1969

General Equipment & Packaging Laboratory

U. S. ARMY NATICK LABORATORIES

Natick, Massachusetts

FOREWORD

This manual for ground-mounted, air-supported single- and double-wall structures has been prepared by Hayes International Corporation, Birmingham, Alabama. The manual presents information on wind tunnel tests conducted in support of design data and an analysis of tent fabric stresses. Configurations investigated include spherical and cylindrical single-wall tents and cylindrical double-wall tents with flat ends. Wind tunnel tests were conducted in the six-foot by six-foot stability tunnel at Virginia Polytechnic Institute, Blacksburg, Virginia. Initial work was conducted for the U. S. Army Natick Laboratories, Natick, Massachusetts under Contract DA19-129-AMC-129(N), during the period of July 1963 to October 1966. Additional analyses and tests were conducted under Contract DA19-129-AMC-953(N) from May 1966 to May 1968. Data presented supplements and supersedes information shown in U. S. Army Natick Laboratories Technical Report 67-36-ME, "Wind Tunnel Tests and Analyses for Ground Mounted Air-Supported Structures", dated October 1966.

Mr. Constantin J. Monego, of the General Equipment & Packaging Laboratory at the Natick Laboratories, was the Army Project Engineer for this program. Mr. A. E. Dietz was the Program Manager, and Messrs. R. B. Proffitt, R. S. Chabot, and E. L. Moak were the principal investigators for the Hayes International Corporation. The assistance provided by Mr. C. J. Monego of the Natick Laboratories, Dr. R. T. Keefe and Prof. F. G. Maher of the Virginia Polytechnic Institute, and the personnel of the Technical Engineering Department of Hayes International Corporation are gratefully acknowledged. In particular, many thanks are due Mr. Joseph I. Bluhm, Chief, Applied Mechanics Research Laboratory, and his staff at the Watertown Arsenal, Watertown, Massachusetts, for review and analysis of this report, which resulted in many valuable comments and recommendations, and to Messrs. J. H. Flanagan, W. C. Whittlesey, and C. W. Weikert for their encouragement and support of this work.

TABLE OF CONTENTS

TABLE OF CONTENTS (Continued)

TABLE OF CONTENTS (Continued)

TABLE OF CONTENTS (Continued)

TABLE OF CONTENTS (Continued)

LIST OF TABLES

LIST OF FIGURES

LIST OF FIGURES (Continued)

LIST OF FIGURES (Continued)

LIST OF FIGURES (Continued)

LIST OF FIGURES (Continued)

LIST OF FIGURES (continued)

LIST OF FIGURES (Continued)

LIST OF FIGURES (Continued)

LIST OF FIGURES (Continued)

LIST OF FIGURES (Continued)

LIST OF FIGURES (Continued)

LIST OF FIGURES (Concluded)

ABSTRACT

The objective of this program is to provide tentage information based on wind tunnel test data that can be applied either to the evaluation and improvement of existing ground-mounted, air-supported tents or to the design of such future structures.

The program consisted of two study, test and analytical investigation phases, the first from July 1963 to October 1966, and the second from May 1966 to May 1968. This second report is a revised and expanded edition of a prior study entitled "Wind Tunnel Tests and Analysis of Ground Mounted Air-Supported Structures". During the study phase a review was made on pertinent literature on experimental techniques, data and analyses applicable to determining maximum aerodynamic force and stresses in fabric structures.

The first wind tunnel investigation consisted of detailed investigations of basic single-wall tent configurations constructed of porous and nonporous fabrics and double-wall tents. The tent configurations tested included shelter shapes such as spheres, cylinders with spherical ends, and cylinders with flat ends. This study was made to expand the scope of the report to include data on cylindrical shelters with elliptical ends, the bending stiffness of an inflated beam, vibration characteristics of single-wall and double-wall shelters, the effect of wind skirts on the ground anchors, and a study of factors to improve the stability of double-wall shelters.

Tests were conducted at stabilized wind speeds up to 110 miles per hour in the Virginia Polytechnic Institute's six-foot by six-foot stability tunnel. In the analytical phase, test data were used to develop fabric stress and aerodynamic coefficient data variation with tent parameters.

Results of the wind tunnel investigations and stress analyses have been incorporated and include comprehensive, practical design data suitable for engineering reliable, stable, single- and double-wall, air-supported shelters. Data, in general, are presented in nondimensional coefficient form, and, therefore, are applicable to full-scale shelters within the range of the parameters investigated. Design information is presented as charts and tables on shelter aerodynamic force and moment coefficients, anchor and guy line coefficients, structural deflection, vibration, and material stresses.

WIND TUNNEL TESTS AND ANALYSES FOR GROUND-MOUNTED, AIR-SUPPORTED STRUCTURES (Revised)

SECTION 1

INTRODUCTION

In March 1956, a revised edition of the Design Manual for Spherical Air Supported Radomes was published by Cornell Aeronautical Laboratory. Since its publication, air-supported structures of other than spherical shapes have been adopted by the Army. Design and fabrication of these tents have generally been limited to the semi-empirical methods outlined in the revised Design Manual for Spherical Air-Supported Tents and data estimated to cover other basic configurations.

In order to assist the tentage engineer to more accurately define the criteria for design of air supported structures, the U. S. Army Natick Laboratories contracted with Hayes International Corporation to formulate practical design criteria for single- and double-wall air supported structures. The program included a comprehensive analytical study and model wind tunnel tests resulting in a Design Manual for ground mounted air supported tents. A more rigorous solution to the analytical determination of fabric stresses is included in this investigation which, combined with the latest materials and accessory equipment information furnished by the Army, has produced more precise tentage design criteria than has heretofore been available to the Army designer.

The Design Manual has been prepared in two parts for the convenience of the user. Wind Tunnel Tests and Analyses for Ground-Mounted, Air-Supported Structures contains a detailed description of the wind tunnel test investigations and data reduction techniques, together with a comprehensive analytical determination of maximum fabric stresses through use of measured tent pressure distributions. Design Manual for Ground-Mounted Air-Supported Structures (Single- and Double-Wall) presents the results of the tests and analyses in a concise form of design tables and curves for both single- and double-wall tents together with sample problems illustrating the use of the data.

SECTION 2

GENERAL DISCUSSION

BACKGROUND

The art of tent making is thousands of years old. For centuries, through trial and error, man has constructed effective shelters for habitation and the housing of equipment. The evolution of this art has covered a myriad of configurations, but only recently has a way been found to eliminate the cumbersome weight of the supports through the use of inflation techniques. The forerunner of air-supported tents dates back to early World War II days when an external enclosure over a radar antenna was found desirable. This use was motivated by the necessity for protection of the radar installation from high winds. These early installations were small in size and the material used ranged from single sheets to molded plexiglas or plywood to multiple layers of sandwich-type construction. The first reported use of a resinimpregnated glass fabric as a radome material stemmed from an attempt to reduce the moisture absorption properties of plywood on the earlier models through the application of a thin protective overlay on the external surface of the radome.

Larger radomes were dictated for use on later World War II radar installations. The advent of radomes ranging in diameter from 35 to 55 feet arose from the necessity to extend the United States Air Defense after World War II to include radar detection systems located in arctic zones of operation. Operational radars of that time were designed to withstand only the wind loads and weather conditions encountered in temperate zones. Wind conditions in the Arctic were known to impose greater loads upon an antenna system and upon its pedestal than those for which the structure was designed. Therefore, it was decided to utilize radomes for environmental protection. Up until this time, the large radomes had been used only as expedient alternative to modification and strengthening of existing radar antenna structures. With the advent of arctic usage, the intrinsic merits of the light weight radome soon became obvious; i.e., environmental protection, reduction in power required to rotate large antenna systems in high winds, and reduction in size and weight of structural members at the cost of a small degradation in system performance due to the presence of the radome.

Modern scientific and technological developments made in military equipment and in support of a mobile army have resulted in the need for advanced tentage structures. The need for new tentage varies from highly specialized items for the missile program to large maintenance tents for ground vehicles and aircraft.

The use of air-supported tents, other than radome, represents one approach taken by the Army to provide shelters of reduced weight, cost, and cubage which can be easily transported, erected and struck for more mobile army operations. With the development of these air-supported

shelters, the technology of tent making is developing, step by step, from a traditional craft to a branch of scientific engineering.

Cornell Aeronautical Laboratories and Massachusetts Institute of Technology have performed several scale tests on radome and missile shelter models. Cornell has produced a Radome Design Manual for spherical radomes based on these tests. Design and fabrication of other than spherical tents has been accomplished largely by extrapolation of the design data contained in the Radome Design Manual and the individual designer's personal "feel" for the problem. A wind tunnel program was initiated to investigate a wide variety of models, both spherical and cylindrical, single-and double-wall. The data obtained from these tests have been reduced and put in parametric form to facilitate future tent design.

GENERAL CHARACTERISTICS

Air-supported structures present the modern mobile army with many advantages over rigid structures. Some of the more important advantages are listed below:

R F Transmissibility - The air-supported structure, as used to house radar antenna, due to its thin-walled construction, very nearly approaches the ideal shelter, i.e. a thin-walled homogeneous sphere. For this reason the same radome can be used for several systems of different frequencies.

Lightweight, Low Bulk and Cubage - The inherent characteristics of an air-supported structure provides a high structural efficiency, which results in very low package weight. Use of thin flexible material for the envelope permits the entire unit to be folded into a small package which facilitates shipment and storage.

Ease of Handling and Logistic Support - Due to its low weight and compactness, the air-supported structure is one of the most portable of all presently available shelters. The durability of the material used for the envelope minimized logistic requirements and maintenance. Standardization of the basic tent sizes reduces the inventory requirement and makes the air-supported structure adaptable to nearly all shelter requirements.

SECTION 3

WIND TUNNEL TESTS AND ANALYSIS

TEST FACILITY

A series of wind tunnel tests was conducted in the Virginia Polytechnic Institute's 6-foot by 6-foot Wind Tunnel (Figure 1) under the direction of the Hayes International Corporation. The VPI tunnel was designed and originally constructed at the Langley Aeronautical Laboratory of the National Aeronautics and Space Administration. The facility is classified as a continuous, closed jet, single return, subsonic wind tunnel with interchangeable round and square test sections. The tunnel is powered by a 600-hp d. c. motor driving a 14-foot propeller. Due to the presence of seven stainless steel turbulence screens in the settling chamber, the tunnel is capable of operating at a turbulence factor as low as 1.08. Effects of turbulence in the air flow are seen as an increase in test Reynolds number as compared to a similar test in free air.

The tunnel is equipped with a six-component, automatic null-balancing, mechanical system for measuring forces and moments associated with models mounted through the floor or sidewall of the tunnel, during static model tests. The output from this balance is fed into a readout printing system which allows the operator to read the six outputs as printed tabulation.

TEST ARTICLES

Model Configurations

A series of air-inflatable, single-and double-wall tents of various shapes were tested. The fabric used in the construction of the models was the highest fabric available and corresponded to approximately 1/10 existing full scale values, while model scales varied from approximately 1/20th to 1/40th full size.

Internal pressure was maintained within the models for support. A remote air supply, regulated in the tunnel control room, was used to provide these pressures within the cells and enclosure as shown in Figure 2. The enclosure pressure, P_e, for single-wall models was varied from 4/5 q to 5/4 q. Cell pressure, P_c, for the double-wall models was varied 5" to 30" H_2O. Free stream total and static pressures were measured and referenced to cell and enclosure pressures as shown in Figure 3. Enclosure pressure for double-wall models was maintained at free stream static values.

Single-wall models tested ranged in shape from spherical to cylindrical with spherical or elliptical ends, and width-to-length ratios of 1:1, 1:2 and 1:4. The height-to-diameter ratios varied from 3/8 to 7/8. Envelope material varied in porosity from 0 to 15 cu. ft./min. /ft.^{2} as shown on Table I.

Double-wall models tested were all cylindrically shaped. Height-to-diameter ratios varied from 3/8 to 3/4 for the cylindrical models and width-to-length ratios varied from 1:1 to 1:4. All double-wall models were constructed of non-porous material.

Tables I and II summarize all model configuration variables. Photographs of typical models are shown in Figures 4 through 9. A clearer illustration of the curtain arrangement is shown as Figure 10.

Model Parameters

In the design of wind tunnel test models it is of paramount importance to insure that all principal non-dimensional parameters are scaled relative to one another in the model as they are found in the full-scale tents. Wind tunnel models are also generally made to as large a scale as the test section of the tunnel will allow without inducing adverse tunnel blockage. In selecting the model designs for this program it was agreed that since the size of the full-scale tent is variable, each model configuration should be designed to the tunnel blockage factor and made as large as possible without regard to scale. To accomplish this prior to the design of the ground plane, an arbitrary figure of one square foot was assumed for the projected frontal area of the ground plane. Assuming a tunnel blockage factor of 10 percent, as recommended by Virginia Polytechnic Institute, and knowing the assumed ground plane frontal area, each model was designed to have maximum projected frontal area of 374 square inches.

The geometry of all existing proposed full-scale tents being unknown, the models were designed allowing engineering judgement and experience to relax the requirements for some parameters known or felt to be unimportant and provide a wide variety of tent shapes of interest to the Army for present and future application.

The design of a flexible model for wind tunnel testing is considerably more complicated than a normal rigid model, whose shape essentially does not change. To obtain aerodynamic and dynamic similarity the following parameters had to be kept the same for scale as for the full-size models.

Geometric Shape - For no wind conditions
Inflation Parameter- Ratio of inflation pressure to free system dynamic pressure
Reynold's Number - Ratio of inertia forces to viscous forces
Mach Number - Ratio of inertia forces to elastic forces
Froude Number - Ratio of inertia forces to gravity forces
Aeroelastic Parameter - Ratio of model diameter, fabric elongation and dynamic pressure to fabric stress
Dynamic Parameter - Ratio of model mass to air density and model diameter cubed

A model under conditions such that it has the same Reynolds and Mach numbers as its full scale counterpart will have forces and moments on it that can be directly scaled and flow patterns that are exactly the same. If the body in question is reacting to gravity, the model should also be maintained at the same Froude number as its full-scale counterpart.

The inflation parameter is of importance because it governs tent stability. This parameter was investigated, wherever possible, to determine the limits of tent stability. The dynamic parameter was allowed to vary with model sizing as the fabric used was the lightest fabric available of sufficient strength to construct the models and the model size was dictated by the maximum allowable for the test section used. Based on the limited observations of the effects of this parameter during these tests, it is recommended that the inflation parameter be maintained at a minimum of unity.

The aeroelastic parameter is important in matching the model deflections with those of the full-scale tents. Based on the fabric stress data computed from the pressure distributions, this parameter can be compared. However, no attempt was made to do so because of the overriding considerations of fabric weight and model sizing as cited above. However, since the bending stiffness of the model fabric is negligible, deflections noted in the models are considered similar to those of full-scale tents.

The Mach number parameter was irrelevant because of the low velocities used for this test series. Based on past experience, below a Mach number of 0.25, the elastic forces of air are at a minimum and can be neglected.

Therefore, the similarity parameters considered to be of major importance were the inflation parameter and Reynolds number.

The values selected for the inflation parameter were 4/5 q, 1.0 q and 5/4 q. In some cases, an estimate was made as to the value of P_e/q that was required to stabilize the tent. It was found that this determination was an individual estimate and therefore only the more severe cases of tent instability were evaluated. The single-wall non-porous tents were tested at all three values of the inflation parameter. The single-wall, porous tents were, in general, tested only at a value of 1.0 q. The double-wall tents were tested at values of P_c equal to 3q, 4q, and 5q.

The Reynolds number parameter determines the flow pattern as it is influenced by viscous effects. As major variation in flow usually occurs below certain critical values of this parameter, it was desirable to test the scale models above this critical value in order to provide more accurate extrapolation of test data to full scale. At the lower test velocity of 35 mph, several models fall below this critical value of Reynolds number, hence the test data does not lend itself to extrapolation as readily as the data obtained from the other models. These conditions were adjusted to bring model Reynolds number above the critical value and thereby enable the data from all models to be scaled to full-size tents. The Reynold's number for these tents was based on the model diameter. Based on that reference

length, past experience and aerodynamic theory predict the critical value of Reynold's number to be between 4.0 and 5.0 x 10^5. The critical Reynold's number establishes the lower values of test conditions in that major variations of flow occur below the test conditions specified by the critical Reynold's number. Test data below the critical Reynold's number have little or no potential for extrapolation to full scale tents and therefore were eliminated from consideration in the design curves.

The model fabric chosen was the lightest gage possible considering fabric flexibility requirements and fabrication. The fabric chosen may be scaled to full-size and is representative of those tents in service today. Fabric porosity was also varied in the construction of the tents to provide data of the influence of porosity on aerodynamic flow characteristics over the tent.

MODEL INSTALLATION

It was determined that more reliable data would be obtained by sting mounting the tent models on a ground plane and turntable arrangement suspended between the walls of the tunnel rather than by mounting them directly on the floor of the tunnel.

The optimum size of the ground plane for this particular tunnel is three times that of the longest model to be tested. The dimensions of the ground plane are, therefore, 72 inches wide by 195 inches long. The models, turntable etc., are mounted in the center of the ground plane within a 70 inch diameter circle. The boundary layer bleed flap was sized and located on the basis of the calculated boundary layer along the ground plane.

In order to better simulate the full scale tents, provision was made to enable the test conductor to exercise a limited amount of control, through adjustment of a bleed flap, over the boundary layer thickness in front of the model. To determine the desired setting for the bleed flap that best simulated actual conditions over the ground, a boundary layer survey was made. This survey investigated dynamic pressures at heights varying from the ground plane surface to approximately two inches above the surface for varying bleed flap settings. These dynamic pressures were plotted versus the height above the surface. The height at which the dynamic pressure recovers to 90 percent of the free stream is defined to be the upper limit of the boundary layer. The results of this survey are presented in Figure 11. The curve corresponding to slot openings of 1.0" and 1.5" was chosen for subsequent use as it was felt that this produced a flow profile which more closely approximated actual free air conditions. Therefore, the data from these tests are restricted to ground-mounted structures only.

The bases of the models were attached to the ground plane by means of cantilevered anchor springs fabricated from 17-4 PH steel heat treated to the TH1050 condition. Figure 12 shows typical strain gage installations at the anchor point and guy line positions. These anchors were spaced about the periphery of each model as shown in Figures 13 and 14. Double-wall

models were secured by guy lines in addition to the anchor springs. Also, one double-wall model was tested with wind aprons installed instead of guy lines.

The wind tunnel installation effects on aerodynamic loads were measured on the earlier tents by removing the tent and mounting base, covering the turn table and measuring the loads as the tunnel speed was varied through the test range. On the later models a dummy tent was constructed of plywood and fiberboard and suspended above the model base. Both methods were used at all test yaw angles and gave equally reliable results. These data were used to correct measured total forces and moments to tent alone measured data.

DATA RECORDING

Aerodynamic Forces and Moments

The tent model aerodynamic forces and moments were recorded in pounds and foot/pounds respectively in the wind axis system. The wind axis system has three orthogonal axes, one oriented in the direction of the wind with drag positive in the downstream direction, another oriented in the vertical direction with lift positive in the upward direction, and a third oriented in the lateral direction normal to the former two with side force positive to the right when looking upstream. These axes are fixed in the wind tunnel and do not vary with yaw angle. Wind tunnel balance data sign convention is presented in Figures 15 and 16.

Pressure Data

Pressure instrumentation was used to sense model test conditions, tent inflation, and tent pressure distribution. Ground plane pressure taps, boundary layer pressure measuring devices (rakes), tunnel wall static pressure taps and a pitot-static tube were used to establish tunnel stream flow conditions ahead of and around the tent models during model tests.

All models were instrumented with controllable inflation pressure provisions to provide enclosure and/or cell inflation pressure. Separate pressure lines were installed in the tents to sense tent enclosure and cell pressures.

Model surface pressure distribution was measured at selected points on the tent surface by installing small, flexible tubing within the model from many surface taps and routing them externally to manometer display boards. Due to the large number of pressure measurements made at each test condition and the requirement for instantaneous reading, the manometer tubes with test run information affixed thereto were photographed for each test condition for subsequent data reduction. Typical pressure tap locations are presented in Figures 17,18 and 19.

Tent Deflections

Tent deflection due to wind load was measured through use of fixed-position, still cameras located external to the test section. One camera provided instantaneous tent elevation film, the other plan view film. Film negatives of no-wind and test-wind conditions having the same enclosure (and cell) pressures were superimposed to provide accurate deflection measurement. Data were measured using a background grid and recorded to maximum deflection points at the front, top and rear of each tent using the symbols and sign conventions of Figure 20.

Tent Vibrations

In order to investigate horizontal vibratory motion of double-wall tents, very small, "Grain of Wheat" lamps were installed on the top centerline of four tents. Tent vibration and amplitude were recorded on movie film by photographing light traces made by the illuminated lamps operating in a dark field. A 70-mm streak-mode camera mounted above and external to the wind tunnel test section was used to photograph the motion. A timing light, actuated by a strobolux, provided a time reference on the film.

DATA PROCESSING

Processing the various type data from the uncorrected, as recorded, to the final corrected data stage required numerous hand and automatic computation steps. The major correction factors applied to the wind tunnel data along with the data reduction procedures are presented in this section.

DATA CORRECTIONS

Mechanical Balance

The results of the overall calibration of the wind tunnel installation at VPI indicated that there were several manufacturing and installation errors present in the mechanical linkage of the balance system. These errors were evaluated as interaction corrections and were applied to the various balance readings to give the true aerodynamic force and moment values.

Factor x Balance Readings	= True Readings
1.000 Lift Reading	= Lift
0.996 Drag Reading	= Drag
0.996 S. F. Reading + 0.004 Drag Reading	= Side Force
0.958 R. M. Reading + 0.015 Lift Reading + 0.054 S. F. Reading	= Rolling Moment
0.953 P. M. Reading - 0.010 Lift Reading + 0.028 Drag Reading - 0.019 R. M. Reading	= Pitching Moment
0.939 Y. M. Reading - 0.018 (Drag Reading - S. F. Reading)	= Yawing Moment

These equations are presented in order to show that for the test runs where one or more of the balance units were inoperative, the other readings were not appreciably affected.

Horizontal Buoyancy

The models tested were scaled only to the extent that the largest model permissible in the test section for each configuration considered was used.

The conditions imposed on the tent models tested in a wind tunnel are not the same as those found on full-scale tents in free air. This test program had the models mounted to a fixed ground plane with the air moving past the model. The longitudinal static pressure gradient usually present in the test section produced extraneous forces that were corrected.

Nearly all wind tunnels with closed test sections have a static pressure variation along the axis of the test section due to the thickening of the boundary layer as it progresses toward the exit cone. This pressure gradient is usually negative and hence there is a tendency for the model to be "drawn" downstream. This tendency of the model to be "drawn" downstream is known as "horizontal buoyancy" and is usually insignificant for wings and other relatively thin objects but may be a significant value for more blunt objects. In this test program, several pressure taps were installed along the tunnel walls adjacent to the model. For this special case, the longitudinal pressure gradient was a straight line (Figure 21) and the equation for this correction becomes:

$$D_B = \Sigma S_x \, (dp/d\ell) \, d\ell \qquad (1)$$

where S_x is the model cross-section area at station x, ℓ is the distance from the model nose and $dp/d\ell$ is the slope of the longitudinal static pressure curve. Since the summation of the model area times the incremental distances $\Sigma S_x d\ell$ is the body volume, this equation reduces to:

$$D_B = - \, (dp/d\ell) \, (\text{Body Volume}) \qquad (2)$$

Figure 21 presents the longitudinal static pressure gradient for a representative model tested in the VPI 6-foot by 6-foot tunnel. Taking the slope of this curve and using the volume of a representative test model, it was found that D_B should be approximately 3.6 pounds for this model installation.

Blockage

The other correction required to be made to the test data is due to the presence of a model in the test section which effectively reduces the area through which the air must flow, and hence in accordance with Bernoulli's law, increases the velocity of the air as it flows around the model. This increase of velocity in the vicinity of the model affects the

dynamic pressure, Reynolds number, pitching moment coefficient, lift coefficient and drag coefficient. A simple form of this blockage correction is:

$$\varepsilon_{SB} = \frac{K \text{ (model volume)}}{S_c^{3/2}} \tag{3}$$

where $K = 0.96$ for a body of revolution and S_c is the wind tunnel section area. Again using the same representative test model as was used for the "horizontal buoyancy" correction, it was determined that a representative value of ε_{SB} would be approximately 0.012.

The equations to be used for correction of the wall effects encountered in this program are summed below. The data with subscript "u" are uncorrected data based on free-stream dynamic pressure, with the exception of drag which must have the buoyancy correction applied before final correction due to "solid blockage".

$$U = U_u (1 + \varepsilon_{SB}) \tag{4}$$

$$q = q_u (1 + 2\varepsilon_{SB}) \tag{5}$$

$$R_N = R_{N_u} (1 + \varepsilon_{SB}) \tag{6}$$

$$C_L = C_{L_u} (1 - \sigma - 2\varepsilon_{SB}) \tag{7}$$

$$C_M = C_{M_u} (1 - 2\varepsilon_{SB}) + \frac{\sigma C_L}{4} \tag{8}$$

$$C_D = C_{D_u} (1 - 3\varepsilon_{SB}) \tag{9}$$

where $\sigma = \frac{\pi^2}{48} \frac{d}{h}^2$ is a model wake correction and "d" is the diameter of the model used.

DATA REDUCTION

The data reduction program was divided into five categories: aerodynamic balance data, anchor load data, external pressure distribution, tent deflection, and tent vibration. Data amenable to automatic data reduction was transferred to a prepared computer load sheet for data reduction on the IBM 360 model 30 computer located at Hayes International Corporation, Birmingham, Alabama. The equations used for this reduction are presented in the following sections.

Aerodynamic Coefficients

The aerodynamic force and anchor load data were reduced to dimensionless coefficient form by dividing the force in pounds by the product of dynamic pressure times the reference area. The aerodynamic moment data were similarly reduced to coefficient form by dividing by the product of dynamic pressure times the reference area times a reference length. These coefficients are defined as follows:

Coefficient	Equation	
Lift	$C_L = L/qA_p$	(10)
Drag	$C_D = D/qA_p$	(11)
Sideforce	$C_Y = P_y/qA_p$	(12)
Pitching Moment	$C_M = M/qA_{pd}$	(13)
Rolling Moment	$C_R = M_y/qA_{pd}$	(14)
Yawing Moment	$C_N = M_m/qA_{pd}$	(15)

The aerodynamic loads and moments used for computing the above coefficients are as follows:

Component	Equation	
Lift	$L = L_r - L_p - L_j$	(16)
Drag	$D = D_r - D_p - D_j$	(17)
Sideforce	$P_y = P_{yr} - P_{yp} - P_{yj}$	(18)
Pitching Moment	$M = M_r - M_p - M_j$	(19)
Rolling Moment	$M_y = M_{yr} - M_{yp} - M_{yj}$	(20)
Yawing Moment	$M_m = M_{mr} - M_{mp} - M_{mj}$	(21)

where the subscripts are defined below. These subscripts are not repeated elsewhere or in list of symbols.

Subscript "r" values are the total readings including contributions due to plate loads and jet flow loads, subscript "p" values are the plate loading contributions only. Subscript "j" values are the reactions due to the additional air flow into the tent enclosure during porous model tests. These values are slopes calculated from the data points in lbs. (or foot/lbs.) per in H_2O.

This program also computes the actual velocity from the tunnel indicated velocity, corrected for pressure, temperature, and Reynolds number as follows:

$$U = \sqrt{\frac{2q}{\rho}} \qquad \text{Velocity} \qquad (22)$$

$$R_N = \frac{\rho U d}{\mu} \qquad \text{Reynolds Number} \qquad (23)$$

Additional corrections were made to the data for the effects of the wind tunnel boundary conditions. The boundary corrections required for the special case of a model mounted on a ground plane were reduced to two. These were solid blockage and horizontal buoyancy. The equations used are as follows:

$$U_\infty = U_u \ (1 + \varepsilon_{SB}) \qquad (24)$$

$$q_\infty = q_u \ (1 + 2\varepsilon_{SB}) \qquad (25)$$

$$R_{N\infty} = R_{Nu} \ (1 + \varepsilon_{SB}) \qquad (26)$$

$$C_L = C_{Lu} \ (1 - \sigma - 2\varepsilon_{SB}) \qquad (27)$$

$$C_M = C_{Mu} \ (1 - 2\varepsilon_{SB}) + \frac{C_L}{4} \qquad (28)$$

$$C_D = C_{Du} \ (1 - 3\varepsilon_{SB}) \qquad (29)$$

where

subscript "u" terms are the uncorrected data based on wind tunnel upstream conditions.

$$\varepsilon_{SB} = \frac{K\overline{V}}{(A_c)^{3/2}} \tag{30}$$

$$\sigma = \frac{\pi^2}{48}\left(\frac{d}{h}\right)^2 \tag{31}$$

where

K = constant 0.96 for bodies of revolution
$\overline{V}$ = tent enclosed volume
A_c = wind tunnel cross section area
d = diameter of model
h = height of wind tunnel test section

The drag coefficient, C_{Du}, based on free stream conditions includes a correction for horiztontal buoyancy. This correction was made as follows:

$$C_{Du} = \frac{D - D_B}{q_u A_p} \tag{32}$$

where

D = net drag

$D_B = -\frac{dp}{d\ell}\ \overline{V}$

q_u = free stream dynamic pressure

A_p = reference area, maximum planform

$\frac{dp}{d\ell}$ = slope of tunnel longitudinal static pressure curve

Model volume for single wall models was computed as follows:

$h > d/2$,

$$\overline{V} = \frac{\pi}{6} d^3 - \frac{\pi}{48} d^3 + \frac{\pi}{3} r_B^2 (h - d/2) + \pi r_2 (\ell_h - 2r) - \frac{r_2}{2\ 2} (\theta - \sin\theta)(\ell - 2r) \tag{33}$$

$h < d/2$,

$$\overline{V} = \frac{2}{3}\pi h \frac{d}{2}^2 - \frac{\pi}{3} r_B^2 (d/2 - h) + \frac{r^2}{2}(\theta - \sin\theta)(\ell_h - 2r_B) \tag{34}$$

where

$$r_b = \sqrt{h\ (d-h)}$$

$h = d/2$

$$\overline{V} = \frac{\pi}{12}\ d^3 + \frac{\pi}{2}\ (r)^2\ (\ell - 2r) \qquad (35)$$

where

r = tent radius

h = tent height, feet

d = diameter, feet

θ = base angle

ℓ_h = length

The maximum planform area for single-wall models was computed as follows:

hemispherical ends,

$$A_p = \pi\ r^2 + 2r\ (\ell_h - 2r) \qquad (36)$$

elliptical ends,

$$A_p = \pi\ ab \qquad (37)$$

where

a = elliptical-end semi-major axis length

b = elliptical-end semi-minor axis length

r = tent radius, feet

ℓ_h = tent length, feet

A_p = planform area, square feet

In the equations for volume and the equations for planform area, model radius and diameter divided by 2 were considered independent numbers in order to make the equations apply to both spherical and cylindrical models.

The final correction made to the aerodynamic balance data was to transform from wind axes to body axes for models oriented at yaw angles of $\psi = 45$. The relationship between wind axis and body axis is presented in Figure 16 . For $\psi = 0^{\circ}$ and 90° , no correction was necessary.

The equations transformed to the body axes are

Coefficient	Equation	
Lift	$C_{LB} = C_L$	(38)
Drag	$C_{DB} = C_D \cos\psi - C_Y \sin\psi$	(39)
Sideforce	$C_{YB} = C_Y \cos\psi - C_D \sin\psi$	(40)
Pitching Moment	$C_{MB} = C_M \cos\psi - C_R \sin\psi$	(41)
Rolling Moment	$C_{RB} = C_R \cos\psi - C_M \sin\psi$	(42)
Yawing Moment	$C_{NB} = C_N$	(43)

Pressure Coefficients

The static pressure distribution data were reduced to coefficient form in like manner to the aerodynamic data using the following equation:

$$C_p = \frac{P_\ell - P_\infty}{q_\infty} \qquad (44)$$

where

C_p = pressure coefficient

P_ℓ = Local static pressure at model surface

P_∞ = tunnel static pressure

q_∞ = tunnel dynamic pressure

Pressure distribution over the model and the base mounting plate was measured at many points. The relative locations of these points varied from model to model. Typical locations are presented in Figures 17 through 19.

Anchor, Guy Line and Curtain Load Coefficients

Using measured anchor, guy line or curtain loads, load coefficients were computed for each active gage used. The corrected loads were computed by first calibrating each active gage with four known loads of 1 lb., 6 lb.,

11 lb., and 16 lb. The slope of the calibration curve obtained was then computed in lb./micro-inches per inch load and multiplied times the strain recorded by that gage under consideration to obtain the applied load. The load coefficients were then computed as follows:

$$C_{AL} = \frac{AL}{qA_p}, \quad C_{GL} = \frac{GL}{qA_p}, \quad C_{CL} = \frac{CL}{qA_p} \qquad (45\ (a,b,c))$$

where

AL = anchor load, lbs.

GL = guyline load, lbs.

CL = curtain load, lbs.

q = dynamic pressure, lbs./ft.^{2}

A_p = planform area, ft.^{2}

The computed loads were summed for each test condition and printed as total aerodynamic and inflation load. These loads were then corrected for inflation loads and printed out as aerodynamic loads. The aerodynamic loads shown include a correction for the fact that not all anchors were "active" or measured strain. This correction was a multiplication factor composed of a ratio of total to active anchor points employed.

The inflation loads used were computed by recording the strain for each gage corresponding to tent inflation pressures of 2 in., 4 in., and 6 in. of water for the single-wall tents and tent cell pressures of 5 in., 6 in., and 30 in. for double-wall tents. Gage readings were converted to anchor loads by multiplying recorded strain values by the slope of the calibration curve for each gage. These individual loads were then summed to give total inflation loads for all test conditions. Figures 13 and 14 present the planform lay-out of the gage locations for two typical models.

Tent Deflections

Using the measured data extracted from superimposed cut-film negatives of the no wind and test condition, corrections were applied to correct for camera position relative to the tent and grid locations. Maximum tent deflection data were then computed and plotted as a ratio of tent deflection to tent radius, δ/r, versus the ratio of tent height to diameter, h/d, for all models tested. These data are usable in determining maximum usable cubage inside the tent structure.

Tent Vibration

Tent vibration data were recorded for two double-wall tent

configurations. Each configuration was investigated for two different cell sizes. Tent frequency and amplitude were photographically recorded by a 70-mm streak mode camera mounted above and external of the wind tunnel test section. The film records were enlarged and manually read to obtain tent frequency and amplitude of oscillation. A timing light actuated by a strobolux provided a time reference on the 70-mm film. Data, as presented, shows double amplitude (peak to peak) values versus cell pressure for horizontal motion in a direction perpendicular to the long axis of the tent. Motion along the long axis of the tent (end to end) was intermittent and small compared with the fore and aft movement.

Data Presentation

Upon completion of the wind tunnel data reduction, results were prepared in tabular and graphical form for both single and double-wall tents. A discussion of the data as presented herein follows:

Tent Lift

From the lift coefficient data for single wall spheres, it can be seen in Figure 22 that C_L increases almost linearly with the ratio of height-to-diameter for single-wall spheres. Increased fabric porosity resulted in increased C_L for this shape.

Cylindrical single-wall tents exhibit a minimum lift coefficient at a height-to-diameter ratio of 0.5, as shown in Figures 23 and 24 . Also, for a W/ℓ_h of 1:2, the C_L at $h/d \leq 0.5$ for a non-porous tent is more moderate than for a W/ℓ_h = 1:4. The reverse is true when $h/d > 0.5$.

Figure 25 shows the effect of using elliptical ends instead of hemispherical ends on single-wall tents. Due to a more efficient aerodynamic shape, the lift coefficient is increased considerably.

Double-wall, cylindrical shapes also show an increase in lift coefficient as h/d and W/ℓ_h increases, as can be seen from Figure 26 . A width-to-length ratio of 1:4 results in a much higher C_L than that of W/ℓ_h = 1:1 or 1:2.

Figure 26 illustrates the effect of guy lines on tent lift coefficient. Benefits of guy lines become more pronounced with increased tent h/d.

Figure 27 presents a comparison of lift coefficient data for a non-porous double-wall tent (1:2 W/ℓ_h, 1/2 h/d) equipped with guy lines, curtains (in lieu of guy lines), and with base anchors only. The lift coefficient (based on basic tent Ap) for the curtain equipped tent is seen to double for the tent with side and end curtains and triple for the side-curtain equipped tent. The additional lift coefficient is due primarily to the increased surface area; however, the end curtain design could not be maintained taut and spoiled some of the additional lift generated.

Tent Drag

Single-wall, spherical shapes show an increase in drag coefficient with increasing h/d as presented in Figure 28. Slight fabric porosity reduces C_D, whereas further increase in porosity increases C_D back to non-porous C_D values.

Single-wall cylindrical shapes of 1:2 width-to-length ratios (Figure 29) indicate an increase in C_D with increasing h/d, but have C_D values lower than shapes of W/ℓ_h = 1:4 (Figure 30). Increasing fabric porosity increases the C_D for cylindrical shapes.

The effects of tent end shape and direction of prevailing wind on the drag coefficient of single-wall cylinders of 1:2 W/ℓ_h are seen in Figures 31 and 32. A quartering wind generally produces the highest drag coefficient. Elliptical end tent design creates a small increase in drag coefficient when compared with the standard hemispherical end tents. This design feature was investigated to eliminate non-usable end space and reduce weight while maintaining acceptable loading characteristics during high winds.

Double-wall shapes, as shown in Figure 33, with an h/d less than 0.5 exhibited lower drag coefficients than did the single-wall shapes. However, an increase in h/d above 0.7 resulted in higher C_D's for the double-wall shapes. Use of guy lines provides some reduction in drag coefficient. Variation in width to length ratio caused a moderate increase in C_D with an increase in W/ℓ_h.

Figure 34 presents the drag coefficient increase due to use of curtains instead of guy lines. A comparison of tent anchored, anchored and guyed, and anchored with curtains is shown for double-wall tents of 1:2 W/ℓ_h.

In summary, it appears that spherical single-wall tents exhibit the lowest drag coefficient with h/d. Use of elliptical ends or wind curtains on tents cause an increase in drag coefficient. An increase in W/ℓ_h or h/d results in an increase in drag coefficient for cylindrical models.

Tent Pitching Moments

Moment coefficients for single wall spherical tents are quite low at low h/d values, and increase to a fairly constant value at h/d 0.5. Increasing porosity to 0-5 resulted in the lowest values of C_M while a further increase in porosity increased C_M to near the non-porous values (Figure 35).

Single-wall cylindrical shapes show an increase in C_M with increasing h/d values. Increasing W/ℓ_h ratios raise C_M values markedly. Fabric porosity values of 0-5 and 10-15 reduce the C_M considerably in W/ℓ_h ratios of 1:2 and cause a moderate decrease in C_M at W/ℓ_h ratios of 1:4 (Figures 36 and 37). Figure 38 presents a comparison of non-porous single-wall tent moment coefficient variation with W/ℓ_h and h/d.

Double-wall shapes have a moderate, linear increase in C_M with increasing h/d ratios (Figure 39). The moment coefficients decreased slightly with a change in W/ℓ_h ratio from 1:1 to 1:2, but showed a marked decrease with a W/ℓ_h ratio of 1:4. Figure 40 shows the decrease in C_M brought about through the use of guy lines. Figure 41 shows the increased C_M produced when curtains replace guy lines as tie downs.

Tent Anchor, Guy Line and Curtain Loads

Base anchor loads of a fabric shelter are the result of aerodynamic forces acting on the tent external surface and the pressure within the enclosure and/or cell. Data is presented as anchor load coefficient. Figure 42 illustrates the typical effect of wind direction on anchor load coefficient and shows some independence of orientation. Figure 43 presents a comparison of maximum anchor load coefficient for 1/2 cylindrical 1:2 single-wall tents, with elliptical and hemispherical ends, considering all wind orientations. Figure 44 presents the anchor load coefficient variation for a double-wall tent. Anchor load coefficient data variation with tent shape is shown in Figures 45, 46 and 47.

Tent guy line coefficient is used to determine guy line loads and guy line vertical anchor loads for double-wall tents. These data are presented in Figure 48 and represent maximum aerodynamic loading with inflation pressure effects eliminated. Enclosure pressure is another variable which influences guy line loads and must be considered jointly when determining total guy line loading.

Figure 49 presents the effect of using curtains in lieu of guy lines on double-wall tents. Data indicated no measurable change with side curtains only but an astronomical load increase due to increased aerodynamic efficiency and size when compared with a tent tied down with guy lines.

Tent Deflection

Maximum tent deflection data are shown as a ratio of tent deflection-to-tent radius, δ/r, versus the ratio of tent height-to-tent diameter. Deflection data is presented for areas at the front, top and rear of each tent using the symbols and sign convention of Figure 20.

Figure 50 shows the effect of tent shape and fabric porosity on tent deflection for single-wall spheres. Tent deflection increases with tent h/d and reduces with increased fabric porosity. Figures 51, 52, and 53 presents similar data for single-wall cylindrical tents of 1:2 and 1:4 W/ℓ_h respectively. Generally, tents with a h/d of approximately 0.5 have the smallest deflections. Spherical single-wall tents have smaller overall deflections than the cylindrical tents.

The effect of porous fabric on reducing tent deflection was investigated only with single-wall tents. Non-porous fabric was used only in the construction of the double-wall tents. The independent effects of cell size, cell pressure and enclosure pressure on tent deflection for a 3/4

cylindrical, double-wall tent of 1:1 W/ℓ_h were investigated to determine their effectiveness.

Figure 54 shows the effect of cell size and pressure on deflection for a constant dynamic pressure of 6" w.g. for a 3/4 cylinder, 1:1 W/ℓ_h having guy lines attached at 0.8 tent height. Tent frontal deflection is improved slightly with increased cell size and considerably with cell pressure. Figure 55 shows the effect of additional guying (0.8 and 0.4 tent height) on reducing tent deflection for the same tent size. Figure 56 shows the additional reduction in tent deflection produced by pressurizing the enclosure volume as well as the tent cells.

Figure 57 presents data for double-wall tents tested in the anchored only and in the anchored and best guy configurations. A more comprehensive number of tent shapes and sizes of single-wall tents were tested than for the double-wall case. Hence, it is felt that the double-wall data is not as well established, so the curves appear as straight lines connecting a minimum of data points. Additional double-wall tent configurations are required to better define curve variation. Due to the general concave curve shape for the single-wall tents; however, it is believed that the double-wall data is conservative in the h/d range of 0.5 to 0.6, and possibly less conservative at higher h/d values.

Figure 58 presents a comparison of deflection data for the various methods of tent restraint; i.e., base anchor only, base anchors and guy lines, and base anchors and wind curtains. Data is presented for a double-wall cylinder 1:2 W/ℓ_h. The data indicates mandatory use of either guys or curtains under wind conditions. The anchor and guy line combination provides the best restraint combination.

Tent Stability

As part of the test program, tent stability was qualitatively investigated by defining instability as any set of conditions producing tent deflection and vibration which, when coupled together, provided objectionable tent motion. Degree of motion was determined visually during wind tunnel tests. In addition, motion pictures were examined of prior wind tunnel tests. For selected double-wall tents, 70-mm streak mode camera dynamic test data was taken. The effects of changes of fabric porosity, enclosure pressure, cell size and pressure, and guy line location were evaluated where applicable. The following general conclusions may be made relative to tent stability and vibration characteristics.

The single tent configurations, with the exception of the 7/8 sphere and all 1:4 width-to-length ratio cylindrical tents, were found to be very stable. For the cylindrical single-wall tents, motion is more pronounced with a wind at 45 degrees attitude. Other spherical and the 1:2 width-to-length ratio cylindrical configurations exhibited very stable properties at all test conditions. The elliptical end tent appeared to be more stable than the hemispherical end tents.

The double-wall tents had flat ends which contributed to flow separation and less stability than the single-wall tents with hemispherical ends. The 3/4 cylindrical, 1:1 width-to-length tents were not 'true' cylindrical tents but, rather, had flat sides which may have contributed to this configuration's exceptionally low stability.

To minimize double wall tent corner deflection and motion, which occur primarily when the tent is oriented 45 degrees to the wind (corner into the wind), guy lines should be attached to each corner of the tent at a point 0.8 tent height to make an angle of approximately 45 degrees with the ground. Corner and end deflections were more pronounced on the double-wall tents and is believed to be aggravated by the flat ends of the double-wall tents. The best guy line configuration consists of a combination high (0.8 tent height) and low (0.4 tent height) line arrangement, with the upper guy lines angled 45 degrees to the tent side and the lower guy lines perpendicular to the tent side when viewed from the top of the tent. When some deflection and vibration is acceptable, the tent shapes tested withstood hurricane force winds without the use of guy lines.

Cell pressure (enclosure pressure for single-wall tents) is an important factor in controlling tent motion. Although permissible tent deflection, as required by tent usage, could establish pressure requirements, tests indicated that only for cell pressures equal to, or in excess of, the tent dynamic pressure did both good stability and deflection characteristics exist. From a stability standpoint, at 110 miles per hour, no significant gains were achieved beyond an inflation pressure of 16 inches water gage; since, insignificant deflection reductions occurred for cell pressures between 16 inches water gage and 30 inches water gage.

Tent cell size was also observed to be a factor in providing better tent stability since an increase in cell size was more rigid for the same cell inflation pressure. A prime consideration in increasing cell size is that, for the same enclosure volume, the tent overall size and weight increase rapidly.

Double-wall tent enclosure pressure should be maintained at ambient or low positive pressure to preclude cell buckling. Test with enclosure pressure less than ambient exhibited a critical buckling tendency on the windward (forward) side of the tent.

Amplitude and frequency of double-wall tent motion were investigated to provide base line data for future evaluation of fabric fatigue. Figures 59 through 61 show natural frequency and deflection of the horizontal tent motion in the direction perpendicular to the long axis of the tent. Deflection data on these curves represent peak to peak amplitude, superimposed on basic tent deflection values. Figure 59 shows tent dynamic motion variation with cell pressure for two tent configurations with two cell sizes, each without guy lines installed. Figure 60 presents similar data with guy lines installed and Figure 61 presents a comparison plot for a cell size of 0.082. Tent natural frequencies as high as 59 cps were recorded and appear independent of guy line configuration for tents with $W/\ell_h \geq 1{:}2$. Amplitude of the vibration was greater for the unguyed tents.

SECTION 4

STRUCTURAL DESIGN

SINGLE-WALL TENTS

Introduction

The analytical determination of stress distribution in any membrane under nonuniform pressure loading requires a satisfactory analytical representation of the pressure distribution which can then be applied to a suitable shell theory. Expressions for wind loading on spherical, ellipsoidal, and cylindrical surfaces were obtained which are considered to be reasonable approximations, relative to the experimental pressure data, for the purposes of this analysis.

In the past, the tent designer has had to use a crude stress analysis and a large factor of safety to conveniently provide structure capable of carrying a given wind load. However, the need to optimize tent structures has created the desire for a more refined analysis of stresses. Although the present analysis is approximate, it is a significant step in refining the structural analysis of air-supported tents.

Application of the Membrane Theory of Shells to Inflated Tents

Although this analysis uses the membrane theory of shells to determine internal loads in the fabric structure of inflated tents under wind load, there are some obvious errors in its application. Whereas the membrane theory of shells is predicated on a homogeneous, elastic material having inherent shear resistance and an equilibrium condition which assumes no distortion of the membrane, a single-ply fabric is inherently capable of resisting only biaxial tension loads in the directions of the weave fibers. However, in the case of an inflated fabric structure, when tensile stresses are present due to internal pressure, external compressive loads may be taken by a reduction in tensile stress. If tensile stress is relieved to the point where the material fibers try to go into compression, the fabric in this area will develop wrinkles normal to the direction of zero stress.

Although typical past design criteria have required the inflation pressure to be maintained at a sufficiently high level to keep the fabric in tension in all areas in order to prevent such wrinkles, such a requirement may be unnecessarily severe. The relief of tensile stress in one principal direction of the fabric weave, due to external compressive load, may cause some increase in tensile stress in the other weave direction from load redistribution; but this increased stress will be no greater, and probably considerably less, than the additional stress induced by increasing the inflation pressure to eliminate wrinkles. It is further noted that local buckling of this type may be readily tolerated, especially under extreme operating conditions, since the deflections can not constitute failure and would be expected to bring about reduction in peak stress values.

To accommodate shear load as a component of diagonal tension without the excessive distortion caused by reorientation of the weave fibers, the usual practice in tentage design is to select a fabric of two-ply construction with the bias ply oriented at an angle of 45 degrees with respect to the other ply. Although this appreciably reduces the distortion, the fabric does not follow the linear membrane theory. A nonlinear theory has been initiated, but much work remains to be done to make it a practical analysis technique. Despite the inadequacies of the linear membrane theory in its application to inflated fabric structures, it is the best analysis technique presently available.

Pressure Distribution

The fabric loads analysis which follows was based on measured external pressure distributions obtained during the wind tunnel test series. The method of measurement chosen was to section the tent off by rows and columns. At the intersection of each row and column, a lightweight tube was attached to the fabric on the inside of the envelope. A small orifice was then drilled through the fabric and into the tube thereby forming a surface static pressure tap. The number of pressure taps per tent model was determined primarily by the model size with some consideration being given to areas of constant pressure distribution. The locations of the pressure taps for two models are presented in Figures 17 and 18.

The method of measurement of the test pressures and the details of data reduction are discussed in SECTION 3. These tests indicate somewhat different pressure distributions than those around tower mounted radomes due to the presence of the ground plane. The boundary layer associated with the ground plane is discussed in SECTION 3; however, it is noted that the boundary layer thickness was adjustable and was set at values deemed reasonable for ground-mounted structures. A discussion of model similarity and data extrapolations is also discussed in SECTION 3.

Past work on spherical radomes has approximated wind load distribution with a three-term trigonometric series, assuming symmetry about the wind axis. Comparison with higher degree series utilizing wind tunnel data shows that a considerably better approximation can be obtained with an eight term expansion.

Spherical Tents

To express the pressure distribution analytically, it is necessary to determine the angles ϕ and θ. See Figure 62(a). They were determined from the models as follows.

$$\left.\begin{aligned} \phi &= S_\phi / r \\ \theta &= 2\pi N \end{aligned}\right\} \quad (46)$$

where S_ϕ is the arc length from vertical axis of rotation to angle ϕ in a meridional plane containing vertical axis of rotation, and N is the number of columns around the spherical model. Columns are the grid lines in the meridional direction.

$$\left.\begin{aligned} \sin \phi_B &= \sqrt{1 - [(d-2h)/r]^2} \\ \cos \phi_B &= (d-2h)/d \end{aligned}\right\} \quad (47)$$

For the purpose of spherical shell membrane analysis, the wind load can be expressed as a trigonometric series in the angles ϕ and θ (assuming symmetry about the plane $\theta = 0, \pi$)

$$P_{ext}/q = \sum_0^N A_n \sin^n \phi \cos^n \theta = \sum_0^N p_n (\phi) \cos n\theta \quad (48)$$

where P_{ext} is the pressure on shell surface minus free-stream static pressure and q is the dynamic pressure. Through a computerized curve-fit program using the principle of least squares, it was determined that N = 7 yields best results with regard to accuracy of fit and time expended. The computer program uses polynominal curves of the form

$$P_{ext}/q = \sum_0^N A_n X^n \quad (49)$$

Setting $X^n = \sin^n \phi \cos^n \theta$, N = 7,

$$\left.\begin{aligned} X^0 &= 1 \\ X &= \sin \phi \cos \theta \\ X^2 &= \tfrac{1}{2} \sin^2 \phi (1 + \cos 2\theta) \\ X^3 &= \tfrac{1}{4} \sin^3 \phi (3 \cos \theta + \cos 3\theta) \\ X^4 &= 1/8 \sin^4 \phi (3 + 4 \cos 2\theta + \cos 4\theta) \\ X^5 &= 1/16 \sin^5 \phi (10 \cos \theta + 5 \cos 3\theta + \cos 5\theta) \\ X^6 &= 1/32 \sin^6 \phi (10 + 15 \cos 2\phi + 6 \cos 4\theta + \cos 6\theta) \\ X^7 &= 1/64 \sin^7 \phi (35 \cos \theta + 21 \cos 3\theta + 7 \cos 5\theta + \cos 7\theta) \end{aligned}\right\} \quad (50)$$

Collecting like terms of cos n θ,

$$\left.\begin{aligned} p_0 &= A_0 + 1/2\, A_2 \sin^2 \phi + 3/8\, A_4 \sin^4 \phi + 5/16\, A_6 \sin^6 \phi \\ p_1 &= A_1 \sin \phi + 3/4\, A_3 \sin^3 \phi + 5/8\, A_5 \sin^5 \phi + 35/64\, A_7 \sin^7 \phi \end{aligned}\right\} \quad (51)$$

$$
\left.
\begin{aligned}
p_2 &= 1/2\ A_2 \sin^2\phi + 1/2\ A_4 \sin^4\phi + 15/32\ A_6 \sin^6\phi \\
p_3 &= 1/4\ A_3 \sin^3\phi + 5/16\ A_5 \sin^5\phi + 21/64\ A_7 \sin^7\phi \\
p_4 &= 1/8\ A_4 \sin^4\phi + 3/16\ A_6 \sin^6\phi \\
p_5 &= 1/16\ A_5 \sin^5\phi + 7/64\ A_7 \sin^7\phi \\
p_6 &= 1/32\ A_6 \sin^6\phi \\
p_7 &= 1/64\ A_7 \sin^7\phi
\end{aligned}
\right\} \quad (51)
$$

A typical pressure distribution is shown in Figure 63.

Cylindrical Portion of Cylindrical Tents

The broadside wind load is considered to be the most critical for the cylindrical portion of a tent. There is assumed to be no variation in the wind load to x (the distance along the axis of the cylinder) so that the pressure coefficient expression takes the form (see Figure 64)

$$
P_{ext}/q = \sum_{0}^{N} A_n \sin^n \phi \qquad (52)
$$

As was done for the spherical shell distribution, the assumed curve is fitted to the wind tunnel data through a least squares analysis.

Spherical Ends of Cylindrical Tents

To express the pressure distribution on the spherical ends of the cylindrical models, it was necessary first to determine the angles α and β and then convert to ϕ, θ coordinates. See Figure 62(b). The angles α and β were found from the models as follows.

$$
\left.
\begin{aligned}
\alpha &= S_\alpha / r \\
\beta &= S_\beta / r
\end{aligned}
\right\} \quad (53)
$$

where S_α is the arc length from stagnation axis for yaw angle equals 90°

to angle α in a meridional plane containing stagnation axis, and S_β is the arc length from vertical axis of rotation to angle β in the plane normal to the stagnation axis and containing vertical axis.

The conversion from α, β to ϕ, θ coordinates takes the following form. See Figure 62(c). Note that ψ and θ are positive counter-clockwise from wind direction.

$$\cos \alpha = \sin \phi \quad \cos \left(\frac{\pi}{2} - \psi + \theta \right) \tag{54(a)}$$

$$\sin \alpha \sin \beta = \sin \phi \sin \left(\frac{\pi}{2} - \psi + \theta \right) \tag{54(b)}$$

$$\cos^2 \left(\frac{\pi}{2} - \psi + \theta \right) = 1 - \sin^2 \left(\frac{\pi}{2} - \psi + \theta \right) = \cos^2 \alpha / \sin^2 \phi \tag{54(c)}$$

$$\sin^2 \left(\frac{\pi}{2} - \psi + \theta \right) = \sin^2 \alpha \sin^2 \beta / \sin^2 \phi \tag{54(d)}$$

Adding Equations 54(c) and 54(d) gives

$$\frac{\cos^2 \alpha + \sin^2 \alpha \sin^2 \beta}{\sin^2 \phi} = 1 \tag{55(a)}$$

$$\sin^2 \phi = 1 - \cos^2 \phi = \cos^2 \alpha + \sin^2 \alpha \sin^2 \beta \tag{55(b)}$$

$$\cos^2 \phi = 1 - \cos^2 \alpha - \sin^2 \alpha \sin^2 \beta = \sin^2 \alpha (1 - \sin^2 \beta) \tag{55(c)}$$

$$\cos \phi = \sin \alpha \cos \beta \tag{55(d)}$$

$$\phi = \cos^{-1} (\sin \alpha \cos \beta) \tag{55(e)}$$

Equation 54(c) by identity is

$$\cos^2 \left(\frac{\pi}{2} - \psi + \theta \right) = \cos^2 \alpha / (1 - \cos^2 \phi) \tag{56}$$

By substitution of Equation 55(d)

$$\cos^2 \left(\frac{\pi}{2} - \psi + \theta \right) = \frac{\cos^2 \alpha}{1 - \sin^2 \alpha \cos^2 \beta} \tag{57}$$

$$\left.\begin{aligned} \cos\left(\tfrac{\pi}{2} - \psi + \theta\right) &= \frac{\cos\alpha}{\sqrt{1 - \sin^2\alpha\cos^2\beta}} \\ \theta &= \cos^{-1}\left[\frac{\cos\alpha}{\sqrt{1 - \sin\alpha\cos\beta}}\right] + \psi - \frac{\pi}{2} \end{aligned}\right\} \quad (57)$$

Now the pressure data can be expressed in terms of ϕ and θ, and the solution obtained as it was for the spherical models.

Ellipsoidal Ends of Cylindrical Tents

It was decided to analyze the ellipsoidal ends by affine transformation to a fictitious spherical shell. To facilitate analysis after the transformation, it was desirable to obtain the wind load on the sphere in the form previously given for the spherical tents, i.e.,

$$P_{ext} = q \sum_{0}^{N} A_n \sin^n \phi^* \cos^n\theta^* = q \sum_{0}^{N} p_n(\phi^*) \cos n\theta^* \qquad (58)$$

Here, the asterisk superscript denotes the fictitious spherical coordinates (See Reference 10, pp. 191-205). To determine the required function for the wind load acting normal to the ellipsoidal shell, then, the following development was made. Pertinent coordinates systems are shown in Figure 65.

$$\left.\begin{aligned} \tan\theta^* &= y^*/x^* = (y/\lambda_2)(x/\lambda_1) = (\lambda_1/\lambda_2)(y/x) = (\lambda_1/\lambda_2)\tan\theta \\ \theta^* &= \tan^{-1}\left[(\lambda_1/\lambda_2)\tan\theta\right] = \cos^{-1}\left(1/\sqrt{1 + (\lambda_1/\lambda_2)^2\tan^2\theta}\right) \\ \cos\theta^* &= 1/\sqrt{1 + (\lambda_1/\lambda_2^2)\tan^2\theta} = \lambda_2\cos\theta/\sqrt{\lambda_1\sin^2\theta + \lambda_2^2\cos^2\theta} \\ \sin\phi^*/\sin\phi &= (dz^*/ds_\phi^*)/(dz/ds_\phi) = ds_\phi/ds_\phi^* \end{aligned}\right\} \quad (59)$$

From Reference 10, p. 202,

$$\sin \phi^*/\sin \phi = \sqrt{(\lambda_1^2 \cos^2 \theta^* + \lambda_2^2 \sin^2 \theta^*)\cos^2 \phi^* + \sin^2 \phi^*} \qquad (60(a))$$

$$\sin^2 \phi^*/\sin^2 \phi = (\lambda_1^2 \cos^2 \theta^* + \lambda_2^2 \sin^2 \theta^*)\ (1 - \sin^2 \phi^*) + \sin^2 \phi^* \qquad (60(b))$$

$$\sin^2 \phi^* = \frac{(\lambda_1^2 \cos^2 \theta^* + \lambda_2^2 \sin^2 \theta^*)\sin^2 \phi}{1 - \sin^2 \phi + (\lambda_1^2 \cos^2 \theta^* + \lambda_2^2 \sin^2 \theta^*)\ \sin^2 \phi} \qquad (60(c))$$

$$\sin^2 \phi^* = \frac{(\lambda_1^2+\lambda_2^2\tan^2 \theta^*)\ \cos^2 \theta^* \sin^2 \phi}{\cos^2 \phi + (\lambda_1^2 + \lambda_2^2 \tan^2 \theta^*)\ \cos^2 \theta^*\ \sin^2 \phi} \qquad (60(d))$$

$$\sin^2 \phi^* = \frac{\lambda_1^2\ (1 + \tan^2 \theta)\ \lambda_2^2 \cos^2 \theta \sin^2 \phi}{(\lambda_1^2 \sin^2\theta + \lambda_2^2\cos^2 \theta)\cos^2\phi + \lambda_1^2(1 + \tan^2\theta)\ \lambda_2^2\cos^2 \theta \sin^2 \phi} \qquad (60(e))$$

$$\sin^2 \phi^* = \frac{\lambda_1 \lambda_2^2 \sin^2 \phi}{(\lambda_1^2 \sin^2 \theta + \lambda_2^2\cos^2 \theta)\ \cos^2 \phi + \lambda_1^2\lambda_2^2 \sin^2 \phi} \qquad (60(f))$$

$$\sin \phi^* = \frac{\lambda_1 \lambda_2 \sin \phi}{\sqrt{(\lambda_1^2 \sin^2 \theta + \lambda_2^2 \cos^2 \theta)\ \cos^2 \phi + \lambda_1^2 \lambda_2^2 \sin^2\phi}} \qquad (60(g))$$

$$\sin\phi^* \cos\theta^* = \frac{\lambda_1 \lambda_2^2 \sin \phi \cos \theta}{\sqrt{\lambda_1^2\lambda_2^2\sin^2\phi(\lambda_1^2\sin^2\theta + \lambda_2^2\cos^2\theta) + \cos^2\phi(\lambda_1^2\sin^2\theta + \lambda_2^2\cos^2\theta)^2}} \qquad (60(h))$$

Hence the function that was used to fit the experimental pressure distributions by the method of least squares is

$$P_{ext} = q \sum_{0}^{N} A_n X^n \tag{61}$$

where

$$X = \frac{\lambda_1 \lambda_2^2 \sin\phi \cos\theta}{\sqrt{\lambda_1^2\lambda_2^2 \sin^2\phi(\lambda_1^2 \sin^2\theta + \lambda_2^2 \cos^2\theta) + \cos^2\phi(\lambda_1^2 \sin^2\theta + \lambda_2^2\cos^2\theta)^2}} \tag{62}$$

This pressure is normal to the ellipsoidal surface at all points, and is positive when directed toward the center of curvature. Figures 66 and 67 illustrate the experimental loads and polynomial representations.

Stress Analysis

The analysis of stress resultants as presented here is not entirely original. The governing system of differential equations and their general solutions can be found in many texts on the theory of shells. They are reviewed here, in anticipation that not every designer has his literature readily available, nor is proficient in the mathematics involved.

Spherical Tents and Spherical Ends of Cylindrical Tents

The equations of equilibrium for a spherical shell element with a distributed radial load are (see Figure 68):

$$\frac{\partial}{\partial\phi}(N_\phi \sin\phi) + \frac{\partial}{\partial\theta}(N_{\phi\theta}) - N_\theta \cos\phi = 0 \tag{63(a)}$$

$$\frac{\partial}{\partial\phi}(N_{\phi\theta} \sin\phi) + \frac{\partial}{\partial\theta}(N_\theta) + N_{\phi\theta} \cos\phi = 0 \tag{63(b)}$$

$$N_\phi + N_\theta = -P_{ext}\, r \tag{63(c)}$$

From Equation 63(c),

$$N_\theta = - N_\phi - P_{ext}\ r \tag{64}$$

Substituting Equation 64 into Equations 63(a) and 63(b), N_θ is eliminated, yielding

$$\frac{\partial}{\partial\phi}\ (N\phi\ \sin\phi) + \frac{\partial}{\partial\theta}\ (N_{\phi\theta}) + (N_\phi + P_{ext}\ r)\ \cos\ \phi = 0 \tag{65(a)}$$

$$\frac{\partial}{\partial\phi}\ (N_{\phi\theta}\ \sin\phi\ ) + \frac{\partial}{\partial\theta}\ (-N_\phi - P_{ext} r) + N_{\phi\theta}\ \cos\phi = 0 \tag{65(b)}$$

For a wind load, which is symmetric with respect to the plane $\theta = 0^\circ$, $\theta = 180^\circ$, the general solution of Equations 65(a) and 65(b) may be represented by

$$N_\phi = r\ q \sum_{0}^{N} S_{\phi n}\ (\phi)\ \cos\ n\ \theta \tag{66(a)}$$

$$N_{\phi\theta} = r\ q \sum_{1}^{N} S_{\phi\theta n}\ (\phi)\ \sin\ n\ \theta \tag{66(b)}$$

Substituting the n-th general term from Equations 66(a), 66(b), and 48 into the Differential Equations 65(a) and 65(b), and simplifying,

$$\frac{d}{d\phi}\ (S_{\phi\ n})\ \sin\ \phi + 2\ S_{\phi n}\ \cos\ \phi + n\ S_{\phi\theta n} + p_n\ \cos\ \phi = 0 \tag{67(b)}$$

$$\frac{d}{d\phi} (S_{\phi\theta n}) \sin \phi + 2 S_{\phi\theta n} \cos \phi + n S_{\phi n} + n p_n = 0 \qquad (67(b))$$

Adding Equations 67(a) and 67(b),

$$\frac{d}{d\phi} (S_{\phi n} + S_{\phi\theta n}) + (2 \cos\phi + n) (S_{\phi n} + S_{\phi\theta n}) / \sin \phi = - (\cos\phi + n) p_n / \sin \phi \qquad (68)$$

Subtracting Equation 67(b) from Equation 67(a) yields

$$\frac{d}{d\phi} (S_{\phi n} - S_{\phi\theta n}) + (2 \cos - n) (S_{\phi n} - S_{\phi\theta n}) / \sin \phi = - (\cos\phi - n) p_n / \sin \phi \qquad (69)$$

Substituting

$$\left.\begin{aligned} U_{1\,n} &= S_{\phi n} + S_{\phi\theta n} \\ U_{2\,n} &= S_{\phi n} - S_{\phi\theta n} \end{aligned}\right\} \qquad (70)$$

into Equations 68 and 69 results in two ordinary linear differential equations of first order.

$$\frac{d}{d\phi} (U_{1n}) + (2 \cos \phi + n) U_{1n} / \sin \phi = - (\cos \phi + n) p_n / \sin \phi \qquad (71(a))$$

$$\frac{d}{d\phi} U_{2n} + (2\cos\phi - n) U_{2n} / \sin\phi = -(\cos\phi - n) P_n / \sin\phi \qquad (71(b))$$

From ordinary differential equations, the general solution of Equation 71(a) is

$$U_{1n} e^{\int \left(\frac{2\cos\phi + n}{\sin\phi}\right) d\phi} = \int -\left(\frac{\cos\phi + n}{\sin\phi}\right) P_n e^{\int \left(\frac{2\cos\phi + n}{\sin\phi}\right) d\phi} d\phi + C_{1n} \qquad (72)$$

where C_{1n} is the n-th general constant of integration. Performing the indicated operations in Equation 72,

$$U_{1n} = -(1 + \cos\phi)^n (I_{1n} + C_{1n}) / (\sin\phi)^{n+2} \qquad (73)$$

where

$$I_{1n} = \int P_n (\cos\phi + n) (1 - \cos\phi)^n (\sin\phi)^{1-n} d\phi \qquad (74)$$

The general solution of Equation 71(b) is

$$U_{2n} e^{\int \left(\frac{2\cos\phi - n}{\sin\phi}\right) d\phi} = \int -\left(\frac{\cos\phi - n}{\sin\phi}\right) P_n e^{\int \left(\frac{2\cos\phi - n}{\sin\phi}\right) d\phi} d\phi + C_{2n} \qquad (75)$$

From Equation 75

$$U_{2\,n} = (1 - \cos\phi)^n \, (I_{2\,n} + C_{2n})/(\sin\phi)^{n+2} \qquad (76)$$

where

$$I_{2\,n} = \int p_n \, (n - \cos\phi) \, (1 + \cos\phi)^n \, (\sin\phi)^{1-n} \, d\phi \qquad (77)$$

Finally from Equations 70(a) and 70(b),

$$S_{\phi\,n} = \frac{1}{2} \, (U_{1\,n} + U_{2\,n}) \qquad (78(a))$$

or

$$S_{\phi\,n} = -\frac{1}{2}\Big[(1 + \cos\phi)^n \, (I_{1\,n} + C_{1\,n}) \, /(\sin\phi)^{n+2} - (1 - \cos\phi)^n \, (I_{2\,n} + C_{2\,n}) \, /(\sin\phi)^{n+2}\Big] \qquad (78(b))$$

$$S_{\phi\theta n} = \frac{1}{2} \, (U_{1\,n} - U_{2\,n}) \qquad (79(a))$$

or

$$S_{\phi\theta n} = -\frac{1}{2}\Big[(1 + \cos\phi)^n \, (I_{1\,n} + C_{1\,n})/(\sin\phi)^{n+2} + (1 - \cos\phi)^n \, (I_{2\,n} + C_{2\,n})/(\sin\phi)^{n+2}\Big] \qquad (79(b))$$

The stresses are

$$N_\phi = q\, r \sum_0^N S_{\phi n} \cos n\theta \qquad (80(a))$$

$$N_\theta = -N_\phi - q\, r \sum_0^N \mu_n \cos n\theta \qquad (80(b))$$

$$N_{\phi\theta} = q\, r \sum_0^N S_{\phi\theta n} \sin n\theta \qquad (80(c))$$

The above results represent the general solution of the Equilibrium Equations 63(a), 63(b), and 63(c). Evaluation of the integration constants in U_{1n} and U_{2n} was accomplished by examining each load term independently and defining boundaries to assure finite stress values and strain compatibility at the tent base ($\phi = \phi_B$).

In each load term there exist two arbitrary constants, C_{1n} and C_{2n}. We can determine C_{1n} for all values of n from Equation 73 by requiring that stress resultants, hence U_{1n}, be finite at the apex ($\phi = 0$). In Equation 73, there is a zero of order n + 2 in the denominator. As can be verified by repeated application of L'Hospital's Rule, a finite value of U_{1n} is given at the apex by setting

$$C_{1n} = -I_{1n}(0), \quad 0 \le n \qquad (81)$$

Similarly for U_{2n}, from Equation 76,

$$C_{2n} = I_{2n}(0), \quad n = 0, 1 \qquad (82)$$

When $n \geq 2$, the above relation becomes indeterminate and C_{2n} remains unknown.

For evaluation of constants C_{2n} $(2 \leq n)$, strain compatibility was required at the base ($\phi = \phi_B$) where hoop strain is zero.

The hoop strain is

$$\varepsilon_\theta = \frac{N_\theta}{E} - \nu \frac{N_\phi}{E} \tag{83(a)}$$

$$0 = \frac{N_\theta}{E} - \nu \frac{N_\phi}{E} \tag{83(b)}$$

Hence,

$$N_\theta = \nu N_\phi \tag{84}$$

From Equations 48 and 64,

$$N_\phi = - N_\theta - q r \sum_0^N p_n (\phi) \cos n \theta \tag{85}$$

Then Equation 84 becomes for each load term

$$S_{\phi n}(\phi_B) = - \frac{1}{1 + \nu} q r p_n (\phi_B) \cos n \theta \tag{86(a)}$$

$$\frac{S_{\phi n}(\phi_B)}{qr} = - \frac{1}{1 + \nu} p_n (\phi_B) \cos n \theta \tag{86(b)}$$

From Equations 80(a) for each load term evaluated at ϕ_B,

$$\frac{S_{\phi n}(\phi_B)}{qr} = S_{\phi n}(\phi_B) \cos n\theta \tag{87}$$

Substituting Equation 86(b) into Equation 87

$$\frac{1}{1+\nu} P_n(\phi_B) = S_{\phi n}(\phi_B) \tag{88(a)}$$

$$S_{\phi n}(\phi_B) = \frac{1}{1+\nu} P_n(\phi_B) \tag{88(b)}$$

Evaluating Equation 78(b) at ϕ_B

$$S_{\phi n}(\phi_B) = -\frac{1}{2}\left[(1+\cos\phi_B)^n (I_{1n}(\phi_B) + C_{1n}) / \sin(\phi_B)^{n+2} - (1-\cos\phi_B)^n (I_{2n}(\phi_B) + C_{2n})/(\sin\phi_B)^{n+2} \right] \tag{89}$$

Substituting Equations 88(b) and 89 and solving, when $2 \leq n$,

$$C_{2n} = \frac{(1+\cos\phi_B)^n}{(1-\cos\phi_B)^n} (I_{1n}(\phi_B) + C_{1n}) - I_{2n}(\phi_B) - \frac{2}{(1+\nu)} \frac{(\sin\phi_B)^{n+2}}{(1-\cos\phi_B)^n} P_n(\phi_B) \tag{90}$$

All constants of integration are thus evaluated and the solution is complete. Integrated values for $I_{i\,n}(\phi)$ for N = 7 are as follows:

$$I_{10} = A_0 \left(\frac{1}{2} \sin^2 \phi \right) + A_2 \left(\frac{1}{8} \sin^4 \phi \right) + A_4 \left(\frac{1}{16} \sin^6 \phi \right) + A_6 \left(\frac{5}{128} \sin^8 \phi \right) \tag{91(a)}$$

$$I_{11} = A_1 \left(-\cos\phi + \frac{1}{3} \cos^3 \phi \right) + A_3 \left(-\frac{3}{20} \cos \phi \sin^4 \phi - \frac{3}{5} \cos \phi + \frac{1}{5} \cos^3 \phi \right) + A_5 \left(-\frac{5}{56} \cos \phi \sin^6 \phi - \frac{3}{28} \cos \phi \sin^4 \phi - \frac{3}{7} \cos \phi + \frac{1}{7} \cos^3 \phi \right) + A_7 \left(-\frac{35}{576} \cos \phi \sin^8 \phi - \frac{5}{72} \cos \phi \sin^6 \phi - \frac{1}{12} \cos \phi \sin^4 \phi - \frac{1}{3} \cos \phi + \frac{1}{9} \cos^3 \phi \right) \tag{91(b)}$$

$$I_{12} = A_2 \left(-\cos \phi - \frac{1}{2} \sin^2 \phi - \frac{1}{8} \sin^4 \phi \right) + A_4 \left(-\cos \phi + \frac{1}{3} \cos^3 \phi - \frac{1}{4} \sin^4 \phi - \frac{1}{12} \sin^6 \phi \right) + A_6 \left(-\frac{3}{4} \cos \phi + \frac{1}{4} \cos^3 \phi - \frac{3}{16} \cos \phi \sin^4 \phi - \frac{5}{32} \sin^6 \phi - \frac{15}{256} \sin^8 \phi \right) \tag{91(c)}$$

$$I_{13} = A_3 \left(-\frac{4}{5} \cos \phi - \frac{2}{5} \cos^3 \phi - \sin^2 \phi + \frac{1}{20} \cos \phi \sin^4 \phi \right) + A_5 \left(-\frac{9}{7} \cos \phi + \frac{3}{7} \cos^3 \phi - \frac{5}{8} \sin^4 \phi + \frac{17}{56} \cos \phi \sin^4 \phi \right)$$

$$+ \frac{5}{112} \cos\phi \sin^6\phi)$$

$$+ A_7 \left(- \cos\phi + \frac{1}{3}\cos^3\phi - \frac{1}{4}\cos\phi \sin^4\phi - \frac{7}{16}\sin^6\phi \right.$$

$$\left. + \frac{11}{48}\cos\phi \sin^6\phi - \frac{7}{192}\cos\phi \sin^8\phi \right) \qquad (91(d))$$

$$I_{14} = A_4 \left(- \frac{1}{2}\cos\phi - \frac{5}{6}\cos^3\phi - \frac{3}{2}\sin^2\phi + \frac{1}{4}\sin^4\phi \right.$$

$$\left. + \frac{1}{48}\sin^6\phi \right)$$

$$+ A_6 \left(- \frac{3}{2}\cos\phi + \frac{1}{2}\cos^3\phi - \frac{9}{8}\sin^4\phi + \frac{3}{4}\cos\phi \sin^4\phi \right.$$

$$\left. + \frac{1}{4}\sin^6\phi + \frac{3}{128}\sin^8\phi \right) \qquad (91(e))$$

$$I_{15} = A_5 \left(- \frac{1}{7}\cos\phi - \frac{9}{7}\cos^3\phi - 2\sin^2\phi + \frac{5}{8}\sin^4\phi \right.$$

$$\left. - \frac{9}{56}\cos\phi \sin^4\phi - \frac{1}{112}\cos\phi \sin^6\phi \right)$$

$$+ A_7 \left(- \frac{5}{3}\cos\phi + \frac{5}{9}\cos^3\phi - \frac{7}{4}\sin^4\phi + \frac{4}{3}\cos\phi \sin^4\phi \right.$$

$$\left. + \frac{35}{48}\sin^6\phi - \frac{29}{144}\cos\phi \sin^6\phi - \frac{7}{576}\cos\phi \sin^8\phi \right) \qquad (91(f))$$

$$I_{16} = A_6 \left(\frac{1}{4}\cos\phi - \frac{7}{4}\cos^3\phi - \frac{5}{2}\sin^2\phi + \frac{9}{8}\sin^4\phi \right.$$

$$\left. - \frac{7}{16}\cos\phi \sin^4\phi - \frac{3}{32}\sin^6\phi - \frac{1}{256}\sin^8\phi \right) \qquad (91(g))$$

$$I_{17} = A_7 \left(\frac{2}{3} \cos \phi - \frac{20}{9} \cos^3 \phi - 3 \sin^2 \phi + \frac{7}{4} \sin^4 \phi \right.$$

$$\left. - \frac{5}{6} \cos \phi \sin^4 \phi - \frac{7}{24} \sin^6 \phi + \frac{1}{18} \cos \phi \sin^6 \phi \right.$$

$$\left. + \frac{1}{576} \cos \phi \sin^8 \phi \right) \qquad (91(h))$$

$$I_{20} = - I_{10} \qquad (92(a))$$

$$I_{21} = I_{10} \qquad (92(b))$$

$$I_{22} = A_2 \left(- \cos \phi + \frac{1}{2} \sin^2 \phi + \frac{1}{8} \sin^4 \phi \right)$$

$$+ A_4 \left(- \cos \phi + \frac{1}{3} \cos^3 \phi + \frac{1}{4} \sin^4 \phi + \frac{1}{12} \sin^6 \phi \right)$$

$$+ A_6 \left(- \frac{3}{4} \cos \phi + \frac{1}{4} \cos^3 \phi - \frac{3}{16} \cos \phi \sin^4 \phi + \frac{5}{32} \sin^6 \phi \right.$$

$$\left. + \frac{15}{256} \sin^8 \phi \right) \qquad (92(c))$$

$$I_{23} = A_3 \left(- \frac{4}{5} \cos \phi - \frac{2}{5} \cos^3 \phi + \sin^2 \phi + \frac{1}{20} \cos \phi \sin^4 \phi \right)$$

$$+ A_5 \left(- \frac{9}{7} \cos \phi + \frac{2}{7} \cos^3 \phi + \frac{5}{8} \sin^4 \phi + \frac{17}{56} \cos \phi \sin^4 \phi \right.$$

$$\left. + \frac{5}{112} \cos \phi \sin^6 \phi \right)$$

$$+ A_7 \left(- \cos\phi + \frac{1}{3}\cos^3\phi - \frac{1}{4}\cos\phi \sin^4\phi + \frac{7}{16}\sin^6\phi \right.$$

$$\left. + \frac{11}{48}\cos\phi \sin^6\phi + \frac{7}{192}\cos\phi \sin^8\phi \right) \qquad (92(d))$$

$$I_{24} = A_4 \left(- \frac{1}{2}\cos\phi - \frac{5}{6}\cos^3\phi + \frac{3}{2}\sin^2\phi - \frac{1}{4}\sin^4\phi - \frac{1}{48}\sin^6\phi \right)$$

$$+ A_6 \left(- \frac{3}{2}\cos\phi + \frac{1}{2}\cos^3\phi + \frac{9}{8}\sin^4\phi + \frac{3}{4}\cos\phi \sin^4\phi \right.$$

$$\left. - \frac{1}{4}\sin^6\phi - \frac{3}{128}\sin^8\phi \right) \qquad (92(e))$$

$$I_{25} = A_5 \left(- \frac{1}{7}\cos\phi - \frac{9}{7}\cos^3\phi + 2\sin^2\phi - \frac{5}{8}\sin^4\phi \right.$$

$$\left. - \frac{9}{56}\cos\phi \sin^4\phi - \frac{1}{112}\cos\phi \sin^6\phi \right)$$

$$+ A_7 \left(- \frac{5}{3}\cos\phi + \frac{5}{9}\cos^3\phi + \frac{7}{4}\sin^4\phi + \frac{4}{3}\cos\phi \sin^4\phi \right.$$

$$\left. - \frac{35}{48}\sin^6\phi - \frac{29}{144}\cos\phi \sin^6\phi - \frac{7}{576}\cos\phi \sin^8\phi \right) \qquad (92(f))$$

$$I_{26} = A_6 \left(\frac{1}{4}\cos\phi - \frac{7}{4}\cos^3\phi + \frac{5}{2}\sin^2\phi - \frac{9}{8}\sin^4\phi \right.$$

$$\left. - \frac{7}{16}\cos\phi \sin^4\phi + \frac{3}{32}\sin^6\phi + \frac{1}{256}\sin^8\phi \right) \qquad (92(g))$$

$$I_{27} = A_7 \left(\frac{2}{3}\cos\phi - \frac{20}{9}\cos^3\phi + 3\sin^2\phi - \frac{7}{4}\sin^4\phi - \frac{5}{6}\cos\phi \sin^4\phi \right.$$

$$\left. + \frac{7}{24}\sin^6\phi + \frac{1}{18}\cos\phi \sin^6\phi + \frac{1}{576}\cos\phi \sin^8\phi \right) \qquad (92(h))$$

Cylindrical Portion of Cylindrical Tents

The cylindrical portion of the tent is considered to be loaded by three separate loads; 1) internal pressure, 2) external pressure from wind load and 3) equilibrium membrane force of the hemispherical section at each end of the cylinder. The forces resulting from the three separate loads are then superimposed to find the maximum membrane stress in each direction. It is theorized that the resulting stresses are conservative because, at lines of force discontinuity, the maximum stress values would be relieved if displacement compatibility were attained between adjoining free bodies.

Radial loads on the cylindrical portion of the tent include internal pressure, P_e, and wind loads, P_{ext}.

$$P_e = q A_e \tag{93(a)}$$

$$P_{ext} = q \sum_{0}^{N} A_n \sin^n \phi \tag{93(b)}$$

The radial loads are combined as indicated giving a resultant radial load, $P_e - P_{ext}$. See Figure 69(a).

The cylindrical membrane when subjected to a radial load varying with ϕ should distort freely such that the circumferential force is constant. This is because we have assumed that there are no tangential loads and that the fabric has zero bending stiffness. It must then follow that the radius would be variable with ϕ in order that equilibrium be maintained through the relation

$$N_\phi = (P_e - P_{ext})\, r\,(\phi) \tag{94}$$

or

$$r\,(\phi) = \frac{N_\phi}{P_e - P_{ext}} \tag{95}$$

The resulting deformation would inversely simulate the load magnitude as shown in Figure 69(b). To evaluate N_ϕ we will consider equilibrium of a cylindrical body of unit length radial load varying with ϕ.

Summation of vertical forces (see Figure 69(c):

$$2 N_\phi \sin\phi_B = \int_{-\phi_B}^{\phi_B} r\, p \cos\phi \, d\phi \tag{96}$$

where

$$p = P_e - P_{ext} \tag{97}$$

therefore

$$N_\phi = \frac{r}{2 \sin\phi_B} \int_{-\phi_B}^{\phi_B} (P_e - q \sum_0^N A_n \sin^n \phi) \cos\phi \, d\phi \tag{98(a)}$$

since N_ϕ is constant. Then

$$N_\phi = \frac{r}{\sin\phi_B} \int_0^{\phi_B} (P_e - q \sum_0^N A_n \sin^n \phi) \cos\phi \, d\phi \tag{98(b)}$$

which reduces to

$$\frac{N_\phi}{q\, r} = \frac{P_e}{q} - \frac{1}{\sin\phi} \sum_0^N \frac{A_n \sin^{n+1}\phi_B}{n+1} \tag{98(c)}$$

Let

$$C = \frac{P_a}{q} - \frac{N_\phi}{q\,r} \tag{99(a)}$$

$$C = \sum_{0}^{N} \frac{A_n \sin^n \phi_B}{n+1} \tag{99(b)}$$

$$\frac{\partial C}{\partial \phi_B} = 0 = \frac{n A_n \cos \phi_B \sin^{n-1} \phi_B}{n+1} \tag{100}$$

$$\therefore \quad \cos \phi_B \sin^{n-1} \phi_B = 0 \tag{101}$$

$$\phi_B = +\frac{\pi}{2} ; \quad n = 0, 1, 2, \ldots N \text{ (maximum)}$$

Since flexibility is apparent and distortion conforms to minimum energy principles, utilization of maximum $\phi_B = \frac{\pi}{2}$ in the calculation of all n values in the expression for C is reasonable and conservative.

$$\therefore \quad C = \sum_{0}^{N} \frac{A_n}{n+1} \tag{102}$$

and

$$\frac{N_\phi}{q\,r} = \frac{P_a}{q} - \sum_{0}^{N} \frac{A_n}{n+1} \tag{103}$$

Axial loads on the cylinder are taken as the loads necessary for equilibrium of the hemispherical ends and are determined by use of the spherical tent solution. The spherical ends are assumed to be joined together to form a sphere with load distribution as determined by the actual test data. The resulting N_θ at $\theta = 0$ and $\theta = \pi$ must then be applied to each end of the cylinder. The only additional axial load on the cylinder is that due to internal pressure or

$$N_{x\theta} = \frac{P_e r}{2} \tag{104}$$

Total axial stress for body equilibrium is given by

$$N_x = N_\theta \quad (\phi,\ \vartheta = 0,\ \pi) + \frac{P_e r}{2} \tag{105(a)}$$

or

$$\frac{N_x}{q r} = \frac{N_\theta}{q r} \quad (\phi,\ \theta = 0,\ \pi) + \frac{P_e}{2q} \tag{105(b)}$$

It is recognized that the above analysis does not provide for displacement compatibility at the sphere-cylinder junction. It is quite apparent that a compatibility solution should provide a reduction in the calculated peak value because of the edge flexibility of the supporting cylinder. It is also noted that the peak stress values for N_θ (necessary for end equilibrium)are consequently regarded as slightly conservative.

It is also recognized that no evaluation of shear ($N_{\phi x}$) is attempted in the cylindrical shell section. The analysis of shear is not considered critical since the material can buckle in shear without consequent failure (rupture) of the fabric. The critical stress components are taken to be tensile membrane forces.

Ellipsoidal Ends of Cylindrical Tents

The short radius tents consist of cylindrical single-wall sections with ellipsoidal ends in lieu of the spherical ends commonly used now. A membrane stress analysis of the ellipsoidal ends from thin shell theory was accomplished through an affine transformation to a fictitious spherical shell, as presented in Reference 10, pp. 191-205. Stress resultants were then found for the sphere with the solution in Reference 10, pp. 48-50, and transformed back to the ellipsoid.

To obtain the sphere, the affine transformation yields

$$x = \lambda_1 x^*, \quad y = \lambda_2 y^*, \quad z = z^* \tag{106}$$

where $\lambda_1 = a/r$ and $\lambda_2 = b/r$ as shown in Figure 65.

The total load on the ellipsoid consists of two parts, the internal pressure required for initial inflation, and the external wind loads. The total load is the sum of these two,

$$p = P_e - P_{ext} \tag{107}$$

The expression for P_{ext} is given in the pressure distribution section, and is negative here because a positive load in this analysis acts outward as opposed to the positive inward sign convention for wind tunnel data reduction which was used in the derivation of P_{ext}.

P_e is given by

$$P_e = q A_e \tag{108}$$

Transformation of the normal load on the ellipsoid to the sphere yields a load with components along all of the spherical coordinate directions, as given by

$$p_\theta^* = \left(\frac{1}{2} L_1 \sin \phi^* \sin 2\theta^* \right) p \tag{109(a)}$$

$$p_\phi^* = \left(\frac{1}{2} L_3 \sin \phi^* \cos \phi^* - \frac{1}{2} L_2 \sin \phi^* \cos \phi^* \cos 2\theta^* \right) p \tag{109(b)}$$

$$p_r^* = \left(L_2 + \frac{1}{2} L_3 \sin^2 \phi^* - \frac{1}{2} L_1 \sin^2 \phi^* \cos 2\theta^* \right) p \tag{109(c)}$$

where $L_1 = \frac{\lambda_1}{\lambda_2} - \frac{\lambda 2}{\lambda_1}$, $L_2 = \lambda_1 \lambda_2$, and $L_3 = \frac{\lambda_1}{\lambda_2} + \frac{\lambda_2}{\lambda_1} - 2\lambda_1 \lambda_2$ (110(a,b,c))

Substituting Equation 107 into Equation 109, and with the relations $\sin 2\theta^* \cos n\theta^* = \frac{1}{2}\sin(2+n)\theta^* + \frac{1}{2}\sin(2-n)\theta^*$, and $\cos 2\theta^* \cos n\theta^* = \frac{1}{2}\cos(2+n)\theta^* + \frac{1}{2}\cos(2-n)\theta^*$, the loads become

$$p_\theta^* = q \sum_{1}^{N+2} P_{\theta n}(\phi^*) \sin n\theta^* \qquad (111(a))$$

$$p_\phi^* = q \sum_{0}^{N+2} P_{\phi n}(\phi^*) \cos n\theta^* \qquad (111(b))$$

$$p_r^* = q \sum_{0}^{N+2} P_{rn}(\phi^*) \cos n\theta^* \qquad (111(c))$$

where

$$P_{\theta 1} = \frac{1}{4} L_1 \sin\phi^* (p_3 - p_1) \qquad (112(a))$$

$$P_{\theta 2} = \frac{1}{4} L_1 \sin\phi^* (p_4 - 2p_0 + 2A_e) \qquad (112(b))$$

$$P_{\theta n} = \frac{1}{4} L_1 \sin\phi^* (p_{n+2} - p_{n-2}),\ n \geq 3 \qquad (112(c))$$

$$P_{\phi 0} = \frac{1}{2}\left[L_3 (A_e - p_0) + \frac{1}{2} L_1 p_2\right] \sin\phi^* \cos\phi^* \qquad (113(a))$$

$$P_{\phi 1} = \frac{1}{2}\left[\frac{1}{2} L_1 (p_1 + p_3) - L_3 p_1\right] \sin\phi^* \cos\phi^* \qquad (113(b))$$

$$P_{\phi 2} = \frac{1}{2}\left[\frac{1}{2} L_1 (p_4 + 2p_0 - 2A_e) - L_3 p_2\right] \sin\phi^* \cos\phi^* \qquad (113(c))$$

$$P_{\phi n} = \frac{1}{2}\left[\frac{1}{2} L_1 (p_{n+2} + p_{n-2}) - L_3 p_n\right] \sin\phi^* \cos\phi^*,\ n \geq 3 \qquad (113(d))$$

$$P_{r0} = \left[\left(L_2 \csc^2 \phi^* + \frac{1}{2} L_3\right)(A_e - p_0) + \frac{1}{4} L_1 p_2\right] \sin^2 \phi^* \qquad (114(a))$$

$$P_{r1} = \left[\frac{1}{4} L_1 (p_1 + p_3) - \left(L_2 \csc^2 \phi^* + \frac{1}{2} L_3\right) p_1\right] \sin^2 \phi^* \qquad (114(b))$$

$$P_{r2} = \left[\frac{1}{4} L_1 (p_4 + 2 p_0 - 2 A_e) - \left(L_2 \csc^2 \phi^* + \frac{1}{2} L_3\right) p_2\right] \sin \qquad (114(c))$$

$$P_{r_n} = \left[\frac{1}{4} L_1 (p_{n+2} + p_{n-2}) - \left(L_2 \csc^2 \phi^* + \frac{1}{2} L_3\right) p_n\right] \sin^2 \phi^*, \; n \geq 3 \qquad (114(d))$$

With the loads expressed in Equation 111 the stress resultants for the sphere are given by the following relations.

$$N_\phi^* = q r \sum_0^{N+2} N_{\phi n}^* \cos n \theta^* \qquad (115(a))$$

$$N_\theta^* = q r \sum_0^{N+2} (P_{rn} - N_{\phi n}^*) \cos n \theta^* \qquad (115(b))$$

$$N_{\phi\theta}^* = q r \sum_1^{N+2} N_{\phi\theta n}^* \sin n \theta^* \qquad (115(c))$$

$$N_{\phi n} = \frac{1}{2} (U_n + V_n) \qquad (116(a))$$

$$N_{\phi\theta n}^* = \frac{1}{2} (U_n - V_n) \qquad (116(b))$$

$$U_n = \csc^2 \phi^* \cot^k \frac{\phi^*}{2} (\bar{A}_n - I_{1n}) \qquad (117(a))$$

$$V_n = \csc^2 \phi^* \tan^n \frac{\phi^*}{2} (\bar{B}_n - I_n) \qquad (117(b))$$

$$I_{1\,n} = \int \left[\left(P_{\phi n} + P_{\theta n} - (n + \cos\phi^*) \csc\phi^* P_{rn} \right) \sin^2\phi^* \tan^n \frac{\phi^*}{2} \right] d\phi^* \quad (118(a))$$

$$I_{2\,n} = \int \left[P_{\phi n} - P_{\theta n} + (n - \cos\phi^*) \csc\phi^* P_{rn} \right] \sin^2\phi^* \cot^n \frac{\phi^*}{2} d\phi^* \quad (118(b))$$

$\overline{A}_n$ and $\overline{B}_n$ are constants of integration. To determine these constants, finite stress resultants at $\phi^* = 0$ and $\phi^* = \pi$ were required. This yields

$$\overline{A}_n = I_{1n}(0), \quad n \geq 0 \quad (119(a))$$

$$\overline{B}_n = I_{2n}(0), \quad n = 0, 1 \quad (119(b))$$

$$\overline{B}_n = I_{2n}(\pi) \quad n \geq 2 \quad (119(c))$$

To obtain the stress resultants in the ellipsoidal shell from those in the sphere, the following relations were used.

$$\left.\begin{aligned} N_\phi &= N_\phi^* \frac{ds_\phi}{ds_\phi^*} \frac{ds_\theta^*}{ds_\theta} \\ N_\theta &= N_\theta^* \frac{ds_\theta}{ds_\theta^*} \frac{ds_\phi^*}{ds_\phi} \\ N_{\phi\theta} &= N_{\phi\theta}^* \end{aligned}\right\} \quad (120)$$

where

$$ds_\phi = ds_\phi^* \sqrt{\lambda_1^2 \cos^2\phi^* \cos^2\theta^* + \lambda_2^2 \cos^2\phi^* \sin^2\theta^* + \sin^2\phi^*} \quad (121(a))$$

$$ds_\theta = ds_{\theta^*} \sqrt{\lambda_1^2 \sin^2 \theta^* + \lambda_2^2 \cos^2 \theta^*} \qquad (121(b))$$

This solution is valid for a load which is symmetric about the x - z plane. By varying λ_1 and λ_2, solutions for broadside or head-on winds may be obtained: for the broadside wind, $\lambda_1 = 1$ and $\lambda_2 = b/r$; for the head-on wind, $\lambda_1 = b/r$ and $\lambda_2 = 1$. See Figure 70.

To effect an analysis of this tent end, N = 3 was selected. This gives us a third degree polynomial representation in X of the wind load.

Introducing N = 3 throughout the analysis yields the following relations necessary to obtain the solution.

$$p_o = A_o + \frac{1}{2} A_2 \sin^2 \phi^* \qquad (122(a))$$

$$p_1 = A_1 \sin \phi^* + \frac{3}{4} A_3 \sin^3 \phi^* \qquad (122(b))$$

$$p_2 = \frac{1}{2} A_2 \sin^2 \phi^* \qquad (112(c))$$

$$p_3 = \frac{1}{4} A_3 \sin^3 \phi^* \qquad (112(d))$$

$$P_{r_o} = (A_e - A_o)(L_2 + \frac{1}{2} L_3 \sin^2 \phi^*) + \frac{1}{2} A_2 \sin^2 \phi^* \left[\frac{1}{2} \sin^2 \phi^* (\frac{1}{2} L_1 - L_3) - L_2\right] \qquad (123(a))$$

$$P_{r1} = A_1 \sin \phi^* \left[\frac{1}{2} \sin^2 \phi^* (\frac{1}{2} L_1 - L_3) - L_2\right] + \frac{3}{4} A_3 \sin^3 \phi^* \left[\sin^2 \phi^* (\frac{1}{3} L_1 - L_3) - L_2\right] \qquad (123(b))$$

$$P_{r2} = (A_o - A_e) \frac{1}{2} L_1 \sin^2 \phi^* + \frac{1}{2} A_2 \sin^2 \phi^* \left[\frac{1}{2} \sin^2 \phi^* (L_1 - L_3) - L_2\right] \qquad (123(c))$$

$$P_{r_3} = \frac{1}{4} A_1 L_1 \sin^3 \phi^* + \frac{1}{4} A_3 \sin^3 \phi^* \left[\frac{1}{2} \sin^2 \phi^* (\frac{3}{2} L_1 - L_3) - L_2\right] \quad (123(d))$$

$$P_{r_4} = \frac{1}{8} A_2 L_1 \sin^4 \phi^* \quad (123(e))$$

$$P_{r5} = \frac{1}{16} A_3 L_1 \sin^5 \phi^* \quad (123(f))$$

$$I_{10} = I_{20} = \frac{1}{2} L_2 (A_o - A_e) \sin^2 \phi^* + \frac{1}{8} L_2 A_2 \sin^4 \phi^* \quad (124(a))$$

$$I_{11} = \frac{1}{16} A_3 (L_1 - L_3) \sin^6 \phi^* + \frac{1}{8} A_1 (L_1 - L_3) \sin^4 \phi^* + \frac{3}{40} A_3 (L_1 - 2L_2 - L_3) \sin^4 \phi^* \cos \phi^* + \quad (124(b))$$

$$(\frac{1}{6} A_1 + \frac{1}{10} A_3)(L_1 - 2L_2 - L_3) \cos \phi^* (\sin^2 \phi^* + 2)$$

$$I_{21} = \frac{1}{16} A_3 (L_1 - L_3) \sin^6 \phi^* + \frac{1}{8} A_1 (L_1 - L_3) \sin^4 \phi^* - \frac{3}{40} A_3 (L_1 - 2L_2 - L_3) \sin^4 \phi^* \cos \phi^* - \quad (124(c))$$

$$(L_1 - 2L_2 - L_3)(\frac{1}{6} A_1 + \frac{1}{10} A_3) \cos \phi^* (\sin^2 \phi^* + 2)$$

$$I_{12} = \left[\frac{1}{2} L_1 (A_e - A_o) + \frac{1}{3} L_2 A_2\right](1 - \cos \phi^*)^3 + \frac{1}{2} L_2 A_2 \left[\frac{1}{3} \cos \phi^* (1 - \cos \phi^*)^3 \right. \quad (124(d))$$

$$\left. + \frac{1}{12} (1 - \cos \phi^*)^4\right] + \frac{1}{2} (L_3 - \frac{3}{2} L_1) A_2 \left[\frac{1}{3} \sin^2 \phi^* (1 - \cos \phi^*)^3 - \frac{1}{6} \cos \phi^* (1 - \cos \phi^*)^4 \right.$$

$$\left. - \frac{1}{30} (1 - \cos \phi^*)^5\right]$$

$$I_{22} = \left[\frac{1}{2} L_1 (A_e - A_o) + \frac{1}{3} L_2 A_2\right](1 + \cos \phi^*)^3 + \frac{1}{2} L_2 A_2 \left[\frac{1}{3} \cos \phi^* (1 + \cos \phi^*)^3 + \right. \quad (124(e))$$

$$\left. \frac{1}{12} (1 + \cos \phi^*)^4\right] + \frac{1}{2} (L_3 - \frac{3}{2} L_1) A_2 \left[\frac{1}{3} \sin^2 \phi^* (1 + \cos \phi^*)^3 + \frac{1}{6} \cos \phi^* (1 + \cos \phi^*)^4 - \right.$$

$$\frac{1}{30}(1+\cos\phi^*)^5\Big]$$

$$I_{13}=\frac{1}{4}\left(\frac{3}{4}A_3L_2-L_1A_1\right)(1-\cos\phi^*)^4+\frac{1}{16}L_2A_3\Big[\cos\phi^*(1-\cos\phi^*)^4+\frac{1}{5}(1-\cos\phi^*)^5\Big] \quad (124(f))$$

$$+\frac{3}{8}A_3(L_3-2L_1)\Big[\frac{1}{4}\sin^2\phi^*(1-\cos\phi^*)^4-\frac{1}{10}\cos\phi^*(1-\cos\phi^*)^5$$

$$-\frac{1}{60}(1-\cos\phi^*)^6\Big]$$

$$I_{23}=\frac{1}{4}\left(\frac{3}{4}A_3L_2-L_1A_1\right)(1+\cos\phi^*)^4-\frac{1}{16}L_2A_3\Big[\cos\phi^*(1+\cos\phi^*)^4-\frac{1}{5}(1+\cos\phi^*)^5\Big]+ \quad (124(g))$$

$$\frac{3}{8}A_3(L_3-2L_1)\Big[\frac{1}{4}\sin^2\phi^*(1+\cos\phi^*)^4-\frac{1}{10}\cos\phi^*(1+\cos\phi^*)^5+\frac{1}{60}(1+\cos\phi^*)^6\Big]$$

$$I_{14}=-\frac{1}{8}L_1A_2(1-\cos\phi^*)^5 \quad (124(h))$$

$$I_{24}=-\frac{1}{8}L_1A_2(1+\cos\phi^*)^5 \quad (124(i))$$

$$I_{15}=-\frac{1}{16}L_1A_3(1-\cos\phi^*)^6 \quad (124(j))$$

$$I_{25}=-\frac{1}{16}L_1A_3(1+\cos\phi^*)^6 \quad (124(k))$$

$$\therefore \quad \bar{A}_n=\bar{B}_n=0, \quad n\neq 1 \quad (125(a))$$

$$\bar{A}_1=-\bar{B}_1=\left(\frac{1}{3}A_1+\frac{1}{5}A_3\right)(L_1-2L_2-L_3) \quad (125(b))$$

Results

Spherical Tents

Available pressure data from all tests on spherical tent models have been analyzed. Stress coefficients were calculated on Hayes' IBM 1620 Computer. Stresses were calculated at 15° intervals, from $\phi = 15°$ to $\phi = \phi_B$ and from $\theta = 0$ to $\theta = 180°$. Typical stress coefficients are illustrated in Figures 71, 72 and 73.

Peak stress coefficients for the non-porous spherical model tents are plotted in Figures 74, 75 and 76. Peak stress values are the maximum occurring in the tent. Peak N_ϕ usually occurs at $\phi = 15°$ and $\theta = 75°$. Peak N_θ usually occurs at $\phi = 15°$ and $\theta = 0$ (see Figures 71 and 72). As is evident on Figures 74 through 76, the stress coefficient curves are drawn above the plotted points and represent maximum peak stress values where internal pressure is varied from 5/4q. No pattern of stress coefficients is discernible due to varying internal pressure within the selected range.

The curves of peak stress coefficients are utilized to prepare design curves as shown in Figures 77, 78, and 79. These design curves provide a direct reading of peak stress coefficients for any given h/d and design dynamic, or impact, pressure, q, where internal tent pressure is approximately equal to q.

Since wind loading can be from any direction, stress variations with θ becomes inconsequential in the spherical design. However it may be advantageous or desirable that the designer be able to determine stress variations with apex angle, ϕ. Figures 80 through 83 have been derived from test data maximum values and provide a ratio of $N_\theta(\phi)$ to $N_\theta(\text{peak})$ for use in design calculations. No comparable curve is prepared for $N_\phi(\theta)$ because the variation in N_ϕ with ϕ is slight (see Figure 71 at $\theta = 75°$).

In the boundary condition requiring strain compatibility at the tent base ($\phi = \phi_B$), Poisson's ratio (ν) is inherent. Because no information is available on Poisson effects in tent fabrics and also because different weaves and fabric compositions would affect the strain characteristics, the analyses above employed a somewhat arbitrary Poisson's ratio equal to one. Since the true value of Poisson's ratio may be significantly less than the assumed value, stress coefficients were recalculated with $\nu = 0.5$. The maximum resulting deviation being less than six percent, it was felt that corrections were not justified.

Cylindrical Tents with Spherical Ends

All tests on cylindrical tent models have been analyzed. The effects of internal pressure were inherently accounted for in these analyses. The internal tent model pressure was set at 4/5 q, 1 q, and 5/4 q for each wind velocity used. Broadside wind direction, normal to the cylindrical section centerline, creates the most severe loading condition and the largest fabric stresses. The aerodynamic pressure data gathered from these tests indicated

much lower values for any wind direction other than broadside which substantiates what may be deduced from observation.

The maximum resulting stress coefficients were calculated on Hayes' IBM 1620 computer and are listed in tabular form in Table III. Typical values of stress coefficients versus the angle θ are presented in Figures 84, 85 and 86. These results are typical of all models tested and thus present all the necessary information required to develope design curves for tents that exist within the set, i. e., h/d ranging from 3/8 to 3/4 and w/ℓ_h ranging from 1/4 to 1/1.

The calculated results of $N_\phi/q\ r$ versus q are plotted in Figure 87 for both the cylindrical section and the spherical ends. The scatter of all results are included within the shaded area and a line of maximum bounding the upper limits describesthe maximum stress level for any wind velocity up to 105 mph.

The calculated results of $N_\theta/q\ r$ versus q are plotted in Figure 88 for the spherical ends. These results are interpreted as above, with one addition: the cylindrical section peak values are assumed constant longitudinally (in the direction of x) except at the interface.

The calculated results of $N_{\phi\theta}/q\ r$ versus q are plotted in Figure 89 for the spherical ends. These results are interpreted as before except the shear is assumed to be zero at the interface and anywhere on the cylindrical section away from the base.

Figure 90 presents an illustration of all maximum values of $N_\phi/q\ r$ stress coefficients as typically presented in Figure 84 combined with the maximum calculated value for the cylindrical section for all tests at all wind velocities for every ϕ from 15° to 75°. The abscissa is divided as a function of d, the basic tent diameter, and the radius projection of various positions of θ in 15° intervals from 0° reference point to $\theta = 180^\circ$. The purpose of this division is to allow a plot of maximum stress coefficients showing the distribution around an end, through the discontinuity region at the interface, and continuity in the cylindrical section. The rear side is split out and rotated 180° in order to better show the distribution. Only one-half of the model is presented because of symmetric loading and results.

Figure 91 presents an illustration of all maximum values of $N_\theta/q\ r$ stress coefficients as typically presented in Figure 84 combined with the extension assumption that the cylindrical equilibrium forces are constant in the cylindrical section for all tests at all wind velocities for every ϕ from 15° to ϕ_B. The remaining explanation of the figure is stated in the preceding paragraph.

Figure 92 presents a cross plot of maximum $N_\phi/q\ r$ stress coefficient as a function of the angular position from $\phi = 0^\circ$ to $\pm\ \phi_B$. These values are representative of maximum interface stress coefficients considering

discontinuity effects at the junction of the cylindrical section and the spherical ends where $\theta = 0^{\circ}$ and 180°.

Figure 93 presents a cross plot of maximum $N_{\theta}/q\,r$ stress coefficient as a function of the angular position from $\phi = 0^{\circ}$ to $\pm\,\phi_B$. These values are again representative of maximum interface stress coefficients combined with the extension assumption that the cylindrical equilibrium forces are constant in the cylindrical section for all tests at all wind velocities at the junction of the cylindrical section and the spherical ends where $\theta = 0^{\circ}$ and 180°.

The purpose of this presentation, as outlined previously, is to develop design data curves from which the design of a cylindrically shaped tent with spherical ends can be made without undue labor or theoretical analysis of stresses. The figures presented in this part enable the designer to predict maximum stress coefficients for various cylindrically shaped spherical ended tent sizes for wind velocities up to 110 mph.

Figures 94 thru 96 present a typical plot of stress coefficients for specific dynamic pressures for W/ℓ_h equal to 1/2. These results represent an attempt to present design data to use as a means to arrive at interpolated values of the stress coefficients for various wind velocities. The curves thus presented represent a minimum of data points and cannot be relied upon to give accurate results. The final design curves described in the following paragraphs constitute the evaluation of data herein presented and should be used in any design problem.

Maximum stress coefficients presented in Table III represent all maximums for all combinations of sizes and wind velocities. The scatter of results as illustrated in Figures 87 through 89. proved that the maximum stress at any point can be predicted for any wind velocity by using a line of maximums which bound the scatter region for any specific model.

The resulting design curves, Figures 97 through 105, utilize this method to predict maximum stress coefficients. The calculated stress coefficient maximums of all tests on all models include all of the specific results within its set and therefore the scatter of the maximums represent all of the results for any specific variation in proportional size.

Resulting stress coefficients in any portion of a cylindrically shaped spherical ended tent can be obtained by using the design stress coefficient curves presented in Figures 97 through 105. To use these curves, the designer would decide upon the proportions of size of the tent to be designed, either by aerodynamic considerations or other requirements, and choose the figure for the specific h/d ratio which applied to the given problem. After this the designer would then enter the graph upon the abscissa at the predetermined W/ℓ_h and read upward to either the curve labled cylindrical section or spherical ends and determine the corresponding stress coefficient by reading across to the ordinate index.

Figure 94 presents the variation of maximum stress coefficient, $(N_\phi/q\ r)$ maximum, versus h/d for a constant $W/\ell_h = 1/2$, for any specific dynamic pressure, in the spherical ends and the cylindrical section.

Figure 95 presents the variation of maximum stress coefficient, $(N_\theta/q\ r)$ maximum, versus h/d for a constant $W/\ell_h = 1/2$, for any specific dynamic pressure, in the spherical ends and the cylindrical section, assuming the extension of equilibrium forces to be constant.

Figure 96 presents the variation of maximum stress coefficient, $(N_{\phi\theta}/q\ r)$ maximum, versus h/d for a constant $W/\ell_h = 1/2$, for any specific dynamic pressure, in the spherical ends. The shear stress coefficients in the cylindrical section are assumed to be zero and their calculation has herein been neglected.

Figures 97, 98 and 99 present maximum stress coefficients, $(N_\phi/q\ r)$ maximum, versus $W/\ell_h = 1/4$ to 1/1 for both spherical ends and the cylindrical section of the tents for all broadside wind loads for h/d ratios of 3/8, 1/2 and 3/4, respectively. These design data curves will provide accurate results of stress coefficients for any tent with these particular proportional sizes for all load conditions. It must be remembered that the stress coefficients depicted from these curves do not represent the total stress condition. The effects of internal pressure must be added to these results.

Figures 100, 101, and 102 present maximum stress coefficient, $(N_\theta/q\ r)$ maximum, versus W/ℓ_h ratios as stated in the preceding paragraph with the equilibrium extension applying throughout the cylindrical section.

Figures 103, 104 and 105 present maximum stress coefficient, $(N_{\phi\theta}/q\ r)$ maximum, versus W/ℓ_h ratios as stated above except in the cylindrical section where the assumed shear stress is zero.

Cylindrical Tents with Ellipsoidal Ends

The short radius tents were analyzed for a broadside wind loading on the Hayes' IBM 360 computer. Figures 106 through 109 show typical stress coefficients for the model tested as a function of the fictitious spherical coordinates which were used in the analysis. This is a more regular system in which to deal, but if it is desirable, Table IV gives the values of the ellipsoidal coordinates corresponding to several of the spherical ones used in the analysis. Results of the analysis of the one model tested (b/r = 1/2, h/d = 1/2, and $W/\ell_h = 1/2$) were extrapolated to yield peak stress coefficients for other configurations.

As may be seen from Figures 110 through 112, stress resultants in the short radius ends are higher than in the spherical ends. The stress ratios are nearly proportional to the inverse of b/r; hence, the more eccentric the ellipsodial ends are, the higher the stress resultants.

Stress Profiles

Stress profiles (lines of constant stress) were prepared for spherical single-wall tents with h/d ratios of 3/8, 1/2 and 3/4; and for cylindrical single-wall tents with spherical ends with W/ℓ_h = 1/2 and h/d ratios of 1/2 and 3/4. These stress profiles are critical for all combinations of internal pressure and wind velocity tested - P_e = 4/5 q, q, 5/4 q, and q = 0.6, 3.0, 6.0 inches of water gage.

These stress profiles were prepared to visualize areas of maximum stress. Since the wind may come from any direction, the variation of stress with the θ coordinate can be ignored. Considering, then, only the variations with respect to ϕ, the stress resultant N_ϕ is constant in the cylindrical portion and nearly constant in the spherical ends. N_θ and N_x, however, both peak near the apex, showing a definite separation at about $\phi = 40^\circ$. This may be seen easily in Figures 113 through 124.

Design Curve Summary and Application

Spherical Tents

The design curves generated in this study and analysis are presented as Figures 77 through 83. Utilization of the design curves is as follows:

1) From design requirements determine tent size and shape and design value for dynamic (or impact) pressure.

2) Enter Figures 77, 78, or 79 with required h/d on the appropriate curve for dynamic pressure and read stress coefficients,

$$\frac{N_\phi}{q\,r}\,,\quad \frac{N_\theta}{q\,r}\,,\quad \frac{N_{\phi\theta}}{q\,r}$$

3) Multiply stress coefficients by design dynamic pressure, q, in p. s. i. and tent radius, r, in inches. Products are stress resultants N_ϕ, N_θ, $N_{\phi\theta}$ in pounds per inch.

4) If variation in N_θ with apex angle, ϕ, is desired, determine stress ratio,

$$\frac{N_\theta(\phi)}{N_\theta\ (\text{peak})}$$

from Figures 80, 81, 82 or 83 depending on appropriate h/d. Multiply stress ratios (from 4) by N_θ (from 3) to get variable values of N_θ versus apex, ϕ.

5) Total stress resultants are:

$$\bar{N}_{\phi} = N_{\phi} \text{ (from 3)} + \frac{P_e\, r}{2}$$

$$\bar{N}_{\theta} = N_{\phi} \text{ (from 3)} + \frac{P_e\, r}{2}$$

$$\bar{N}_{\phi\theta} = N_{\phi\theta} \text{ (from 3)}$$

Cylindrical Tents with Spherical Ends

The design curves presented in this study and analysis are included as Figures 97 through 105. Utilization of the design curves is as follows:

1) From design requirements determine tent size and shape and dynamic (or impact) pressure design value.

2) Enter Figures 97 through 102 (choosing the appropriate figure by knowing the h/d ratio) with the required W/ℓ_h and read stress coefficients, $N_{\phi}/q\,r$, $N_{\theta}/q\,r$, and $N_{\phi\theta}/q\,r$ for both the cylindrical section and the spherical ends. For stress coefficient values which would exist for other sizes than those presented, linear interpolation within the range given will yield corresponding results.

3) Multiply stress coefficients by design dynamic pressure, q, in p. s. i. and tent radius, r, in inches. Products are stress resultants N_{ϕ}, N_{θ}, $N_{\phi\theta}$ in pounds per inch.

4) Total stress resultants are:

$\bar{N}_{\phi} = P_e\, r + N_{\phi}$ (from 3) — Cylinder

$\bar{N}_{\phi} = P_e r/2 + N_{\phi}$ (from 3) — Spherical Ends

$\bar{N}_{\theta} = N_x = P_e\, r/2 + N_{\theta}$ (from 3) — Both

$\bar{N}_{\phi\theta} = N_{\phi\theta}$ (from 3) — Spherical Ends

Cylindrical Tents with Ellipsoidal Ends

The design curves resulting from this study and analysis are presented as Figures 109 through 112. Utilization of the design curves is as follows:

1) From design requirements determine tent size and shape and dynamic (or impact) pressure design value.

2) Enter Figure 109 and read the basic stress coefficients ($N_\phi/q\ r$ and $N_\theta/q\ r$, and $N\phi\theta/q\ r$) for the design dynamic pressure, q.

3) Enter Figures 110 through 112 and read the correction factors for P_e/q ($C_{q\phi}$, $C_{q\theta}$), h/d ($C_{h\phi}$, $C_{h\theta}$), W/ℓ_h ($C_{W\phi}$, $C_{W\theta}$), and b/r ($C_{b\phi}$, $C_{b\theta}$) for the cylindrical portion and ellipsoidal end.

4) Multiply corresponding correction factors with the basic stress coefficients and the dynamic pressure and tent radius to get the total stress resultant.

Ends; using the correction factors for the ends:

$$\bar{N}_\phi = C_{q\phi}\ C_{h\phi}\ C_{W\phi}\ C_{b\phi}\ (N_\phi/q\ r)\ q\ r$$

$$\bar{N}_\theta = C_{q\theta}\ C_{h\theta}\ C_{W\theta}\ C_{b\theta}\ (N_\theta/q\ r)\ q\ r$$

$$\bar{N}_{\phi\theta} = C_{q\phi\theta}\ C_{h\phi\theta}\ C_{W\phi\theta}\ C_{b\phi\theta}\ (N_{\phi\theta}/q\ r)\ q\ r$$

Center; using the correction factors for the cylindrical portion:

$$\bar{N}_\phi = C_{q\phi}\ C_{h\phi}\ C_{W\phi}\ C_{b\phi}\ (N_\phi/q\ r)\ q\ r$$

$$\bar{N}_x = C_{q\theta}\ C_{h\theta}\ C_{W\theta}\ C_{b\theta}\ (N_x/q\ r)\ q\ r$$

CELLULAR BEAM TESTS

Introduction

In order to engineer air-supported structures, it is necessary to be able to tailor designs for specific requirements thereby placing the strength where it is needed without penalizing other areas with unnecessary weight. To accomplish this, accurate methods of analysis are required, methods which do not unduly restrict the designer or analyst to certain shapes or sizes which have been used in the past. Only a cursory glance, however, is needed to realize the vast complexities which arise in analyzing fabric, air supported cellular structures. Rather than attack the problem from a completely analytical standpoint, then, it was decided to empirically correct a relatively simple deflection theory using data gathered from tests of fabric, air inflated cellular beams.

Because of the importance of wind loads in the design of double-wall tents, the manner of loading chosen for the tests was air pressure, uniformly distributed over one side of the beam. The deflections of the beams were measured and recorded as a function of beam position, load, and cell pressure. This procedure was repeated several times, for twelve models, to assure valid results.

Test Specimens

The models tested consisted of twelve inflated fabric beams, approximately three feet wide and four feet long (along the cell axis). There were basically three different cell sizes, one of each size for the straight beams and three of each for the nine curved models. All beams were fabricated of a Lincoln Fabric, Style Number 9199, which weighs 2.5 oz/sq yd. Care was taken during fabrication to keep the warp direction along the beam axis. This necessitated, in the curved beams, splicing several short pieces of fabric together to make the webs. Such a technique yields a nearly uniform modulus of elasticity along the beam axis.

Prior to testing, the models were measured and average (or typical) dimensions recorded. These dimensions, and others calculated from these, are tabulated in Table V. Direct measurement was made of d, w, n, W_b, and ℓ_b. The beam radius r, base angle ϕ_B, and cell angle α_c had to be calculated. The cell angle, being particularly sensitive to measurement, was calculated through the following relation, which averages the cell width and beam width measurements.

$$\alpha_c = \sin^{-1}\left(\frac{1}{2}\left\{W_b + \left[(W_b/W_c) - 1\right]/(n-1)\right\}\right) \qquad (126)$$

The beam radius and base angle of the curved models were found from an iterative solution of the following relations.

$$\ell_b = 2\, r\, \phi_B \qquad 127(a)$$

$$\ell_c = 2\, r \sin \phi_B \qquad 127(b),$$

These quantities are pictured in Figure 125.

Test Fixture

To statically load the models with a uniform air load, it was decided to use a test chamber with one side open. The model itself was employed as the remaining side to form a closed air chanber. Figure 126 is a schematic of the test fixture with a beam installed, and Figure 127 is a photograph of the test chamber without the beam. As may be seen in these figures, the end conditions were a pin and a roller. The beam models were supplied with extra material on all four sides. The ends were fastened to the chamber and roller as shown in the schematic of Figure 126. The fabric along the sides was then taped to the sides of the chamber as shown in Figures 128 and 129. This was necessary to completely seal the chamber. There was approximately an inch gap between the beam edge and the chamber wall. The additional load due to this gap, since beam width was 34 inches, is less than 3 percent ($\triangleq$ 1/34). Furthermore, its effect diminishes with distance from the beam edge, being a minimum at the center of the beam where deflections were measured. Hence, net effect of the side curtains was negligible.

Inflation pressure of the beams was measured on a vertical water manometer board. The pressure tube supplying this manometer originated on the underside of the beam, several cells removed from the beam pressure inlet. This was done to account for pressure reduction from leakage through beam fabric and seams. The chamber pressure was measured on an inclined water manometer board with a 10:1 slope (horizontal : vertical). This approach was necessary to accurately record the very small loads imposed on the beams. These manometer boards can be seen on the right hand side of Figure 127.

Test Procedure

The general procedure followed to statically test the beams was as follows:

1. Install beam in test fixture
2. Install deflection measuring devices.
3. Inflate beam to test inflation pressure.
4. Record zero deflections.
5. Pressurize test chamber to initial test pressure and

record beam deflection readings.

6. Increase test chamber pressure incrementally, holding the beam pressure constant. Record the deflection readings at each chamber pressure until the maximum deflection is reached.

7. Decrease chamber pressure to zero.

8. Repeat steps 4 through 7 for confirmation.

9. Increase beam inflation pressure incrementally, repeating steps 4 through 8 at each pressure until these steps have been completed for the maximum beam pressure.

10. Remove beam from test fixture.

This procedure was followed until tests of all twelve beams were completed and data repeatability obtained.

Results

Basic data collected from the tests consisted of horizontal beam deflection at the roller end vertical deflection of the movable beams support plate, vertical deflections at several points between the end and the center of each beam, applied load at initial wrinkle, and cell pressure. The basic data was reduced to yield deflections relative to the ends of the beams; i.e., the deflection of the plate which was used to obtain the roller boundary condition is accounted for in the final data reduction.

Load-deflection curves were plotted for all beams and compared with theoretical predictions generated from techniques described in DOUBLE WALL TENTS Stress Analysis. Discrepancies between the data were eliminated by reduction of the wrinkling value of $M/P_T r_c$ and the section moment of inertia. Through trial and error, these values were reduced to graphical form, dependent on the cell pressure and the beam to cell radius ratio. Figure 130 is the final product of this phase of the effort. Figures 131 and 132 show the agreement between theoretical and experimental results after empirical adjustment of the theory.

DOUBLE-WALL TENTS

Introduction

Double-wall tents provide inexpensive, easily portable environmental protection without the need to completely enclose the working area. Furthermore, by providing for independent cell inflation, a tear or hole in one portion of the tent will not initiate collapse of the entire structure. Obviously, the overall strength of the tent will be reduced, but under ordinary circumstances, the tent will continue to perform with little or no noticeable effect.

In the design of a double-wall tent, weight, package cube, and enclosed volume are of prime importance. For this reason, a weight-to-volume ratio is theoretically minimized in the following study. Results of the study provide a relationship between the number of cells in a tent and the cell angle.

Stress analysis of double-wall tents is extended into the nonlinear, post-wrinkling stage. Nonlinear load-deformation relations are derived, and after piece-wise linearization, are used to derive transfer matrices for the basic beam elements. With empirical data gained from inflated beam tests, these transfer matrices are used to analyze double-wall tents subjected to broadside wind loads.

Weight Study

To effect a least-weight analysis, it is necessary to derive approximate relations for the weight and enclosed volume of a tent. The cross-sectional area inside the tent shown in Figure 133 is approximately

$$A_t = r\,(r\,\phi_B + 2h_r \csc\phi_B) + (r^2 + h_r^2)\cot\phi_B. \tag{128}$$

The enclosed volume is $A_t \ell_h$ or

$$V = 2n\,r_c \sin\alpha_c \left[r\,(r\,\phi_B + 2h_r \csc\phi_B) + (r^2 + h_r^2)\cot\phi_B\right] \tag{129}$$

The weight of the fabric used to form n cells is

$$Wt = 4\Omega\left[r_c\,2n\,\alpha_c + (n+1)\cos\alpha_c\right]\left[(r + r_c)(\phi_B + \cot\phi_B) + h_r \csc\phi_B\right] \tag{130}$$

where Ω = fabric weight per unit surface area. The other parameters are shown in Figure 133.

To obtain a least-weight design requires the maximum volume-to-weight ratio. Dividing Equation 129 by Equation 130, and defining $\gamma = V/Wt$,

$$\gamma = \frac{n \sin\alpha \left[r_c(r\,\phi_B + 2h_r \csc\phi_B) + (r^2 + h_r^2)\cot\phi_B\right]}{2\left[2\,n\,\alpha_c + (n+1)\cos\alpha_c\right]\left[(r + r_c)(\phi_B + \cot\phi_B) + h_r \csc\phi_B\right]} \tag{131}$$

The intended use of the tent would set certain of the parameters, r, ϕ_B, h_r, and n, which would be a function of the length; and strength requirements would determine Ω. The two remaining independent variables, α_c and r_c,

determine the cell configuration directly. To establish whether or not γ obtains a finite maximum with regard to α_c and r_c, take the partial derivatives of γ with respect to α_c and r_c, and set them equal to zero.

From $\frac{\partial \gamma}{\partial r_c} = 0$, no maximum exists; so for minimum weight, the smallest radius practical should be used. The radius will therefore be dictated by strength and stability criteria.

Taking the partial derivative of γ with respect to α_c, and defining

$$C = \frac{\left[n\, r\, (r\, \phi_B + h_r \csc \phi_B) + (r^2 + h_r^2) \cot \phi_B\right]}{2\, \Omega \left[(r + r_c)(\phi_B + \cot \phi_B) + h_r \csc \phi_B\right]} \tag{132}$$

we obtain

$$\frac{\partial \gamma}{\partial \alpha_c} = C\, \frac{2n\, (\alpha_c \cos \alpha_c - \sin \alpha_c) + n + 1}{2\, n\, \alpha_c + (n + 1) \cos^2 \alpha_c} \tag{133}$$

Setting Equation 133 equal to zero,

$$\sin \alpha_c - \alpha_c \cos \alpha_c = \frac{n + 1}{2n} \tag{134}$$

The maximum (if it is a maximum) value of γ is, then, dependent only upon the number of cells, n. As a limiting value,

$$\lim_{n \to \infty} \frac{n + 1}{2n} = 1/2 \tag{135}$$

so that for large values of n,

$$\sin \alpha_c - \alpha_c \cos \alpha_c = 1/2 \tag{136}$$

A trial and error solution yields $\alpha_c = 68^\circ - 54'$. Obviously, for n = 1, $\alpha_c = 90^\circ$.

Since there is only one root of Equation 136 for $0 \leq \alpha_c \leq 90^\circ$, to determine if this is a maximum value, examine the sign of $\partial\gamma/\partial\alpha_c$ on both sides of the solved value of α_c. Setting n = 10, from Equation 133

$$\frac{\partial\gamma}{\partial\alpha_c} = \left[\frac{C}{(20\ \alpha_c + 11\cos\alpha_c)^2}\right] (20\ \alpha_c \cos\alpha_c - 20\sin\alpha_c + 11) \quad (137)$$

Since the brackets in Equation 137 will always be positive, and only the magnitude of Equation 137 is of interest, examine only

$$20\ (\alpha_c \cos\alpha_c - \sin\alpha_c) + 11 \quad (138)$$

Setting Equation 138 equal to zero, $\alpha_c \doteq 71.5^\circ$ for n = 10. Now setting $\alpha_c = 50^\circ$ in Equation 138 yields a positive sign, and $\alpha_c = 85^\circ$ results in a negative sign. Similar results are obtained for all values of n, so the result is the desired maximum volume-to-weight ratio in terms of α_c as a function of n. Figure 134 illustrates the variance of α_c and n for maximum γ.

As an illustration, consider an existing tent which shall be referred to as Tent 1. It has the following parameters: n = 12, Ω = 15 oz/sq yd, r = 9' - 6", h_r = 2' - 6", $\phi_B = 81^\circ$, r_c = 10", and $\alpha_c = 35^\circ - 48'$. Using Equations 129 and 130, V = 2234.1 cu ft and Wt = 166.5 lb. The tent is 140.4" long. The weight, as given in the above reference, is 264 lbs for the shelter section. This extra 97.5 lb is comprised of such items as carrying handles, zippers, weather seal flaps, local reinforcement, stitching, etc.

Now redesign Tent 1, varying only α_c and n and call it Tent 2. Approximately the same volume will be retained, and the weight will be reduced. The cell width will be approximately $2\ r_c \sin 70^\circ = 18.8"$. Require then, that $n \geq 140.0/18.8 = 7.5$. From Figure 134, for n = 8, $\alpha_c = 72^\circ$. Again using Equations 129 and 130, V = 2421.6 cu ft, and Wt = 149.3 lb. The length of Tent 2 is 152.5". Since the weight of the miscellaneous items on Tent 1 will be approximately the same for Tent 2, the final shelter section weight is 246.8 lb. These changes are tabulated in Table VI for easy comparison, and Figure 135 shows the relative sizes of the tent cells.

This comparison shows a 7% reduction in weight assuming the fabric weight remains the same. Because the beam stiffness is reduced, though, it is likely that a higher internal pressure will be required to provide the necessary stiffness, and possibly that a heavier fabric will be required to withstand the higher stresses. These and other considerations could override the previously predicted weight savings.

Pressure Distribution

For analysis of double-wall tents, the pressure distribution from a broadside wind load is taken to be a series of constant loads on short beam elements. The pressure distributions were taken from available wind tunnel data, and extrapolated to include any shapes for which data was not available. These experimental distributions were plotted, a curve placed through these points, and a representative constant load found for every five-degree increment along the tent. Typical pressure distributions for various tents are shown in Figures 136 and 137. A separate distribution was obtained for every combination of tent shape and wind velocity, for both guyed and unguyed conditions, to assure accuracy in the calculations of design curves.

Strength Study

It is apparent that geometric optimization alone is insufficient for complete weight control. Selection of fabric must be made with full consideration of material strength-to-weight ratio. While no formal procedure is developed herein for fabric selection, it is recognized that proper fabric design and/or selection can have paramount effect on the attempts to minimize weight. Study of physical properties of fabric is a significant and separate endeavor which should merit additional research and development outside the scope of this contract. Principal criteria for fabric weight optimization should require high strength-to-weight ratio and minimum safety margin.

Assuming a linear strain variation in a wrinkled fabric beam, and zero stress in the wrinkled portion, nonlinear moment-curvature and tension-strain relations are derived. After piece-wise linearization of these relations, they are substituted into the differential equations governing the deflections of a beam with a constant distributed load, and the resulting equations are solved subject to general boundary conditions at one end. In addition to the boundary conditions, the solutions are also made to yield a zero deflection state when the beam is subjected only to internal pressure. Hence the resulting solution is a function only of applied loads.

To analyze a structure with varying distributed load, the structure is broken into finite elements, each with constant load to approximate the true loading condition. The deflections and conditions of equilibrium for each element are placed in an extended transfer matrix, and the matrices for the entire structure assembled. Boundary conditions will appear as knowns in the appropriate state vectors.

Static Stability

Static instability of an "m" times redundant structure will occur when (m + 1) points have buckled. Since the tent fabric cannot carry compression load, static instability is also assumed to occur when the axial compression load equals the axial tension load due to inflation pressure.

Shear Deformation

Shear deformation is an important part of the deflection of air-supported cellular fabric beams (Reference 27). In this analysis, as in Reference 28, shear deformation is superimposed upon flexural deformation to obtain the total theoretical deformations of the structure. In Reference 27, the manner in which internal pressure influences shearing deflections, and how this effect is combined with the beam edge shearing stiffness, is clearly defined. Utilizing this approach, and assuming a constant shear strain on the beam cross-section, the shear strain is

$$\gamma_b = V/(P_c A_e + GA_c) \tag{139}$$

This is Equation (15) in Reference 27, with $A_c = kt$.

In Reference 28, an approximate shear modulus is derived for uncoated single-ply fabrics based on the state of biaxial stress. A comparison of this derivation with the coordinate system of the tent beams reveals that σ_x in Reference 28 is the web stress N_w. The shear modulus is, then

$$G = N_w = 2 P_c r_c \sin \alpha_c \tag{140}$$

Substituting this into Equation 139,

$$\gamma_b = V/P_c(A_e + 2 A_c r_c \sin \alpha_c) \tag{141}$$

Hence, the usual shear rigidity, AG, is replaced by the corresponding quantity in Equation 141, dependent not only upon the physical characteristics of the beam, but also on the internal pressure.

Fabric Modulus of Elasticity

The modulus of elasticity which was used in this study is a linear approximation to the warp stress-strain curve at a warp filling stress ratio of 1:2. This is approximately the stress ratio which exists at inflation. It was used to empirically correct the theory which follows, so should be used in any future analyses.

Deflection curves, however, are a result of aerodynamic tests, so the modulus of elasticity as used in stress calculations was not critical.

The modulus of elasticity that was used for the model fabric was

$$E = 200 \text{ lb/in}$$

as obtained from stress-strain data for this fabric.

Nonlinear Load-Deformation Relations

It is assumed that the state of strain in a fabric beam is

$$\varepsilon_\phi = \varepsilon_{\phi NA} + y\kappa \tag{142}$$

where κ is the change in curvature caused by the bending moment. Assuming Hooke's Law holds in the unwrinkled region, and a state of zero stress results in the wrinkled portion, the state of stress is (see Figure 138)

$$N_\phi = 0 \qquad y \geq c \tag{143(a)}$$

$$N_\phi = E\varepsilon_\phi = E\varepsilon_{\phi NA} + Ey\kappa \qquad y \leq c \tag{143(b)}$$

The axial load and bending moment are given by

$$P_T = \int N_\phi \, dA \tag{144(a)}$$

$$M = \int N_\phi \, y dA \tag{144(b)}$$

A fabric beam cross section is pictured in Figure 139. Cross-section properties are

$$A_c = 2r_c[\pi + (n-1)(2\alpha_c + \cos \alpha_c)] \tag{145(a)}$$

$$A_e = r_c^2 [\pi + 2(n-1)(\alpha_c + \sin \alpha_c \cos \alpha_c)] \tag{145(b)}$$

$$I = r_c^3 [\pi + 2(n-1)(\alpha_c + \sin \alpha_c \cos \alpha_c + \frac{1}{3} \cos^3 \alpha_c)] \tag{145(c)}$$

Prior to wrinkling, Equations 144 yield the usual relations.

$$P_T = N_{\phi NA} A_c \tag{146(a)}$$

$$M = \frac{I}{r_c} (N_{\phi max} - N_{\phi NA}) \tag{146(b)}$$

At initial wrinkle, when $c = r$, $N_{\phi max} = 2 N_{\phi NA}$ so that

$$\frac{M}{P_T r_c} = \frac{I(2 N_{\phi NA} - N_{\phi NA})}{r_c (N_{\phi NA} A_c r_c)} = \frac{I}{A_c r_c^2} \tag{147}$$

After wrinkling begins, there are three explicit sets of relations between the stresses and stress resultants, depending on how far wrinkling has progressed through the cross section. When wrinkling has begun, but has not reached the web, Equation 144 yields the following:

$$r_c \cos \alpha_c \leq c \leq r_c, \quad \theta_1 = \cos^{-1} \left(\frac{c}{r_c}\right) \tag{148(a)}$$

$$P_T = \pi r_c^2 \left(\frac{N_{\phi max}}{r_c + c}\right) \left\{ n \cos \theta_1 \left[\tan \theta_1 - \theta_1 + 2 \alpha_c + \cos \alpha_c\right] + \cos \theta_1 \left[\pi - 2\alpha_c - \cos \alpha_c\right] \right\}, \tag{148(b)}$$

$$M = 2 r_c^3 \left(\frac{N_{\phi max}}{r_c + c}\right) \left\{ n \left[\alpha_c + \sin \alpha_c \cos \alpha_c + \frac{1}{3} \cos^3 \alpha_c - \frac{1}{2} (\theta_1 - \sin \theta_1 \cos \theta_1) \right] + \left[\frac{\pi}{2} - \alpha_c - \sin \alpha_c \cos \alpha_c - \frac{1}{3} \cos^3 \alpha_c\right] \right\} \tag{148(c)}$$

After wrinkling progresses into the web:

$$-r_c \cos\alpha_c \le c \le r_c \cos\alpha_c,\ \theta_2 = \cos^{-1}\left(\frac{c}{r_c}\right) \tag{149(a)}$$

$$\begin{aligned} P_T = 2r_c^2\left(\frac{N_{\phi max}}{r_c + c}\right)\Big\{ & n\left[\sin\alpha_c + \frac{c}{r_c}\alpha_c + \frac{1}{4}\left(\frac{c}{r_c} + \cos\alpha_c\right)^2\right] \\ & + \left[(\pi - \alpha_c\ \theta_2)\cos\theta_2 - \sin\alpha_c + \sin\theta_2\right. \\ & \left. - \frac{1}{4}\left(\frac{c}{r_c} + \cos\alpha_c\right)^2\right]\Big\} \end{aligned} \tag{149(b)}$$

$$\begin{aligned} M = 2r_c\left(\frac{N_{\phi max}}{r_c + c}\right)\Big\{ & n\Big[\frac{1}{2}(\alpha_c + \sin\alpha_c\cos\alpha_c) + \sin\alpha_c\cos\theta_2 \\ & + \frac{1}{6}\left(\frac{c^3}{r_c^3} + \cos^3\alpha_c\right) - \frac{1}{4}\frac{c}{r}\left(\frac{c^2}{r_c^2} - \cos^2\alpha_c\right)\Big] \\ & + \frac{1}{4}\Big[\frac{c}{r_c}\left(\frac{c^2}{r_c^2} - \cos^2\alpha_c\right) - \frac{1}{6}\left(\frac{c^3}{r_c^3} + \cos^3\alpha_c\right) \\ & - \sin\alpha_c\cos\theta_2 - \frac{1}{2}\sin\alpha_c\cos\alpha_c \\ & + \frac{1}{2}\sin\theta_2\cos\theta_2 + \frac{1}{2}(\pi - \alpha_c - \theta_2)\Big]\Big\} \end{aligned} \tag{149(c)}$$

And finally, after wrinkling has gone completely through the web:

$$-r_c \le c \le -r_c\cos\alpha_c,\ \theta_3 = \cos^{-1}\left(-\frac{c}{r_c}\right) \tag{150(a)}$$

$$P_T = 2nr_c^2\left(\frac{N_{\phi max}}{r_c + c}\right)(\sin\theta_3 - \theta_3\cos\theta_3) \tag{150(b)}$$

$$M = nr_c^3\left(\frac{N_{\phi max}}{r_c + c}\right)(\theta_3 - \sin\theta_3\cos\theta_3) \tag{150(c)}$$

Figure 140 illustrates the physical significance of the parameters defining the extent of wrinkling.

Defining

$$D_1 = 2n\cos\theta_1\left[\tan\theta_1 - \theta_1 + \cos\alpha_c + 2\alpha_c\right] + 2\cos\theta_1\left[\pi - 2\alpha_c - \cos\alpha_c\right] \quad (151(a))$$

$$D_2 = 2n\left[\alpha_c + \sin\alpha_c\cos\alpha_c + \frac{1}{3}\cos^3\alpha_c - \frac{1}{2}(\theta_1 - \sin\theta_1\cos\theta_1)\right] + 2\left[\frac{\pi}{2} - \alpha_c - \sin\alpha_c\cos\alpha_c - \frac{1}{3}\cos^3\alpha_c\right] \quad (151(b))$$

$$D_3 = 2n\left[\sin\alpha_c + \frac{c}{r_c}\alpha_c + \frac{1}{4}\left(\frac{c}{r_c}\right) + \cos\alpha_c\right] + 2n\left[(\pi - \alpha_c - \theta_2)\cos\theta_2 - \sin\alpha_c + \sin\theta_2 - \frac{1}{4}\left(\frac{c}{r} + \cos\alpha_c\right)^2\right] \quad (151(c))$$

$$D_4 = 2n\left[\frac{1}{2}(\alpha_c + \sin\alpha_c\cos\alpha_c) + \sin\alpha_c\cos\theta_2 + \frac{1}{6}\left(\frac{c^3}{r_c^3} + \cos^3\alpha_c\right) - \frac{1}{4}\frac{c}{r_c}\left(\frac{c^2}{r_c^2} - \cos^2\alpha_c\right)\right] + 2\left[\frac{1}{4}\frac{c}{r_c}\left(\frac{c^2}{r_c^2} - \cos^2\alpha_c\right) - \frac{1}{6}\left(\frac{c^3}{r_c^3} + \cos^3\alpha_c\right) - \sin\alpha_c\cos\theta_2 - \frac{1}{2}\sin\alpha_c\cos\alpha_c + \frac{1}{2}\sin\theta_2\cos\theta_2 + \frac{1}{2}(\pi - \alpha_c - \theta_2)\right] \quad (151(d))$$

$$D_5 = 2n(\sin\theta_3 - \theta_3\cos\theta_3) \quad (151(e))$$

$$D_6 = n(\theta_3 - \sin\theta_3\cos\theta_3) \quad (151(f))$$

Equations 148 - 150 may be written more concisely as

$$r_c \cos \alpha_c \leq c \leq r_c$$

$$P_T = r_c^2 \left(\frac{N_{\phi max}}{r_c + c}\right) D_1 \qquad (152(a))$$

$$M = r_c^3 \left(\frac{N_{\phi max}}{r_c + c}\right) D_2 \qquad (152(b))$$

$$- r_c \cos \alpha_c \leq c \leq \cos \alpha_c$$

$$P_T = r_c^2 \left(\frac{N_{\phi max}}{r_c + c}\right) D_3 \qquad (153(a))$$

$$M = r_c^3 \left(\frac{N_{\phi max}}{r_c + c}\right) D_4 \qquad (153(b))$$

$$- r_c \leq c \leq - r_c \cos \alpha_c$$

$$P_T = r_c^2 \left(\frac{N_{\phi max}}{r_c + c}\right) D_5 \qquad (154(a))$$

$$M = r_c^3 \left(\frac{N_{\phi max}}{r_c + c}\right) D_6$$

The extent of wrinkling is controlled by the dimensionless ratio $M/P_T r_c$. Equation 147 defines this ratio for initial wrinkle in terms of the physical characteristics of the beam. As $M/P_T r_c$ increases, the extent of wrinkling increases. From equations 152 through 154 this ratio is

$$r_c \cos \alpha_c \leq c \leq r_c$$

$$\frac{M}{P_T r_c} = \frac{D_2}{D_1} \tag{155}$$

$$- r_c \cos \alpha_c \leq c \leq r_c \cos \alpha_c$$

$$\frac{M}{P_T r_c} = \frac{D_4}{D_3} \tag{156}$$

$$- r_c \leq c \leq - r_c \cos \alpha_c$$

$$\frac{M}{P_T r_c} = \frac{D_6}{D_5} \tag{157}$$

Now the equation of stress in the wrinkled beam which was used in the the integration of Equation 144 is:

$$N_\phi = \frac{N_{\phi max}}{r_c + c}(c - y) = \frac{N_{\phi max}}{r_c + c} c - \frac{N_{\phi max}}{r_c + c} y \qquad (158)$$

Comparison of Equations 143 and 158 yields two expressions for $\frac{N_{\phi max}}{r_c + c}$

$$\frac{N_{\phi max}}{r_c + c} = \frac{E\varepsilon_{\phi NA}}{c} \qquad (159(a))$$

$$\frac{N_{\phi max}}{r_c + c} = - E\kappa \qquad (159(b))$$

Substituting Equations 159 into Equations 152, 153, and 154

$$r_c \cos \alpha_c \leq c \leq r_c$$

$$P_T = E\varepsilon_{\phi NA} r_c (D_1/\cos \theta_1) \qquad (160(a))$$

$$M = E\kappa r_c^3 D_2 \qquad (160(b))$$

$$- r_c \cos \alpha_c \leq c \leq r_c \cos \alpha_c$$

$$P_T = E\varepsilon_{\phi NA} r_c D_3 (r_c/c) \qquad (161(a))$$

$$M = - E\kappa r_c^3 D_4 \qquad (161(b))$$

$$- r_c \leq \phi \leq - r_c \cos \alpha_c$$

$$P_T = E\varepsilon_{\phi NA}\, r_c\, (- D_5/\cos \theta_3) \tag{162(a)}$$

$$M = - E\kappa\, r_c^3\, D_6 \tag{162(b)}$$

where $c = r \cos \theta_1$ was used in Equation 160 and $c = - r \cos \theta_3$ was used in Equation 162.

Equations 160 through 162 yield the nonlinear relations between the moment and curvature and the axial load and strain at the neutral axis in terms of $M/P_T r_c$. The curves will be as shown in Figure 141. By piece-wise linearization, these equations may be written

$$\frac{EI\kappa}{M} = C_1 + C_2 \frac{P_T r_c}{M} \tag{163(a)}$$

$$\frac{A_c E\varepsilon_{\phi NA}}{P_T} = C_3 + C_4 \frac{M}{P_T r_c} \tag{163(b)}$$

where the constants, C_1, assume different values as $M/P_T r_c$ varies. The upper limit of $M/P_T r_c$ is obtained from Equation 157 by letting $\frac{c}{r} \to - 1$ $(\theta_3 \to 0)$

$$\left.\begin{aligned} \lim_{\theta_3 \to 0} \frac{M}{P_T r_c} &= \lim_{\theta_3 \to 0} \frac{D_6}{D_5} = \lim_{\theta_3 \to 0} \frac{n(\theta_3 - \sin \theta_3 \cos \theta_3)}{2n(\sin \theta_3 - \theta_3 \cos \theta_3)} \\ &= \lim_{\theta_3 \to 0} \frac{1 - \cos^2 \theta_3 + \sin^2 \theta_3}{2\,\theta_3 \sin \theta_3} = \lim_{\theta_3 \to 0} \frac{\sin \theta_3}{\theta_3} \\ &= \lim_{\theta_3 \to 0} \frac{\cos \theta_3}{1} = 1 \end{aligned}\right\} \tag{164}$$

This limit is shown in Figure 141.

With Equations 142 and 163 , the relation between strain and stress resultants is

$$\varepsilon_\phi = \frac{1}{A_c E r_c} = (C_3\ P_T r_c + C_4\ M) + y\frac{1}{EI}\ (C_1\ M + C_2\ P_T r_c) \qquad (165)$$

Transfer Matrix for Straight Beams

Consider the beam element shown in Figure 142. The neutral axis strain is

$$\varepsilon_{NA} = \frac{\widehat{C'B'}}{\widehat{CD}} = \frac{\rho_b d\omega - dx}{dx} \qquad (166)$$

The strain at a distance y above the neutral axis is

$$\left.\begin{aligned} \varepsilon &= \frac{A'B' - AB}{AB} = \frac{(\rho_b - y)\ d\omega - y\ \gamma_b + y\ (\gamma_b + d\gamma_b) - dx}{dx} \\ &= \frac{\rho_b d\omega - dx}{dx} - y\frac{d\psi_b}{dx} = \varepsilon_{NA} - y\frac{d\psi_b}{dx} \end{aligned}\right\} (167)$$

To evaluate the radius of curvature and rotation in terms of displacements, write

$$\left.\begin{aligned} &\overrightarrow{CC'} + \overrightarrow{C'O'} + \overrightarrow{CD} + \overrightarrow{DD'} + \overrightarrow{D'O'} \\ &u\hat{i} + v\hat{j} + \rho_b\hat{e}_n = dx\hat{i} + (u + du)\hat{i} + (v + dv)\hat{j} + \rho_b\hat{e}'_n \end{aligned}\right\} (168)$$

The normal unit vectors are

$$\left.\begin{aligned} \hat{e}_n &= -\sin\omega\hat{i} + \cos\omega\hat{j} \\ \hat{e}'_n &= -\sin(\omega + d\omega)\hat{i} + \cos(\omega + d\omega)\hat{j} \end{aligned}\right\} (169(a))$$

$$\left.\begin{aligned} \text{or}\quad \hat{e}'_n &= -\left[\sin\omega\cos d\omega + \cos\omega\sin d\omega\right]\hat{i} \\ &\quad + \left[\cos\omega\cos d\omega - \sin\omega\sin d\omega\right]\hat{j} \end{aligned}\right\} (169(b))$$

For small deformations, $\cos\omega = \cos d\omega \doteq 1$, $\sin\omega \doteq \omega$, and $\sin d\omega \doteq d\omega$. With these, the normal unit vectors are

$$\left.\begin{aligned} \hat{e}_n &= -\omega\hat{i} + \hat{j} \\ \hat{e}'_n &= -(\omega + d\omega)\hat{i} + (1 - \omega d\omega)\hat{j} \end{aligned}\right\} \quad (170)$$

Substituting Equation 170 into Equation 168

$$(u - \rho_b\omega)\hat{i} + (v + \rho_b)\hat{j} = (u + du + dx - \rho_b\omega - \rho_b d\omega)\hat{i} + (v + dv + \rho_b - \rho_b b\omega)\hat{i} \quad (171)$$

The scalar equations thus formed are

$$0 = du + dx - \rho_b d\omega \quad (172(a))$$

$$0 = dv - \rho_b d\omega \quad (172(b))$$

Substituting Equation 172(a) into Equation 166 yields

$$\varepsilon_{NA} = \frac{du}{dx} \quad (173)$$

Substituting $\rho_b d\omega = du + dx$ from Equation 172(a) into Equation 172(b) yields

$$\left.\begin{aligned} dv &= \omega(du + dx) = \omega du + \omega dx \\ \frac{dv}{dx} &= \omega + \omega\frac{du}{dx} = \omega + \omega\varepsilon_{NA} \doteq \omega \end{aligned}\right\} \quad (174)$$

neglecting $\omega\varepsilon_{NA}$. Substituting Equation 173 into Equation 167

$$\varepsilon = \frac{du}{dx} - y\frac{d\psi_b}{dx} \quad (175)$$

Comparing Equations 165 and 175 , and substituting $\omega = \psi_b + \gamma_b$ in Equation 174b yields the following three differential equations governing the displacement of the straight beam element:

$$\frac{du}{dx} = \frac{1}{A_c E r_c} (C_3 P_T r_c + C_4 M) \qquad (176(a))$$

$$\frac{d\psi}{dx} = - \frac{1}{EI} (C_1 M + C_2 P_T r_c) \qquad (176(b))$$

$$\frac{dv}{dx} = \psi_b + \gamma_b \qquad (176(c))$$

where

u is the longitudinal displacement,

v is the transverse displacement,

ψ_b is the rotation of a fiber originally perpendicular to the neutral axis, and

γ_b is the shear strain.

The equations of equilibrium for a straight beam element loaded by a uniform load are

$$P_T = P_{T_i} \qquad (177(a))$$

$$V = V_i - P_{ext} x \qquad (177(b))$$

$$M = M_i - V_i x + \frac{1}{2} P_{ext} x^2 \qquad (177(c))$$

where

$$P_{ext} = P_{ext}' + P_{ext}''$$

positive as shown in Figure 143.

Substituting Equation 177 into Equation 176 (a)

$$\frac{du}{dx} = \frac{1}{A_c E r_c}(C_3 P_T r_c + C_4 M_i - C_4 V_i x + \frac{1}{2} C_4 P_{ext} x^2) \qquad (178)$$

Integration yields

$$u = \frac{1}{A_c E r_c}(C_3 P_{Ti} r_c x + C_4 M_i x - \frac{1}{2} C_4 V_i x + \frac{1}{6} C_4 P_{ext} x^3) + a \qquad (179)$$

The constant of integration, a, is evaluated with the boundary condition, $u(o) = u_i$. Hence,

$$u = u_i + \frac{1}{A_c E r_c}(C_4 x M_i - C_3 r_c x P_{Ti} - \frac{1}{2} C_4 x^2 V_i + \frac{1}{6} C_4 x^3 P_{ext}) \qquad (180)$$

Substituting Equation 177 into Equation 176(b),

$$\frac{d\psi_b}{dx} = -\frac{1}{EI}(C_1 M_i - C_1 V_i x + \frac{1}{2} C_1 P_{ext} x^2 + C_2 P_{Ti} r) \qquad (181)$$

Integrating,

$$\psi_b = -\frac{1}{EI}(C_1 M_i x - \frac{1}{2} C_1 V_i x^2 + \frac{1}{6} C_1 P_{ext} x^3 + C_2 P_{Ti} r x) + a \qquad (182)$$

The constant of integration, a, is evaluated with the boundary condition, $\psi_b(0) = \psi_{bi}$. Hence,

$$\psi_b = \psi_{bi} - \frac{1}{EI}(C_1 x M_i + C_2 r_c x P_{Ti} - \frac{1}{2} C_1 x^2 V_i + \frac{1}{6} C_1 x^3 P_{ext}) \qquad (183)$$

Substituting Equation 177 into Equation 176(c) and with $\gamma_b = V/A_c G$,

$$\frac{d\phi}{dx} = \psi_{bi} - \frac{1}{EI}(C_1 M_i x + C_2 r_c P_{Ti} x - \frac{1}{2} C_1 V_i x^2 + \frac{1}{6} C_1 P_{ext} x^3) \pm \frac{1}{A_c G}(V_i - P_{ext} x) \qquad (184)$$

$$V = \psi_{bi} x - \frac{1}{EI}\left(\frac{1}{2} C_1 M_i x^2 + \frac{1}{2} C_2 r_c P_{Ti} x^2 - \frac{1}{6} C_1 V_i x^3 + \frac{1}{24} C_1 P_{ext} x^4\right) + \frac{1}{A_c G}\left(V_i x - \frac{1}{2} P_{ext} x^2\right) + a \qquad (185)$$

The constant of integration, a, is evaluated from the boundary condition, $V(0) = V_i$. Hence

$$V = V_i + \psi_{bi} - \frac{1}{EI}\left(\frac{1}{2} C_1 x^2 M_i + \frac{1}{2} C_2 r_c x^2 P_{Ti} - \frac{1}{6} C_1 x^3 V_i + \frac{1}{24} C_1 x^4 P_{ext}\right) + \frac{1}{A_c G}\left(x V_i - \frac{1}{2} x^2 P_{ext}\right) \qquad (186)$$

To yield a zero displacement condition when the beam segment is subjected only to internal pressurization ($P_T = P_o$), substitute $P_A = P_T - P_o$ for P_T in Equations 177 thru 186. P_A is the axial load resulting from external loading. With this substitution, then, Equations 177 thru 186 yield the following extended transfer matrix equation.

$$\begin{Bmatrix} v \\ u \\ \psi_b \\ M \\ P_A \\ V \\ 1 \end{Bmatrix} = \begin{bmatrix} 1 & 0 & x & -\frac{C_1 x^2}{2EI} & -\frac{C_2 r_c x^2}{2EI} & \frac{C_1 x^3}{6EI} + \frac{x}{A_c G} & -\frac{C_1 x^4 P_{ext}}{24EI} - \frac{x^2 P_{ext}}{2 A_c G} \\ 0 & 1 & 0 & \frac{C_4 x}{A_c E r_c} & \frac{C_3 x}{A_c E} & -\frac{C_4 x^2}{2 A_c E r_c} & \frac{C_4 x^3 P_{ext}}{6 A_c E r_c} \\ 0 & 0 & 1 & -\frac{C_1 x}{EI} & -\frac{C_2 r_c x}{EI} & \frac{C_1 x^2}{2EI} & -\frac{C_1 x^3 P_{ext}}{6EI} \\ 0 & 0 & 0 & 1 & 0 & -x & \frac{x^2 P_{ext}}{2} \\ 0 & 0 & 0 & 0 & 1 & 0 & 0 \\ 0 & 0 & 0 & 0 & 0 & 1 & -x P_{ext} \\ 0 & 0 & 0 & 0 & 0 & 0 & 1 \end{bmatrix} \begin{Bmatrix} v_i \\ u_i \\ \psi_{bi} \\ M_i \\ P_{Ai} \\ V_i \\ 1 \end{Bmatrix} \qquad (187(a))$$

In shorthand notation, this is written

$$\{z\} = [F]\ \{z\}_i \qquad (187(b))$$

Transfer Matrix for Circular Beams

Consider the beam element in Figure 144.

The middle surface strain is given by

$$\varepsilon_{\phi NA} = \frac{C'D' - C\,D}{C\,D} \quad \frac{\rho_b(d\phi - d\omega) - r\,d\phi}{r\,d\phi} \quad \frac{1}{r}\ (\rho_b - r - \rho_b \frac{d\omega}{d\phi}) \qquad (188)$$

The strain at a distance y from the middle surface is

$$\varepsilon_\phi = \frac{E'F' - E\,F}{E\,F} \quad \frac{(\rho_b + y)(d\phi - d\omega) + y(\gamma_b + d\gamma_b) - y(\gamma_b) - (r + y)\,d\phi}{(r + y)\,d\phi} \qquad (189(a))$$

$$\varepsilon_\phi = \frac{1}{r + y}\ (\rho_b - r - \rho_b \frac{d\omega}{d\phi} - y \frac{d\psi_b}{d\phi} = \frac{1}{r+y}\ (r\,\varepsilon_{\phi NA} - y \frac{d\psi_b}{d\phi} \qquad (189(b))$$

with Equation 188. Now

$$\frac{1}{r + y} = \frac{1}{r} \frac{1}{1 + \frac{y}{r}} = \frac{1}{r} \sum_{n=o}^{n=\infty} (-\frac{y}{r})^n \qquad (190)$$

for $y < r$. Introducing Equation 190 into Equation 189(b)

$$\varepsilon_\phi = \varepsilon_{\phi NA} \sum_{n=o}^{n=\infty} (-\frac{y}{r})^n - \frac{y}{r} \frac{d\psi_b}{d\phi} \sum_{n=o}^{n=\infty} (-\frac{y}{r})^n \qquad (191(a))$$

$$\varepsilon_\phi = \varepsilon_{\phi NA} (1 - \frac{y}{r} + \frac{y^2}{r^2} + ---) - \frac{d\psi_b}{d\phi} \frac{y}{r} (1 - \frac{y}{r} + \frac{y^2}{r^2} + ---) \qquad (191(b))$$

$$\varepsilon_\phi = \varepsilon_{\phi NA} - \frac{y}{r} (\varepsilon_{\phi NA} + \frac{d\psi_b}{d\phi}) + \frac{y^2}{r^2} (\varepsilon_{\phi NA} + \frac{d\psi_b}{d\phi}) + - - - \qquad (191(c))$$

If $\frac{y}{r} << 1$, then

$$\varepsilon_{\phi} = \varepsilon_{\phi NA} - \frac{y}{r}\left(\varepsilon_{\phi NA} + \frac{dw_o}{d\phi}\right) \qquad (192)$$

To determine the strain-displacement relations, write

$$\vec{OC} + \vec{CC'} + \vec{C'O'} = \vec{OD} + \vec{DD'} + \vec{D'O'} \qquad (193(a))$$

$$r\hat{e}_r + v\hat{e}_r + u\hat{e}_\phi - \rho_b\hat{e}_n = r\hat{e}'_r + (v + dv)\,\hat{e}'_r + (u + du)\,\hat{e}'_\phi - \rho_b\hat{e}'_n \qquad (193(b))$$

The unit vectors are, in terms of $\hat{e}'_r$ and $\hat{e}'_\phi$,

$$\hat{e}_r = \cos d\phi\,\hat{e}'_r - \sin d\phi\,\hat{e}'_\phi \qquad (194(a))$$

$$\hat{e}_\phi = \cos d\phi\,\hat{e}'_\phi + \sin d\phi\,\hat{e}'_r \qquad (194(b))$$

$$\hat{e}_n = \cos(\omega + d\phi)\,\hat{e}'_r - \sin(\omega + d\phi)\,\hat{e}'_\phi \qquad (194(c))$$

$$\hat{e}_n = (\cos\omega\cos d\phi - \sin\omega\sin d\phi)\,\hat{e}'_r - (\sin\omega\cos d\phi + \cos\omega\sin d\phi)\hat{e}'_\phi \qquad (194(d))$$

$$\hat{e}'_n = \cos(\omega + d\omega)\,\hat{e}'_r - \sin(\omega + d\omega)\hat{e}'_\phi \qquad (194(e))$$

$$\hat{e}'_n = (\cos\omega\cos d\omega - \sin\omega\sin d\omega)\hat{e}'_r - (\sin\omega\cos d\omega + \cos\omega\sin d\omega)\hat{e}'_\phi \qquad (194(f))$$

For small deformations, $\cos\omega \doteq \cos d\omega \doteq \cos d\phi \doteq 1$, $\sin\omega \doteq \omega$, $\sin d\omega \doteq d\omega$, and $\sin d\phi \doteq d\phi$. With these substitutions, Equations 194 are written

$$\hat{e}_r = \hat{e}'_r - d\phi\,\hat{e}'_\phi \qquad (195(a))$$

$$\hat{e}_\phi = \hat{e}'_\phi + d\phi\,\hat{e}'_r \qquad (195(b))$$

$$\hat{e}_n = (1 - \omega d\phi)\,\hat{e}'_r - (\omega + d\phi)\,\hat{e}'_\phi \qquad (195(c))$$

$$\hat{e}'_n = (1 - \omega d\omega)\,\hat{e}'_r - (\omega + d\omega)\,\hat{e}'_\phi \qquad (195(d))$$

Substituting Equations 195 into Equation 193(b),

$$\left.\begin{aligned} r\hat{e}'_r - rd\phi\,\hat{e}'_\phi + v\hat{e}'_r - vd\phi\hat{e}'_\phi + u\hat{e}'_\phi + ud\phi\hat{e}'_r \\ - \rho_b\,(1 - \omega d\phi)\,\hat{e}'_r + \rho_b\,(\omega + d\phi)\,\hat{e}'_\phi = \\ r\hat{e}'_r + (v + dv)\,\hat{e}'_r + (u + du)\,\hat{e}'_\phi \\ - \rho_b\,(1 - \omega d\omega)\,\hat{e}'_r + \rho_b\,(\omega + d\omega)\,\hat{e}'_\phi \end{aligned}\right\} (196(a))$$

$$\left.\begin{aligned} (ud\phi + \rho_b\omega d)\,\hat{e}'_r + (-d\phi - vd\phi + \rho_b d\phi)\,\hat{e}'_\phi = \\ (dv + \rho_b\omega d\omega)\,\hat{e}'_r + (du + \rho_b d\omega)\,\hat{e}'_\phi \end{aligned}\right\} (196(b))$$

The scalar equations thus formed are

$$ud\phi + \rho_b\omega d\phi - dv - \rho_b\omega d\omega = 0 \qquad (197(a))$$

$$-rd\phi - vd\phi + \rho_b d\phi - du - \rho_b\omega = 0 \qquad (197(b))$$

From Equation 197(a),

$$\frac{dv}{d\phi} - u = \rho_b\omega - \rho_b\omega\,\frac{d\omega}{d\phi} \qquad (198(a))$$

$$\frac{du}{d\phi} + v = \rho_b - r - \rho_b\,\frac{d\omega}{d\phi} \qquad (198(b))$$

Rearranging Equation 198(b),

$$\rho_b - \rho_b\,\frac{d\omega}{d\phi} = r\,(1 + \varepsilon_{\phi NA}) \qquad (199)$$

Substituting Equation 199 into Equation 198(a)

$$\frac{dv}{d\phi} - u = r\omega\,(1 + \varepsilon_{\phi NA}) \qquad (200)$$

Neglecting the product $\omega\varepsilon_{\phi NA}$ in Equation 200,

$$\frac{dv}{d\phi} - u = r\omega \tag{201}$$

Substituting Equation 199 into Equation 198(b),

$$\frac{du}{d\phi} + v = r\varepsilon_{\phi NA} \tag{202}$$

Substituting Equation 202 into Equation 192,

$$\varepsilon_{\phi} = \frac{1}{r}\left(\frac{du}{d\phi} + v\right) - \frac{y}{r}\left[\frac{1}{r}\left(\frac{du}{d\phi} + v\right) + \frac{d\psi_b}{d\phi}\right] \tag{203}$$

Comparison of Equations 165 and 203 yields

$$\frac{du}{d\phi} + v = \frac{r}{A_c E r_c}\left(C_3 P_T r_c + C_4 M\right) \tag{204}$$

$$\frac{1}{r}\left(\frac{du}{d\phi} + v\right) + \frac{d\psi_b}{d\phi} = -\frac{r}{EI}\left(C_1 M + C_2 P_T r_c\right) \tag{205}$$

Substituting for $\left(\frac{du}{d\phi} + v\right)$ from Equation 204 into Equation 205 yields

$$\frac{d\psi_b}{d\phi} = -\left(\frac{C_1 r}{EI} + \frac{C_4}{A_c E r_c}\right) M - \left(\frac{C_2 r r_c}{EI} + \frac{C_3}{A_c E}\right) P_T \tag{206}$$

Substituting $\omega = \psi_b + \gamma_b$ into Equation 201 yields

$$\frac{dv}{d\phi} - u = r\psi_b + r\gamma_b = r\psi_b + \frac{r}{A_c G} V \tag{207}$$

Solution of Equation 206 and substitution of the solution into Equation 207 yields an equation which with Equation 204 forms the system of equations governing the displacement of the circular beam.

The equations of equilibrium for the circular beam segment shown in Figure 145 are

$$P_T = P_{Ti}\cos\phi - V_i \sin\phi + P_{ext} r\,(1 - \cos\phi) \qquad (208(a))$$

$$V = P_{Ti}\sin\phi + V_i \cos\phi - P_{ext} r \sin\phi \qquad (208(b))$$

$$M = M_i - P_{Ti} r\,(1 - \cos\phi) - V_i r \sin\phi + P_{ext} r^2 (1 - \cos\phi) \qquad (208(c))$$

where

$$P_{ext} = P'_{ext}\left(1 - \frac{r_c}{r}\right) + P''_{ext}\left(1 + \frac{r_c}{r}\right)$$

positive as shown in Figure 145.

Substituting Equation 208 into Equation 206,

$$\frac{d\psi_b}{d\phi} = -\left(\frac{C_1 r}{EI} + \frac{C_4}{A_c E r_c}\right)\left[M_i - P_{Ti} r\,(1 - \cos\phi) - V_i r \sin\phi + P_{ext} r^2 (1 - \cos\phi)\right]$$
$$-\left(\frac{C_2 r r_c}{EI} + \frac{C_3}{A_c E}\right)\left[P_{Ti}\cos\phi - V_i \sin\phi + P_{ext} r\,(1 - \cos\phi)\right] \qquad (209)$$

Integrating,

$$\psi_b = -\left(\frac{C_1 r}{EI} + \frac{C_4}{A_c E r_c}\right)\left[M_i\phi - P_{Ti} r\,(\phi - \sin\phi) + V_i r \cos\phi + P_{ext} r^2 (\phi - \sin\phi)\right]$$
$$-\left(\frac{C_2 r r_c}{EI} + \frac{C_3}{A_c E}\right)\left[P_{Ti}\sin\phi + V_i \cos\phi + P_{ext} r\,(\phi - \sin\phi)\right] + a \qquad (210)$$

The constant of integration, a, is evaluated from the boundary condition, $\psi_b(o) = \psi_{bi}$. Hence

$$\psi_b = \psi_{bi} - \left(\frac{C_1 r}{EI} + \frac{C_4}{A_c E r_c}\right)\left[M_i\phi - P_{Ti} r\,(\phi - \sin\phi) - V_i r\,(1 - \cos\phi)\right.$$
$$\left. + P_{ext} r^2 (\phi - \sin\phi)\right] - \left(\frac{C_2 r r_c}{EI} + \frac{C_3}{A_c E}\right)\left[P_{Ti}\sin\phi - V_i (1 - \cos\phi)\right.$$
$$\left. + P_{ext} r\,(\phi - \sin\phi)\right] \qquad (211)$$

Substitution of Equations 208 and 211 into Equation 207 yields

$$\frac{dv}{d\phi} - u = r\,\psi_{bi} - \left(\frac{C_1 r^2}{EI} + \frac{C_4 r}{A_c E r_c}\right)\left[M_i\phi - P_{Ti} r\,(\phi - \sin\phi) - V_i r\,(1 - \cos\phi) + P_{ext} r^2\,(\phi - \sin\phi)\right] - \left(\frac{C_2 r^2 r_c}{EI} + \frac{C_3 r}{A_c E}\right)\left[P_{Ti}\sin\phi - V_i\,(1 - \cos\phi) + P_{ext} r\,(\phi - \sin\phi)\right] + \frac{r}{A_c G}\left[P_{Ti}\sin\phi + V_i\cos\phi - P_{ext} r\sin\phi\right] \qquad (212(a))$$

Substitution of Equation 208 into Equation 204 yields

$$\frac{du}{d\phi} + v = \frac{C_3 r}{A_c E}\left[P_{Ti}\cos\phi - V_i\sin\phi + P_{ext} r\,(1 - \cos\phi)\right] + \frac{C_4 r}{A_c E r_c}\left[M_i - P_{Ti} R_c\,(1 - \cos\phi) - V_i r\sin\phi + P_{ext} r^2 (1 - \cos\phi)\right] \qquad (212(b))$$

Equations 212 are solved by Laplace transform with the initial (or boundary in this case) conditions that $u(o) = u_i$ and $v(o) = v_i$. Equations 212 are first rearranged to give

$$\frac{dv}{d\phi} - u = a + b\phi + c\sin\phi + d\cos\phi \qquad (213(a))$$

$$\frac{du}{d\phi} + v = e + f\sin\phi + g\cos\phi \qquad (213(b))$$

where

$$a = r\,\psi_{bi} + S\,r\,V_i + T\,V_i \qquad (214(a))$$

$$b = S\,M_i + S\,r\,P_{Ti} - S\,r^2 P_{ext} - T\,r\,P_{ext} \qquad (214(b))$$

$$c = -S\,r\,P_{Ti} + \frac{r}{A_c G}\,P_{Ti} - T\,P_{Ti} + Sr^2 P_{ext} + TrP_{ext} - \frac{r^2 P_{ext}}{A_c G} \qquad (214(c))$$

$$d = -S\,r\,V_i - T\,V_i + \frac{r}{A_c G}\,V_i \qquad (214(d))$$

$$e = -S'r\,P_{Ti} + T'r\,P_{ext} + S'r^2 P_{ext} + S'M_i \qquad (214(e))$$

$$f = -S'r\,V_i - T'\,V_i \tag{214(f)}$$

$$g = S'P_{Ti} + T'P_{Ti} - S'r^2P_{ext} - T'r\,P_{ext} \tag{214(g)}$$

$$S' = \frac{C_4 r}{A_c E r_c} \tag{214(h)}$$

$$T' = \frac{C_3 r}{A_c E} \tag{214(i)}$$

$$S = S' + \frac{C_1 r^2}{EI} \tag{214(j)}$$

$$T = T' + \frac{C_2 r^2 r_c}{EI} \tag{214(k)}$$

Denoting $L(u) = U$ and $L(v) = V$, transformation of Equation 213 yields

$$\left.\begin{aligned} sV - v_i - U &= \frac{a}{s} + \frac{b}{s^2} + \frac{c}{1+s^2} + \frac{ds}{1+s^2} \\ sU - u_i + V &= \frac{e}{s} + \frac{f}{1+s^2} + \frac{gs}{1+s^2} \end{aligned}\right\} \tag{215}$$

This is written

$$\begin{bmatrix} s & -1 \\ 1 & s \end{bmatrix} \begin{Bmatrix} V \\ U \end{Bmatrix} = \left\{ \begin{aligned} &\frac{a}{s} + \frac{b}{s^2} + \frac{c}{1+s^2} + \frac{ds}{1+s^2} + v_i \\ &\frac{e}{s} + \frac{f}{1+s^2} + \frac{gs}{1+s^2} + u_i \end{aligned} \right\} \tag{216}$$

The solution is

$$\begin{Bmatrix} V \\ U \end{Bmatrix} = \frac{1}{1+s^2} \begin{bmatrix} s & +1 \\ -1 & s \end{bmatrix} \left\{ \begin{aligned} &\frac{a}{s} + \frac{b}{s^2} + \frac{c}{1+s^2} + \frac{ds}{1+s^2} + v_i \\ &\frac{e}{s} + \frac{f}{1+s^2} + \frac{gs}{1+s^2} + u_i \end{aligned} \right\} \tag{217}$$

Multiplication and inverse transformation yields

$$v = (a + u_i)\sin\phi + v_i\cos\phi + (b + e)(1 - \cos\phi) + \frac{1}{2} f(\sin\phi - \cos\phi) + \frac{1}{2}(c + g)\phi\sin\phi + \frac{1}{2} d(\sin\phi + \phi\cos\phi) \quad (218(a))$$

$$u = (e - v_i)\sin\phi + u_i\cos\phi - a(1 - \cos\phi) - b(\phi - \sin\phi) - \frac{1}{2} c(\sin\phi - \phi\cos\phi) + \frac{1}{2}(f - d)\phi\sin\phi + \frac{1}{2} g(\sin\phi + \phi\cos\phi) \quad (218(b))$$

Substituting Equation 214 into Equation 218, and after some manipulation,

$$v = v_i\cos\phi + u_i\sin\phi + r\psi_{bi}\sin - \frac{C_1 r^2}{EI}(1 - \cos\phi) M_i + \left[\frac{C_1 r^3}{EI}(1 - \cos\phi - \frac{1}{2}\phi\sin\phi) + \frac{1}{2}\frac{r}{A_c G} - \frac{C_2 r^2 r_c}{EI}\phi\sin\phi\right] P_{Ti} + \left[\frac{r^2}{2EI}(C_1 r + C_2 r)(\sin\phi - \phi\cos\phi) + \frac{r}{2A_c G}(\sin\phi + \phi\cos\phi)\right] V_i - \left[\frac{r^3}{EI}(C_1 r + C_2 r)(1 - \cos\phi - \frac{1}{2}\phi\sin\phi) + \frac{r2}{2A_c G}\phi\sin\phi\right] P_{ext} \quad (219)$$

$$u = -v_i\sin\phi + u_i\cos\phi - r\psi_{bi}(1 - \cos\phi) + \left[\left(\frac{C_1 r^2}{EI} + \frac{C_4 r}{A_c E r_c}\right)\phi - \frac{C_1 r^2}{EI}\sin\phi\right] M_i + \left[\frac{C_1 r^3}{EI}\left(\frac{3}{2}\sin\phi - \phi - \frac{1}{2}\phi\cos\phi\right) + \left(\frac{C_2 r^2 r_c}{EI} - \frac{r}{A_c G}\right)\left(\frac{1}{2}\sin\phi - \frac{1}{2}\phi\cos\phi\right) + \frac{C_3 r}{A_c E}\sin\phi + \frac{C_4 r^2}{A_c E r}(\sin\phi - \phi)\right] P_{Ti} + \left[\frac{r^2}{EI}(C_1 r + C_2 r_c)\left(\frac{1}{2}\phi\sin\phi - 1 + \cos\phi\right) - \frac{r}{A_c E r_c}(C_3 r_c + C_4 r)(1 - \cos\phi) - \frac{r}{2A_c G}\phi\sin\phi\right] V_i \quad (220)$$

$$+\left[\frac{r^3}{EI}(C_1 r + C_2 r_c)\left(\frac{\phi}{} + \frac{1}{2}\ \phi\cos\phi - \frac{3}{2}\sin\phi\right)\right.$$

$$\left.+\frac{r^2}{A_c E r_c}(C_3 r_c + C_4 r)\ (\phi\ - \sin\phi) + \frac{r^2}{A_c G}\ \left(\frac{1}{2}\sin\phi - \frac{1}{2}\phi\cos\phi\right)\right] P_{ext}\Bigg\} \quad (220)$$

To yield a zero displacement condition when the beam segment is subjected only to internal pressurization ($P_T = P_o$), substitute $P_A = P_T - P_o$ for P_T in Equations 208 thru 220. N is the axial load resulting from external loading. With this substitution, then, Equations 208 thru 220 yield the following extended transfer matrix equation.

$$\begin{Bmatrix} v \\ u \\ \psi_b \\ M \\ P_A \\ V \\ 1 \end{Bmatrix} = \left[\begin{array}{ccccccc} \cos\phi & \sin\phi & r\sin\phi & F_{14} & F_{15} & F_{16} & F_{17} \\ -\sin\phi & \cos\phi & -r(1-\cos\phi) & F_{24} & F_{25} & F_{26} & F_{27} \\ 0 & 0 & 1 & F_{34} & F_{35} & F_{36} & F_{37} \\ 0 & 0 & 0 & 1 & -r(1-\cos\phi) & -r\sin\phi & P_{ext}r(1-\cos\phi) \\ 0 & 0 & 0 & 0 & \cos\phi & -\sin\phi & P_{ext}r(1-\cos\phi) \\ 0 & 0 & 0 & 0 & \sin\phi & \cos\phi & -P_{ext}r\sin\phi \\ 0 & 0 & 0 & 0 & 0 & 0 & 1 \end{array}\right] \begin{Bmatrix} v_i \\ u_i \\ \psi_{bi} \\ M_i \\ P_{Ai} \\ V_i \\ 1 \end{Bmatrix} \quad (221(a))$$

In shorthand notation, this is written

$$\{z\} = [F]\ \{z\}_i \quad (221(b))$$

where

$$F_{14} = -\frac{C_1 r^2}{EI}\ (1 - \cos\phi) \quad (222(a))$$

$$F_{15} = \frac{C_1 r^3}{EI}\ (1 - \cos\phi - \frac{1}{2}\phi\sin\phi) + \frac{1}{2}\ \frac{r}{A_c G} - \frac{C_2 r^2 r_c}{EI}\ \phi\ \sin\phi \quad (222(b))$$

$$F_{16} = \frac{r^2}{2EI}(C_1 r + C_2 r_c)(\sin\phi - \phi\cos\phi) + \frac{r}{2A_cG}(\sin\phi + \phi\cos\phi) \quad (222(c))$$

$$F_{17} = \frac{P_{ext} r^3}{EI}(C_1 r + C_2 r)(1 - \cos\phi - \frac{1}{2}\phi\sin\phi) + \frac{P_{ext} r^2}{2A_cG}\phi\sin\phi \quad (222(d))$$

$$F_{24} = \frac{C_1 r^2}{EI} + \frac{C_4 r}{A_c E r_c}\phi - \frac{C_1 r^2}{EI}\sin\phi \quad (222(e))$$

$$F_{25} = \frac{C_1 r^3}{EI}(\frac{3}{2}\sin\phi - \phi - \frac{1}{2}\phi\cos\phi) + \frac{C_2 r^2 r_c}{EI} - \frac{r}{A_cG}(\frac{1}{2}\sin\phi - \frac{1}{2}\phi\cos\phi) + \frac{C_3 r}{A_c E}\sin\phi + \frac{C_4 r^3}{A_c E r_c}(\sin\phi - \phi) \quad (222(f))$$

$$F_{26} = \frac{r^2}{EI}(C_1 r + C_2 r_c)(\frac{1}{2}\phi\sin\phi - 1 + \cos\phi) - \frac{r}{A_c E r_c}(C_3 r_c + C_4 r)(1 - \cos\phi) - \frac{r}{2A_cG}\phi\sin\phi \quad (222(g))$$

$$F_{27} = \frac{qr^3}{EI}(C_1 r + C_2 r_c)(\phi + \frac{1}{2}\phi\cos\phi - \frac{3}{2}\sin\phi) + \frac{P_{ext} r^2}{A_c E r_c}(C_3 r + C_4 r)(\phi - \sin\phi) + \frac{P_{ext} r^2}{A_cG}(\frac{1}{2}\sin\phi - \frac{1}{2}\phi\cos\phi) \quad (222(h))$$

$$F_{34} = -\frac{C_1 r}{EI} + \frac{C_4}{A_c E r_c}\phi \quad (222(i))$$

$$F_{35} = \frac{C_1 r}{EI} + \frac{C_4}{A_c E r_c} r(\phi - \sin\phi) - \frac{C_2 r r_c}{EI} + \frac{C_3}{A_c E}\sin\phi \quad (222(j))$$

$$F_{36} = \frac{C_1 r}{EI} + \frac{C_4}{A_c E r_c} r(1 - \cos\phi) + \frac{C_2 r r_c}{EI} + \frac{C_3}{A_c E}(1 - \cos\phi) \quad (222(k))$$

$$F_{37} = - P_{ext} \left(\frac{C_1 r}{EI} + \frac{C_4}{A_c E_c} \right) r^2 \, (\phi - \sin\phi) - P_{ext} \left(\frac{C_2 r r_c}{EI} + \frac{C_3}{A_c E} r \, (\phi - \sin\phi) \right) \quad (222(1))$$

Empirical Corrections

From the beam tests described in CELLULAR BEAM TESTS come two empirical corrections to the theoretical development just concluded. They consist of λ, which must be multiplied with the geometric moment of inertia to give an effective moment of inertia to be used in the expression for the flexural rigidity, and the ratio of $M/P_T r_c$ at initial wrinkle, to be used in place of the theoretical value previously derived. These corrections are functions of the beam size and curvature, w/d , and the internal pressure, P_c. They are shown in Figure 130.

Stress Analysis

Application of the foregoing developments to the analysis of tents subject to wind loads is covered in three parts: Unguyed Tents, Guyed Tents, and Nonlinear Solution. The purpose of developing the analysis in this manner is to first develop the equations and logic necessary for their solution for the most straightforward case, and to then introduce special complexities which are not always present. The boundary conditions for all tents will be taken as zero displacements (not rotation) and zero bending moment at the ground support, which are the boundary conditions for a hinged end.

It is convenient here to introduce the notation necessary for analysis of complex structures. Locate a Cartesian coordinate system, x, y, arbitrarily with respect to the system to be analyzed. Number the elements consecutively, beginning with (1). Place an element of infinitesimal dimensions between each beam element, numbered as shown in Figure 146. This infinitesimal element will be called a point, and it will possess no elastic properties. Denote the angle between the vertical and the normal to the center line of element (i) at point i-1 as $\theta_{i-1}^{(i)}$ positive in the counterclockwise sense. Point i will be located by $\bar{x}_i$, and $\bar{y}_i$, so that the coordinates of the ends of element (i) will be $\bar{x}_{i-1}$, $\bar{y}_{i-1}$ and $\bar{x}_i$, $\bar{y}_i$.

Now the state vector at point i associated with element (i) is $\{z\}^{(i)}_i$ and the one at point i associated with element (i + 1) is $\{z\}^{(i+1)}_i$. With this nomenclature, Equations 187 and 221 are written

$$\{z\}_i^{(i)} = [F]^{(i)} \{z\}_{i-1}^{(i)} \quad (223)$$

where $[F]^{(i)}$ is the transfer matrix for the i-th element.

Unguyed Tents

The analysis of unguyed tents composed only of curved elements is accomplished with Equation 221. Consider the tent shown in Figure 147. In general, the wind load will be as shown by the continuous line. The tent will be broken into N elements, each assumed to have a constant load and radius. The radius for each element may be determined through the condition that the element for analysis must pass through the end points and another point (usually chosen near the center) as shown in Figure 148. Temporarily denote the i-th element by the curved line segment $\overset{\frown}{ABC}$. The points A, B, C, and D are located by Cartesian coordinates $\overline{x}_A$, $\overline{y}_A$, $\overline{x}_B$, $\overline{y}_B$, $\overline{x}_C$, $\overline{y}_C$, and $\overline{x}_D$, $\overline{y}_D$ respectively. The point D is the center of curvature of the analytical beam element. From Figure 148,

$$r \sin \theta_A = \overline{x}_A - \overline{x}_D \tag{224(a)}$$

$$r \cos \theta_A = \overline{y}_A - \overline{y}_D \tag{224(b)}$$

$$r \sin \theta_C = \overline{x}_C - \overline{x}_D \tag{224(c)}$$

$$r \cos \theta_C = \overline{y}_C - \overline{y}_D \tag{224(d)}$$

$$(\overline{x}_B - \overline{x}_D)^2 + (\overline{y}_B - \overline{y}_D)^2 = r^2 \tag{224(e)}$$

a system of five equations in the five unknowns, r, θ_A, θ_C, $\overline{x}_D$, and $\overline{y}_D$. Solution of Equation 224 results in

$$\overline{x}_D = \overline{B}/\overline{A} \tag{225(a)}$$

$$\overline{y}_D = \overline{C}/\overline{A} \tag{225(b)}$$

$$r = \sqrt{(\overline{x}_A - \overline{B}/\overline{A})^2 + (\overline{y}_A - \overline{C}/\overline{A})^2} \tag{225(c)}$$

$$\theta_A = \tan^{-1}\left[(\bar{x}_A - \bar{B}/\bar{A})/(\bar{y}_A - \bar{C}/\bar{A}) \right] \qquad (225(d))$$

$$\theta_C = \tan^{-1}\left[(\bar{x}_C - \bar{B}/\bar{A})/(\bar{y}_C - \bar{C}/\bar{A}) \right] \qquad (225(e))$$

where

$$\bar{A} = 2\left[\bar{x}_A(\bar{y}_C - \bar{y}_B) + \bar{x}_B(\bar{y}_A - \bar{y}_C) + \bar{x}_C(\bar{y}_B - \bar{y}_A)\right] \qquad (226(a))$$

$$\bar{B} = (\bar{x}_A^2 + \bar{y}_A^2)(\bar{y}_C - \bar{y}_B) + (\bar{x}_B^2 + \bar{y}_B^2)(\bar{y}_A - \bar{y}_C) + (\bar{x}_C^2 + \bar{y}_C^2)(\bar{y}_B - \bar{y}_A) \qquad (226(b))$$

$$\bar{C} = (\bar{x}_A^2 + \bar{y}_A^2)(\bar{x}_B - \bar{x}_C) + (\bar{x}_B^2 + \bar{y}_B^2)(\bar{x}_C - \bar{x}_A) + (\bar{x}_C^2 + \bar{y}_C^2)(\bar{x}_A - \bar{x}_B) \qquad (226(c))$$

The amount of work involved in calculating the quantities in Equation 225 is obviously prohibitive for an individual if there are many elements to be calculated, even though symmetry may reduce the number of elements in half. These equations are easily programmed for solution on a digital computer, however, with the $\bar{x}$ and $\bar{y}$ coordinates for each point as the input. For use in the transfer matrix $\phi = |\theta_C - \theta_A|$ or $\phi^{(i)} = |\theta_i^{(i)} - \theta_{i-1}^{(i)}|$ in the notation adopted for analysis (see Figure 149).

Once these quantities have been computed for each element, it is necessary to relate the forces and displacements at one end of an element to those at the corresponding end of the bordering element. These quantities will not be the same unless $\theta_i^{(i)} = \theta_i^{(i+1)}$ (see Figure 149). The relationship between the corresponding state vectors of elements (i) and (i + 1) are most easily visualized by examination of the point between the two. From Figure 150, the state vectors are related by

$$\begin{Bmatrix} v \\ u \\ \psi_b \\ M \\ P_A \\ V \\ 1 \end{Bmatrix}^{(i+1)}_i = \begin{bmatrix} \cos\Delta\theta_i & \sin\Delta\theta_i & 0 & 0 & 0 & 0 & 0 \\ \sin\Delta\theta_i & \cos\Delta\theta_i & 0 & 0 & 0 & 0 & 0 \\ 0 & 0 & 1 & 0 & 0 & 0 & 0 \\ 0 & 0 & 0 & 1 & 0 & 0 & 0 \\ 0 & 0 & 0 & 0 & \cos\Delta\theta_i & -\sin\Delta\theta_i & 0 \\ 0 & 0 & 0 & 0 & \sin\Delta\theta_i & -\cos\Delta\theta_i & 0 \\ 0 & 0 & 0 & 0 & 0 & 0 & 1 \end{bmatrix}_i \begin{Bmatrix} v \\ u \\ \psi_b \\ M \\ P_A \\ V \\ 1 \end{Bmatrix}^{(i)}_i \qquad (227)$$

where

$$\Delta\theta_i = \theta_i^{(i+1)} - \theta_i^{(i)} \tag{228}$$

Equation 227 is written

$$\{z\}_i^{(i+1)} = [P]_i \{z\}_i^{(i)} \tag{229}$$

where $[P]_i$ is the extended point matrix of point i, $\{z\}_i^{(i+1)}$ is the extended state vector at point i associated with element (i + 1), and $\{z\}_i^{(i)}$ is the extended state vector at point i associated with element (i).

Synthesis of the transfer and point matrices is accomplished by multiplication. For example, consider the beam shown in Figure 151. It has five elements, and is hinged at both ends. The state vectors at the ends, $\{z\}_o^{(i)}$ and $\{z\}_5^{(5)}$ are given by

$$\{z\}_o^{(1)} = \{0 \quad 0 \quad \psi_b \quad 0 \quad P_A \quad V \quad 1\}_o^{(1)} \tag{230(a)}$$

$$\{z\}_5^{(5)} \quad \{0 \quad 0 \quad \psi_b \quad 0 \quad P_A \quad V \quad 1\}_5^{(5)} \tag{230(b)}$$

The set of equations describing the beam in Figure 151 is

$$\{z\}_5^{(5)} = [F]^{(5)} [P]_4 [F]^{(4)} [P]_3 [F]^{(3)} [P]_2 [F]^{(2)} [P]_1 [F]^{(1)} \{z\}_o^{(1)} \tag{231}$$

which is six equations in the six unknown boundary state vector elements.

There is another method of specifying element dimensions which will eliminate the need for the point matrices, $[P]_i$. Its use, however, requires a careful and judicious choice of elements to obtain good representation of the true beam. Instead of requiring the analytical element to pass through three points on the true element, require the analytical element to pass through the end points of the true element, and to match the terminal slope of the preceding analytical element. From Figure 152, with the quantities

θ_A, $\bar{x}_A$, $\bar{y}_A$, and $\bar{x}_C$, $\bar{y}_C$ known

$$r \sin \theta_A = \bar{x}_A - \bar{x}_D \tag{232(a)}$$

$$r \cos \theta_A = \bar{y}_A - \bar{y}_D \tag{232(b)}$$

$$r \sin \theta_C = \bar{x}_C - \bar{x}_D \tag{232(c)}$$

$$r \cos \theta_C = \bar{y}_C - \bar{y}_D \tag{232(d)}$$

which are four equations in the four unknowns, r, θ_C, $\bar{x}_D$, and $\bar{y}_D$. Solution of Equations 232 yields

$$\bar{x}_D = \bar{x}_A - \bar{D} \sin \theta_A / \bar{E} \tag{233(a)}$$

$$\bar{y}_D = \bar{y}_A - \bar{D} \cos \theta_A / \bar{E} \tag{233(b)}$$

$$r = \bar{D}/\bar{E} \tag{233(c)}$$

$$\theta_C = \tan^{-1}\left[\frac{\bar{x}_C - \bar{x}_A + \bar{D} \sin \theta_A/\bar{E}}{\bar{y}_C - \bar{y}_C + \bar{D} \cos \theta_A/\bar{E}}\right] \tag{233(d)}$$

where

$$\bar{D} = (\bar{x}_A + \bar{x}_C)^2 + (\bar{y}_A + \bar{y}_C)^2 \tag{234(a)}$$

$$\bar{E} = 2\left[(\bar{x}_A - \bar{x}_C) \sin \theta_A + (\bar{y}_A - \bar{y}_C) \cos \theta_A\right] \tag{234(b)}$$

By using Equation 233 to specify element geometry, Equation 231 may be written without the point matrices as

$$\{z\}_5^{(5)} = [F]^{(5)} [F]^{(4)} [\sim]^{(3)} [F]^{(2)} [F]^{(1)} \{z\}_o^{(1)} \tag{235}$$

Also, the two methods can be used in combination to yield good beam representation with fewer point matrices. Of course, for circular tents, there is no need for the point matrices.

Consider now tents with curved and straight sections. Assume for clarity that no point matrices are required. Since there is no difference in the point matrix between curved and straight elements, nothing will be lost from their exclusion. It will be necessary to distinguish between state vectors and transfer matrices for curved and straight elements. To that end, denote the state vectors and transfer matrices for the straight elements by $\{\overset{s}{z}\}$ and $[\overset{s}{F}]$, and for the curved elements by $\{\overset{c}{z}\}$ and $[\overset{c}{F}]$. Now the solution of the tent in Figure 153 is given simply by

$$\{\overset{s}{z}\}_5^{(5)} = [\overset{s}{F}]^{(5)} \quad [\overset{s}{F}]^{(4)} \quad [\overset{c}{F}]^{(3)} \quad [\overset{c}{F}]^{(2)} [\overset{c}{F}]^{(1)} \{\overset{c}{z}\}_0^{(1)} \tag{236}$$

where $\{\overset{s}{z}\}_5^{(5)}$ and $\{\overset{s}{z}\}_5^{(5)}$ are given by Equation 187.

Denote in Equation 236,

$$[U] = [\overset{s}{F}]^{(5)} \quad [\overset{s}{F}]^{(4)} [\overset{c}{F}]^{(3)} [\overset{c}{F}]^{(2)} [\overset{c}{F}]^{(1)} \tag{237}$$

This also represents Equations 231 and 235. Applying the boundary conditions,

$$\begin{Bmatrix} v \\ u \\ M \end{Bmatrix}_5^{(5)} = \begin{Bmatrix} 0 \\ 0 \\ 0 \end{Bmatrix} = \begin{bmatrix} U_{13} & U_{15} & U_{16} \\ U_{23} & U_{25} & U_{26} \\ U_{43} & U_{45} & U_{46} \end{bmatrix} \begin{Bmatrix} \psi \\ P_A \\ V \end{Bmatrix}_0^{(1)} + \begin{Bmatrix} U_{17} \\ U_{27} \\ U_{47} \end{Bmatrix} \tag{238}$$

The unknowns, $\psi_o^{(1)}$, $P_{Ao}^{(1)}$, and $V_o^{(1)}$, can be found after inversion of the 3×3 coefficient matrix. The other state vectors are then found from

$$\{z\}_1^{(1)} = [F]^{(1)} \quad z_0^{(1)} \tag{239(a)}$$

$$\{z\}_2^{(2)} = [F]^{(2)} [F]^{(1)} \quad z_o^{(1)} \tag{239(b)}$$

etc.

Guyed Tents

In many cases, tents are guyed to increase stability in high winds, Guy wires are attached to the tents through patches, usually spaced so that deformation across the tent is nearly uniform along the line of guy attachment.

The guy line tension T^*, is another redundant and is introduced into an enlarged extended state vector as an eighth element. The assumptions governing deformation of guyed tents are: guy lines are inextensible and accept only tensile loads; and deflection of the tent at the point of guy line attachment is perpendicular to the guy line if the guy line is loaded. Figure 154 illustrates the physical significance of these assumptions. With these assumptions, the limiting state vector at point j + 1 associated with element (j) is (see Figure 155)

$$\{z\}^{(j)}_{j+1} = \{v \;\; -v \tan \Delta\theta^*_{j+1} \;\; \psi_b \;\; M \;\; P_A \;\; V \;\; 1 \;\; T^*\}^{(j)}_{j+1} \tag{240}$$

where

$$\Delta\theta^{*(j)}_{j+1} = \theta^{(j)}_{j+1} - \theta^*_{j+1} \tag{241}$$

A special enlarged extended field matrix is also necessary at this point. It is, for element (j) (see Figure 156),

$$[\bar{F}^*]^{(j)} = \left[\begin{array}{ccc|c} & & & 0 \\ & & & 0 \\ & & & 0 \\ & [F]^{(j)} & & -r\cos\Delta\theta^*_{j+1} \\ & & & \cos\Delta\theta^*_{j+1} \\ & & & -\sin\Delta\theta^*_{j+1} \\ & & & 0 \\ \hline 0 & 0 & 0 \;\; 0 \;\; 0 \;\; 0 \;\; 0 & 1 \end{array}\right]^{(j)} \tag{242}$$

where $[F]^{(j)}$ is the usual field matrix for element (j). Enlarged field matrices for elements to which there are no guy lines attached, or leeward elements with guy lines, as shown here.

$$[\tilde{F}]^{(i)} = \begin{bmatrix} & & & & & & & 0 \\ & & & & & & & 0 \\ & & & & & & & 0 \\ & & [F]^{(i)} & & & & & 0 \\ & & & & & & & 0 \\ & & & & & & & 0 \\ & & & & & & & 0 \\ 0 & 0 & 0 & 0 & 0 & 0 & 0 & 1 \end{bmatrix}^{(i)} \tag{243}$$

Consider the circular tent shown in Figure 157(a). The boundary conditions at the ends are applied through

$$\{\tilde{z}\}_5 = [\tilde{F}]^{(5)} [\tilde{F}]^{(4)} [\tilde{F}]^{(3)} [\tilde{F}]^{(2)} [\tilde{F}]^{(1)} \{\tilde{z}\}_0 \tag{244}$$

Here the superscript on the state vector has been dropped because for circular beams, or whenever point matrices are unnecessary, the superscript is redundant. The other boundary condition for this tent comes from

$$\{\tilde{z}\}_2 = [\tilde{F}^*]^{(2)} [\tilde{F}]^{(1)} \{z\}_0 \tag{245}$$

As in Equation 237, denote

$$\begin{aligned} [U] &= [\tilde{F}]^{(5)} [\tilde{F}]^{(4)} [\tilde{F}]^{(3)} [\tilde{F}^*]^{(2)} [\tilde{F}]^{(1)} \\ [U^*] &= [\tilde{F}^*]^{(2)} [\tilde{F}]^{(1)} \end{aligned} \tag{246}$$

From Equation 244,

$$\begin{Bmatrix} v \\ u \\ M \end{Bmatrix}_5 = \begin{Bmatrix} 0 \\ 0 \\ 0 \end{Bmatrix} = \begin{bmatrix} U_{13} & U_{15} & U_{16} & U_{18} \\ U_{23} & U_{25} & U_{26} & U_{28} \\ U_{43} & U_{45} & U_{46} & U_{48} \end{bmatrix} \begin{Bmatrix} \psi_b \\ P_A \\ V \\ T^* \end{Bmatrix}_0 + \begin{Bmatrix} U_{17} \\ U_{27} \\ U_{47} \end{Bmatrix} \tag{247}$$

From Equation 245,

$$v_2 = U^*_{13}\,\psi_{bo} + U^*_{15}\,P_{Ao} + U^*_{16}\,V_o + U^*_{18}\,T^* + U^*_{17} \tag{248(a)}$$

$$-v_2 \tan\Delta\theta^*_2 = U^*_{23}\,\psi_{bo} + U^*_{25}\,P_{Ao} + U^*_{26}\,V_o + U^*_{28}\,T^* + U^*_{27} \tag{248(b)}$$

A subscript on T^* is unnecessary. Multiplying the first of Equations by $\tan\Delta\theta^*$ and adding the two gives

$$(U^*_{13}\tan\Delta\theta^* + U^*_{23})\,\psi_{bo} + (U^*_{15}\tan\Delta\theta^* + U^*_{25})\,P_{Ao} + (U^*_{16}\tan\Delta\theta^* + U^*_{26})V_o + (U^*_{18}\tan\Delta\theta^* + U^*_{28})\,T^* + (U^*_{17}\tan\Delta\theta^* + U^*_{27}) = 0 \tag{249}$$

This combined with Equation 247 to give

$$\begin{bmatrix} U_{13} & U_{15} & U_{16} & U_{18} \\ U_{23} & U_{25} & U_{26} & U_{28} \\ U_{43} & U_{45} & U_{46} & U_{48} \\ U^*_{13}\tan\Delta\theta^* + U^*_{23} & U^*_{15}\tan\Delta\theta^* + U^*_{25} & U^*_{16}\tan\Delta\theta^* + U^*_{26} & U^*_{18}\tan\Delta\theta^* + U^*_{28} \end{bmatrix} \begin{Bmatrix} \psi_b \\ P_A \\ V \\ T^* \end{Bmatrix}_0 \begin{Bmatrix} -U_{17} \\ -U_{27} \\ -U_{47} \\ -U^*_{17}\tan\Delta\theta^* - U^*_{27} \end{Bmatrix} \tag{250}$$

Solution of the unknowns, ψ_{bo}, P_{Ao}, V_o, and T^*, is accomplished through inversion of the 4 × 4 coefficient matrix. The other state vectors are then found from

$$\{\tilde{z}\}_1 = [\tilde{F}]^{(1)}\,\{\tilde{z}\}_o \tag{251(a)}$$

$$\{\tilde{z}\}_2 = [\tilde{F}^*]^{(2)}\,[\tilde{F}]^{(1)}\,\{\tilde{z}\}_o \tag{251(b)}$$

etc.

To illustrate the solution of a tent with guy lines at two heights, consider Figure 157(b). For two guy lines, twice enlarged extended field matrices and state vectors are formed. The state vector is given by

$$\{\overset{*}{z}\}_i = \{v \quad u \quad \psi_b \quad M \quad P_A \quad V \quad 1 \quad T^* \quad T^\dagger\}_i \qquad (252)$$

The field matrix for element (1) is

$$\overset{\sim}{[\overset{*}{F}]}^{(1)} = \left[\begin{array}{cccccccc|cc} & & & & & & & & 0 & 0 \\ & & & & & & & & 0 & 0 \\ & & & & & & & & 0 & 0 \\ & & & & & & & & -r\cos\Delta\theta^* & 0 \\ & & & & [F]^{(1)} & & & & \cos\Delta\theta^* & 0 \\ & & & & & & & & -\sin\Delta\theta^* & 0 \\ & & & & & & & & 0 & 0 \\ \hline 0 & 0 & 0 & 0 & 0 & 0 & 0 & & 1 & 0 \\ 0 & 0 & 0 & 0 & 0 & 0 & 0 & & 0 & 1 \end{array}\right]^{(1)} \qquad (253)$$

The field matrix for element (2) is

$$\overset{\sim}{[F^\dagger]}^{(2)} = \left[\begin{array}{cccccccc|cc} & & & & & & & & 0 & 0 \\ & & & & & & & & 0 & 0 \\ & & & & & & & & 0 & 0 \\ & & & & & & & & 0 & -r\cos\Delta\theta^\dagger \\ & & & & [F]^{(1)} & & & & 0 & \cos\Delta\theta^\dagger \\ & & & & & & & & 0 & -\sin\Delta\theta^\dagger \\ & & & & & & & & 0 & 0 \\ \hline 0 & 0 & 0 & 0 & 0 & 0 & 0 & & 1 & 0 \\ 0 & 0 & 0 & 0 & 0 & 0 & 0 & & 0 & 1 \end{array}\right]^{(2)} \qquad (254)$$

where

$$\Delta\theta^{\dagger}{}^{(2)} = \theta_2 - \theta_2^{\dagger} \tag{255}$$

as shown in Figure 157(b). The other field matrices are given by

$$\tilde{[F]}^{(i)} \quad [F]^{(i)} \quad \begin{bmatrix} & & & & & & 0 & 0 \\ & & & & & & 0 & 0 \\ & & & & & & 0 & 0 \\ & & & & & & 0 & 0 \\ & & & & & & 0 & 0 \\ & & & & & & 0 & 0 \\ & & & & & & 0 & 0 \\ 0 & 0 & 0 & 0 & 0 & 0 & 1 & 0 \\ 0 & 0 & 0 & 0 & 0 & 0 & 0 & 1 \end{bmatrix}^{(i)} \tag{256}$$

A procedure similar to that for a single guy line leads to

$$\begin{bmatrix} U_{13} & U_{15} & U_{16} & U_{18} & U_{19} \\ U_{23} & U_{25} & U_{26} & U_{28} & U_{29} \\ U_{43} & U_{45} & U_{46} & U_{48} & U_{49} \\ U_{13}^{*}\tan\Delta\theta^{*} + U_{23}^{*} & U_{15}^{*}\tan\Delta\theta^{*} + U_{25}^{*} & U_{16}^{*}\tan\Delta\theta^{*} + U_{26}^{*} & U_{18}^{*}\tan\Delta\theta^{*} + U_{28}^{*} & U_{19}^{*}\tan\Delta\theta^{*} + U_{29}^{*} \\ U_{13}^{\dagger}\tan\Delta\theta^{\dagger} + U_{23}^{\dagger} & U_{15}^{\dagger}\tan\Delta\theta + U_{25}^{\dagger} & U_{16}^{\dagger}\tan\Delta\theta^{\dagger} + U_{26}^{\dagger} & U_{18}^{\dagger}\tan\Delta\theta^{\dagger} + U_{28}^{\dagger} & U_{19}^{\dagger}\tan\Delta\theta^{\dagger} + U_{29}^{\dagger} \end{bmatrix} \begin{Bmatrix} \psi_L \\ P_A \\ V \\ T^{*} \\ T^{\dagger} \end{Bmatrix} \begin{Bmatrix} U_{17} \\ U_{27} \\ U_{47} \\ -U_{17}^{*}\tan\Delta\theta^{*} - U_{27}^{*} \\ -U_{17}^{\dagger}\tan\Delta\theta^{\dagger} - U_{27}^{\dagger} \end{Bmatrix} \tag{257}$$

Again, the unknowns can be found after inversion of the coefficient matrix, and the other state vectors are then found by

$$\{\tilde{z}\}_1 = [\tilde{F}^*]^{(1)} \{\tilde{z}\}_0 \qquad (258(a))$$

$$\{\tilde{z}\}_2 = [\tilde{F}^+]^{(2)} [\tilde{F}^*]^{(1)} \{\tilde{z}\}_0 \qquad (258(b))$$

etc.

Nonlinear Solution

It is not recommended that tents be designed to operate in the post wrinkling range, even for extreme operating conditions, because the deflections incurred after wrinkling begins are excessive. An iterative technique is included in this report, however, to illustrate how the effects of wrinkling could be determined on unguyed tents.

Partition an element transfer matrix so that, for unguyed tents,

$$\{z\}_{i+1} = \begin{Bmatrix} 3\times 1 \\ \tilde{u} \\ \hline 4\times 1 \\ \tilde{p} \end{Bmatrix}_{i+1} = \left[\begin{array}{c|c} 3\times 3 & 3\times 4 \\ A & B \\ \hline 4\times 3 & 4\times 4 \\ 0 & C \end{array}\right] \begin{Bmatrix} 3\times 1 \\ \tilde{u} \\ \hline 4\times 1 \\ \tilde{p} \end{Bmatrix}_i = [F]^{(i)} \{z\}_i \qquad (259)$$

where the matrices, A, B, and C, are defined by Equation 187 for straight elements and by Equation 221 for circular elements. The state vectors are partitioned as follows.

$$\{z\}_i = \begin{Bmatrix} \tilde{u} \\ \hline \tilde{p} \end{Bmatrix}_i = \begin{Bmatrix} z_1 \\ z_2 \\ z_3 \\ \hline z_4 \\ z_5 \\ z_6 \\ 1 \end{Bmatrix}_i = \begin{Bmatrix} v \\ u \\ \psi_b \\ \hline M \\ P_A \\ V \\ 1 \end{Bmatrix}_i \qquad (260)$$

Referencing Figure 158,

$$\left\{\begin{matrix}\tilde{u}\\ \tilde{p}\end{matrix}\right\}_N = \left[\begin{array}{c|c}\bar{A} & \bar{B}\\ \hline 0 & \bar{C}\end{array}\right]\left\{\begin{matrix}\tilde{u}\\ \tilde{p}\end{matrix}\right\}_o \qquad (261(a))$$

where

$$[\bar{A}] = \left[\begin{array}{c|c|c}\cos\phi & \sin\phi & r\sin\phi\\ \hline -\sin\phi & \cos\phi & -r(1-\cos\phi)\\ \hline 0 & 0 & 1\end{array}\right] \qquad (261(b))$$

$$[\bar{B}] = \begin{bmatrix}\bar{B}_{11} & \bar{B}_{12} & \bar{B}_{13} & \bar{B}_{14}\\ \bar{B}_{21} & \bar{B}_{22} & \bar{B}_{23} & \bar{B}_{24}\\ \bar{B}_{31} & \bar{B}_{32} & \bar{B}_{33} & \bar{B}_{34}\end{bmatrix} \qquad (261(c))$$

$$[\bar{C}] = \begin{bmatrix}1 & -r(1-\cos\phi) & -r\sin\phi & \bar{C}_{14}\\ 0 & \cos\phi & -\sin\phi & \bar{C}_{24}\\ 0 & \sin\phi & \cos\phi & \bar{C}_{34}\\ 0 & 0 & 0 & 1\end{bmatrix} \qquad (261(d))$$

The boundary conditions are

$$\begin{aligned} v_o &= z_{1,o} = 0 & \qquad v_N &= z_{1,N} = 0\\ u_o &= z_{2,o} = 0 & \qquad u_N &= z_{2,N} = 0\\ M_o &= z_{4,o} = 0 & \qquad M_N &= z_{4,N} = 0 \end{aligned} \qquad (262)$$

From Equation 261,

$$\{\tilde{p}\}_N = [\bar{C}]\{\tilde{p}\}_o \qquad (263)$$

Applying the zero moment boundary conditions.

$$0 = - r\,(1 - \cos\Phi)\, z_{5,o} - r \sin\Phi \;\; z_{6,o} + \overline{C}_{14} \tag{264(a)}$$

Since $(1 - \cos\Phi) \neq 0$ for $0 < \Phi < 360^{o}$, write

$$z_{5,o} = \frac{1}{1 - \cos\Phi}\left(\frac{1}{r}\,\overline{C}_{14} - \sin\Phi \;\; z_{6,o}\right) \tag{264(b)}$$

$$\{\tilde{u}\}_{N} = [\overline{A}] \;\; \{\tilde{u}\}_{o} + [\overline{B}] \;\; \{\tilde{p}\}_{o} \tag{265(a)}$$

In expanded form, this is (with Equation 261),

$$\begin{Bmatrix} 0 \\ 0 \\ z_3 \end{Bmatrix}_{N} = \begin{bmatrix} \cos\Phi & \sin\Phi & r\sin\Phi \\ -\sin\Phi & \cos\Phi & -r(1-\cos\Phi) \\ 0 & 0 & 1 \end{bmatrix} \begin{Bmatrix} 0 \\ 0 \\ z_3 \end{Bmatrix}_{o} + \begin{bmatrix} \overline{B}_{11} & \overline{B}_{12} & \overline{B}_{13} & \overline{B}_{14} \\ \overline{B}_{21} & \overline{B}_{22} & \overline{B}_{23} & \overline{B}_{24} \\ \overline{B}_{31} & \overline{B}_{32} & \overline{B}_{33} & \overline{B}_{34} \end{bmatrix} \begin{Bmatrix} 0 \\ \dfrac{1}{r}\,\overline{C}_{14} - \sin\Phi \; z_6 \\ \hline 1 - \cos\Phi \\ z_6 \\ 1 \end{Bmatrix}_{o} \tag{265(b)}$$

The first two equations yield, after some manipulation,

$$z_{3,o} = \frac{\left[\overline{B}_{23} - \overline{B}_{22} \sin\Phi/(1 - \cos\Phi)\right] z_{6,o} + \overline{B}_{24} + \overline{B}_{22}\,\overline{C}_{14}/r(1 - \cos\Phi)}{r\,(1 - \cos\Phi)} \tag{266(a)}$$

$$z_{6,o} = \frac{r \sin\Phi \; z_{3,o} + \overline{B}_{14} + \overline{B}_{12}\,\overline{C}_{14}/r\,(1 - \cos\Phi)}{\overline{B}_{13} - \overline{B}_{12} \sin\Phi\,/(1 - \cos\Phi)} \tag{266(b)}$$

The iterative procedure is:

1) Extract $\overline{C}_{14}$ from

$$[\overline{C}] = \prod_{n=1}^{n=N} [\overline{C}]^{(n)} \tag{267}$$

2) Assume $z_{6,o} = - D$

3) Calculate $z_{5,o}$ from Equation 264(b).

4) Calculate $z_{4,1}$, $z_{5,1}$, and $z_{6,1}$ from

$$\{\tilde{p}\}_1 = [C]^{(1)} \{\tilde{p}\}_o \tag{268}$$

5) Calculate

$$(M/P_T r_c)_o = z_{4,o}/r_c \ (P_o + z_{5,o}) \tag{269(a)}$$

$$(M/P_T r_c)_1 = z_{4,1}/r_c \ (P_o + z_{5,1}) \tag{269(b)}$$

6) Calculate

$$M_{avg} = \left| \left[(M/P_T r_c)_o + (M/P_T r_c)_1\right]/2 \right| \tag{270}$$

7) With the proper value of $(M/P_T r_c)_{wr}$ from Figure 130 choose the constant, C_i, from the following:

a) $0 \leq M_{avg} \leq (M/P_T r_c)_{wr}$

$C_1 = -1.00,\ C_2 = 0,\ C_3 = 1.00,\ C_4 = 0$

b) $(M/P_T r_c)_{wr} < M_{avg} \leq (M/P_T r_c)_{wr} + .1$

$C_1 = -1.70,\ C_2 = 0.42,\ C_3 = 1.48,\ C_4 = 0.80$

c) $(M/P_T r_c)_{wr} + .1 < M_{avg} \leq (M/P_T r_c)_{wr} + .2$

$C_1 = -4.62,\ C_2 = 2.46,\ C_3 = 3.86,\ C_4 = -4.20$

d) $(M/P_T r_c)_{wr} + .2 < M_{avg} \leq (M/P_T r_c)_{wr} + .3$

$C_1 = -18.46,\ C_2 = 13.54,\ C_3 = 19.70,\ C_4 = -24.00$

e) $(M/P_T r_c)_{wr} + .3 \leq M_{avg}$

$C_1 = -274.83,\ C_2 = 244.29,\ C_3 = 340.10,\ C_4 = -380.00$

8) With the proper set of constants, form the first field matrix, $[F]^{(1)}$

9) Repeat steps 4) through 8), incrementing the subscripts and superscripts by one each time, until the last field matrix, $[F]^{(N)}$, is formed.

10) Calculate

$$[\bar{F}] = \prod_{n=N}^{n=1} [F]^{(n)} \tag{271}$$

11) Extract $[\bar{B}]$ from

$$[\bar{F}] = \begin{bmatrix} \bar{A} & \bar{B} \\ 0 & \bar{C} \end{bmatrix} \tag{272}$$

12) Calculate $z_{3,o}$ from Equation 266(a).

13) Calculate $z_{6,o}$ from Equation 266(b).

14) Compare the values of $z_{6,o}$ from steps 2) and 13).

15) If the values of $z_{6,o}$ are not in reasonable agreement, repeat steps 3) through 14) using the value of $z_{6,o}$ from step 13), stopping when good agreement between these two values is reached.

Results

The double-wall tent was analyzed for stresses as an arch structure comprised of a series of connecting beam elements of arbitrary lengths chosen to fit the load pattern and also to provide a smooth pattern of discrete valves of internal forces, meridional moment, meridional force, and radial shear. Analysis utilized the theorem of least work and was programmed on the Hayes IBM 1620 computer. The tent was first analyzed with no buckled section. When analysis indicated that a buckled section existed, a new flexibility coefficient was inserted at the buckled section and computer analysis was continued. The new flexibility coefficient allows a near-pinned condition at that point.

Results were then printed out in keeping with the following relations:

Meridional stress resultant,

$$N_\phi = \frac{M r_c}{I} + \frac{P_T}{A_c} \tag{273}$$

Hoop stress resultant,

$$N_h = (P_c - P_{ext})\, r_c \tag{274}$$

Web stress resultant, from equilibrium of the skin-web junction,

$$\left.\begin{aligned} N_w &= N_h\,(2 \sin \alpha_c) \\ N_w &= (P_c - P_{ext})\, 2\, r_c \sin \alpha_c \end{aligned}\right\} \tag{275}$$

Three arbitrary tent sizes were used as analytical models to determine stresses. They are identified as:

Tent #1 - h/d = .5, d = 238 inches
Tent #2 - h/d = .75, d = 194 inches
Tent #3 - h = 163 inches, d = 266 inches; this tent has flat sides 9° from vertical

Pressure coefficients were taken from wind tunnel data and converted into a two-dimensional pressure distribution around the tents for q = .6, 3, and 6 inches of water (gage). It was assumed that the wind load did not vary along the length of the tent, and average values of the pressures along the tent length were used in the analysis. Shear, moment and meridional forces were obtained for each loading. When the meridional compression force exceeded the tension force due to inflation pressure p_c, the tent was assumed unstable.

For all stable conditions, the maximum fabric stress resultants were computed and graphed vs. q in inches of water (gage). Fabric web and hoop stress resultants calculated and graphed as a function of cell radius, internal pressure, and cell angle, α_c.

In addition, using the latest pressure distribution data and the results of the beam tests, values of internal pressures which prevent wrinkling for various wind velocities and tent configurations were computed through an iterative process on the Hayes IBM 360 computer. Beam segments of 5° were used to assure accurate representation of the pressure distribution. Results are presented as design curves, Figures 159 through 170, for guyed and unguyed tents.

Design Curve Summary and Application

The design curves for double-wall tents with flat ends are presented as Figures 159 through 170. The necessary internal pressure to safely withstand various wind velocities were calculated and graphed for a full range of tent parameters. The meridional stress resultants were computed and plotted versus the dynamic pressure. The fabric web and hoop stresses were

plotted as a function of cell radius, internal pressure, and cell angle.

The design curves are utilized in the design of double wall tents (both guyed and unguyed) as follows:

1) From the design requirements, determine the tent size and shape and the dynamic pressure design value.

2) Determine cell width to tent diameter ratio; w/d = 0.123 was found to be the best of the models tested in the wind tunnel from a stability and weight standpoint.

3) Enter Figure 159 with h/d and w/d and find the basic pressure coefficient, P_c/q. Find the correction factors, C_q and C_W, for the design values of q and W/ℓ_h. The required cell pressure is given by

$$P_c = (P_c/q)\, C_q\, C_W\, q$$

P_c should never be under 7 in. w.g.

4) Enter Figure 160 to obtain web stress in pounds per inch.

5) Enter Figure 161 to obtain hoop stress in pounds per inch.

6) Find the meridional stress in pounds per inch from Figures 162 through 170.

SECTION 5

FABRIC MATERIALS

SELECTION

The increasing use of fabrics for engineering materials in air-supported structures where weight, durability, and reliability are important has emphasized the need for, first, the careful selection of fabrics for mechanical strength, and second, the selection of coatings for seam strength, cold weather flexibility, and increased durability. In addition, good quality control is essential to insure uniformity of product. The structural data presented in this design manual show that each structure and its intended use presents special and unique engineering problems. The full potential of lightness in weight, durability, and reliability of a structure can only be realized by engineering a fabric to match the exacting mechanical and environmental conditions of use specified for the tent.

The selection of a fabric meeting the exacting end use conditions for a tent must be based on a critical evaluation of all fiber and fabric properties. A comprehensive review of even the most essential fabric characteristics is beyond the scope of this manual. The information relative to fabric properties can best be obtained from fiber and fabric manufacturers, military specifications, and from literature (11, 12, 13, 14). However, fabric engineering can be only as effective as the extent that information relative to the desired characteristics of a fabric is known. Since this manual provides the necessary information to determine the strength of fabric required for a given structure, the stress/strain behavior of fibers and fabrics is considered pertinent and is included for ready reference. The relationship between tensile strength and weight of fabrics is also given. The strength-weight relationship is necessary to establish the weight of fabric required for the tent, and to estimate the weight of the final structure. Two other fabric properties which can restrict the selection of coated fabrics for air-supported tents are mentioned briefly because of their interest to the Military and the satellite and communications industry. The two fabric properties are low temperature flexibility and dielectric constant.

Fiber Type

The Army and Air Force have to date found nylon and polyester fibers more satisfactory for air-supported tent fabrics than fiberglas, acrylic, modacrylic and cellulose type fabrics. Both fibers have a high strength to weight ratio. The two fibers can be used to produce thin, flat fabrics of high strength. Thin, relatively flat fabrics are essential for light weight coated fabric, since the thickness of fabric controls the amount and therefore the weight of coating compound required to fill the interstices and protect the fabrics. Nylon and polyester fibers are still considered the more acceptable fibers to use for air-supported tents. However, fiber producers are continually improving their fibers, and the three other fiber types which show promise for future use are included. The additional fibers

are glass fiber, acrylic, and polypropylene. Of these, glass fiber is not new. It is a high strength, low elongation fiber. It has better weathering and chemical resistance properties than either nylon or polyester. It has been used as a radome fabric, but was found to crack on sharp creases which occurred in the fabric as a result of folding the tent for storage. Glass fiber technology has improved, and modern glass fabrics show an improved resistance to cracking in folds. Acrylic fibers are included because of their better weathering resistance and radio frequency transmission characteristics when compared to nylon and polyester. The potential field of applications for acrylic fibers is in the realm of extremely low porosity, uncoated fabrics for single-wall air-supported tents. High tenacity polypropylene is included because of its high resistance to abrasion and good mechanical properties. For a plain weave polypropylene fabric, the strength-to-weight ratio was found to be higher than that of nylon and polyester fabrics. However, its strength degrades rapidly on weathering and the fabric can only be used with a protective coating. To date, difficulty is experienced in attaining a satisfactory adhesion of coatings to polypropylene. As soon as a satisfactory solution can be found for coating polypropylene fabrics, its high strength-to-weight ratio will make possible still lighter weight fabrics than can be attained with present day nylon and polyester fibers.

CHARACTERISTICS

Fiber Strength Characteristics

The load-elongation behavior of the five fiber types is shown in Figure 171. The unit for load in both figures is fiber tenacity in grams per denier. To convert the load-elongation curves to the standard engineering stress-strain curves, it is necessary to convert fiber tenacity in grams per denier to tensile strength in pounds per square inch. The conversion factor for this is shown in the Wellington Sears Handbook, Reference 11, is as follows:

$$\text{Tensile Strength (psi)} = 12{,}800 \times \text{sp gr} \times \text{Tenacity (gpd)}$$

It is readily apparent from the load-elongation curves that, except for glass fibers, the fiber elongation is not linearly proportional to the applied load. Each curve shows an initial elastic region at low elongation followed by a complex flow and stiffening characteristic as the fiber is elongated to rupture. To obtain an appreciation for fibers with non-linear load elongation characteristics, reference is made to Dr. Susich's work on the mechanical conditioning of fibers. In his paper[15] Dr. Susich compares the load-elongation characteristics of fibers after repeated loading at several predetermined tensions. The results are reported in terms of the length recovered after the load is removed. The results are given in percent of initial length. Dr. Susich uses three terms to describe the load recovery properties of fibers, the first is percent of length recovered immediately after removal of the load, Immediate Elastic Recovery, (IER); the second term represents the contraction of fiber length at some time after the removal of load, Delayed Recovery, (DR); the third term

represents a permanent extension of the fiber after the load is removed, Permanent Set (PS). The results Dr. Susich found for the fibers considered in this manual were extracted from his report and presented in Table VII. It should be noted that the relative proportion of each type of deformation varies with percent of elongation, the higher the percent of elongation, the lower the elastic recovery and the higher the permanent set. This is characteristic of viscoelastic material. A detailed interpretation of the fiber load elongation curve is beyond the scope of this manual. This information is summarized in the Wellington Sears Handbook and in selected individual papers, References 11, 18, 19, 21, 22, 24, 27, and 28.

The information provided by the fiber load-elongation curve is useful for predicting, as a first approximation, the strength and energy absorbing characteristics of the fabric. Hence these can be used to select the fiber type which will best fulfill the particular engineering application.

Fabric Strength Characteristics

The load elongation characteristics of a fabric differ from that of its component fiber. The load elongation curve for nylon fiber and fabric is shown in Figure 172 and that for Polyester in Figure 173. The unit for load is given as a percent of rupture load for convenience in comparing fiber and fabric curves. In order to obtain a better understanding of the difference in fiber and fabric curves, a brief review of the behavior of fabrics under stress is in order.

Dr. Haas considered the deformation of a plain weave fabric to be the result of three distinct but mutually interacting mechanisms [21]. The first of these is thread shear, where the mutually perpendicular warp and filling yarn rotate, changing the angles between the yarns; the second mechanism is termed thread straightening and results from the over and under characteristics of the plain weave, each set of yarns bending over the other set. This bending is also known as crimp. When the loads are applied to the two yarn systems, the system under the highest stress will tend to straighten, transferring part of its crimp to the other set of yarns. This mechanism is termed crimp interchange. The third mechanism is that of yarn extension within the weave. Pierce and others have identified a fourth mechanism which will influence the load elongation behavior of a plain weave fabric. This is concerned with the compressive properties and the bending stiffness of the yarn. Each yarn is subjected to both lateral compression and bending at every thread crossing. Lateral compression causes the yarn to flatten under load and allows the weave to extend, and bending rigidity in increased resistance to extension of the weave.

The sequence with which the interacting mechanism operates is assumed to be as follows: when the load is first applied, the mechanisms of shear and crimp interchange predominate. These two mechanisms operate by a geometric rearrangement of the yarns in the weave rather than by yarn extension. Thus, the results of initial fabric deformation under load is independent of the theological properties of the fiber. This mechanism is indicated in Figures 172 and 173 by the fabric exhibiting a greater extension

at break than the fiber. This is due primarily to the crimp in the yarns. Filling yarns having a greater initial crimp will show a greater extension at all loads. As the loads are increased, the strain due to shear and crimp interchange reaches a limiting value which is governed by the limiting extension of the fabric. The limiting extension is reached sooner in a densely woven fabric, such as the polyester of Figure 173 than in fabrics of a looser construction such as the nylon fabric of Figure 172. This phenomenon is best illustrated by examining the filling yarn extension for both fabrics. The polyester filling yarn curve shows a steeper slope at low loads than the nylon filling curve. Increasing the load at this point will lead to yarn extension and yarn flattening. The latter two mechanisms predominate as the applied stress approaches the rupture load. Also tensile fibers are viscoelastic. Hence, where fabric loads reach a level when yarn extension occurs within the fabric, the results of strain becomes time dependent and thus extension results can vary with the rate of loading of the material. This is particularly important when rupture strain is considered. If the rate of increase of loading is slow, there is more time for creep to occur and the breaking extension can be reached at a lower load.

From the above, it is evident that the load elongation response of a fabric can be highly influenced by the modes with which the loads are applied and the time rate of loading. Further, the mechanical behavior of fabrics in air-supported structures, where the fabrics are simultaneously stressed in all directions, cannot be fully predicted on the basis of uniaxial stress data shown above. It is in this area of study, relative to the mechanical behavior of fabrics under biaxial stress condition, that much work remains to be done. A more comprehensive and accurate theory of the mechanism of fabric stress behavior at low loads, and at increasing loads to rupture, would be of considerable value in developing fabrics of minimum weight for a given structural application. Studies in this area are underway and will be included in this section as results become available.

To provide the fabric weight relationships required for this manual, it is necessary to evaluate the rupture load of a series of plain weave fabrics for each of the fiber types listed below. The rupture load for each fabric is divided by the fabric weight. Therefore the units of the weight-strength relationship developed are pounds-square yard per inch-ounce.

In this manual safety factors will be introduced which will enable the use of the full fabric values shown in Table VII.

It should be recognized that the strength in pounds per inch per ounce of fabric represents the fabric rupture loads. The percent of rupture load which can be fully utilized in order to reduce the weight of the fabric cannot at this time be accurately determined. Experience with radome construction has indicated that base fabric loads, as determined from the radome manual and before the addition of a safety factor, can be as high as 20% of the rupture load of the fabric. At this level of rupture load, fabric extensions are easily obtained and found to vary considerably even with fabrics produced according to a given Military

specification. Hence, it is difficult to determine the percent of yarn extension from fabric load elongation curves alone. With the development of an accurate theory of the mechanism of fabric deformation it may be possible for the designer to exercise his engineering judgement and use a higher percentage of the breaking load, leading to lighter weight fabrics. However, each of these problems becomes an individual determination relying fully upon the load elongation characteristic of the fabrics and the fiber.

Low Temperature Flexibility

The military requirement for tents to be operational at -65°F is a difficult one to meet for coated fabrics. MIL-C-43086 is the specification for vinyl-coated nylon fabric developed for air-supported tents for use in the temperate zone. It is recommended for use with temperatures no lower than -10°F. The weight of thermoplastic vinyl coating for both durability and seam strength is 8 ounces per square yard for light weight fabrics and 15 ounces for heavier fabrics as shown in Figure 174. The solid line shows the estimated amount of vinyl coating required as a function of base fabric weight for single-ply fabrics. The dashed line shows the estimated amount of coating required for two-ply fabrics.

MIL-C-43285 is the specification for chloroprene-chorosulfonated polyethylene coated nylon or polyester fabric developed for tents designed for arctic use. The weight of thermosetting chloroprene base coating and chlorosulfonated polyethylene top coating was found to be 10 ounces per square yard as shown in Figure 174. The small dash line represents a single fabric, the dash dot line represents the 2 ply fabric.

It should be pointed out that the coating weights as shown in Figure 174 represent an estimated average weight. The actual amount and the distribution of coating face-to-back of the fabric depends on end use conditions. Each problem becomes a matter for individual determination relying fully on durability and seam strength data, which must be obtained to insure integrity of the tent.

It should be noted that while the chloroprene- chorosulfonated polyethylene coating is considered by the Army to be the best cold weather coating for air-supported tents, the flexing of this coated fabric is restricted to temperatures no lower than -40°F. There is an urgent need for a durable low temperature coating compound which will remain flexible at -65°F and which can be joined with a seam strong enough to withstand the tension loads developed by air supported tents.

Dielectric Constant

A low dielectric constant is necessary for good radio frequency (RF) transmission, an essential requirement for air-supported radomes housing operating radar equipment. In the past the rough rule-of-thumb guide to good RF transmission was to keep the thickness of the fabric small in comparison to the wavelength and to use fabrics and coatings with low dielectric constants. Reference is made to the publication "Studies of

Quantitative Correlation between Bulk Density and Thickness of Fabrics and their Radar Transmission Characteristics" for a more complete coverage of the electrical characteristics of fabrics.

SECTION 6

CONCLUSIONS

As a result of the wind tunnel tests and analyses represented herein, certain conclusions relative to ground-mounted air-supported tent design and operation may be made. These conclusions are listed below in very brief form.

1. Stable single-and double-wall air-supported tent configurations have been successfully tested up to wind velocities of 110 miles per hour.

2. Of the major design variables investigated (other than type and shape factors), which included fabric porosity, operating pressures, cell size and guy line arrangement, the operating pressures are most important.

3. The use of porous fabric in single-wall tent construction produced the following general tent characteristics:

   a. Tent lift increased with an increase in fabric porosity for spherical and cylindrical tents with a 1:2 W/ℓ_h and decreased for tents with a 1:4 W/ℓ_h.

   b. Tent drag increased with increased porosity for spherical and cylindrical tents.

   c. Low porosity fabric reduced tent deflection slightly with no marked improvement in tent stability.

   d. Aerodynamic forces exerted on a tent with elliptical ends are greater than with hemispherical ends; however, the tent with elliptical ends had improved stability characteristics.

4. The following tent deflection characteristics prevailed:

   a. Minimum tent deflections for single-wall tents occurred at a height-to-diameter ratio of one-half for all tent configurations.

   b. As would be expected, tent deflection was greatest in the frontal, windward sector of the tent.

   c. Spherical single-wall tents have smaller overall deflections than the cylindrical tents.

   d. For the double-wall tents, an increase in cell size; i.e., cell width to enclosure diameter ratio, increased tent rigidity and resulted in less tent deflection.

e. Wind tunnel tests on double wall tents without guy lines have indicated that guy lines are mandatory to prevent excessive deformation in high winds.

f. For the double wall tents, a guy line configuration wherein lines are attached at 0.80 and 0.40 tent height and have angled corner lines produced smallest deflections.

5. Tent enclosure and cell pressures and cell size are all important factors affecting tent stability. Stability test concluded that:

a. For satisfactory tent stability characteristics, single wall enclosure and double wall cell pressures of at least free stream dynamic pressure are required.

b. Enclosure pressure equal to ambient static, or greater, must be maintained in double-wall tents to preclude early tent buckling.

c. The stability of cylindrical double-wall tents was found to be less than for cylindrical single-wall tents and is believed to result from flow conditions around the double-wall tent flat ends.

d. No significant gains in double-wall tent stability were achieved beyond a cell pressure of sixteen inches water gage.

e. Proper guy line arrangement provides some additional stability at recommended operating pressures. The best guy line configuration tested consisted of a combination high (0.8 tent height) and a low (0.4 tent height) side line arrangement and angled corner lines.

f. The use of wind sprons around a tent reduces its motion in a steady wind stream. However, at critical wind attitude (quartering winds) the loading is greater than with guylines.

6. Additional information is required to determine the effect of tent vibration on fabric properties before useful information can be supplied to the tent designer.

7. Double-wall tent vibrational frequencies as high as 59 cycles per second were measured during testing for both the guyed and unguyed configurations. Vibration amplitude was, as expected, greater for the unguyed than for the guyed tent.

8. Stress analyses of spherical and cylindrical single-wall tents within proportions tested can be accomplished using the design curves developed in this study for the Design Manual for Ground-Mounted Air-Supported Structures (single-and double-wall). Stress variation with apex angle, ϕ, can be determined for spherical

shaped tents. Additional theory development and analysis is needed to refine stress profiles on cylindrical models.

9. In the strength study of the double-wall tent, the maximum stress resultants were found in either the hoop or web stresses. Hoop stresses were greatest when cell angle, α_c, was greater than 30^o and when α_c was less than 30^o, the web stress is greatest. Meridional stress resultants were smaller than the other components in both cases. Fabric stresses were found to increase with an increase in cell pressure.

10. In the cellular beam tests, it was found that the value of $M/P_T r_c$ at which initial wrinkle occurs varies with the cell width-to-tent diameter ratio and the internal pressure, and is lower than generally believed. The flexural rigidity, too, was found to vary with regard to the same parameters. Curves are included in this document to show the variation of the quantities.

    Comparison of theoretical pressures calculated to prevent wrinkling at various dynamic pressures with wind tunnel tests indicates that the pressures actually required are 1/5 of those calculated. Design curves reflect this fact.

11. The design of double-wall tents should not allow wrinkling, even for the severest of the design loads. The tests and the theoretical studies both show that deformation becomes excessive almost immediately after wrinkling begins.

SECTION 7

RECOMMENDATIONS

The following areas of investigation warrant further study and testing as a result of the information obtained from this program in order to increase the utility and accuracy of the design presented herein.

1. Additional double-wall tent tests are required to firmly establish the data variation with tent shape parameters as for the single-wall case.

2. The effects of adjacent tents or structures on tent loads and stability characteristics were not measured during these tests and possibly should be evaluated in future tests.

3. Additional wind tunnel tests should be performed on selected single-and double-wall tent configurations to obtain sufficient vibrational data to evaluate tent shape and material fabric fatigue.

4. Further analyses and tests are required to fully evaluate the use of wind aprons to improve tent stability and anchor loads.

5. Analyses and static beam tests should be accomplished to determine the effect of concentrated loads on inflated beams.

6. Fabric studies should be made to investigate fabric orientation or skew on stiffness of inflated beams.

7. Full-scale tentage tests should be made to evaluate Reynold's number effects on tentage data presented in the Design Manual.

SECTION 8

SUMMARY

The objective of this program is to provide information based on wind tunnel test data that can be applied either to the evaluation and improvement of existing ground-mounted air-supported tents or to the design of such future structures. The data presented are the results of a program conducted by the Hayes International Corporation of Birmingham, Alabama under Contracts DA 19-129-AMC-129(N) and DA 19-129-AMC-953(N) for the U. S. Army Natick Laboratories, Natick, Massachusetts.

The program consisted of study, test and analytical investigation phases which began in July 1963 and concluded in May 1968. During the study phase, a review was made of pertinent literature on experimental techniques, data and analyses applicable to determining maximum aerodynamic force on and stresses in fabric structures. The wind tunnel investigations consisted of detailed testing of thirty-six tent models to include seventeen single-wall tents (eleven with non-porous and six with porous fabric) and nineteen double-wall tents. Tests were conducted at stabilized wind speeds up to 110 miles per hour in the Virginia Polytechnic Institute's 6' x 6' stability tunnel. In the analytical phase, test data were used to develop fabric stress and aerodynamic coefficient data variation with tent parameters.

The results of the wind tunnel investigations and the stress analyses have been incorporated into this manual and includes comprehensive, practical design data suitable for engineering reliable, stable, single-and double-wall air-supported tents of minimum weight and cubage. Data, in general, are presented in non-dimensional coefficient form, and therefore, are applicable to full-scale tents within the range of parameters investigated. Design information is presented as charts and tables on such items as tent aerodynamic force and moment coefficients, anchor and guy line coefficients, surface deflection, material stresses and specifications, usable volume, and weight.

SECTION 9

BIBLIOGRAPHY

1. Bird, Walter W., "Design Manual for Spherical Air Supported Radomes" Report No. UB-664-D-1, Cornell Aeronautical Laboratory, Buffalo, New York, October 1950.

2. Bicknell, J. and R. Yeghiayan, "Wind Tunnel Tests on an Air Supported Tent Model". Report No. 1024, Massachusetts Institute of Technology, Cambridge, Massachusetts, June 1963.

3. Pope, Alan, "Wind Tunnel Testing". Second Edition, John Wiley and Sons, Inc., New York, New York, 1954.

4. Liepmann, H. W. and A. Roshko, "Elements of Gasdynamics". John Wiley and Sons, Inc., New York, New York, 1957.

5. Dwinnell, J. H., "Principles of Aerodynamics". McGraw-Hill Book Company, Inc., New York, New York, 1949.

6. "Ground Radome Study, Final Report" WD:-TR-1936, Philco Western Development Laboratories, Palo Alto, California, December 1962.

7. Sevin, Eugene, "Analytical and Experimental Studies of Spherical Rigid Ground Radomes" Final Report 8154, Armour Research Foundation, Chicago, Illinois, February 1961.

8. Foerster, A. F., "Stress Distribution and Stability Criteria of Spherical Ground Radomes Subjected to Wind Loads". Proceedings of the OSU-WADC Radome Symposium, WADC-TR58-272, Vol. 1, Ohio State University, Columbus, Ohio, June 1958.

9. Timeshenko, S., Theory of Plates and Shells, McGraw-Hill Book Company, Inc., New York, New York, 1940.

10. Flugge, Wilhelm, Stresses in Shells, Springer-Verlag, Berlin/ Gottingen/Heidelberg, Germany, 1962.

11. Wellington Sears Handbook of Industrial Textiles, Wellington Sears Company, Inc., West Point, Georgia, 1963.

12. ASTM Committee D-13 ASTM Standards on Textile Materials, American Society for Testing Materials, Philadelphia, Pennsylvania, 1964.

13. American Association of Textile Chemists and Colorists Volume No. 40, Howes Publishing Co., Inc., New York, New York, 1964.

14. Federal Specifications, Textile Test Methods CCCT191, General Services Administration, Business Service Center, Region 3, Washington, D. C., 1951.

15. Cornell Aeronautical Laboratory, Inc., "Design Manual for Spherical Air Supported Radomes (Revised)". Contract AF 30(602)-976, Rome Air Development Center, Griffiss Air Force Base, Rome, New York, ASTIA Report No. UB-909-D-2, 1958.

16. Monego, C. J., "Air Supported Tents for Military Use" ME-3, U. S. Army Natick Laboratory, Natick, Massachusetts, 1965.

17. Monego, C. J., "Studies of Quantitative Correlation Between Bulk Density and Thickness of Fabrics and Their Radar Transmission Characteristics". U. S. Army Materiel Command, U. S. Army Natick Laboratories Technical Report ME-2, Natick, Massachusetts, 1965.

18. Susich, G. and S. Backer, "Tensile Recovery Behavior of Textile Fibers", Textile Research Journal 21, Princeton, New Jersey, 1951, pp. 482.

19. Hamburger, W. J., H. M. Morgan, and M. M. Platt, "Mechanics of Elastic Performance of Textile Materials; Part X, Some Aspects of Elastic Behavior at Low Strains", Textile Research Journal 22, Princeton, New Jersey, 1952, pp. 695.

20. DuPont, E. I. de Nemours & Co., Tensile Stress-Strain Properties of Fibers, Bulletin X-82, Wilmington, Delaware, May 1958.

21. Haas, R. Dietzen, "National Advisory Committee for Aeronautics Report No. 16" - Annual Report, 1917, pp 144-271; translated by K. K. Darrow originally, published by Springer-Verlag, Berlin 1912.

22. Pierce, F. T., "The Geometry of Cloth Structure", Journal Textile Institute, 1937, 28 p T45.

23. Monego, C. J., "The Biaxial Stress-Strain Behavior of Fabrics". Presentation before the Fiber Society in Wilmington, Delaware, 5 October 1964.

24. Textile World, Man-Made Fiber Chart, McGraw-Hill Publishing Company, Inc., New York, New York, 1964.

25. Crory, F., R. Reed, W. Tezzard, and G. Font-Journey, "Installation and Testing of Arrowhead Universal Ground Anchors in Frozen and Thawed Ground" U. S. Army Cold Regions Research and Engineering Laboratory, Hanover, New Hampshire, 1964.

26. Marks, Lionel S., Mechanical Engineers Handbook, McGraw-Hill Publishing Company, Inc., New York, New York, 1941.

27. Topping, A. D., "Shear Deflections and Buckling Characteristics of Inflated Members", J. Aircraft, September-October 1964.

28. Topping, A. D., "An Introduction to Biaxial Stress Problems in Fabric Structures", Aerospace Engineering, April 1961.

GLOSSARY OF TERMS

Reynold's Number - A dimensionless parametric ratio of the inertia forces and the viscous forces acting on a body immersed in a moving fluid. The mathematical expression for Reynold's Number is

$$R_N = \frac{\rho U d}{\mu}$$

Critical Reynold's Number - The Reynold's Number at which the boundary layer upstream of a point of separation changes from laminar to turbulent flow. The critical Reynold's Number for both spheres and cylinder is approximately 500,000.

Dynamic Pressure - Also referred to as impact pressure or velocity pressure and is that portion of the stagnation pressure which results from the motion of the fluid. The mathematical expression for dynamic pressure is

$$q = \frac{1}{2} \rho U^2$$

Potential Flow - A theoretical treatment of fluid flow which assumes the fluid to be inviscid. Consequently, a body in motion with potential flow has a symmetrical pressure distribution which results in zero drag forces.

Horizontal Buoyancy - The general tendency for the model in a closed jet wind tunnel to be "drawn" downstream due to the longitudinal static pressure gradient that exists in the test section.

Solid Blocking - The increase in air velocity due to the presence of a model in a wind tunnel test section caused by the reduction in the area through which the air is allowed to flow.

Planform Area - Maximum projected area in horizontal plane.

in. w.g. - Gage pressure expressed in inches of water.

SYMBOLS

A_c	Cross-sectional area (l)
A_e	Cell Cross Sectional area (l^2)
A_f	Floor area (l^2)
A_o	Orifice area (l^2)
A_p	Planform area (l^2)
A_s	Surface area (l^2)
A_t	Tent enclosed cross-sectional area (l^2)
a	Ellipsoidal semimajor axis (l)
AL	Anchor load (f)
b	Ellipsoidal semiminor axis (l)
C_{AL}	Anchor load coefficient, single-wall tent
C_{BL}	Base anchor load coefficient, double-wall tent
C_c	Coefficient of contraction
C_D	Drag coefficient
C_{GL}	Guy line coefficient
C_L	Lift coefficient
C_M	Pitching moment coefficient
C_N	Yawing moment coefficient
C_o	Orifice coefficient
C_R	Rolling moment coefficient
C_Y	Side force coefficient
C_1, C_2, C_3, C_4	Constants in piece-wise linear deflection solution
c	Linear measure of wrinkling (l)
CL	Curtain Load (f)
D	Drag (f)

D_B	Drag correction due to horizontal buoyancy (f)
d	Tent diameter (l)
E	Modulus of elasticity (fl^{-1})
G	Shear modulus (fl^{-1})
GL	Guyline load (f)
h	Tent height (l)
h_r	Distance from ground plane to center of curvature (l)
I	Moment of inertia about centroidal axis (l^{-3})
K	Tent model shape factor
k_p	Impact pressure correction factor
L	Lift (f)
L_B	Lift along body axis (f)
ℓ_b	Beam length (l)
ℓ_h	Tent length (l)
ℓ	Distance from model nose
M	Bending moment (fl)
M_m	Yawing moment (fl)
M_y	Rolling moment (fl)
N_h	Hoop stress resultant (fl^{-1})
N_w	Web stress resultant (fl^{-1})
N_x	Longitudinal stress resultant (fl^{-1})
N_θ	Circumferential stress resultant (fl^{-1})
N_ϕ	Meridional stress resultant (fl^{-1})
$N_{\phi x}, N_{\phi\theta}$	Shear stress resultants (fl^{-1})
n	Number of cells
$(\ )_n, (\ )^n$	n th term of general equation

P	Static pressure (fl^{-2})
P_A	Applied axial load (f)
P_c	Cell pressure (fl^{-2})
P_e	Tent enclosure pressure (fl^{-2})
P_{ext}	External load (fl^{-1})
P_o	Initial axial load (f)
P_T	Total axial load (f)
P_t	Stagnation pressure (fl^{-2})
P_y	Side force (f)
P_{yr}	Side force in body coordinate system (f)
p	Static pressure
Q	Volume flow (l^3t^{-1})
q	Dynamic (impact) pressure (fl^{-2})
R	Universal gas constant
R_N	Reynolds number
r	Tent radius (l)
r_c	Cell Radius (l)
r_i	Inside tent radius (l)
r_o	Outside tent radius (l)
S_c	Wind tunnel test section cross sectional area
S_x	Model cross sectional area
S_α, S_β, S_ϕ	Arc lengths in α, β, ϕ directions (l)
T	Absolute temperature (τ)
T^*, T^+	Guy wire tension (f)
U	Velocity (lt^{-1})
u, v	Displacements (l)

V	Shear (f)
V_c	Cell volume (l^3)
$\overline{V}$	Tent enclosed volume (l^3)
W	Tent width (l)
w	Cell width (l)
$x, y, z, \overline{x}, \overline{y}, \overline{z}$	Cartesian coordinates (l)

GREEK SYMBOLS

α, β	Tent reference angles
α_c	Cell angle
γ	Ratio of tent volume to weight ($l^3 f^{-1}$)
γ_b	Shear strain
δ_B	Rear tent deflection (l)
δ_F	Front tent deflection (l)
δ_H	Top tent deflection (l)
ϵ_{SB}	Correction factor for solid blocking of wind tunnel due to model presence
ϵ_θ	Circumferential strain
ϵ_ϕ	Meridional strain
ζ	Correction factor for wake gradients
θ, ϕ	Curvilinear coordinates
$\theta_1, \theta_2, \theta_3$	Angular measure of wrinkling
κ	Curvature (l^{-1})
λ	Ratio of effective to geometric moment of inertia
λ_1, λ_2	Eccentricity parameters
μ	Viscosity of air
ν	Poissons ratio
ζ, T, X	Unit vectors
ρ	Density of air (fl^{-3})
ρ_b	Radius of curvature (l)
Ψ	Angle subtended by curved beam
ψ	Tent yaw angle
ψ_b	Flexural rotation of face of beam

Ω	Fabric unit weight (fl^{-4})
ω	Rotation of beam centerline

MATRIX SYMBOLS

$\{s\}$	Extended stress resultant vector
$\{u\}$	Displacement vector
$\{z\}$	Extended state vector
$[A]$	Rigid body transfer matrix
$[B]$	Element flexibility matrix
$[C]$	Extended equilibrium matrix
$[F]$	Extended field matrix
$[P]$	Extended point matrix
$[U]$	Extended accumulated matrix

---

f denotes units of force

l denotes units of length

t denotes units of time

τ denotes units of temperature

Table I

Wind Tunnel Model Dimensional Data

Single-Wall Tents

Configuration	Width / Length	Width	Length	Height	Fabric Porosity cu.ft./min. ft.^{2}
7/8 Sphere	1:1	23.4	23.4	20.5	0
3/4 Sphere	1:1	27.0	27.0	20.3	0
1/2 Sphere	1:1	30.8	30.8	15.4	0
1/2 Sphere	1:1	30.8	30.8	15.4	0-5
1/2 Sphere	1:1	30.8	30.8	15.4	10-15
3/8 Sphere	1:1	37.2	37.2	13.9	0
3/4 Cylinder	1:2	15.8	34.9	11.9	0
3/4 Cylinder	1:4	11.2	46.1	8.4	0
3/4 Cylinder	1:4	11.2	46.1	8.4	10-15
1/2 Cylinder	1:2	19.4	42.8	9.7	0
1/2 Cylinder*	1:2	19.4	38.8	9.7	0
1/2 Cylinder	1:2	19.4	42.8	9.7	0-5
1/2 Cylinder	1:2	19.4	42.8	9.7	10-15
1/2 Cylinder	1:4	13.8	57.1	6.9	0
3/8 Cylinder	1:2	22.0	49.6	8.6	0
3/8 Cylinder	1:4	15.4	66.5	6.0	0
3/8 Cylinder	1:4	15.4	66.5	6.0	0-5

Notes:

1. All dimensions are in inches.

2. All models had hemispherical ends with the exception of the model configuration indicated with an asterisk (*). This model was equipped with an elliptical end at semi-axes 4.8" and 9.7".

Table II

Wind Tunnel Model Dimensional Data

Double-Wall Tents

Configuration	Width / Length	Width	Length	Height	Cell Width / Encl. Diam.
3/4 Cylinder	1:1	22.4	22.4	16.8	0.082
3/4 Cylinder	1:1	22.4	22.4	16.8	0.123
3/4 Cylinder	1:1	22.4	22.4	16.8	0.164
3/4 Cylinder	1:2	15.8	31.6	11.9	0.123
1/2 Cylinder	1:1	27.4	27.4	13.7	0.082
1/2 Cylinder	1:1	27.4	27.4	13.7	0.123
1/2 Cylinder*	1:2	19.4	38.8	9.7	0.123
1/2 Cylinder	1:4	13.8	57.8	6.9	0.123
3/8 Cylinder	1:1	31.1	31.1	12.1	0.123
3/8 Cylinder	1:2	21.8	43.5	8.6	0.082
3/8 Cylinder	1:2	21.8	43.5	8.6	0.123

Notes:

1. All dimensions are in inches.
2. (*) model tested with and without wind curtain installed.

Table III - Maximum Stress Coefficients

Configuration: Single-Wall Cylindrical Tents with Hemispherical Ends

Test Condition: Broadside Wind Load

h/d	W/ℓ_h	*	(N_ϕ/qr) Max.			(N_θ/qr) Max.			$(N_{\phi\theta}/qr)$ Max.		
			q = .6	q = 3.0	q = 6.0	q = .6	q = 3.0	q = 6.0	q = .6	q = 3.0	q = 6.0
3/4	1/2	S	1.436	1.447	1.532	1.339	1.384	1.464	1.356	1.249	1.306
		C	.737	.820	.818	1.339	1.384	1.464	0	0	0
1/2	1/2	S	1.433	1.322	1.159	1.382	1.217	1.108	.669	.646	.546
		C	.796	.494	.571	1.382	1.217	1.108	0	0	0
1/2	1/4	S	1.235	1.503	-	1.100	1.418	-	.615	.679	-
		C	.525	.651	-	1.100	1.418	-	0	0	0
3/8	1/2	S	1.237	1.167	1.177	1.251	1.256	1.296	.548	.491	.520
		C	.907	.679	.712	1.251	1.256	1.296	0	0	0
3/8	1/4	S	1.485	1.829	-	1.552	1.936	-	.659	.805	-
		C	.804	.789	-	1.552	1.936	-	0	0	0

Legend (*):

S - Stress Coefficients in Hemispherical Ends of Cylindrical Tents
C - Stress Coefficients in Cylindrical Portion of Tents

Note: For the cylindrical portion of the tent, N_θ is actually N_x and $N_{\phi\theta}$ is $N_{\phi x}$.

Table IV

Spherical-Ellipsoidal Coordinates

$\lambda_1 = 1$ $\lambda_2 = 1/2$

ϕ^*	θ^*	ϕ	θ
15	0	5.000	0.000
15	30	5.544	16.102
15	60	7.535	40.893
15	90	9.925	90.000
15	120	7.535	139.107
15	150	5.544	163.898
15	180	5.000	180.000
45	0	45.000	0.000
45	30	47.969	16.102
45	60	56.518	40.893
45	90	63.435	90.000
45	120	56.518	139.107
45	150	47.969	163.898
45	180	45.000	180.000
90	0	90.000	0.000
90	30	90.000	16.102
90	60	90.000	40.893
90	90	90.000	90.000
90	120	90.000	139.107
90	150	90.000	163.898
90	180	90.000	180.000

le V. Inflated Test Beam Summa

w(in.)	w_g(in.)	n	[illegible])	^{w}b(in.)	^{h}b(in.)	r(in.)	[illegible]	f(c [illegible])	A_e(in^2)	I(in^4)
2.000	1.250	27	38°-20' .669	34.00	48.12	∞	0	116.6	63.2	7[illegible].6
1.938	1.250	27	39°-23' .687	33.38	41.62	17.94	66.5 1.16	114.3	60.4	65.8
2.000	1.1875	27	36°-31' .637	33.00	46.25	19.94	66.5 1.16	114.3	61.1	70.1
1.938	1.1875	27	38°-29' .672	33.75	49.88	21.68	66 1.15	112.9	59.5	65.2
3.000	1.875	18	38°-30' .672	34.62	48.00	∞	0	117.8	95.8	161.9
[illegible].875	1.750	18	38[illegible]-32' .[illegible]73	34.00	44.12	19.02	66.5 1.16	113.0	87.9	142.4
[illegible].938	1.750	18	37[illegible]-31' .[illegible]75	34.00	56.44	25.65	63 1.10	11[illegible].2	90.2	150.2
[illegible].938	1.875	18	[illegible]-16' [illegible]05	[illegible]4.25	51.69	32.30	46 .8[illegible]	11[illegible].4	92.9	152.9
4.000	2.4375	13	3[illegible]-42' .[illegible]73	33.44	48.12	∞	[illegible]	11[illegible].7	122.2	277.[illegible]
3.750	2.4375	13	-[illegible]-32' .[illegible]27	33.00	50.19	24.36	59 1.03	10[illegible].6	112.4	233.9
4.000	2.500	13	38°-48' .677	34.12	58.25	26.97	62 1.08	115.1	124.5	279.3
3.875	2.375	13	38°-30' .672	33.25	50.38	30.72	47 .82	111.0	116.2	253.1

Table VI

Effect of α_c,n on Double-Wall Tent Weight

Parameter	Tent 1	Tent 2	Absolute Difference	Percent Difference
n	12	8	Down 4	33
α_c	35^o - 48'	72^o - 00'	Up 36^o - 12'	101
Volume	2234.1 $ft.^3$	2421.6 $ft.^3$	Up 187.5 $ft.^3$	8
Weight	264.0 lb	246.8 lb	Down 17.2 lb	7
Length	140.4 in.	152.2 in.	Up 11.8 in.	8

Table VII

Load Recovery Properties of Fibers

From Susich & Backer

Fiber / Cond.	Polyester	Nylon	Spun Acrylic	Filament Acrylic*	Glass Fiber**	Polypropylene*
	At 5% Strain					
IER***	38	38	42	NA	-	NA
DR***	52	59	30	NA	-	NA
PS***	10	3	28	NA	-	NA
	At 10% Strain					
IER	27	28	27	NA	-	NA
DR	46	67	43	NA	-	NA
PS	27	5	30	NA	-	NA
	At 50% Elongation at Break					
IER	28	27	30	NA	78	NA
DR	50	67	45	NA	19	NA
PS	22	6	25	NA	3	NA
	At 50% of Breaking Tenacity					
IER	33	29	33	NA	78	NA
DR	52	67	52	NA	19	NA
PS	15	4	15	NA	3	NA

*Data not available

**Breaking extension 5%

***IER: Immediate Elastic Recovery; DR: Delayed Recovery; PS: Permanent Set

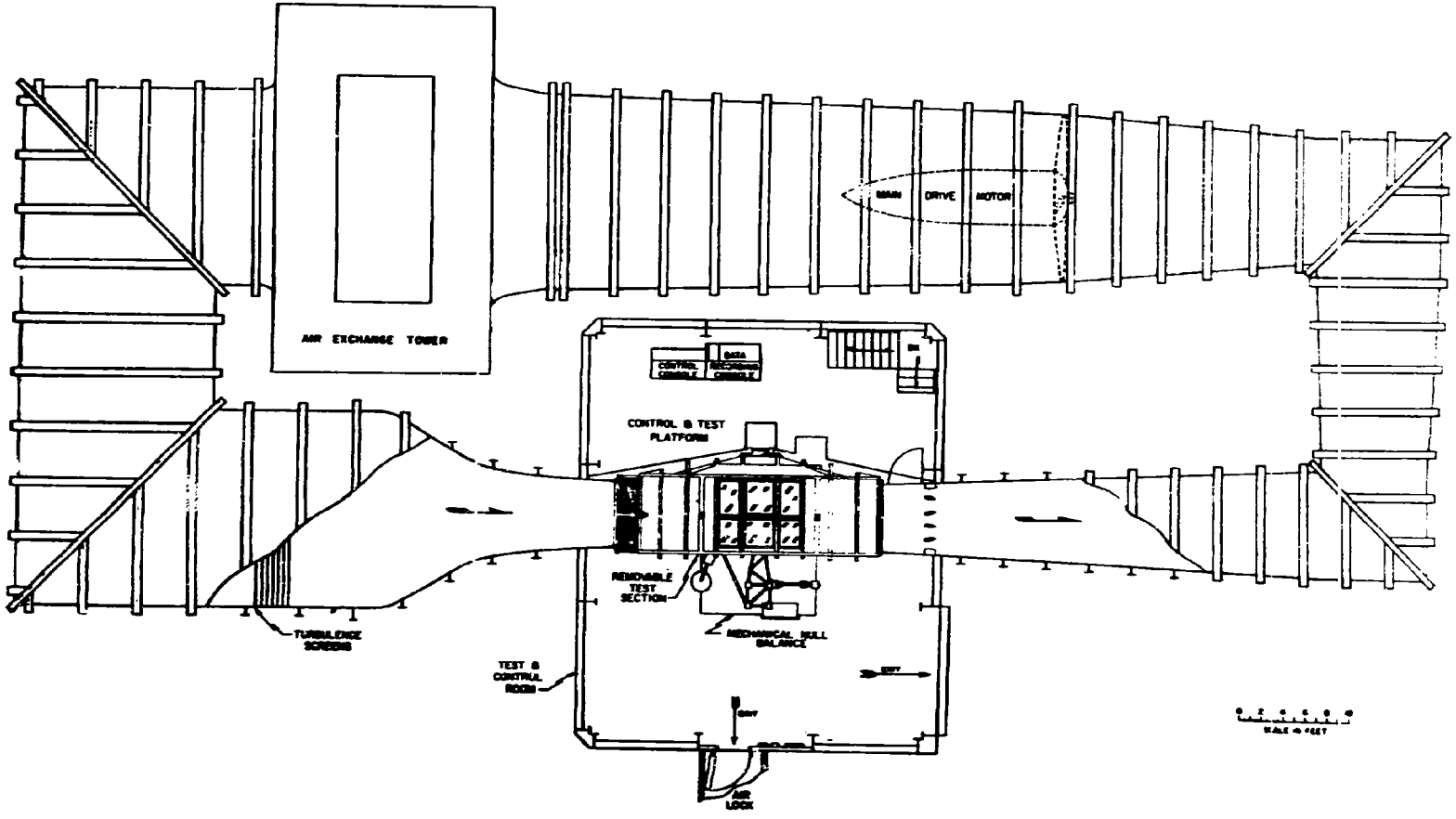

Figure 1. Virginia Polytechnic Institute Subsonic Wind Tunnel Facility

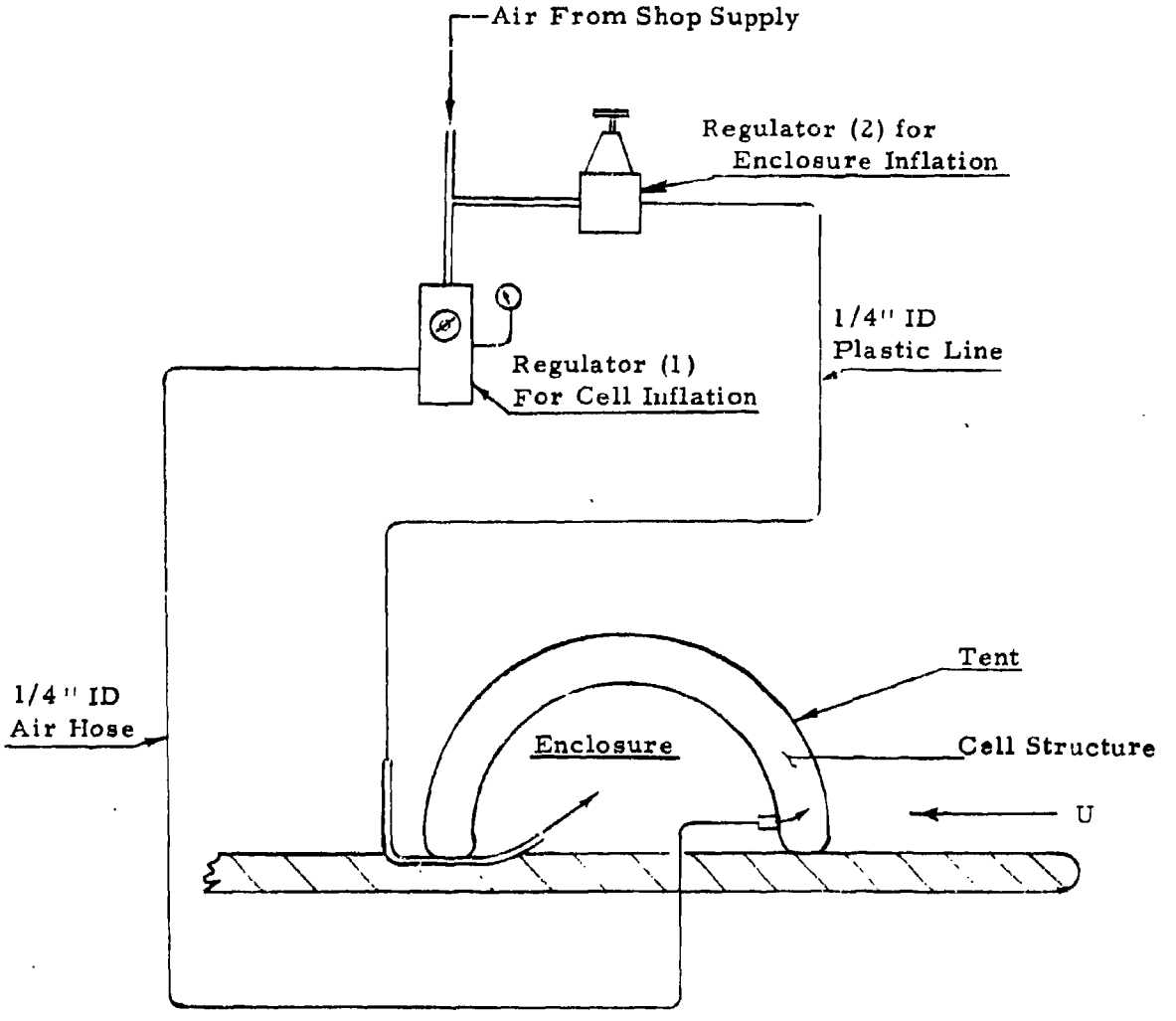

Figure 2. Tent Inflation Schematic

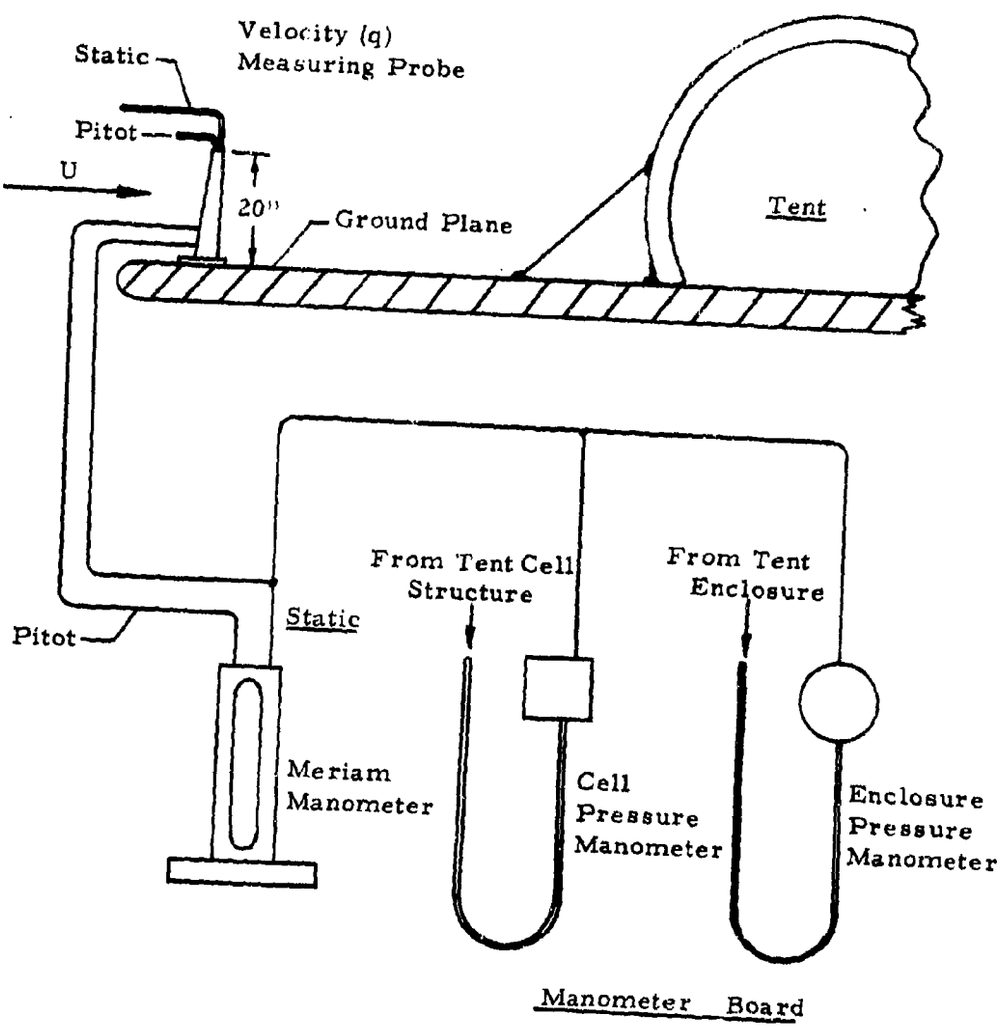

Figure 3. Pressure Instrumentation Schematic

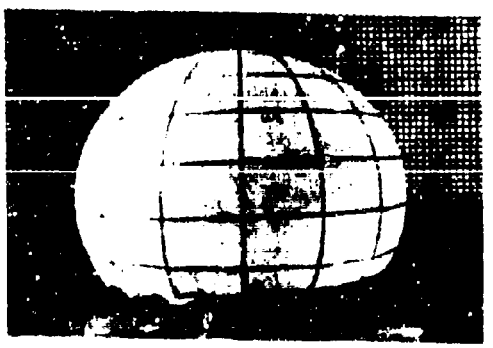

3/4 Sphere

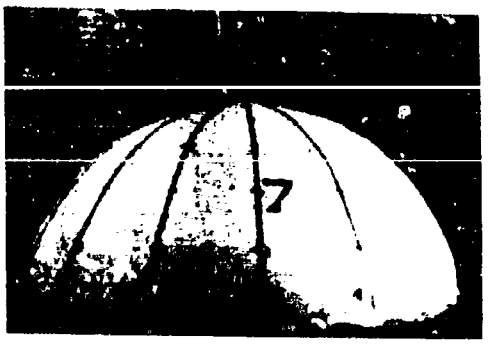

3/8 Sphere

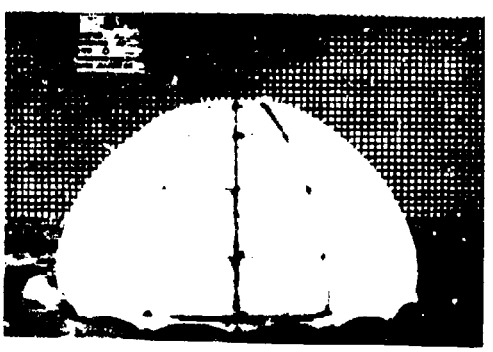

1/2 Sphere

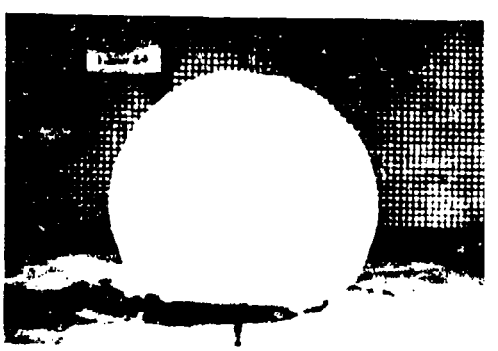

7/8 Sphere

Figure 4. Single-Wall Spherical Tents

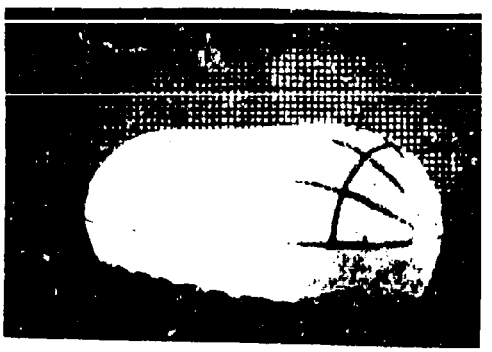

3/4 Cylinder
Hemispherical Ends

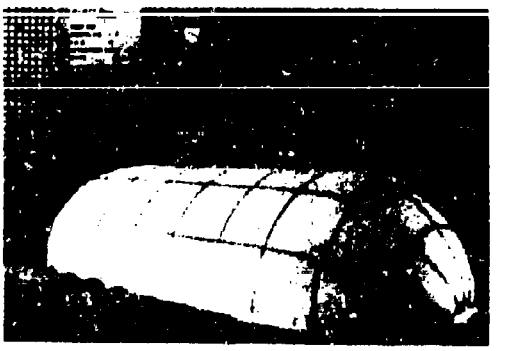

1/2 Cylinder
Hemispherical Ends

3/8 Cylinder
Hemispherical Ends

1/2 Cylinder
Elliptical Ends

Figure 5. Single-Wall Cylindrical Tents, $W/\ell_h = 1/2$

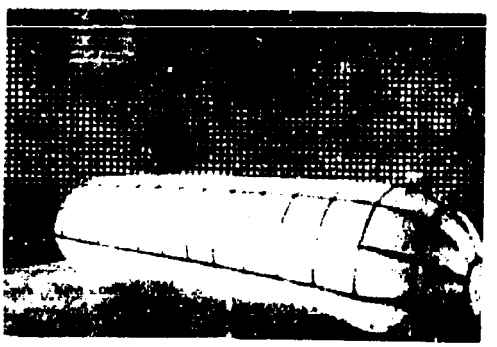

3/4 Cylinder
Hemispherical Ends

1/2 Cylinder
Hemispherical Ends

3/8 Cylinder
Hemispherical Ends

Figure 6. Single-Wall Cylindrical Tents, $W/\ell_h = 1/4$

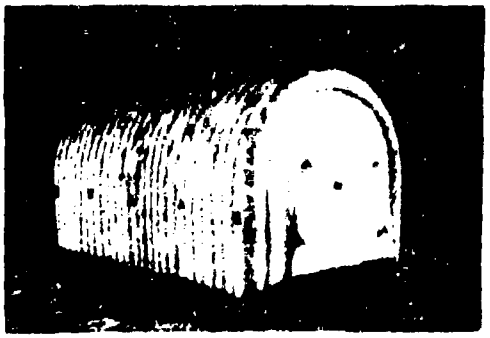

3/4 Cylinder
Cell Width/Enclosure Dia. = 0.082
Vertical Sides

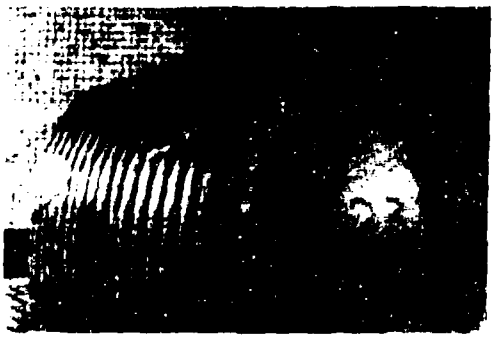

3/4 Cylinder
Cell Width/Enclosure Dia. = 0.123
Sloping Sides

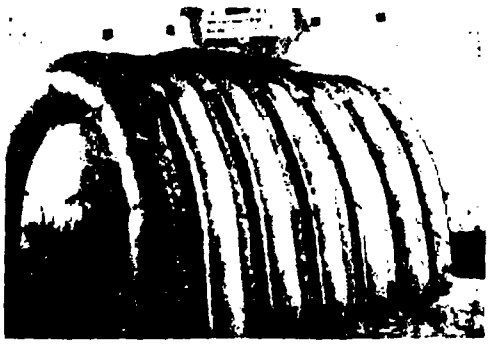

3/4 Cylinder
Cell Width/Enclosure Dia. = 0.164
Sloping Sides

3/4 Cylinder
Cell Width/Enclosure Dia. = 0.082
Sloping Sides

Figure 7. Double-Wall Cylindrical Tents, W/ℓ_h = 1/1

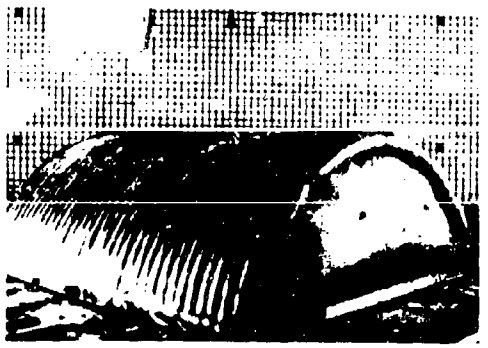

3/8 Cylinder
W/ℓ_h = 1/1

3/4 Cylinder
W/ℓ_h = 1/2

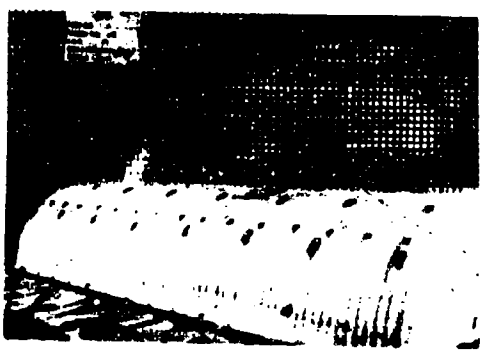

1/2 Cylinder
W/ℓ_h= 1/2

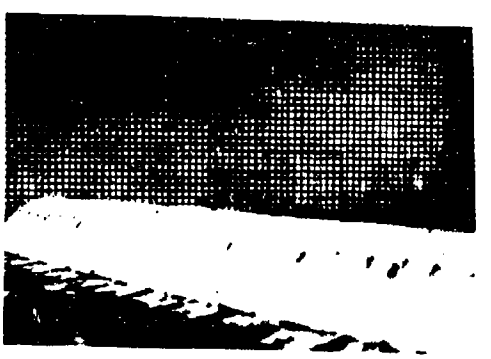

1/2 Cylinder
W/ℓ_h=1/4

Figure 8. Double-Wall Cylindrical Tents, W/ℓ_h = 1/1, 1/2 & 1/4

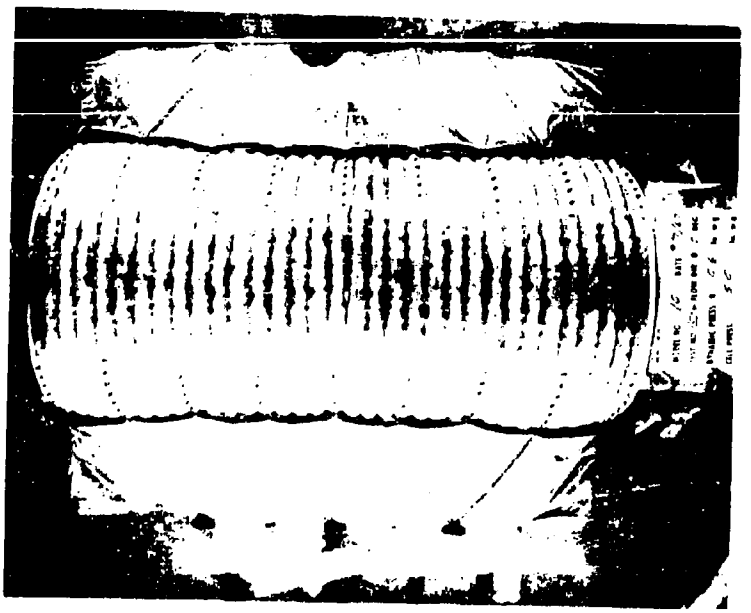

Side Curtain

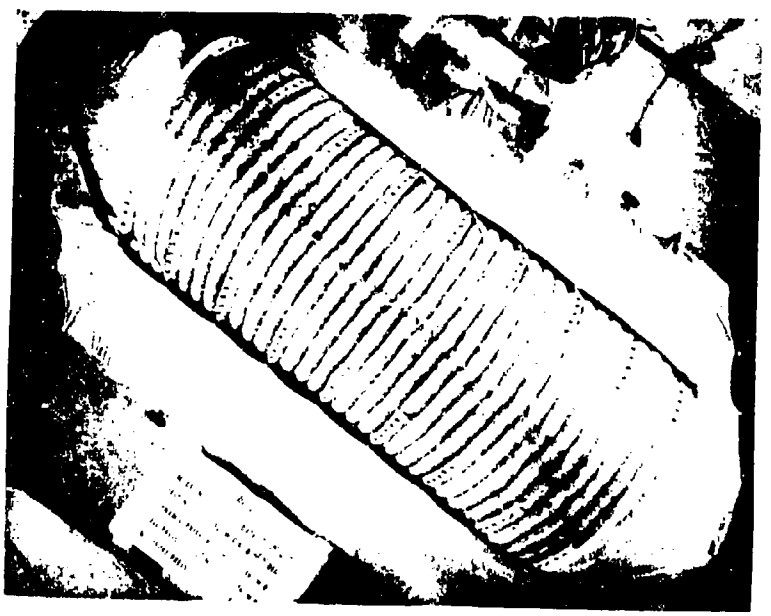

Side and End Curtains

Figure 9. Curtain Configurations for Double-Wall Tents, 1/2 Cylinder, $W/\ell_h = 1/2$

WIND CURTAIN CONFIGURATIONS

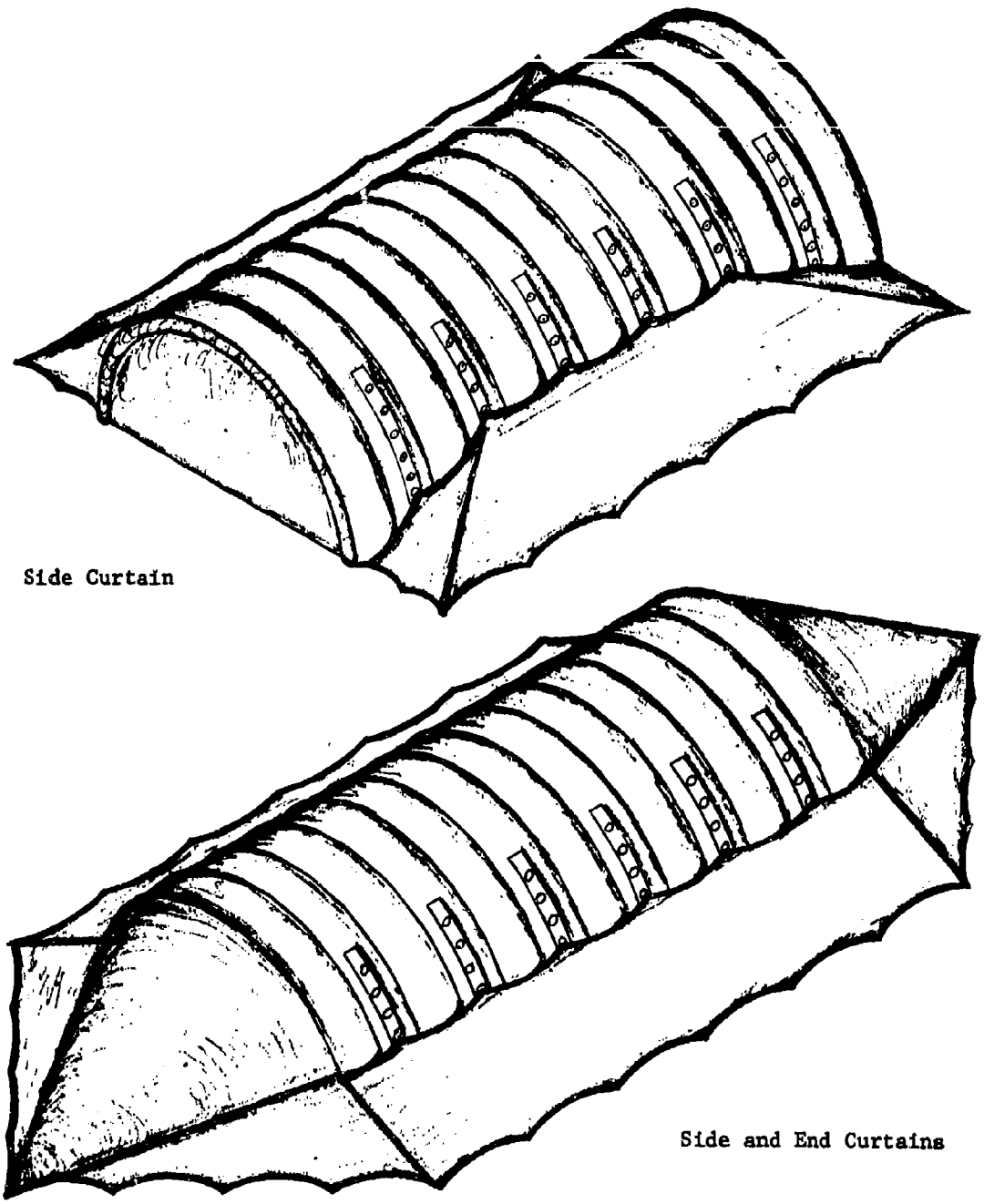

Figure 10. Illustration of Curtain Configurations for Double-Wall Tents, 1/2 Cylinder, $W/\ell_h = 1/2$

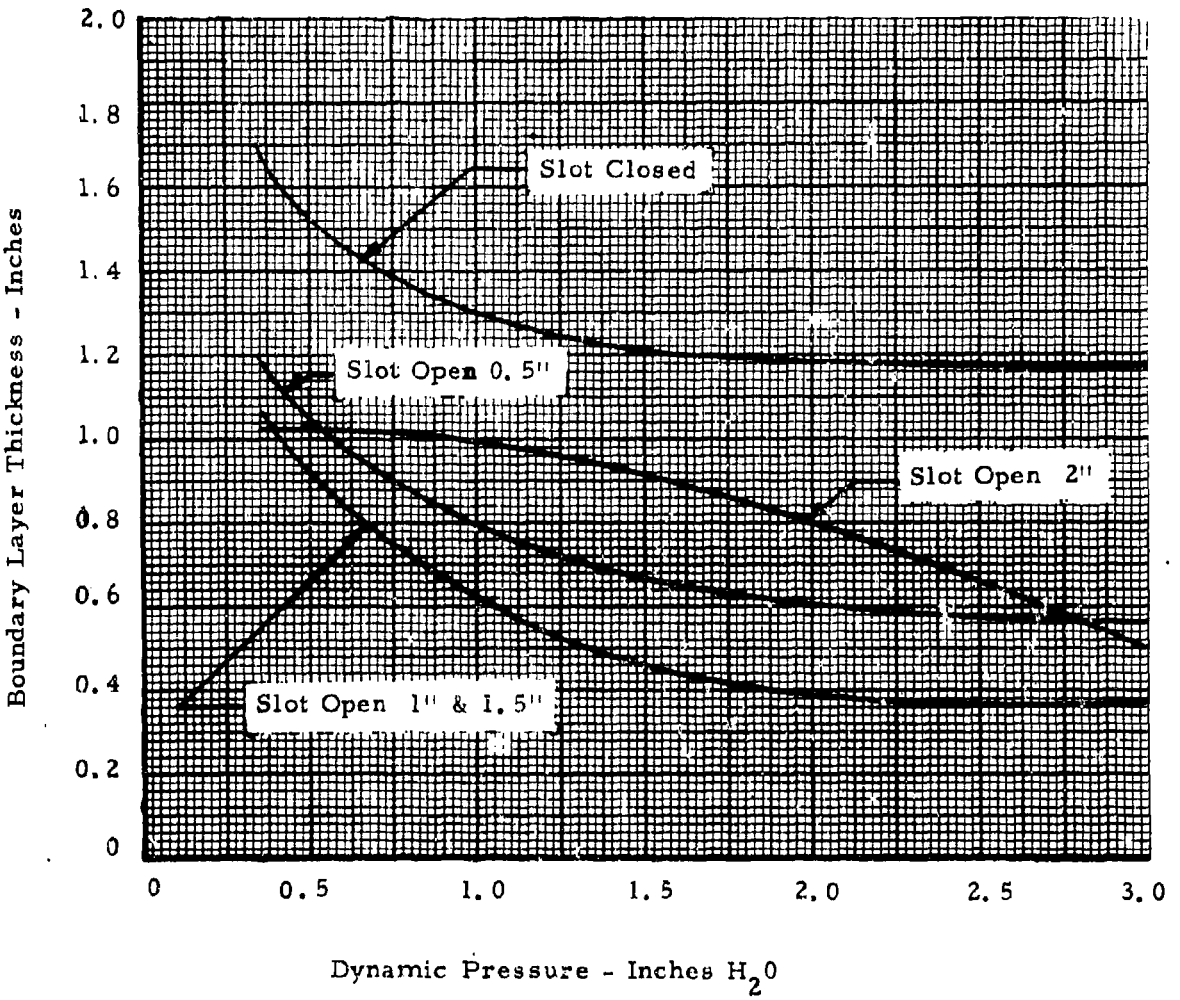

Figure 11. Boundary Layer Thickness Above the Ground Plane

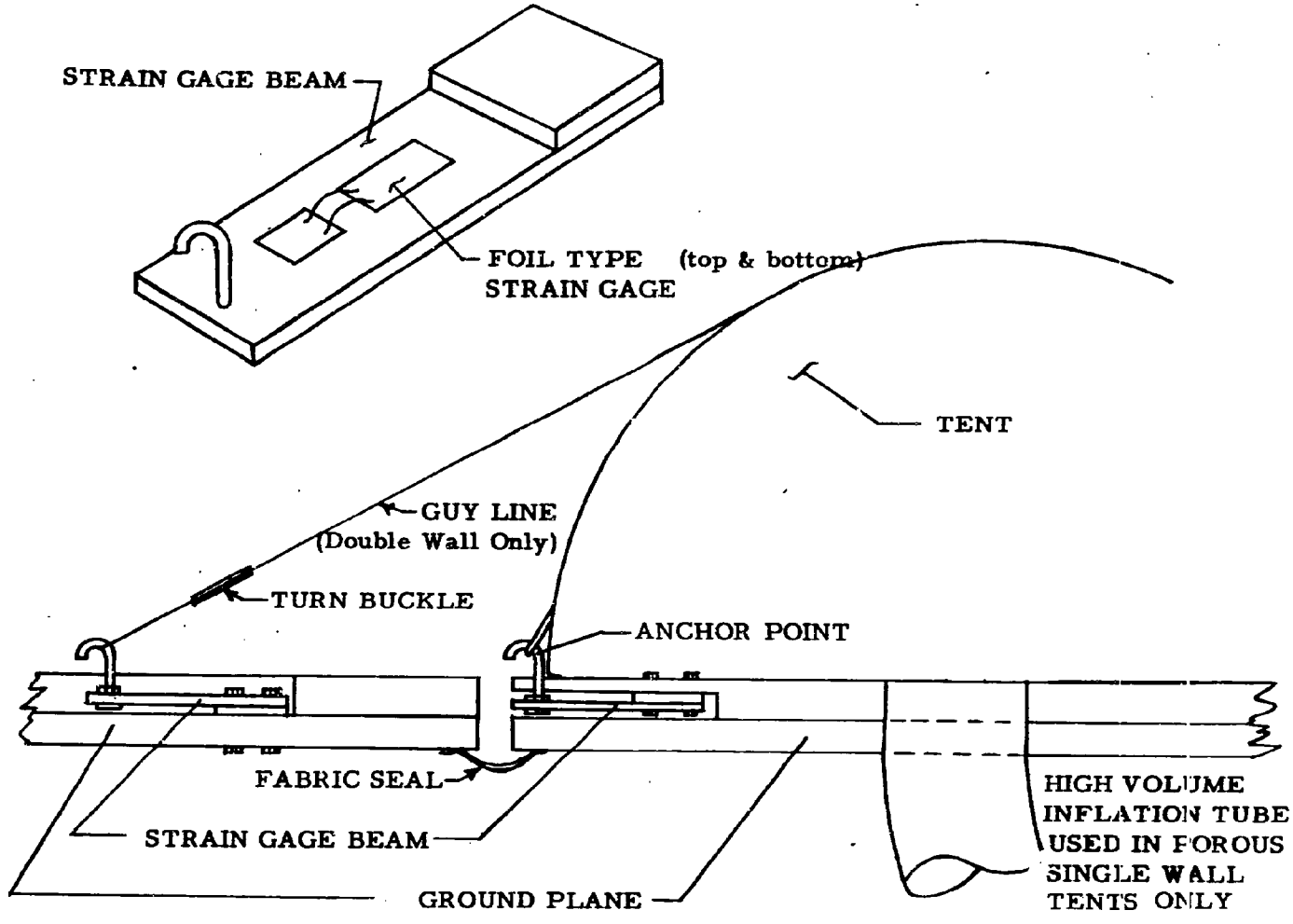

Figure 12. Typical Strain Gage Installation on the Ground Plane

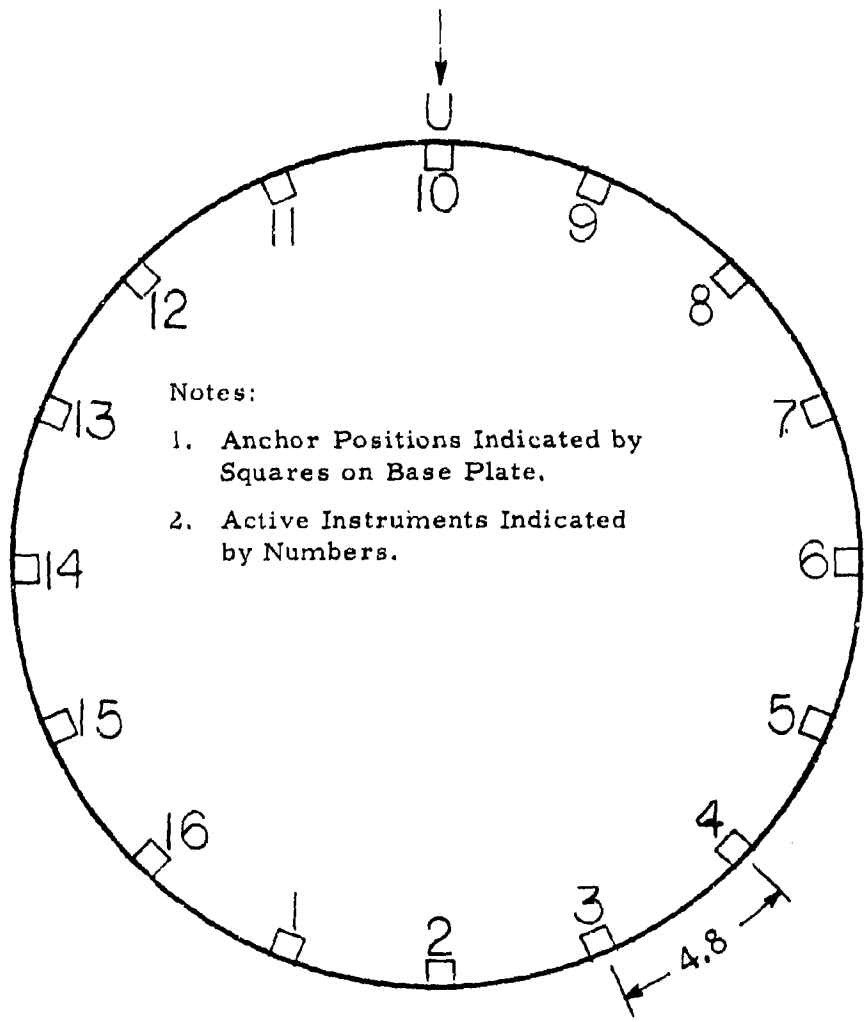

Figure 13. Single-Wall Tent Strain Gage Locations, 3/4 Sphere

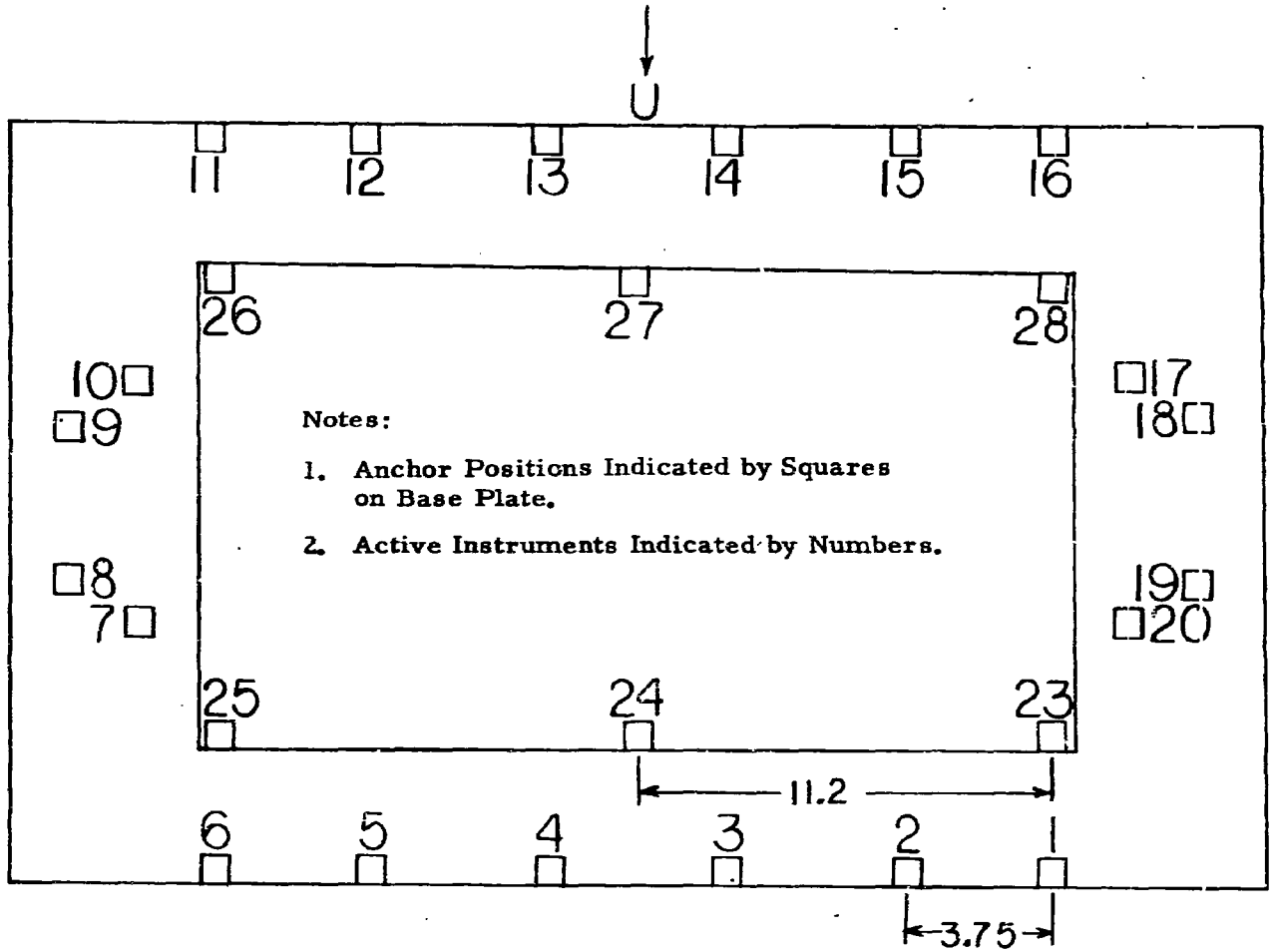

Figure 14. Double-Wall Tent Strain Gage Locations, 3/4 Cylinder, $W/\ell_h = 1/1$

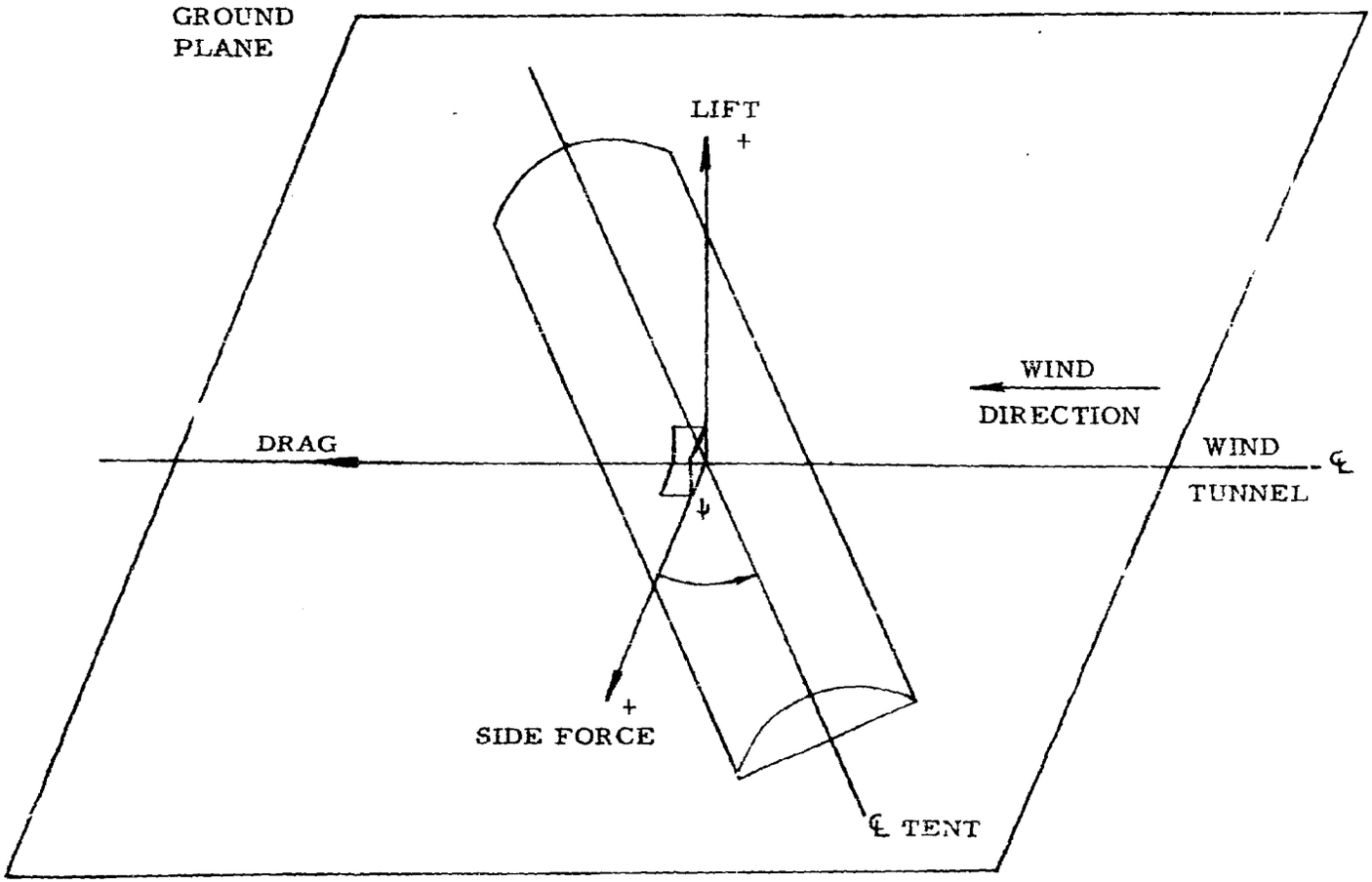

Figure 15. Wind Axes System

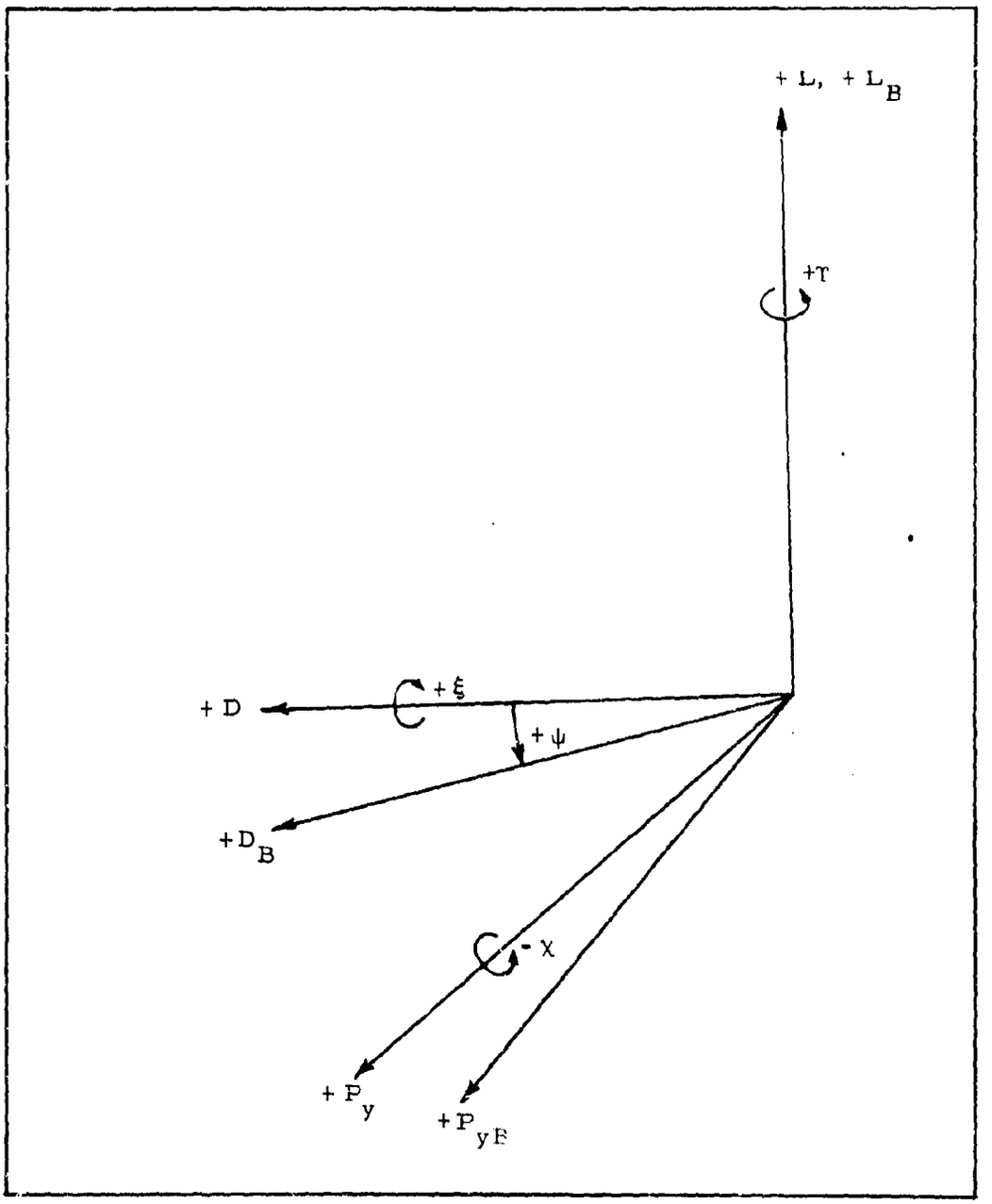

Figure 16. Coordinate System for Transformation from Wind Axes to Body Axes

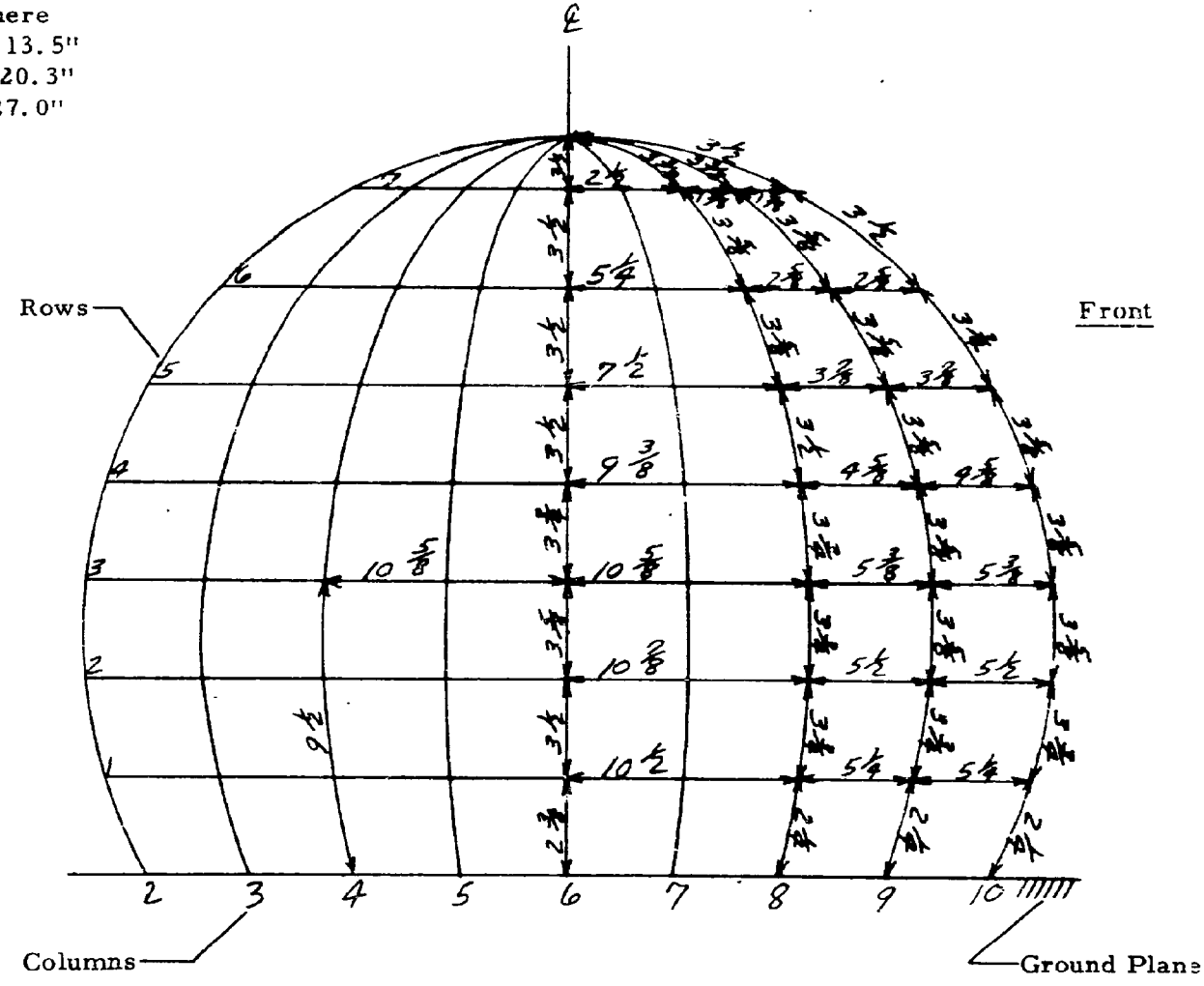

Figure 17. Pressure Tap Locations, 3/4 Sphere

3/4 Cylinder $W/\ell_h = 1/1$
Radius 11.2"
Height 16.8"
Width 22.4"

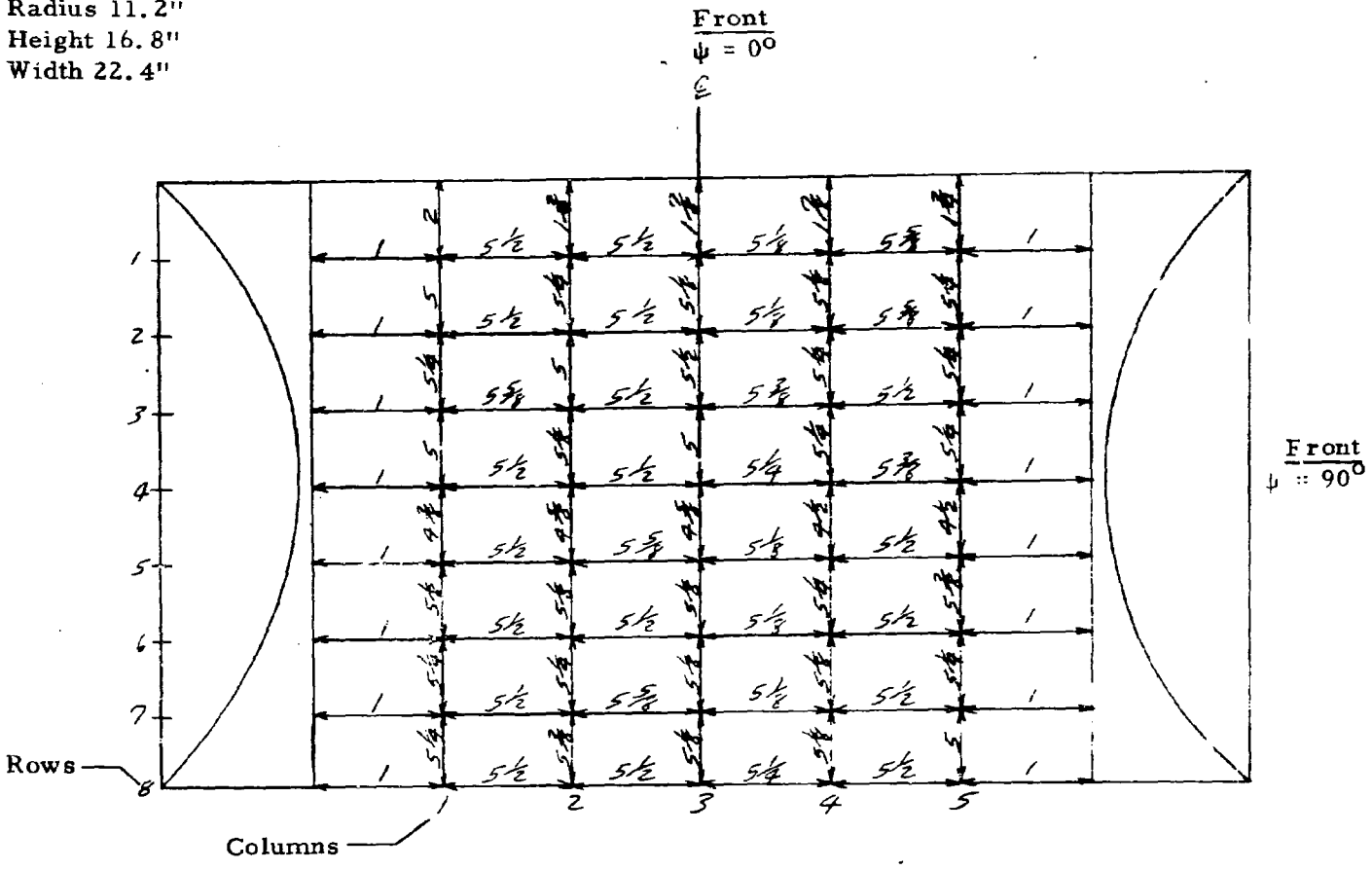

Figure 18. Pressure Tap Locations, 3/4 Cylinder, $W/\ell_h = 1/1$

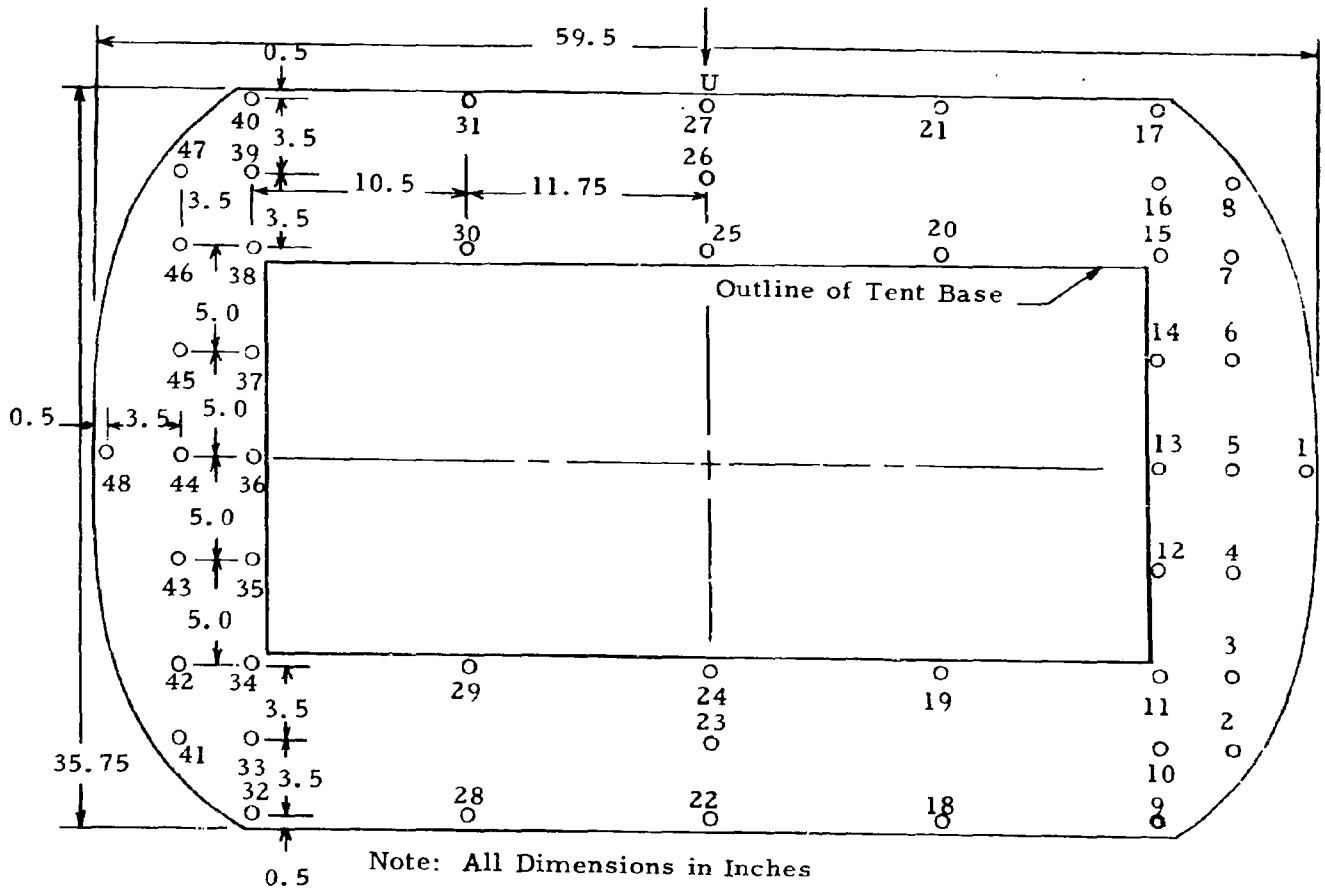

Figure 19. Pickup Locations for Pressure Distribution Measurement on a Double-Wall Model Base 1/2 Cylinder, $W/\ell_h = 1/2$

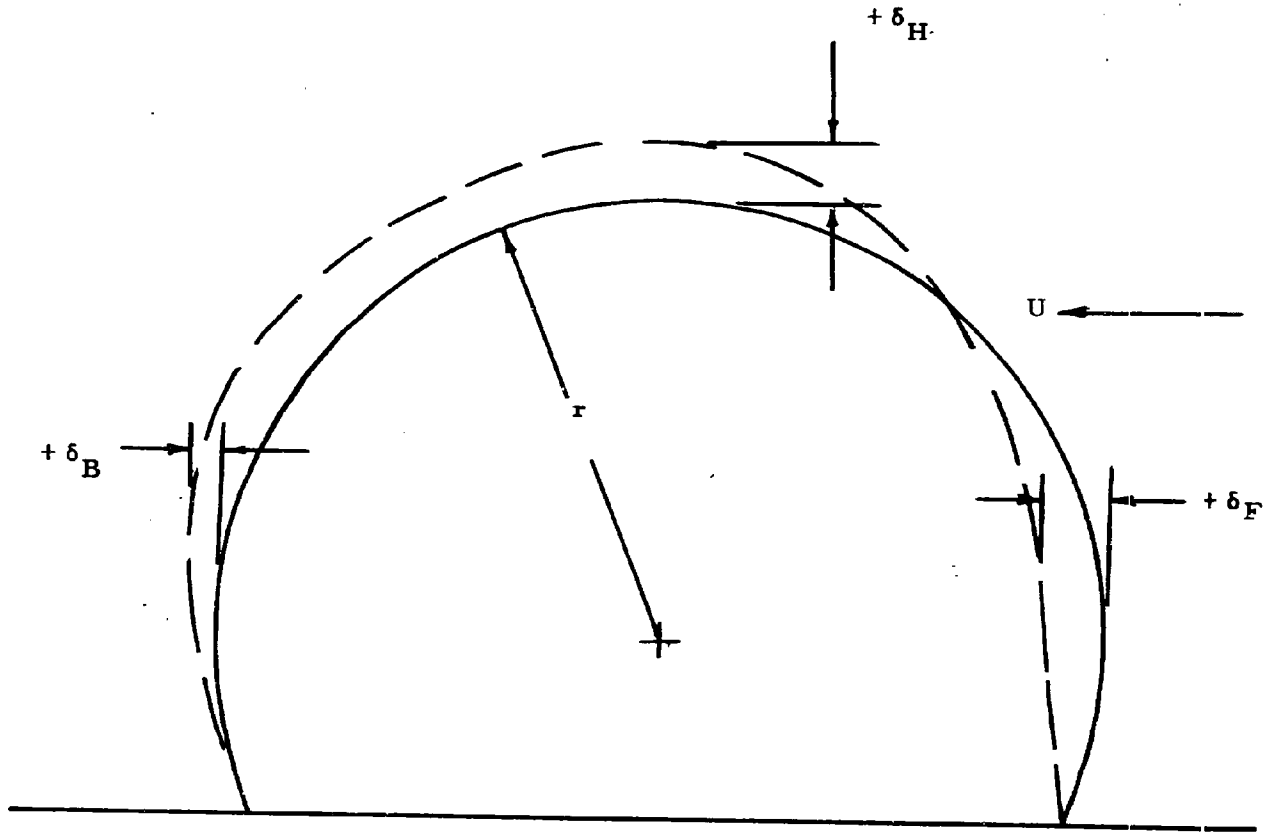

Figure 20. Tent Deflection Notation

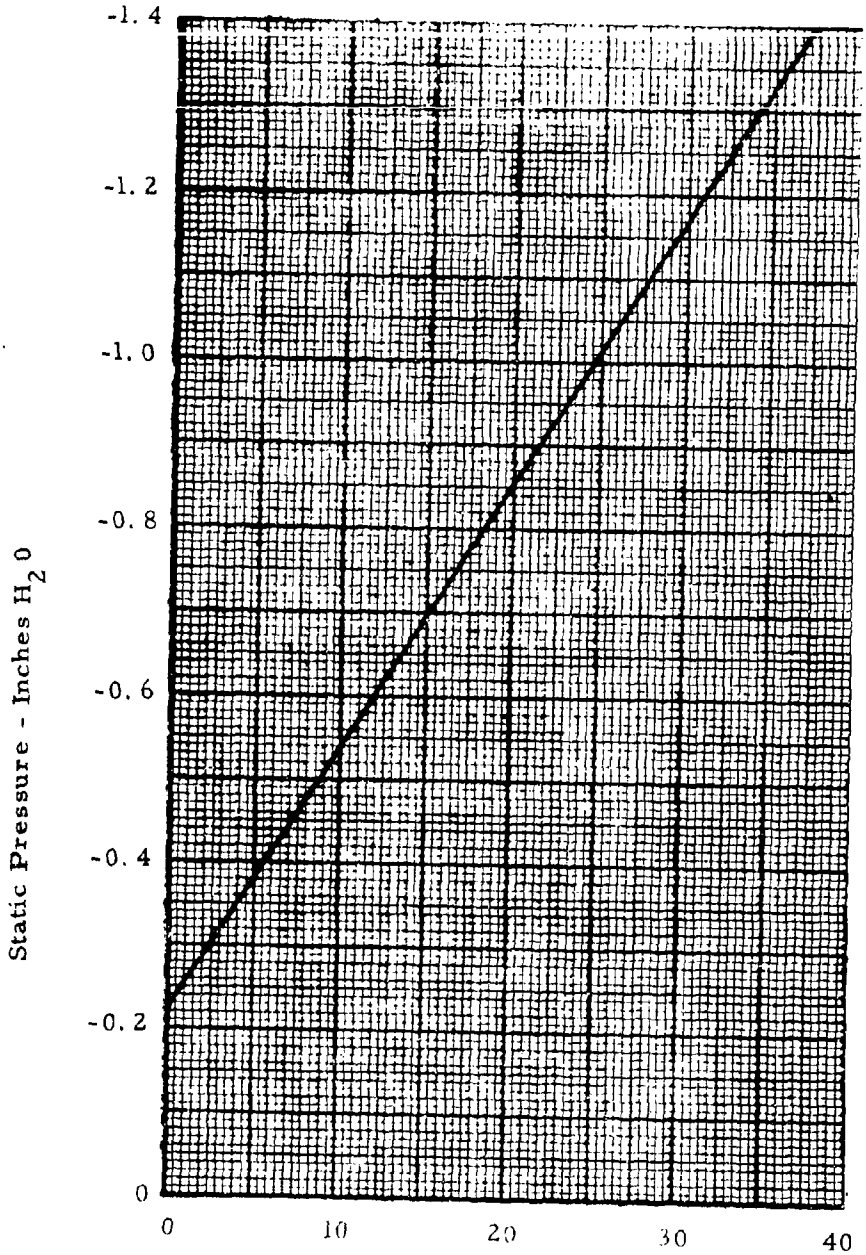

Figure 21. Wind Tunnel Static Pressure Gradient

MAXIMUM LIFT COEFFICIENT
SINGLE-WALL SPHERES

Note:
(*) Fabric porosity, cu. ft. / min./sq. ft. @ 6 in. w. g.

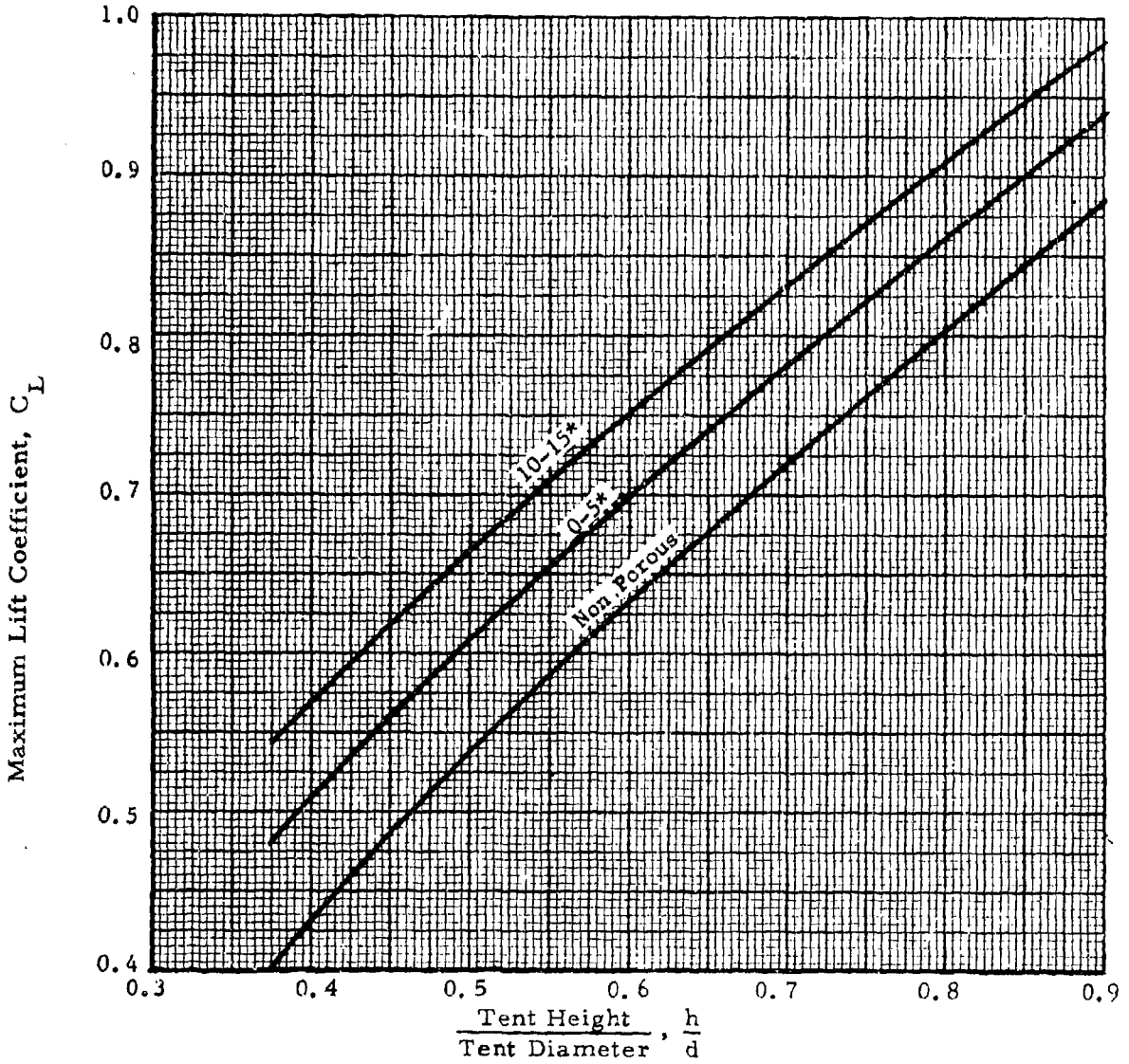

Figure 22. Variation of Lift Coefficient with Shape and Fabric Porosity (Spherical Single-Wall Tents)

MAXIMUM LIFT COEFFICIENT
SINGLE-WALL 1:2 CYLINDERS
(Hemispherical Ends)

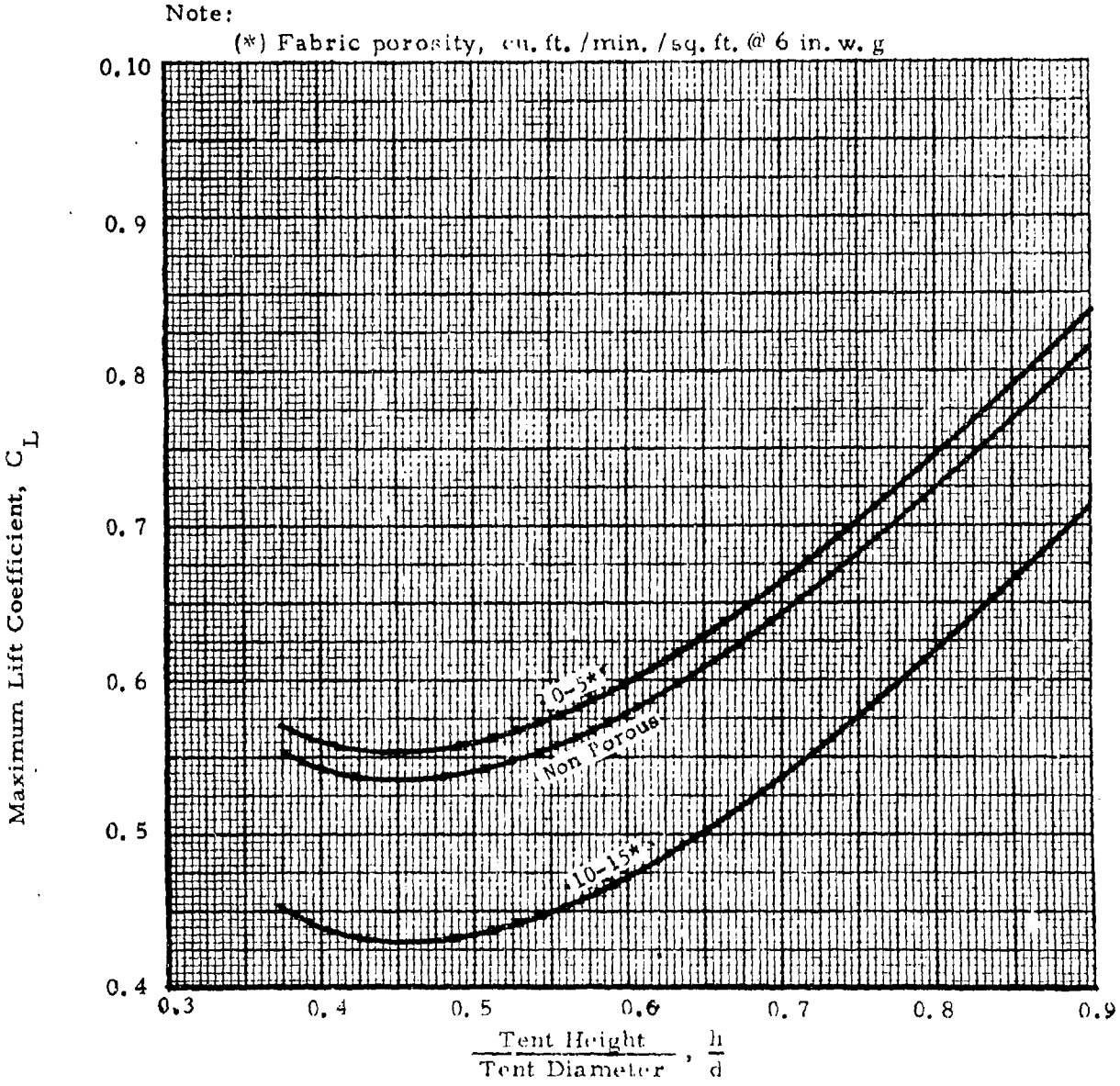

Figure 23. Variation of Lift Coefficient with Shape and Fabric Porosity (Cylindrical Single-Wall Tents; 1:2 W/ℓ_h)

MAXIMUM LIFT COEFFICIENT
SINGLE-WALL 1:4 CYLINDERS
(Hemispherical Ends)

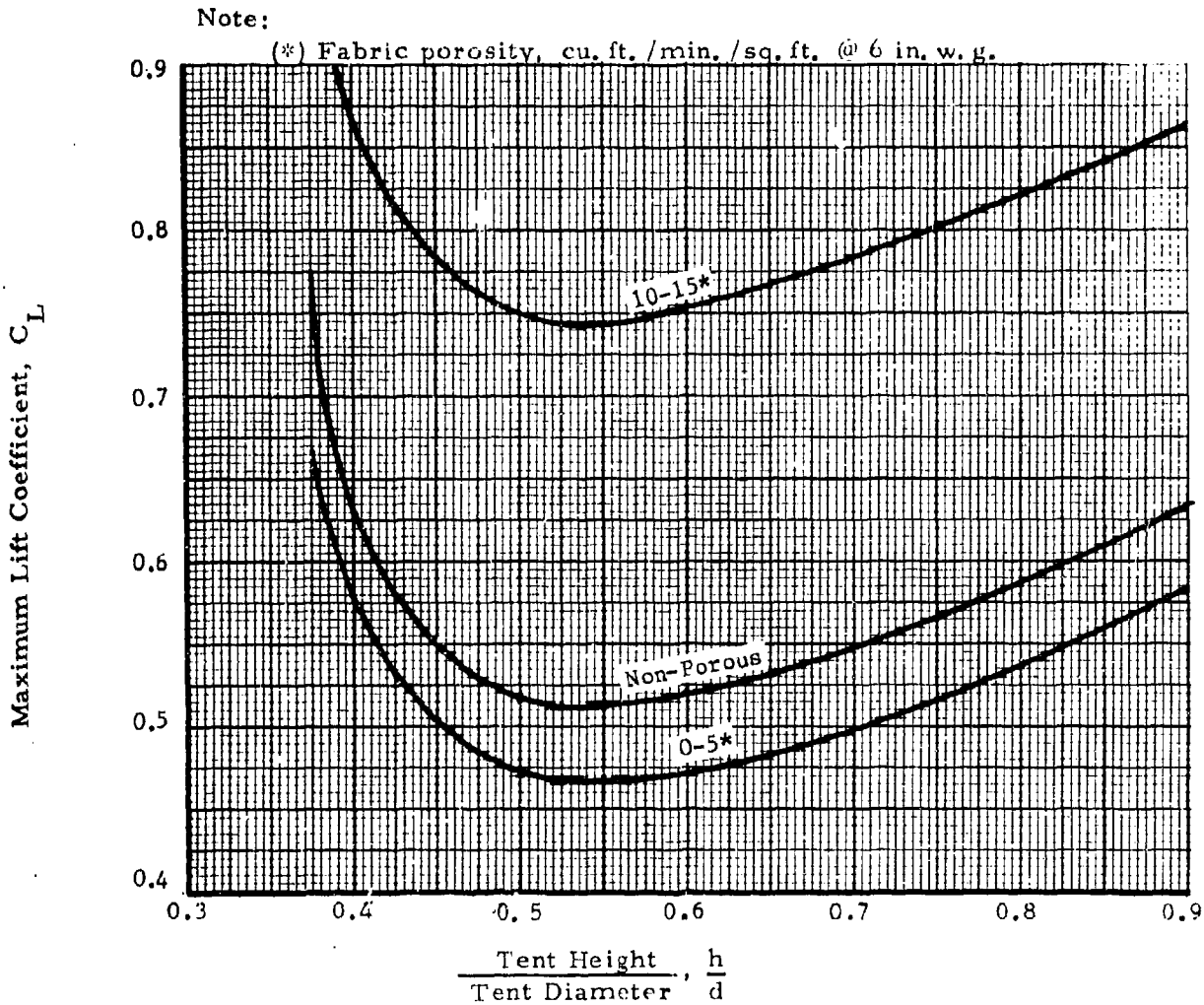

Figure 24. Variation of Lift Coefficient with Shape and Fabric Porosity (Cylindrical Single-Wall Tents, 1:4 W/ℓ_h)

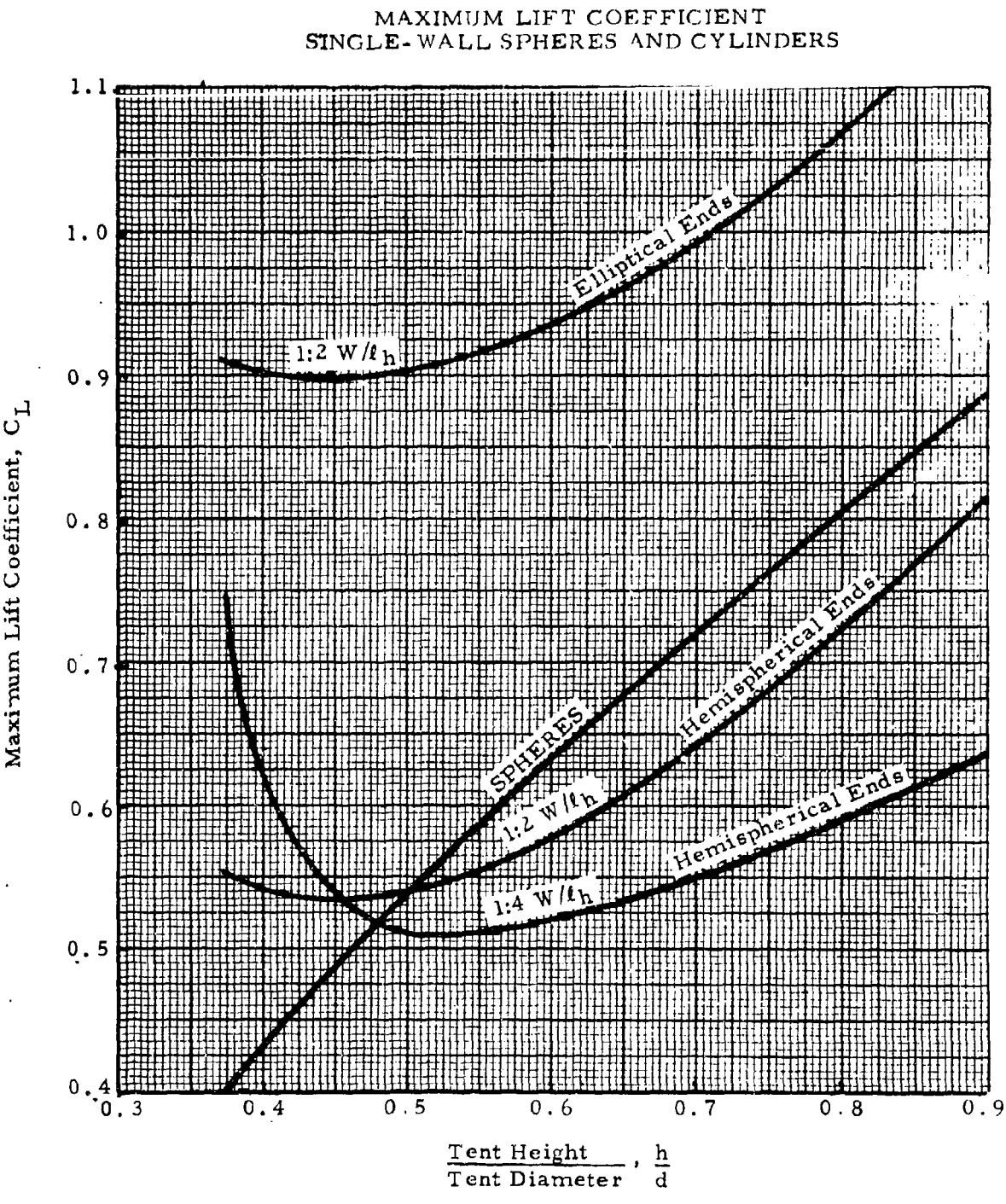

Figure 25. Variation of Lift Coefficient with Shape (Non-Porous Spherical and Cylindrical Single-Wall Tents; 1:2, 1:4, W/ℓ_h)

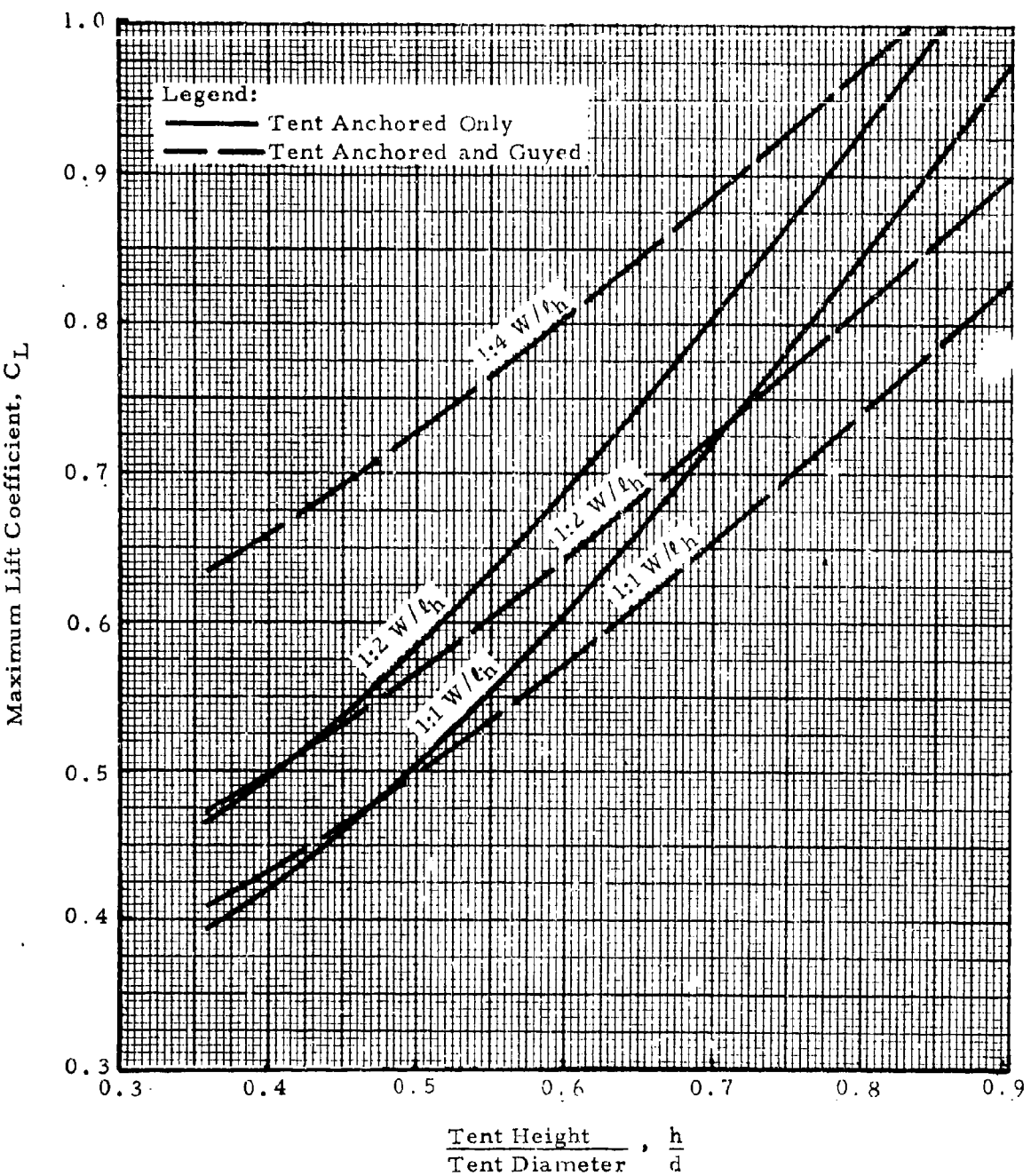

Figure 26. Variation of Lift Coefficient With Shape
(Non-Porous Double-Wall Tents; 1:1, 1:2, 1:4 W/ℓ_h)

MAXIMUM LIFT COEFFICIENT
DOUBLE-WALL CYLINDERS

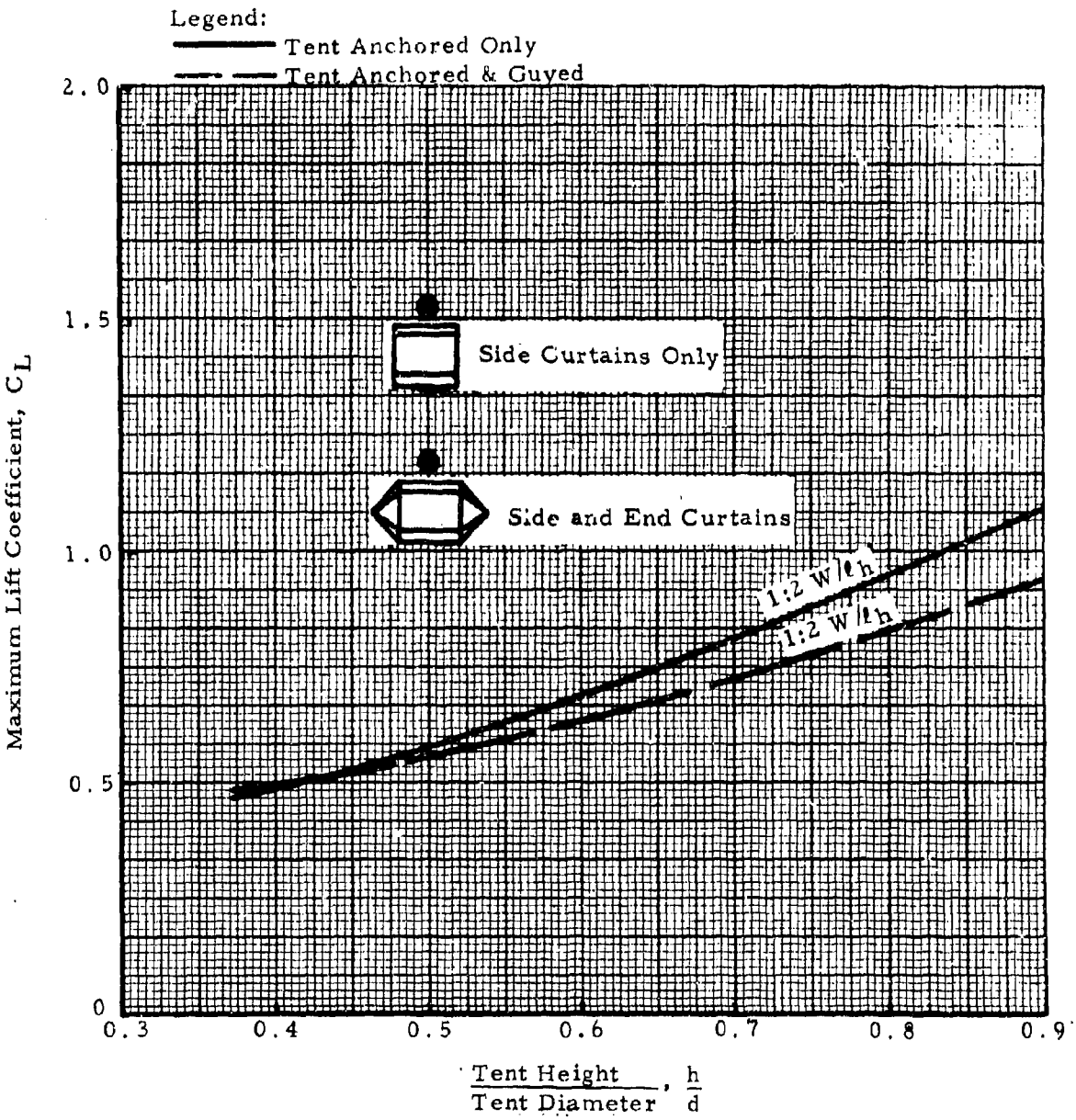

Figure 27. Variation of Lift Coefficient with Shape
(Non-Porous Double-Wall Tents; 1:2 W/ℓ_h)

MAXIMUM DRAG COEFFICIENT
SINGLE-WALL SPHERES

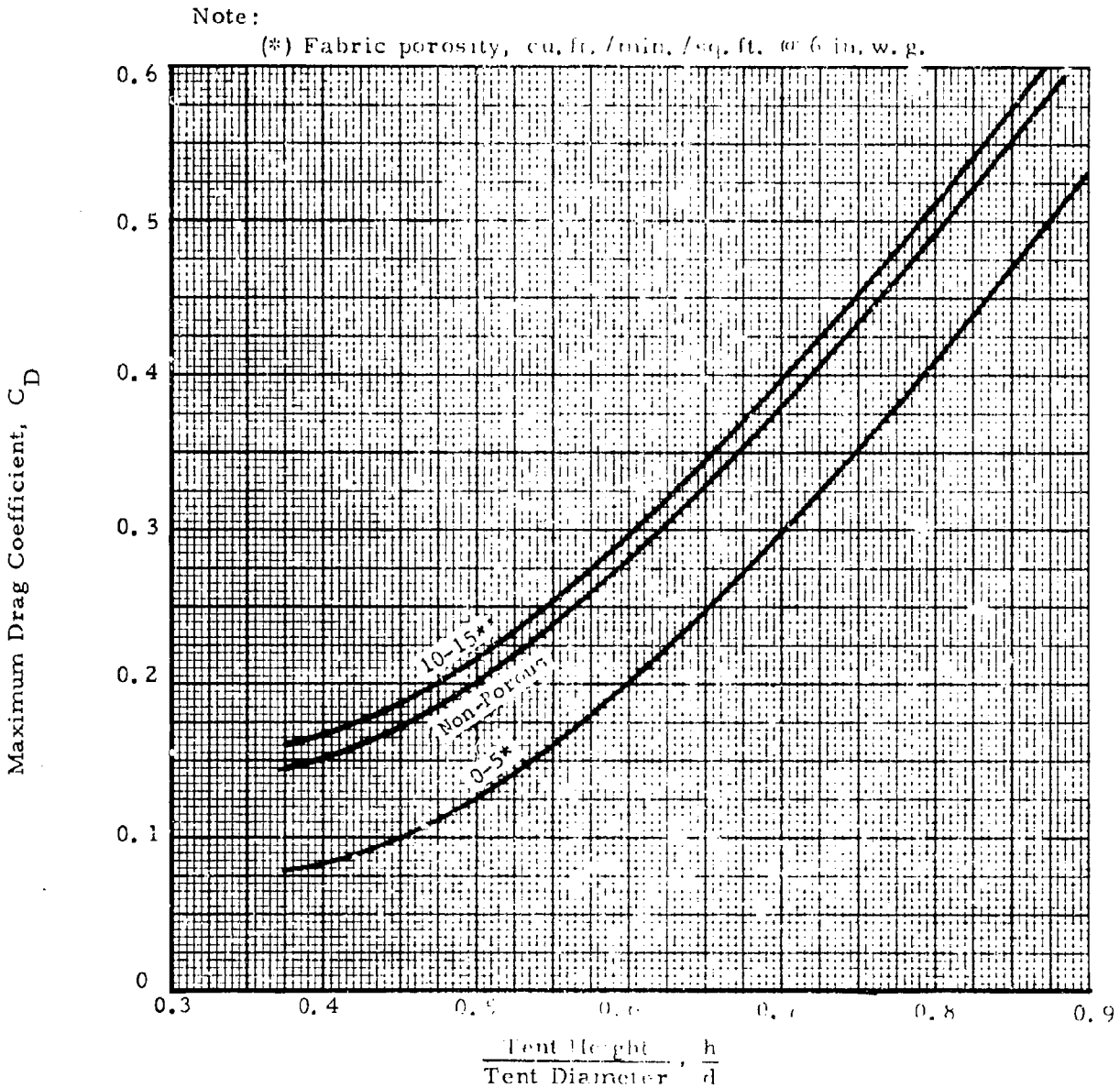

Figure 28. Variation of Drag Coefficient with Shape and Fabric Porosity (Spherical Single-Wall Tents)

MAXIMUM DRAG COEFFICIENT
SINGLE-WALL 1:2 CYLINDERS
(Hemispherical Ends)

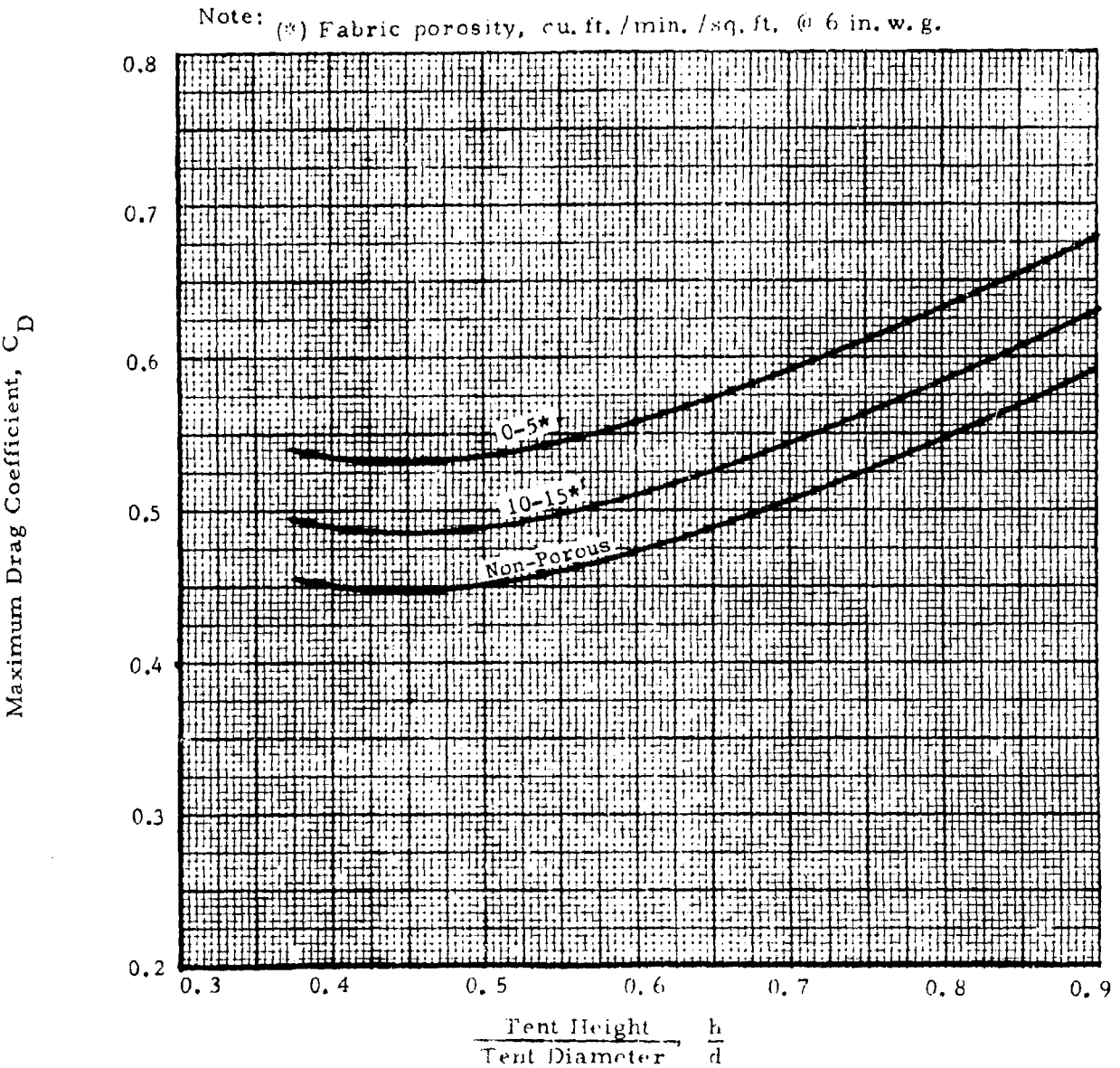

Figure 29. Variation of Drag Coefficient with Shape and Fabric Porosity (Cylindrical Single-Wall Tents, 1:2 W/ℓ_h)

MAXIMUM DRAG COEFFICIENT
SINGLE-WALL 1:4 CYLINDERS

(Hemispherical Ends)

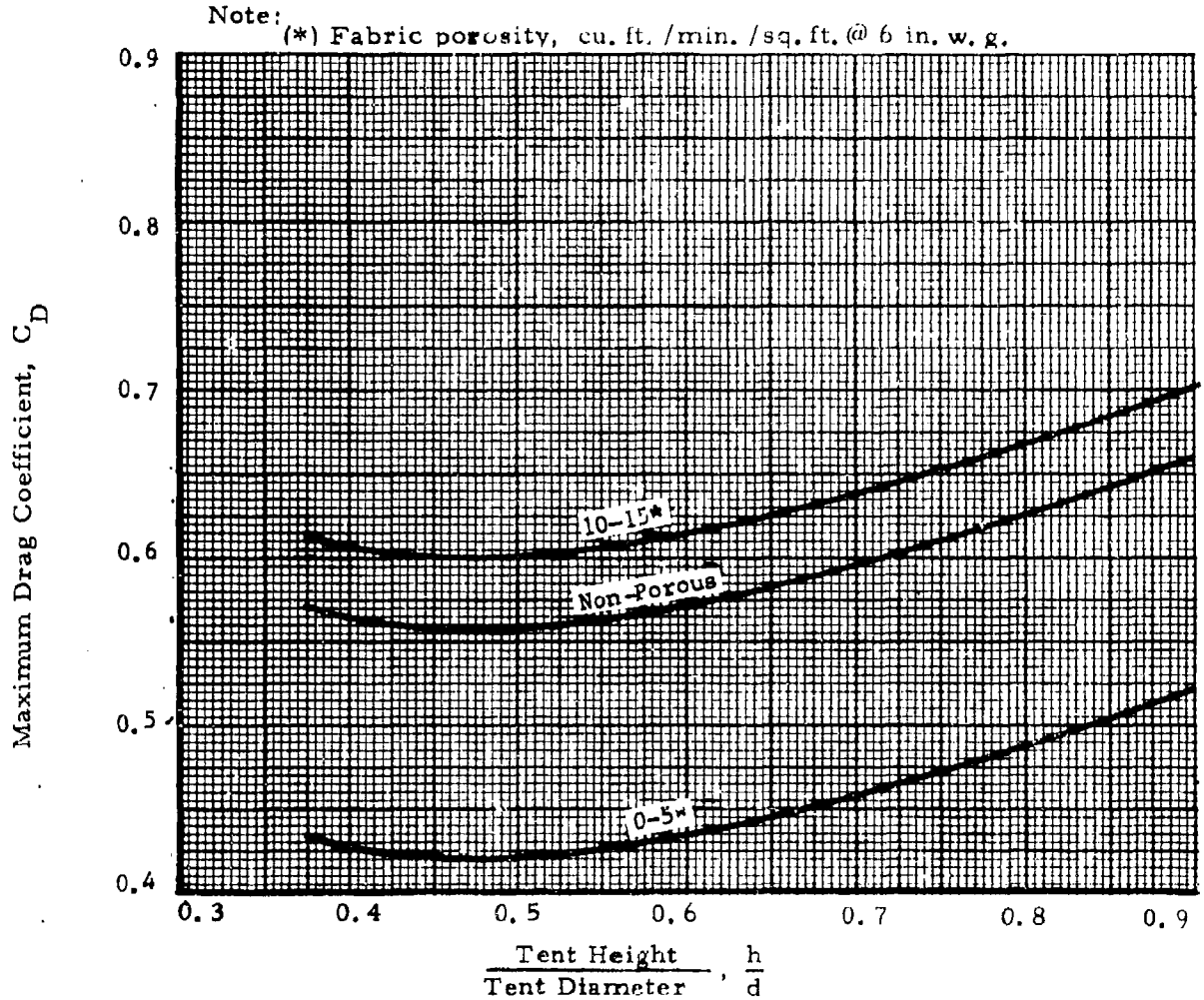

Figure 30. Variation of Drag Coefficient with Shape and Fabric Porosity (Cylindrical Single-Wall Tents, 1:4 W_h)

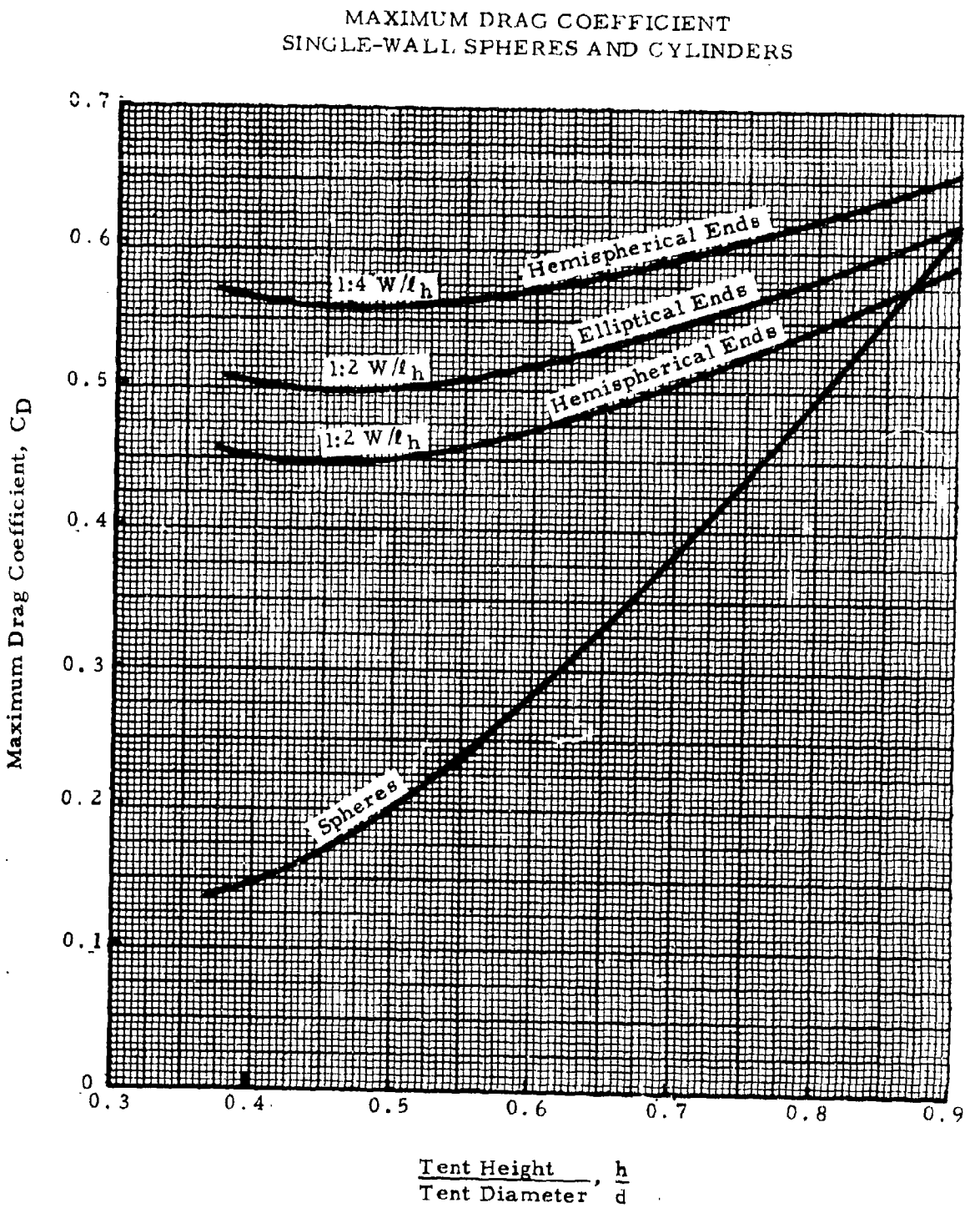

Figure 31. Variation of Drag Coefficient With Shape (Spherical and Cylindrical Single-Wall Tents; 1:2, 1:4 W/ℓ_h)

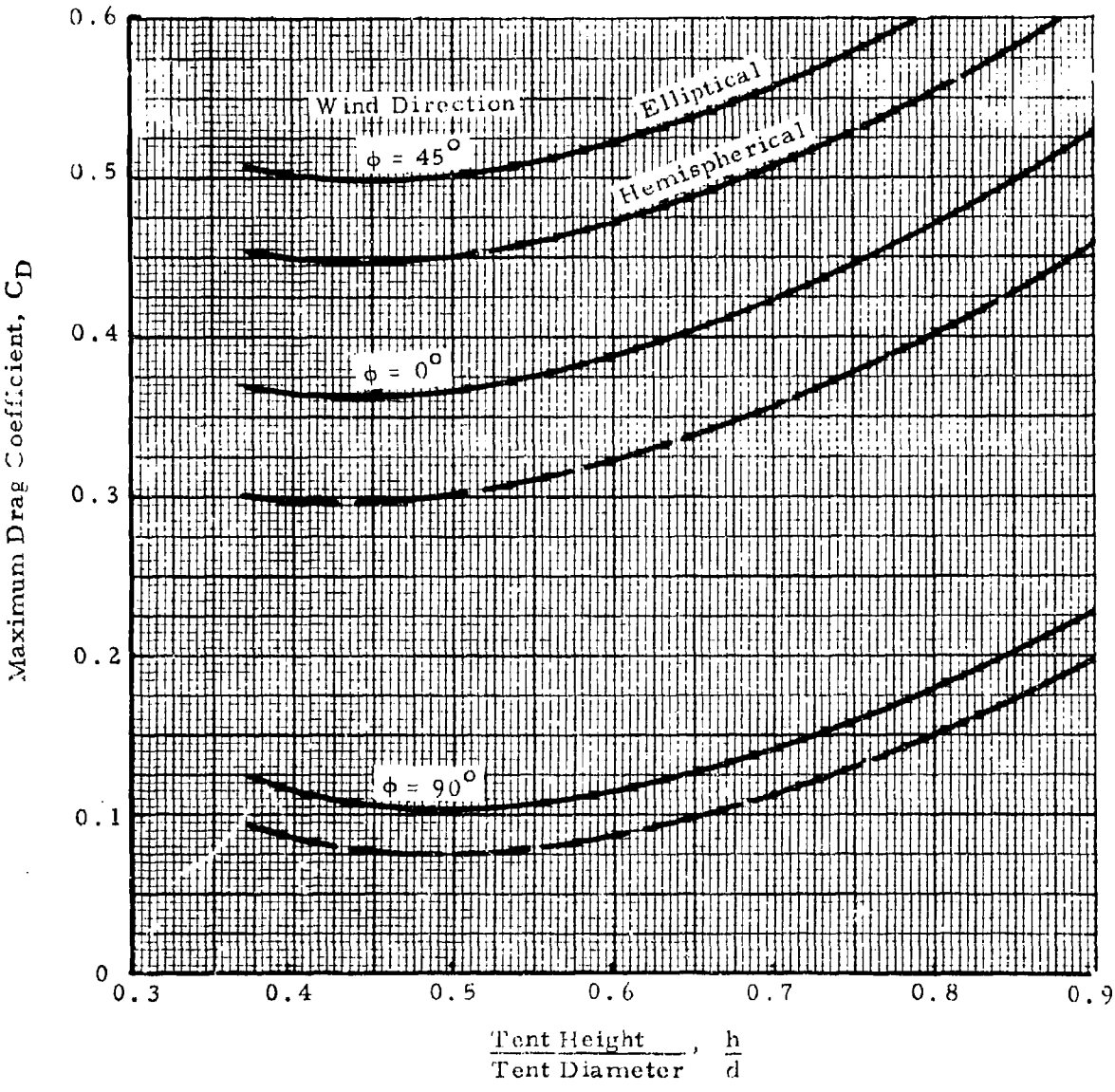

Figure 32. Variation of Drag Coefficient with Shape and Wind Direction; (Cylindrical Single-Wall Tents, 1:2 W/ℓ_h)

MAXIMUM DRAG COEFFICIENT
DOUBLE-WALL CYLINDERS

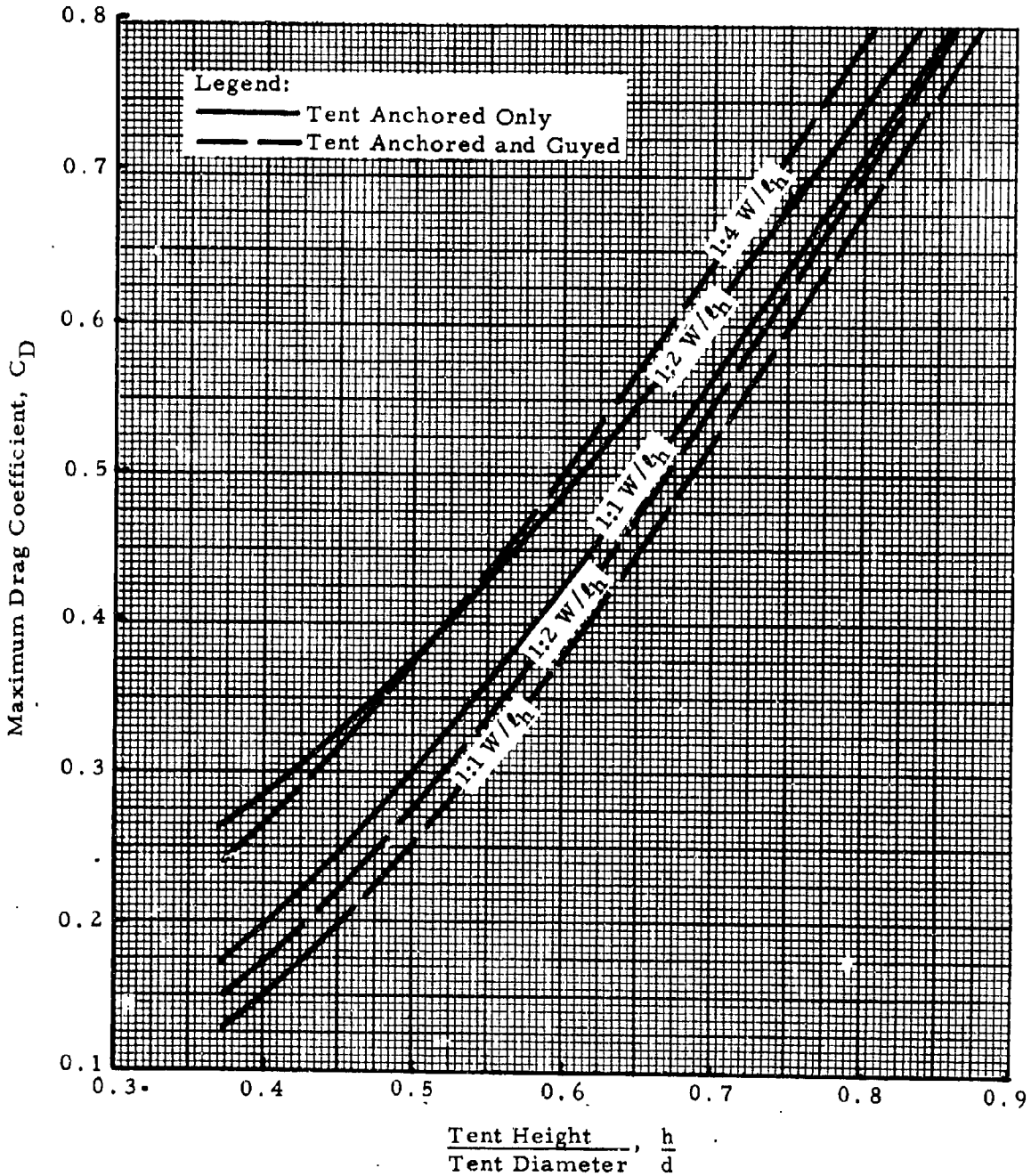

Figure 33. Variation of Drag Coefficient with Shape
(Non-Porous Double-Wall Tents; 1:1, 1:2, 1:4 W/ℓ_h)

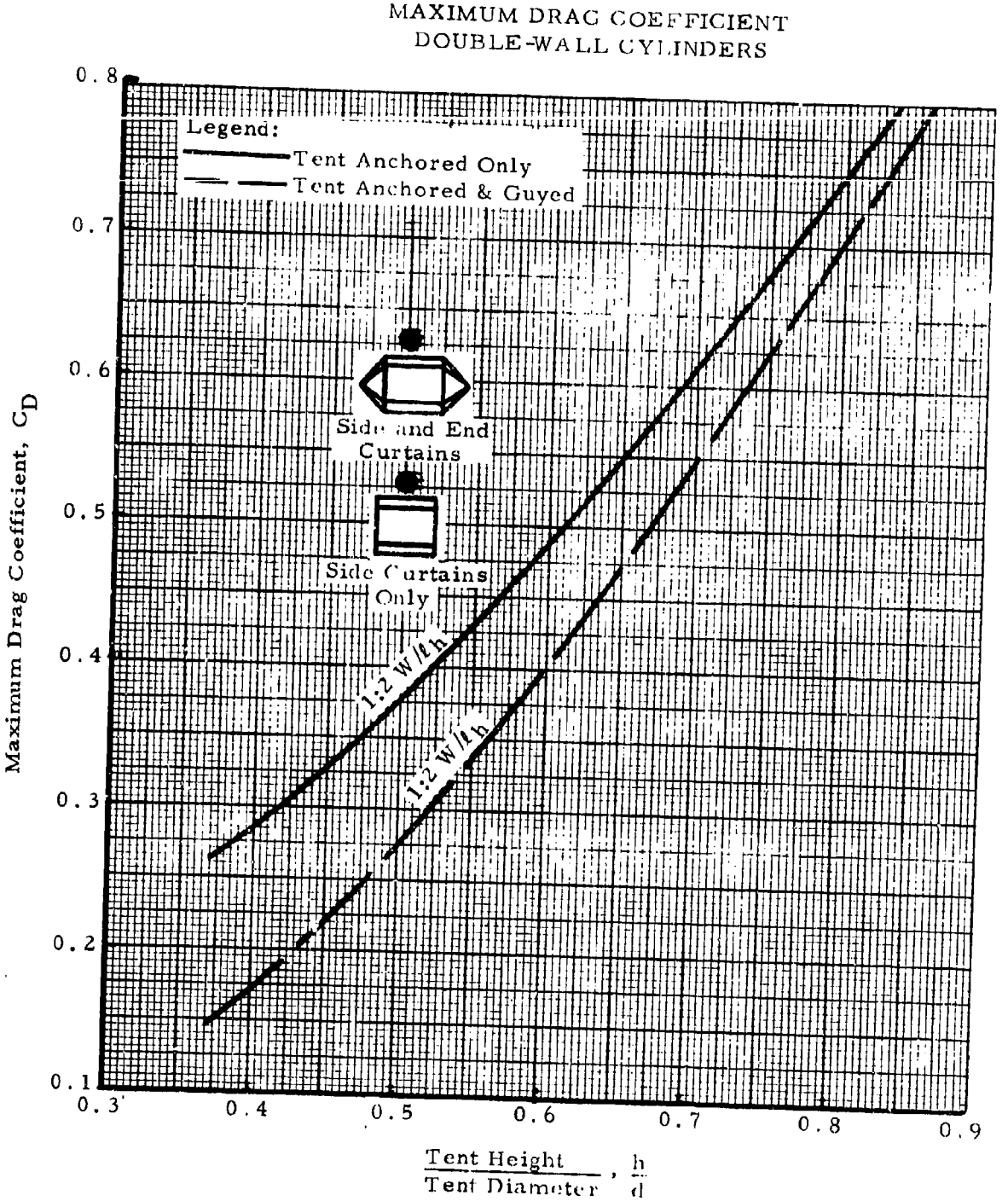

Figure 34. Variation of Drag Coefficient with Shape (Non-Porous Double-Wall Tents; 1:2 W/ℓ_h)

MAXIMUM MOMENT COEFFICIENT
SINGLE-WALL SPHERES

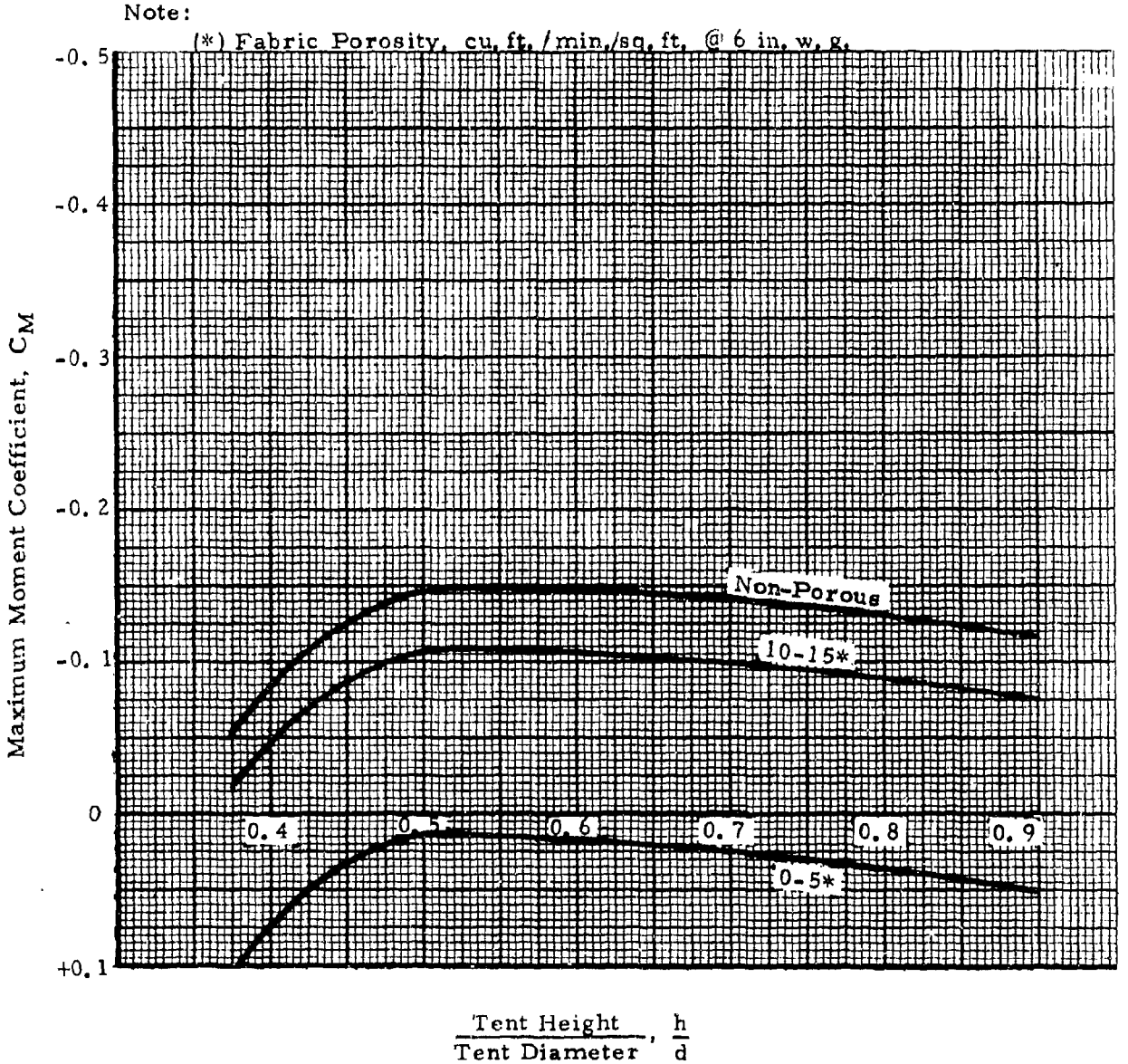

Figure 35. Variation of Moment Coefficient with Shape and Fabric Porosity (Spherical Single-Wall Tents)

MAXIMUM MOMENT COEFFICIENT
SINGLE-WALL 1:2 CYLINDERS
(Hemispherical Ends)

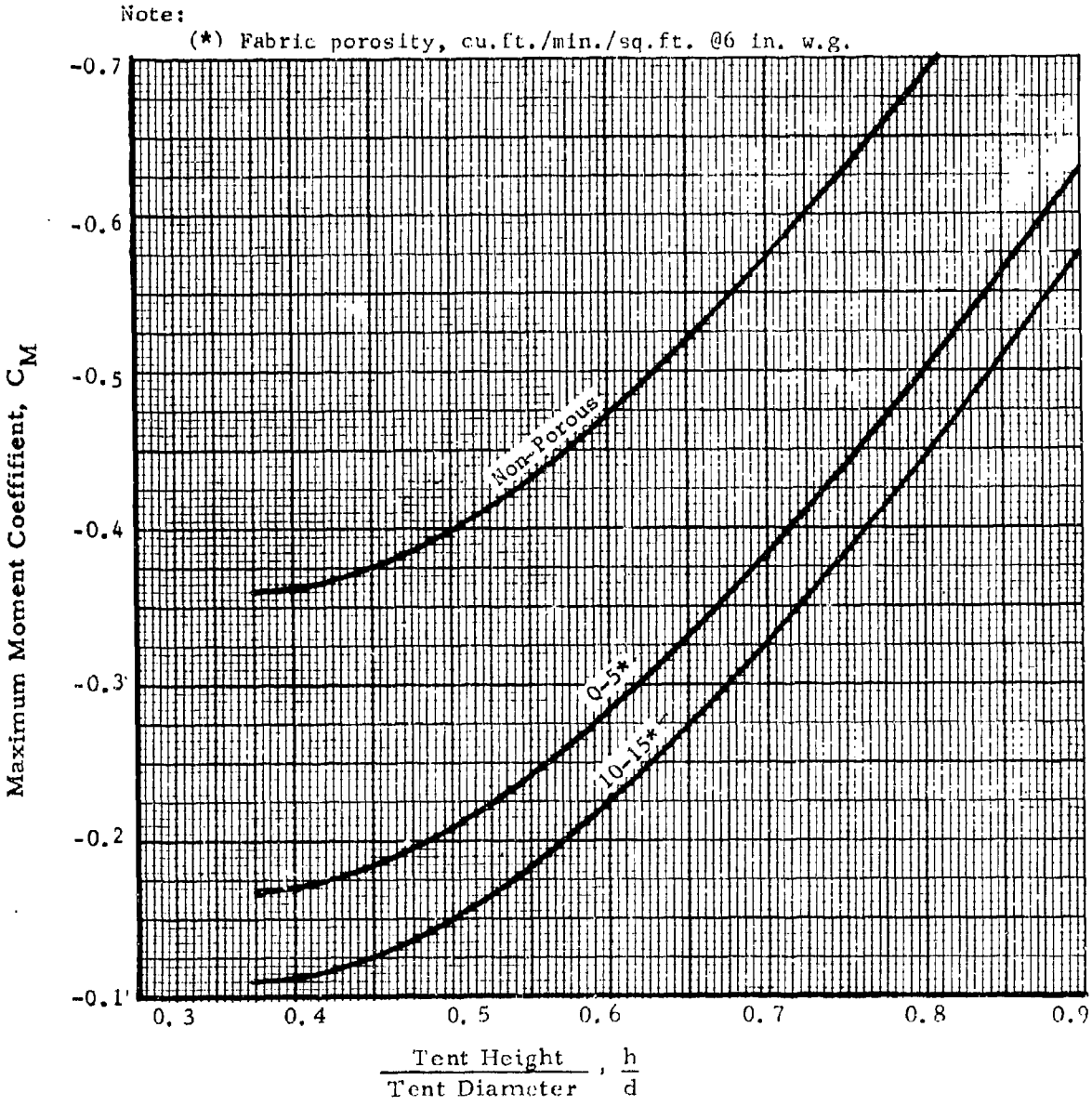

Figure 36. Variation of Moment Coefficient with Shape and Fabric Porosity (Cylindrical Single-Wall Tents, 1:2 W/l_h)

MAXIMUM MOMENT COEFFICIENT
SINGLE-WALL 1:4 CYLINDERS
(Hemispherical Ends)

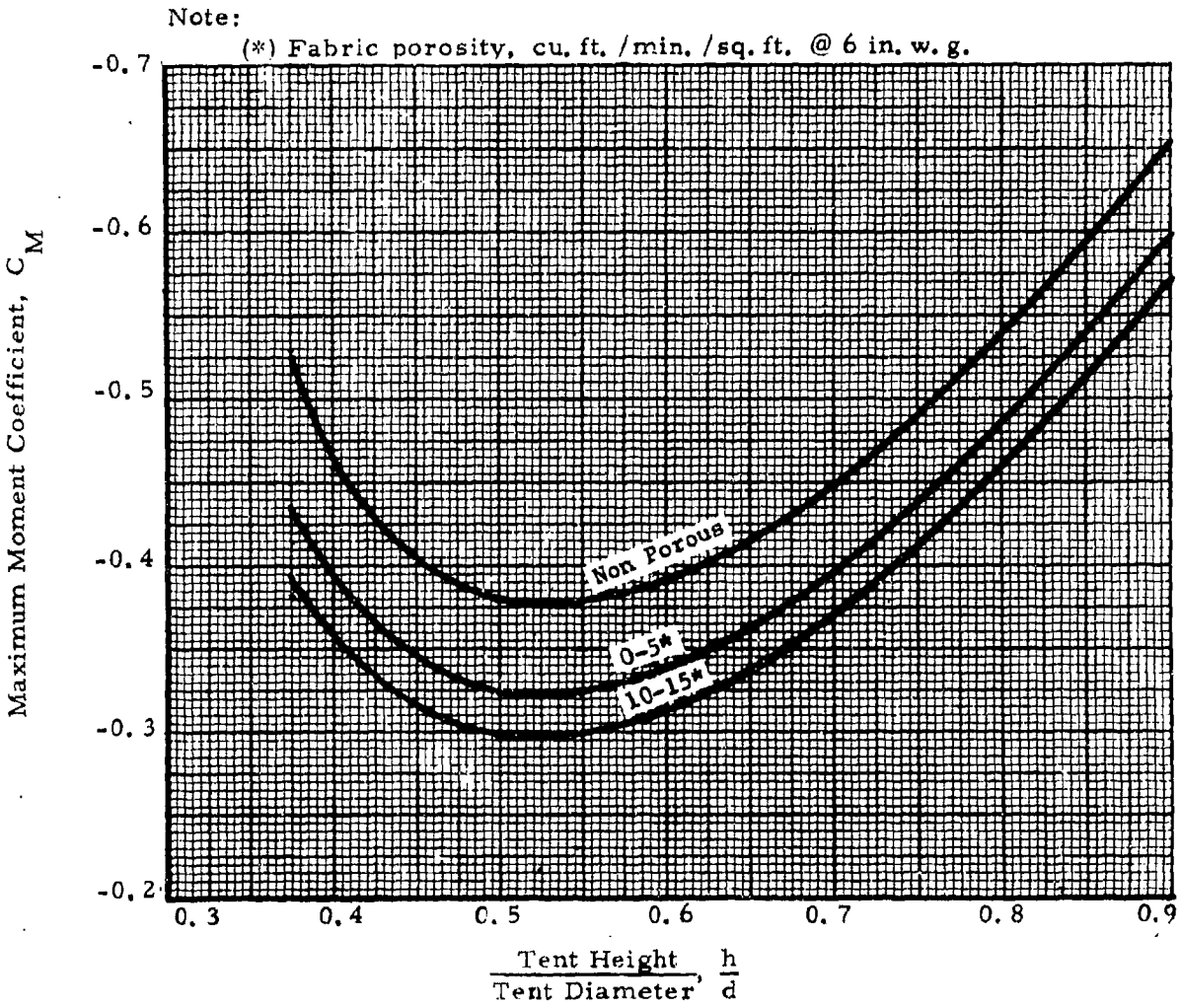

Figure 37. Variation of Moment Coefficient with Shape and Fabric Porosity (Cylindrical Single-Wall Tents, 1:4 $W/_h$)

MAXIMUM MOMENT COEFFICIENT
SINGLE-WALL SPHERES AND CYLINDERS

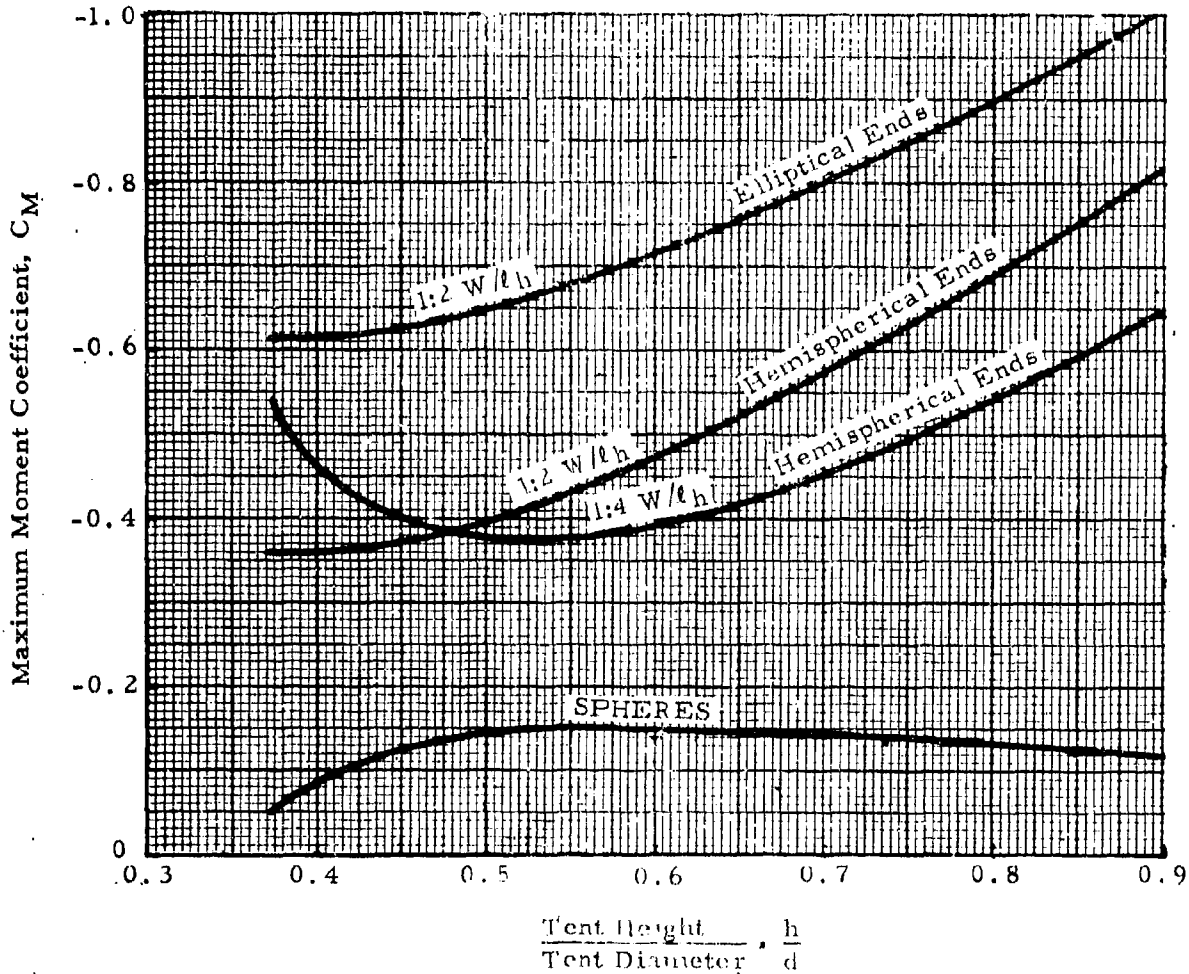

Figure 38. Variation of Moment Coefficient with Shape (Spherical and Cylindrical Single-Wall Tents; 1:2, 1:4, W/ℓ_h)

MAXIMUM MOMENT COEFFICIENT
DOUBLE-WALL CYLINDERS

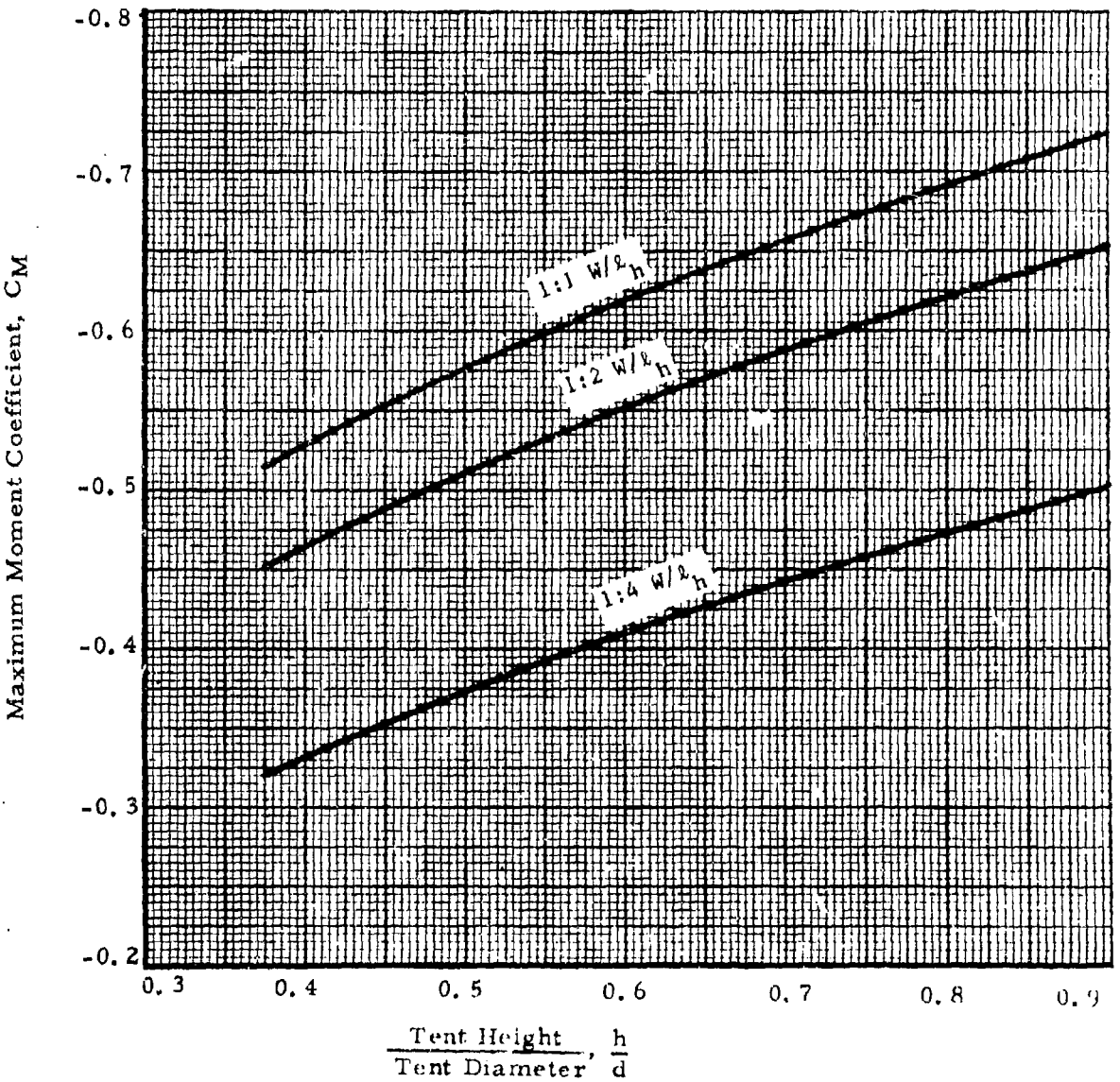

Figure 39. Variation of Moment Coefficient with Shape (Non-Porous Double-Wall Tents; 1:1, 1:2, 1:4, W/ℓ_h)

MAXIMUM MOMENT COEFFICIENT
DOUBLE-WALL CYLINDERS

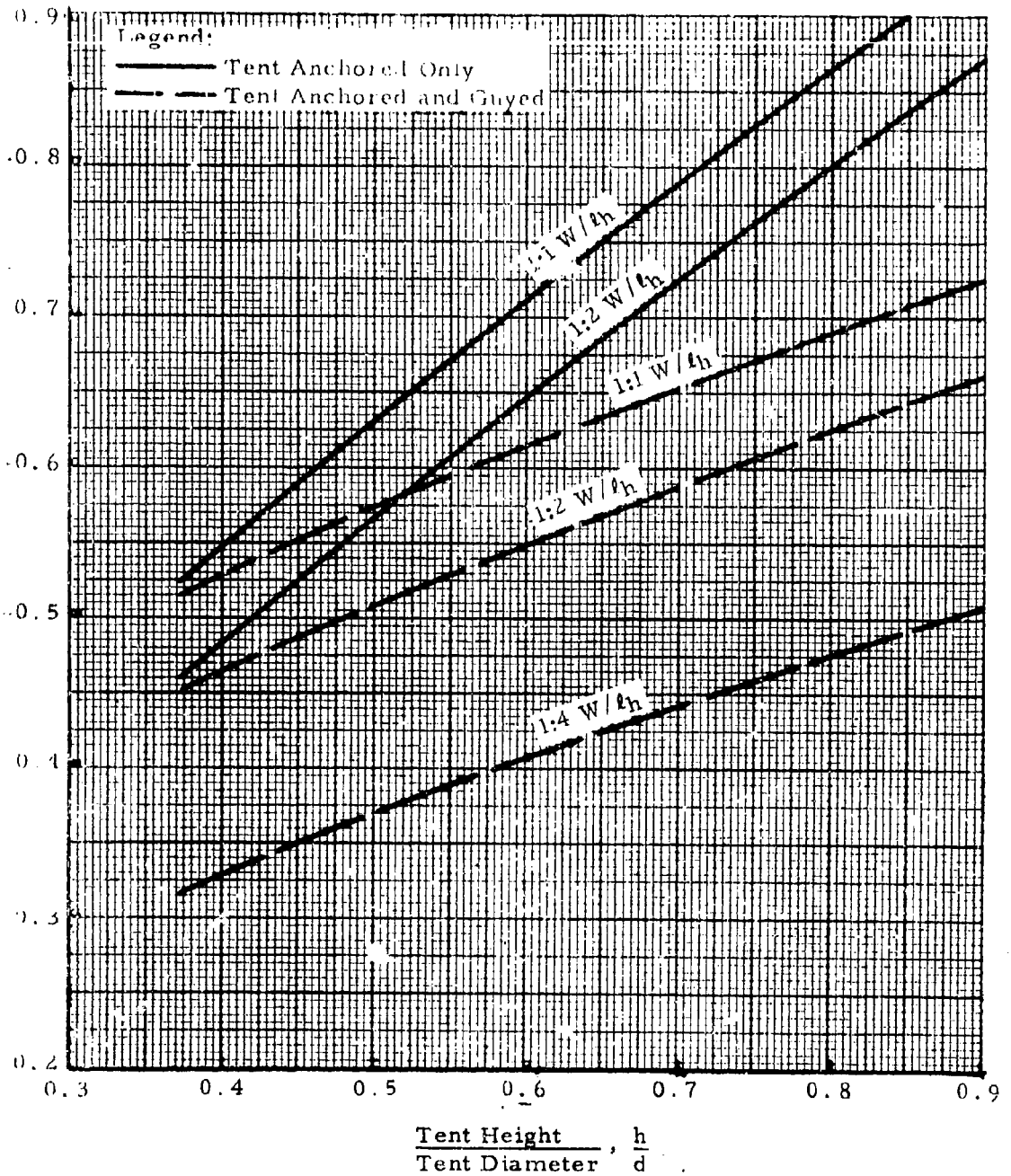

Figure 40. Variation of Moment Coefficient with Shape & Guying (Non-Porous Double-Wall Tents; 1:1, 1:2, 1:4 W/ℓ_h)

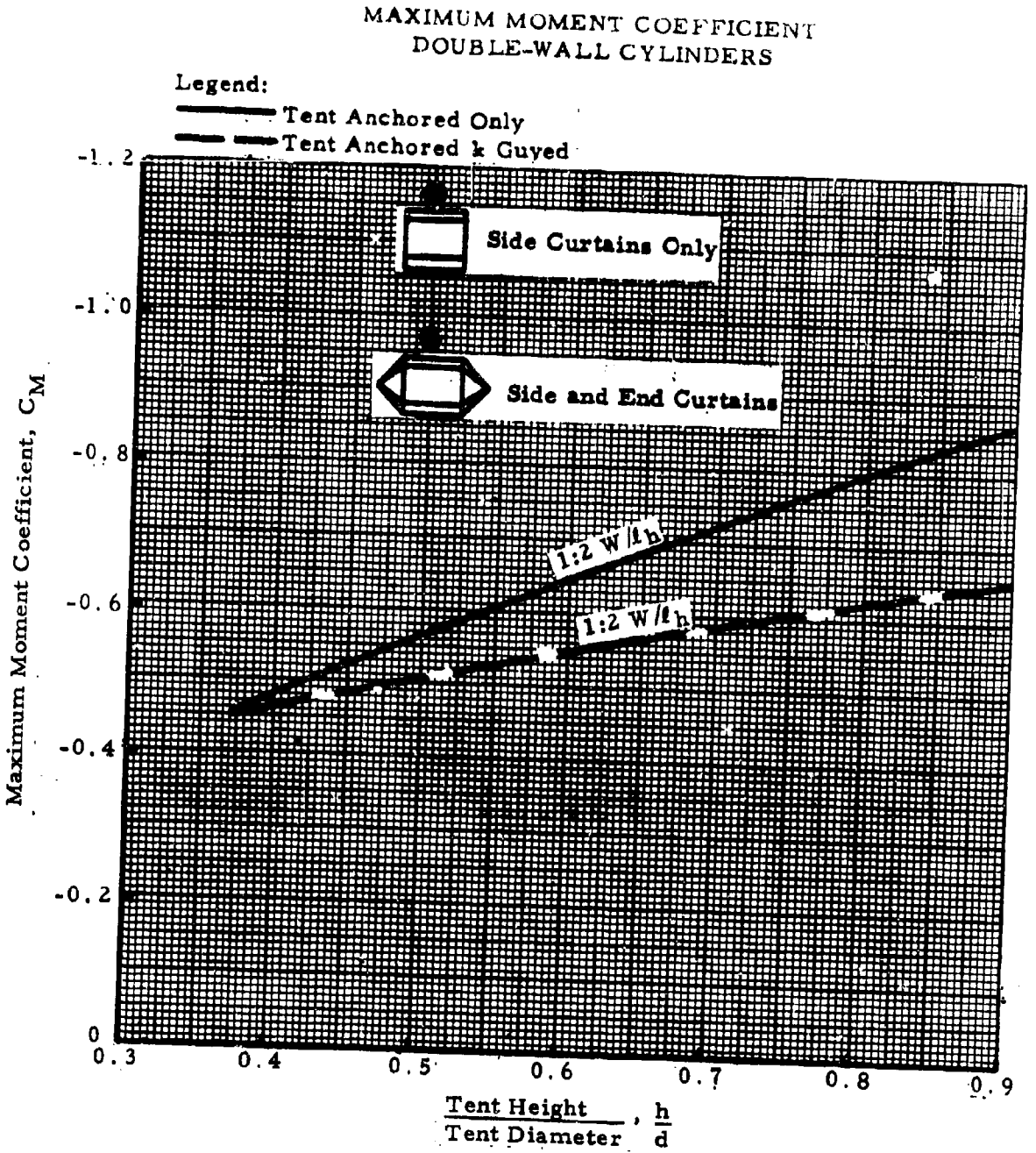

Figure 41. Variation of Moment Coefficient with Shape (Non-Porous Double-Wall Tents; 1:? W/ℓ_h)

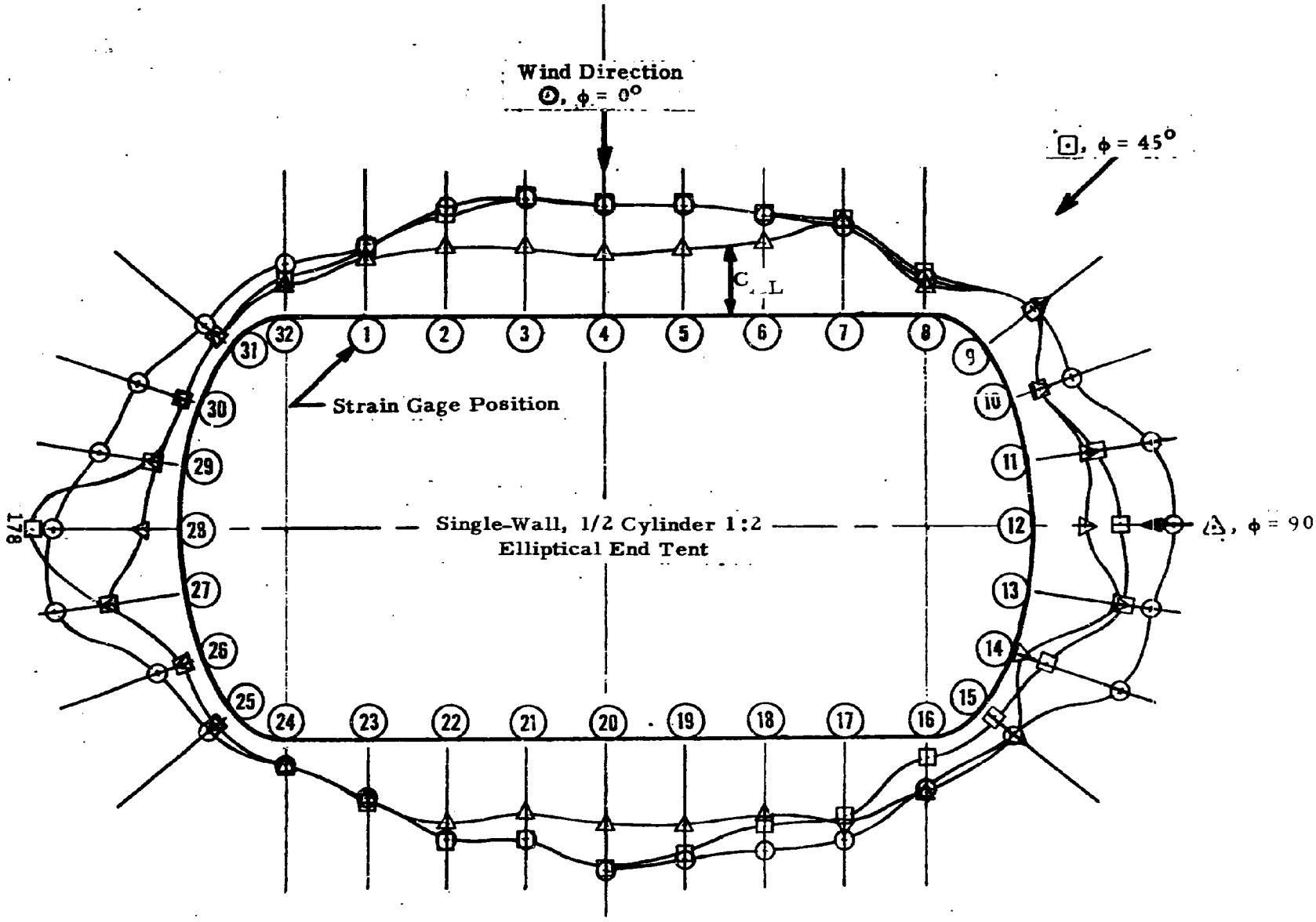

Figure 42. Variation of Individual Anchor Load Coefficient with Wind Direction, Single-Wall Tents

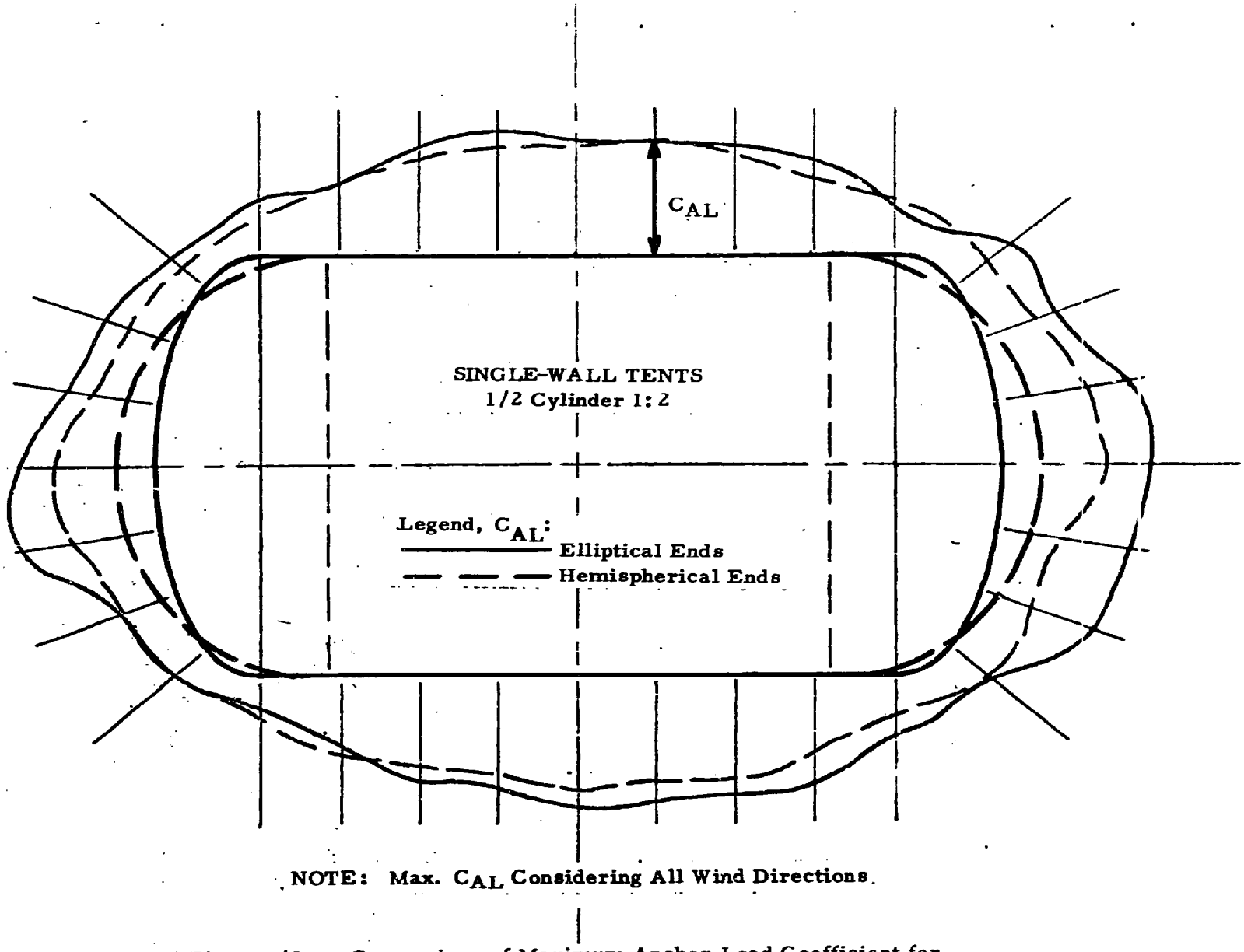

NOTE: Max. C_{AL} Considering All Wind Directions.

Figure 43. Comparison of Maximum Anchor Load Coefficient for Single-Wall Tents with Elliptical and Hemispherical Ends

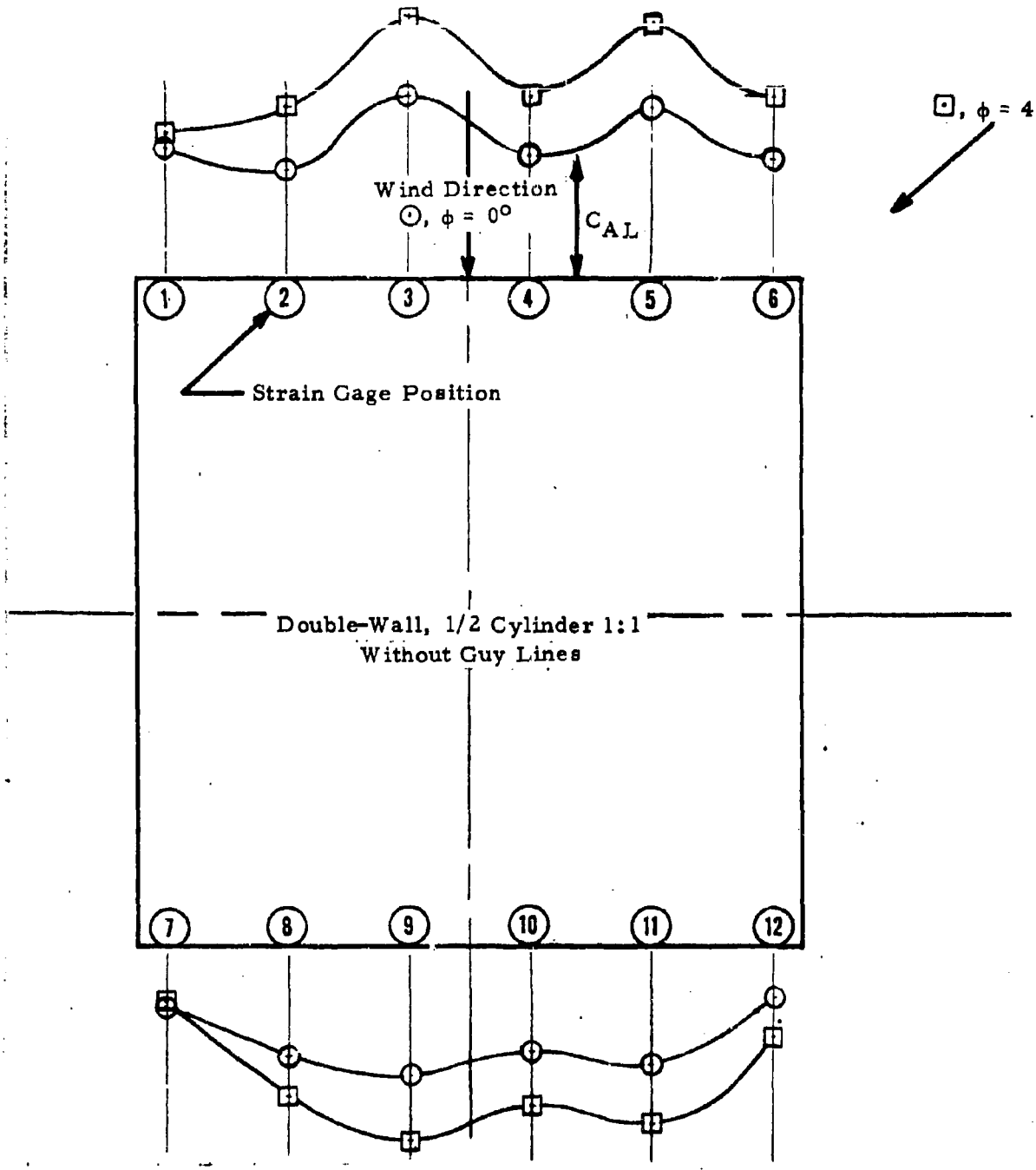

Figure 44. Variation of Anchor Load Coefficient with Wind Direction, Double-Wall Tents

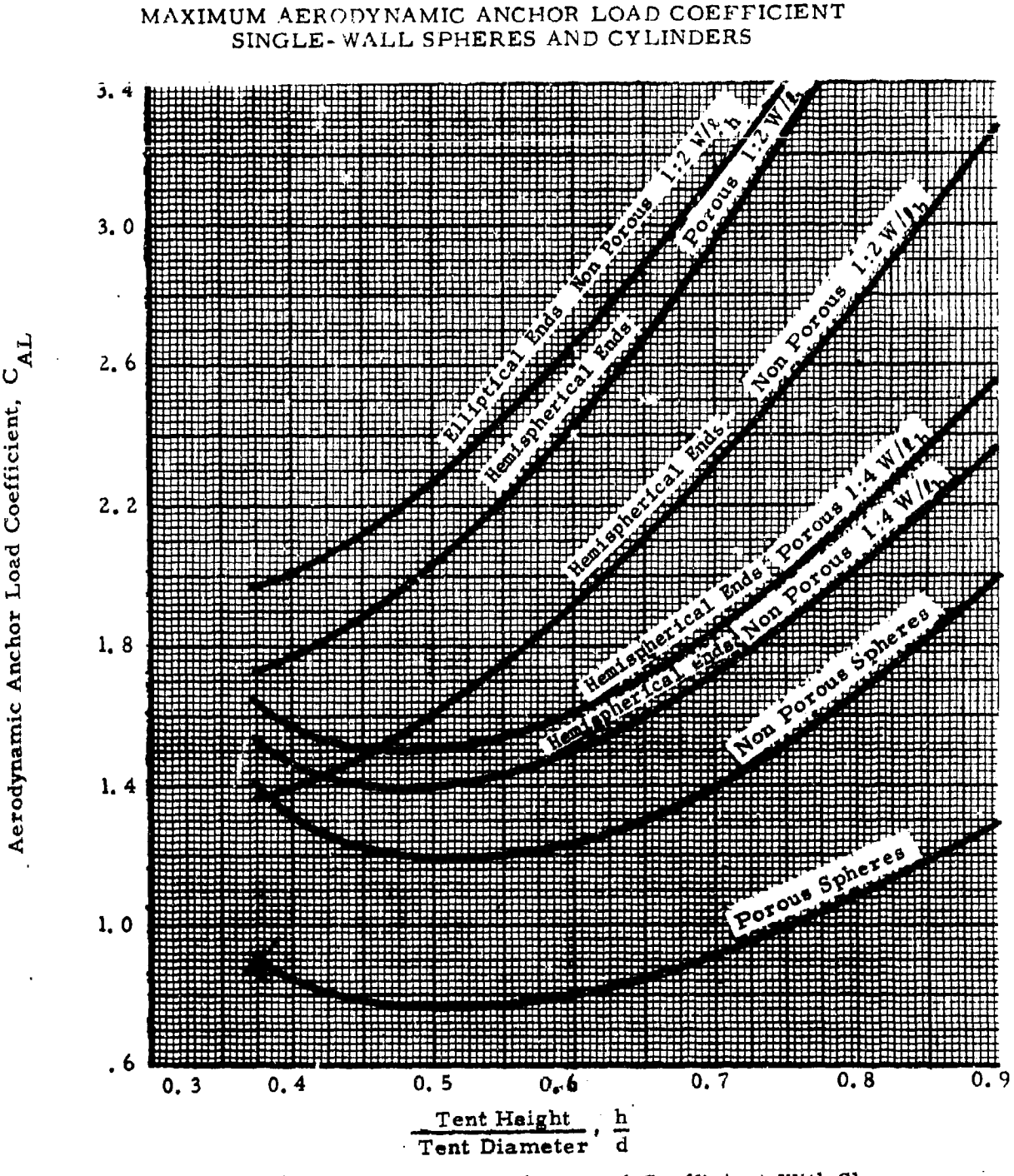

Figure 45. Variation of Anchor Load Coefficient With Shape, Single-Wall Tents

MAXIMUM BASE ANCHOR LOAD COEFFICIENTS
DOUBLE-WALL CYLINDERS

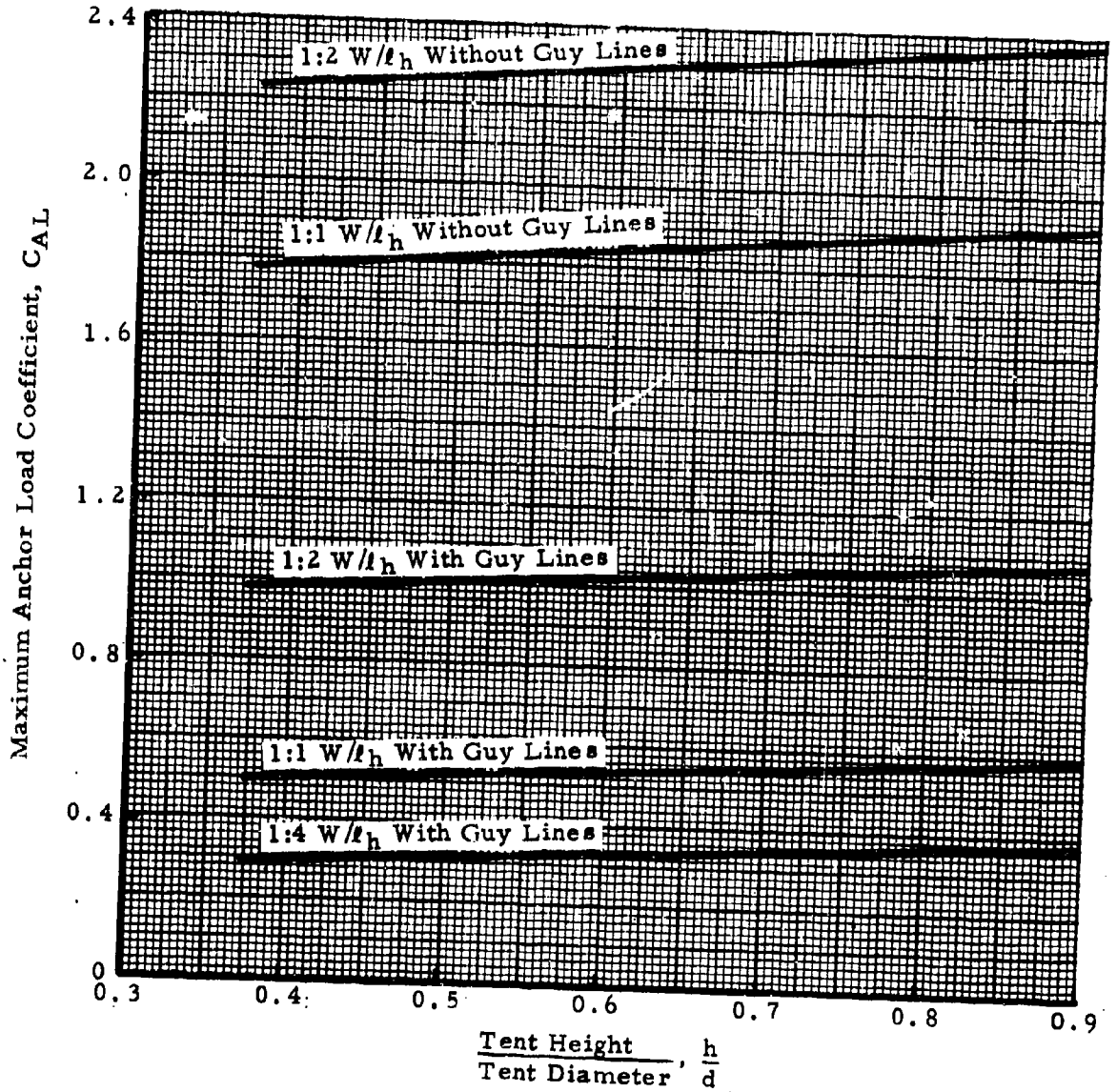

Figure 46. Variation of Base Anchor Load Coefficient with Shape, Double-Wall Tents

MAXIMUM BASE ANCHOR LOAD COEFFICIENTS
DOUBLE-WALL CYLINDERS

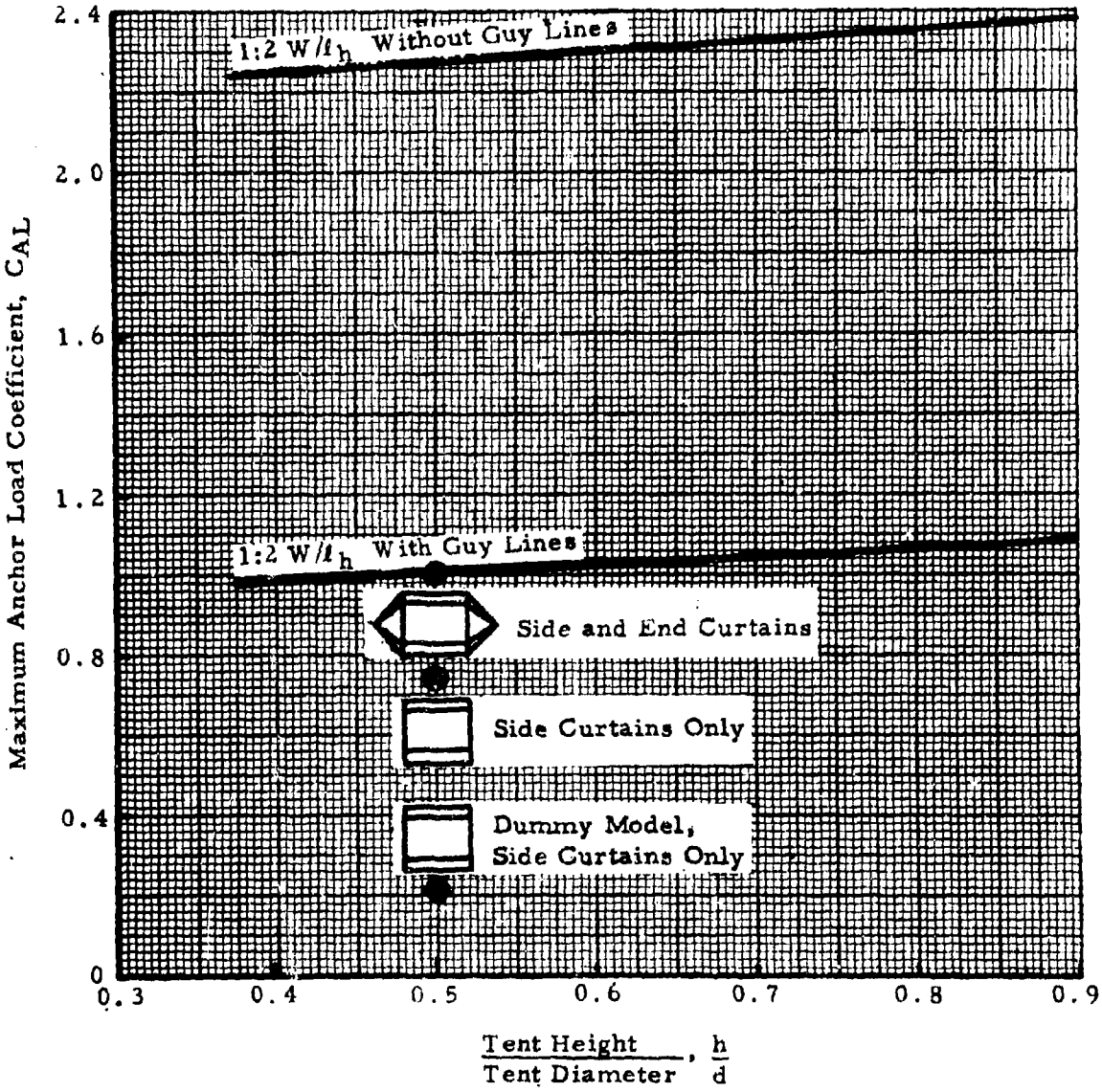

Figure 47. Variation of Base Anchor Load Coefficient with Shape, Double-Wall Tents

MAXIMUM GUY LINE LOAD COEFFICIENT
DOUBLE-WALL CYLINDER

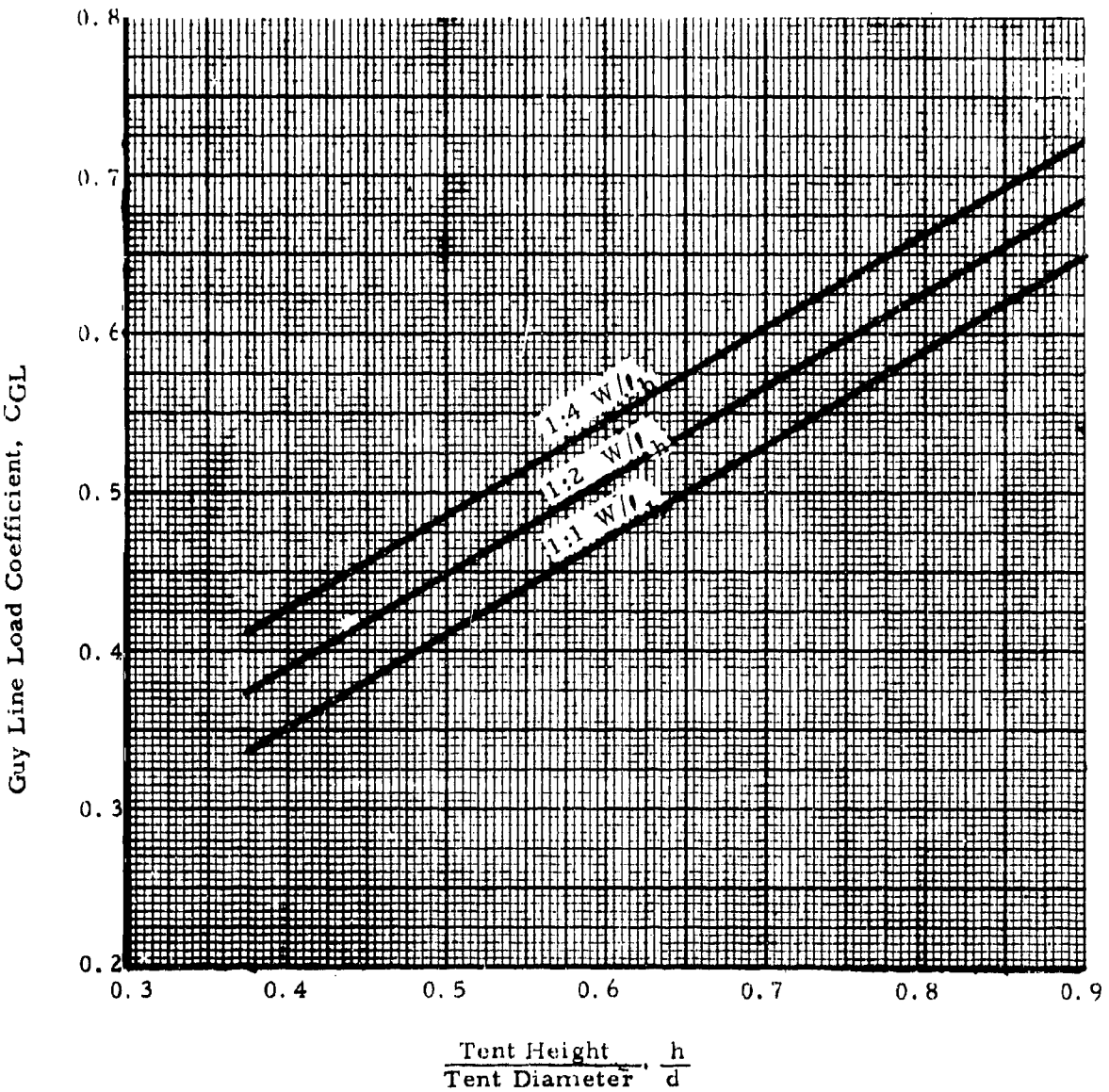

Figure 48 . Variation of Guy Line Load Coefficient With Shape

MAXIMUM GUY LINE LOAD COEFFICIENT
DOUBLE-WALL CYLINDER

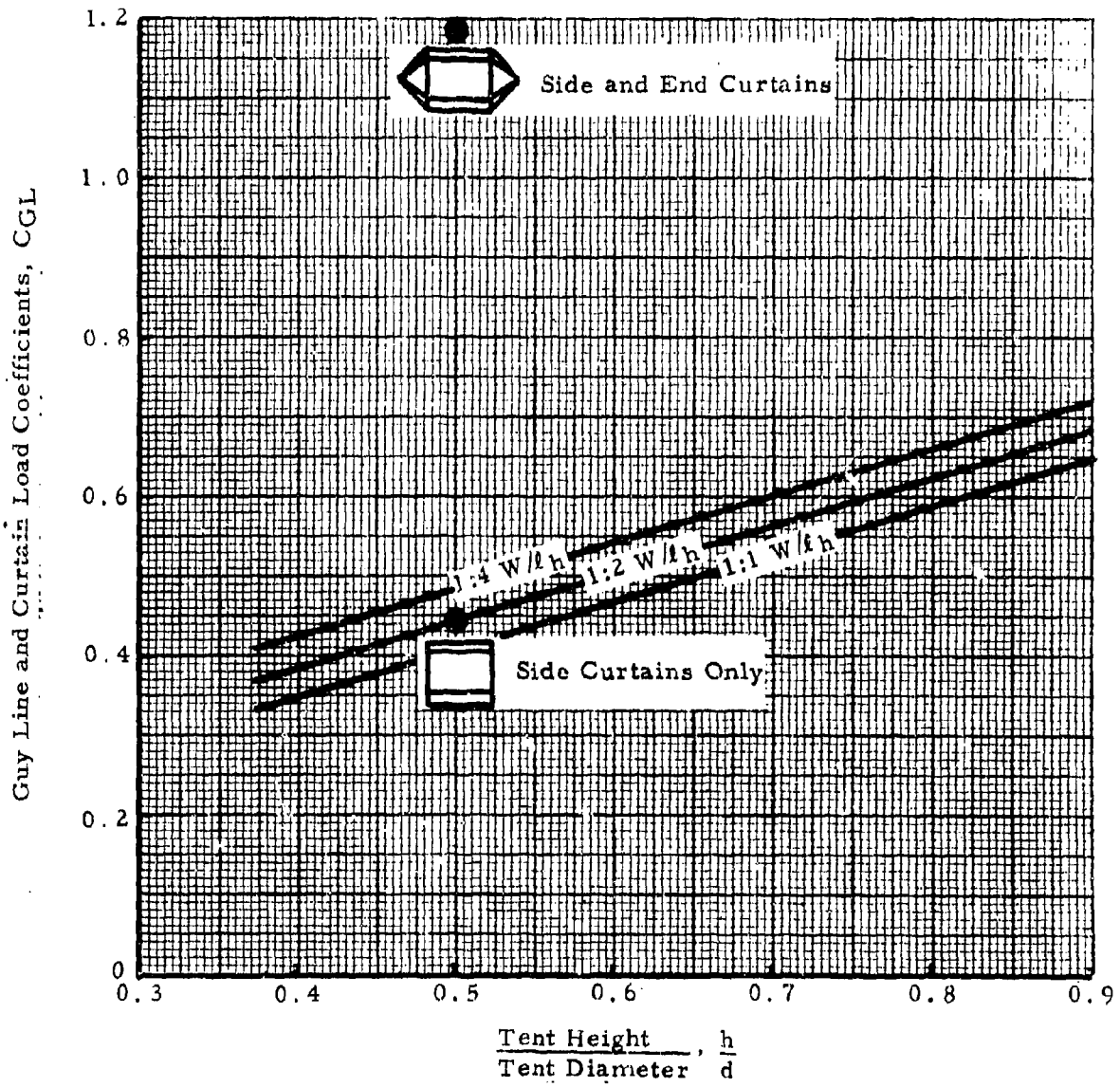

Figure 49. Variation of Guy Line Load Coefficient with Shape

MAXIMUM TENT DEFLECTION
SINGLE-WALL SPHERES

Note:
(*) Fabric porosity, cu. ft. / min. / sq. ft. @ 6 in. w. g.

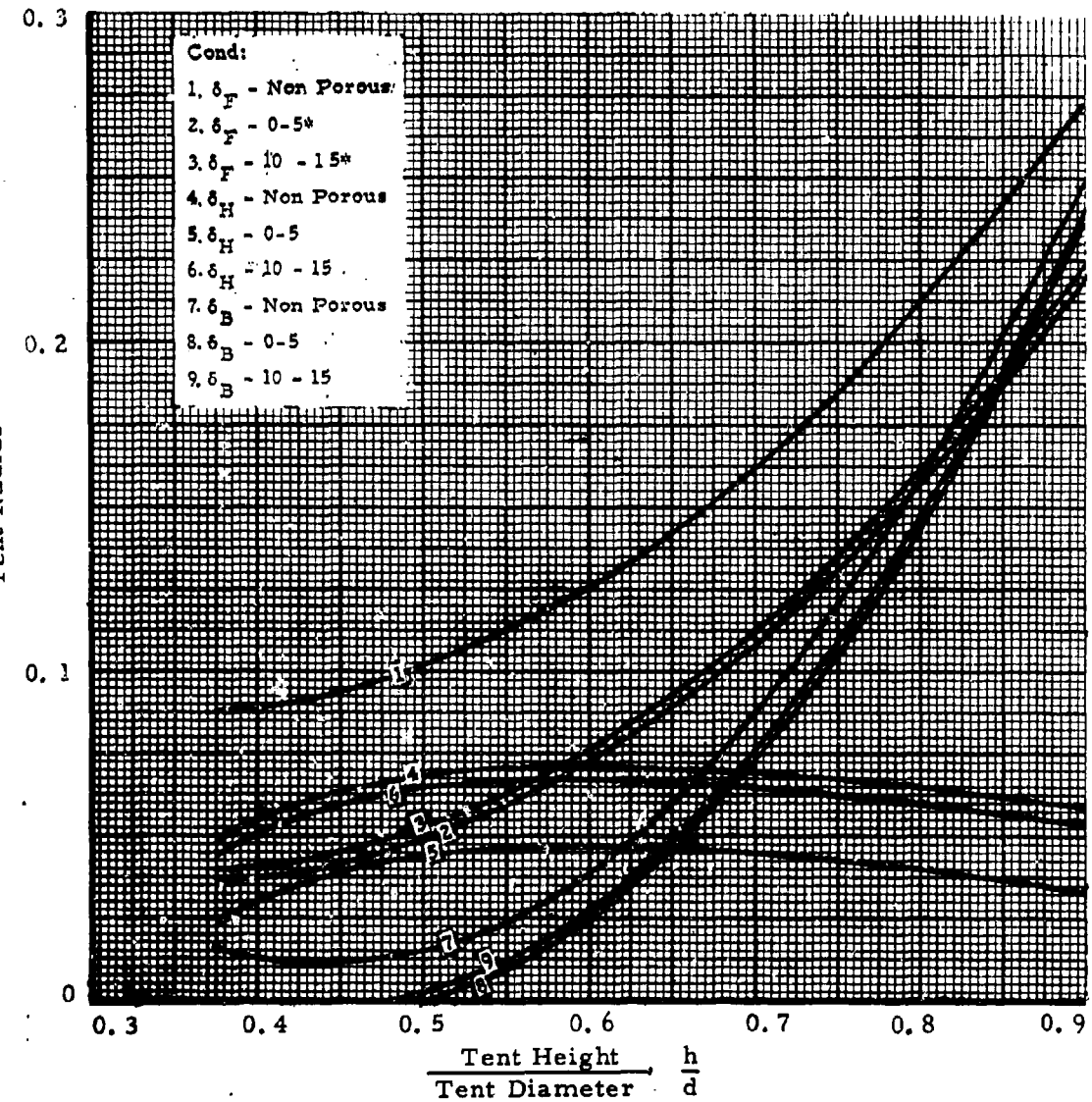

Figure 50. Variation of Tent Deflection with Shape and Fabric Porosity (Spherical Single-Wall Tents)

MAXIMUM TENT DEFLECTION
SINGLE-WALL 1:2 CYLINDERS
(Hemispherical Ends)

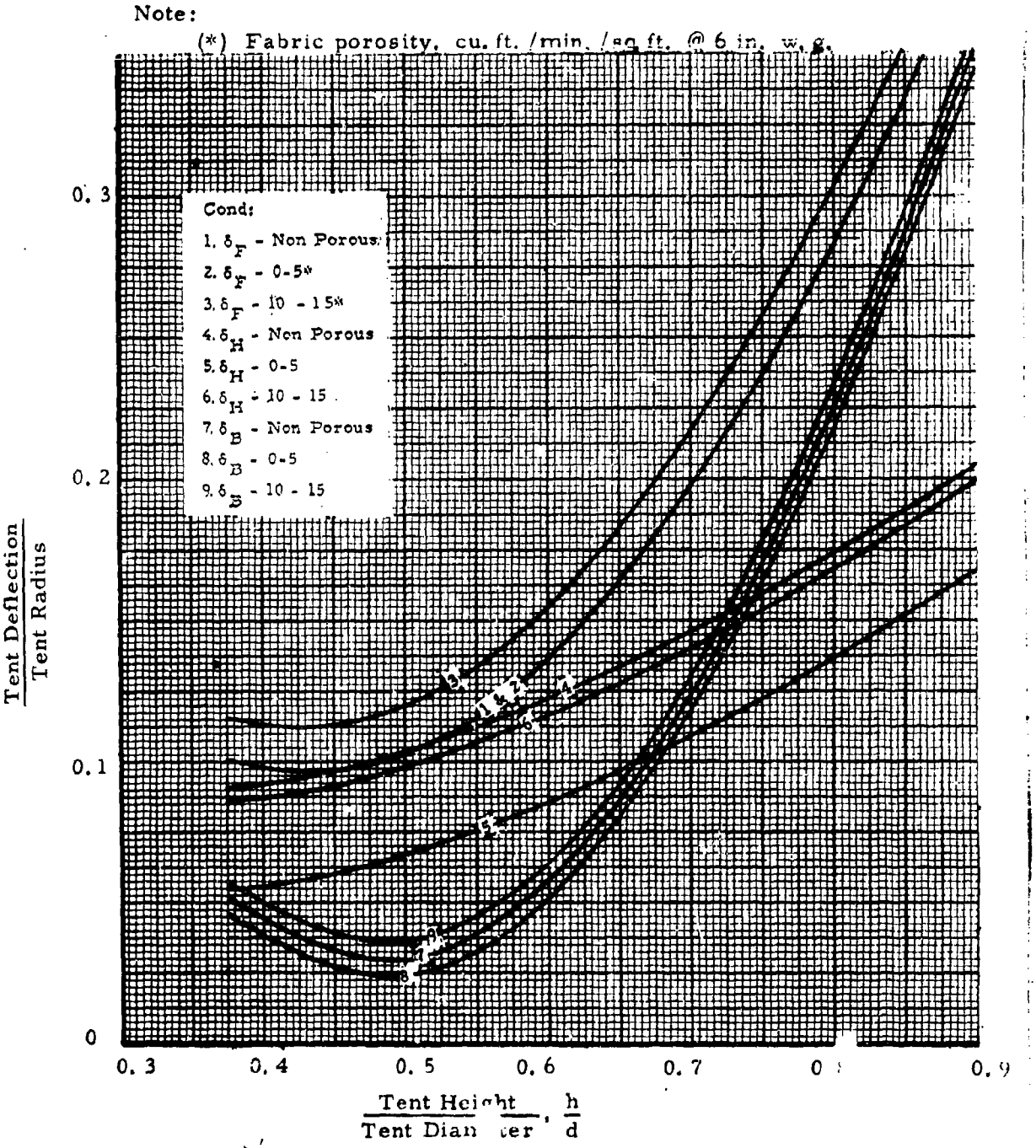

Figure 51. Variation of Tent Deflection with Shape and Fabric Porosity (Cylindrical Single-Wall Tents, 1:2 $W/_H$)

MAXIMUM TENT DEFLECTION
SINGLE-WALL 1:2 CYLINDERS

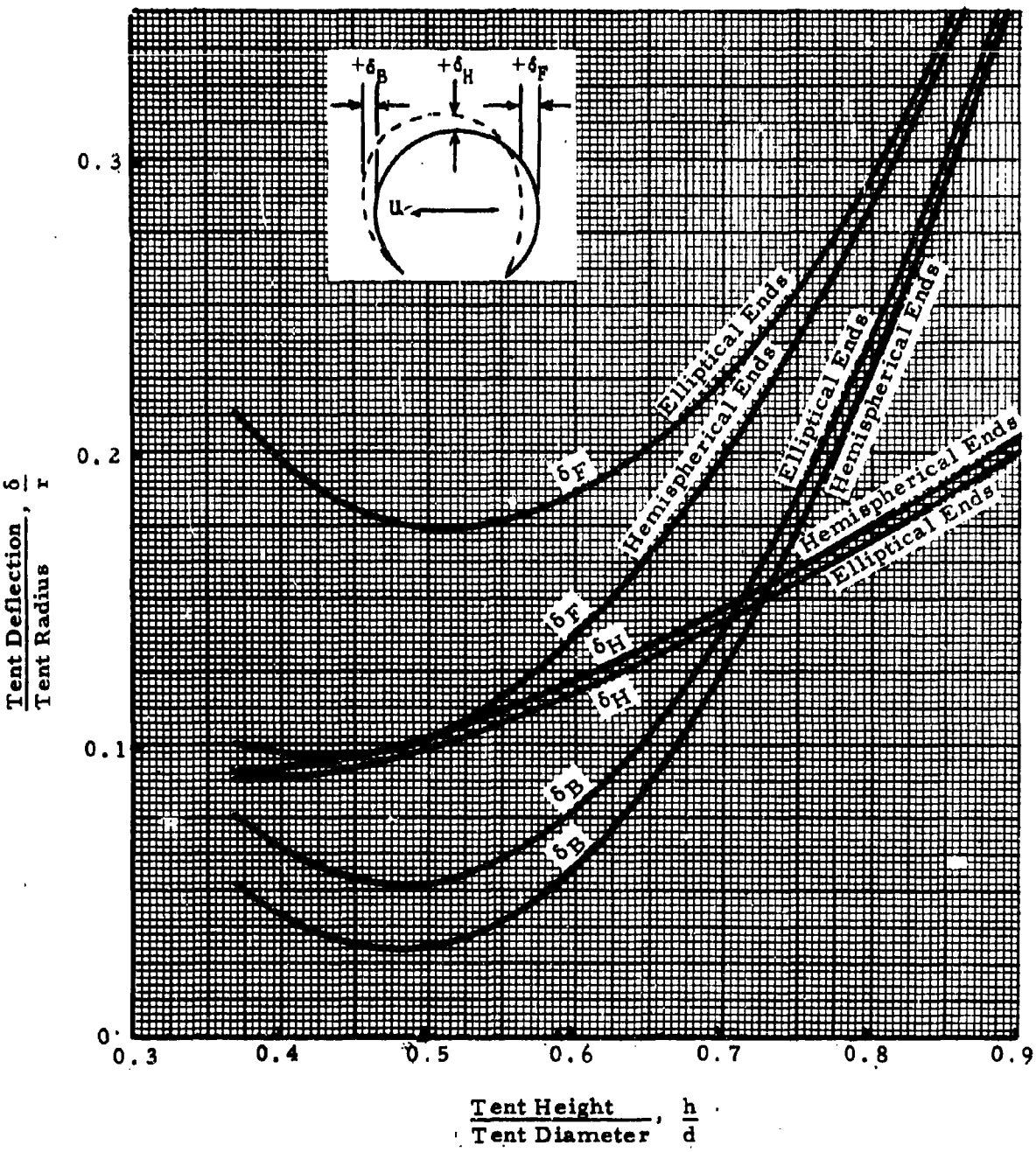

Figure 52. Comparison of Non-Porous Tent Deflection with Shape (Cylindrical Single-Wall Tents, 1:2 W/ℓ_h)

MAXIMUM TENT DEFLECTION
SINGLE-WALL 1:4 CYLINDERS
(Hemispherical Ends)

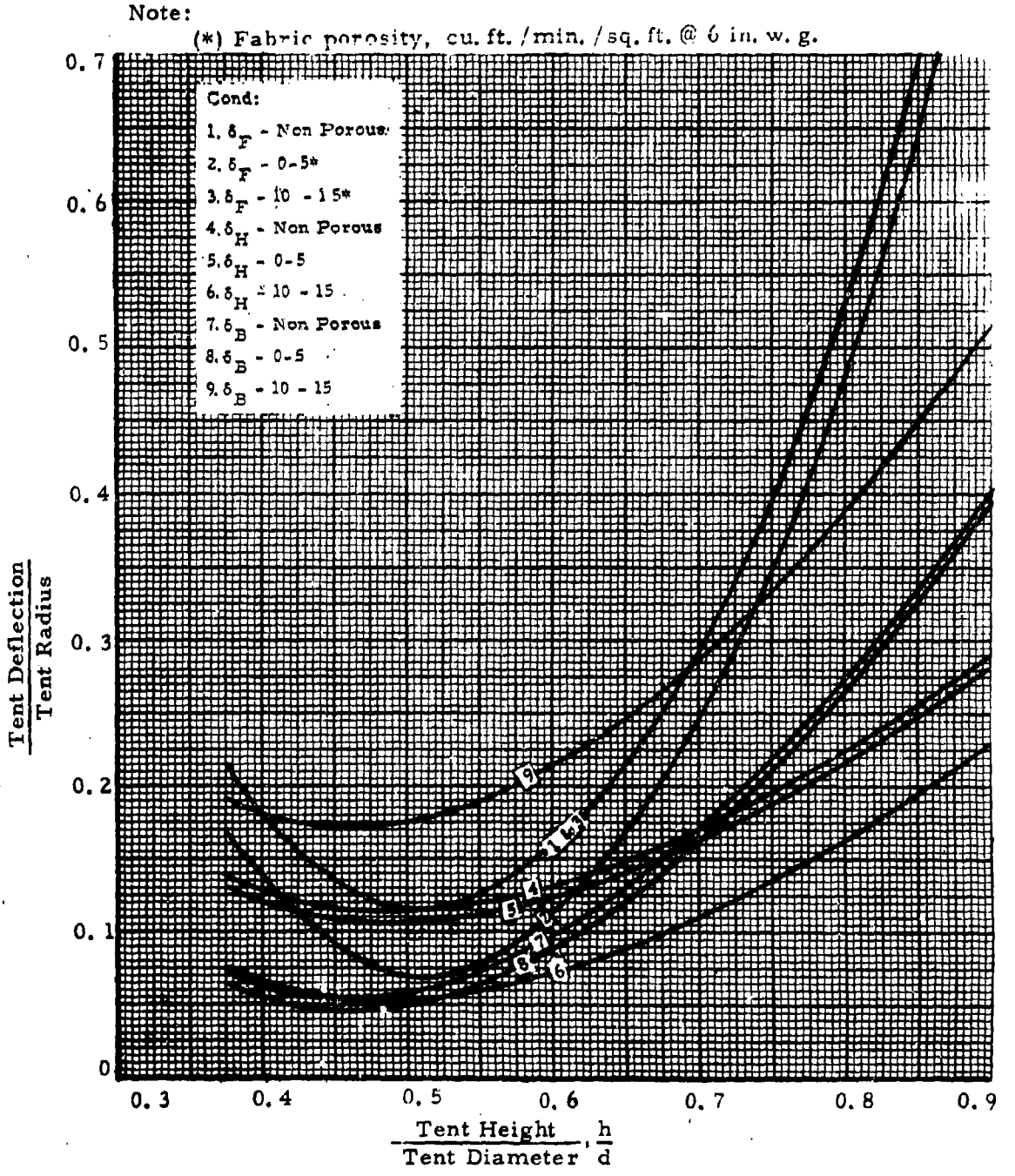

Figure 53 Variation of Tent Deflection with Shape and Fabric Porosity (Cylindrical Single-Wall Tents, 1:4 W/ℓ_h)

DOUBLE-WALL, 3/4 CYLINDER, 1:1 WIDTH/LENGTH RATIO
GUY LINES ATTACHED 0.80 TENT HEIGHT

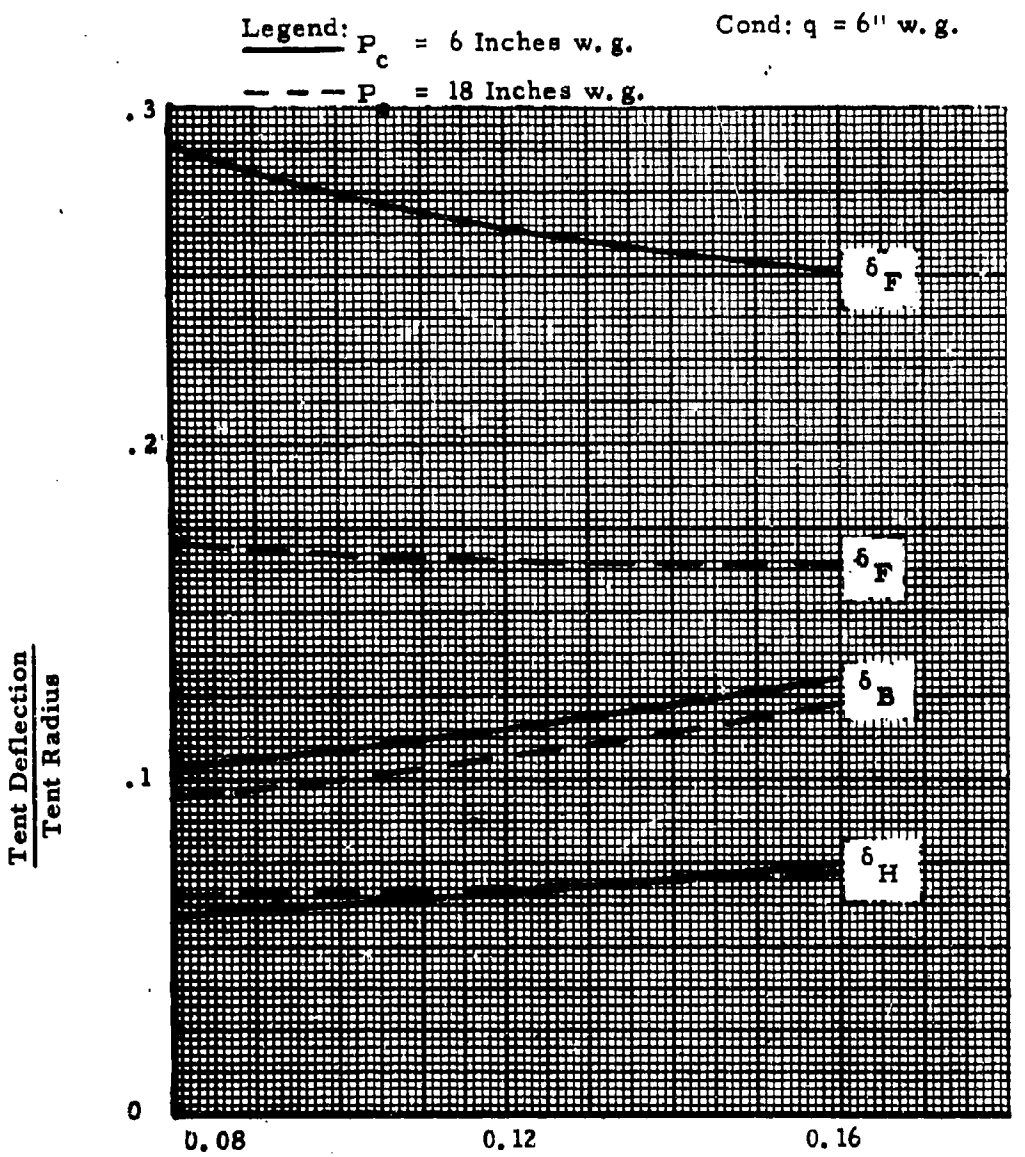

Figure 54. Effect of Cell Size on Tent Deflection

DOUBLE-WALL, 3/4 CYLINDER, 1:1 WIDTH/LENGTH RATIO
GUY LINES ATTACHED 0.80 and 0.40 TENT HEIGHT

Note: Cell Width/Enclosure Diameter = 0.123

Cond: q = 6.0" w.g.

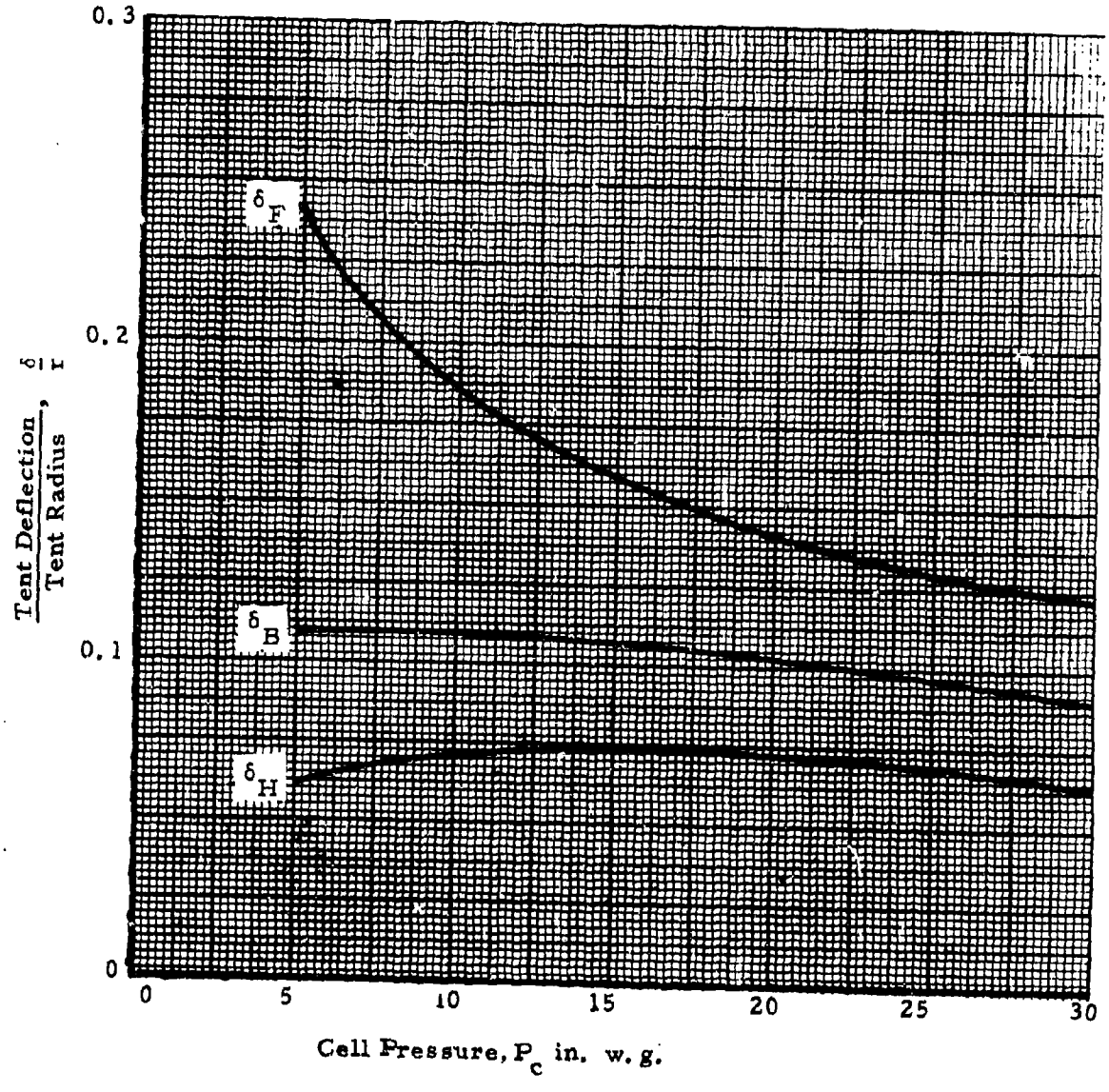

Figure 55. - Variation of Tent Deflection with Cell Pressure. Guy Lines Attached at 0.80 and 0.40 Tent Height

DOUBLE-WALL, 3/4 CYLINDER, 1:1 WIDTH/LENGTH RATIO

Cond: $q = 6.0$" w. g.
$P_c = 5.0$" w. g.

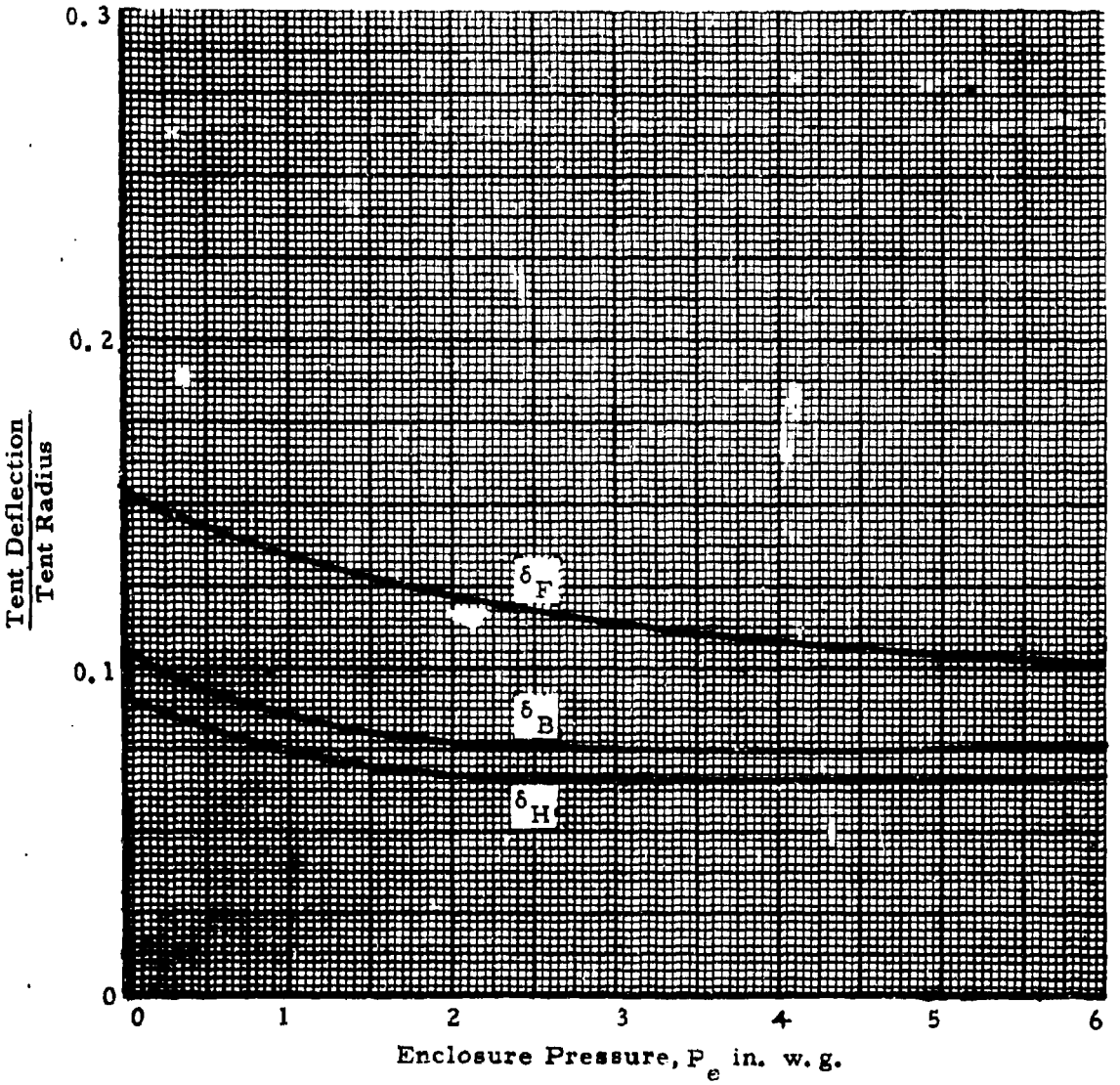

Figure 56. Variation of Tent Deflection With Enclosure Pressure, No Guy Lines, Constant Cell Pressure = 5.0"w. g., Broadside to Wind ($\psi = 0°$)

MAXIMUM TENT DEFLECTION
DOUBLE-WALL CYLINDERS

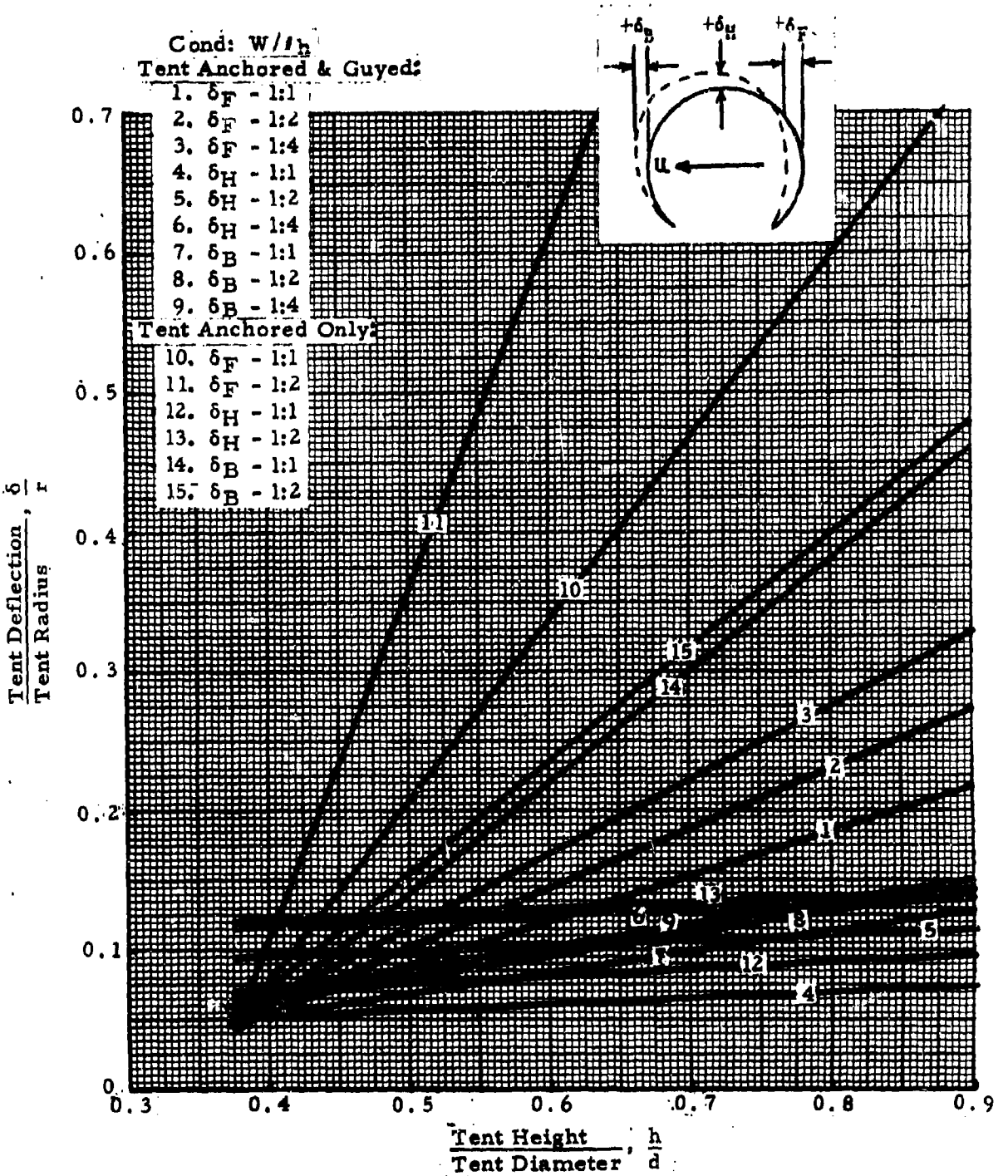

Figure 57. Variation of Tent Deflection with Shape
(Non-Porous Double-Wall Tents 1:1, 1:2, 1:4 (W/ℓh)

MAXIMUM TENT DEFLECTION
DOUBLE WALL CYLINDERS
1:2 W/ℓ_h

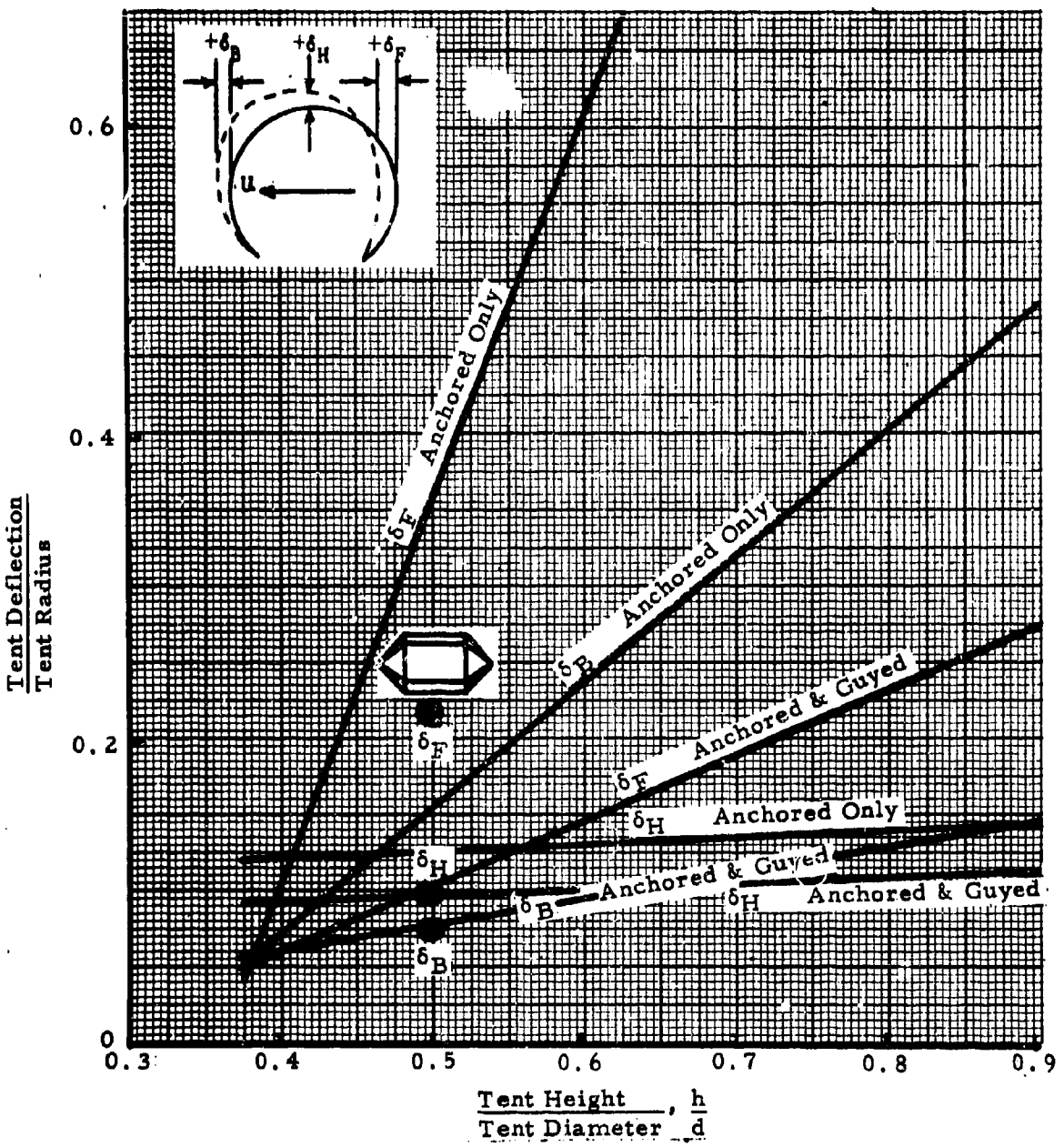

Figure 58. Variation of Tent Deflection with Shape
(Non-Porous Double Wall Tents; 1:2 W/ℓ_h)

TENT DYNAMICS
Without Guy Lines Installed

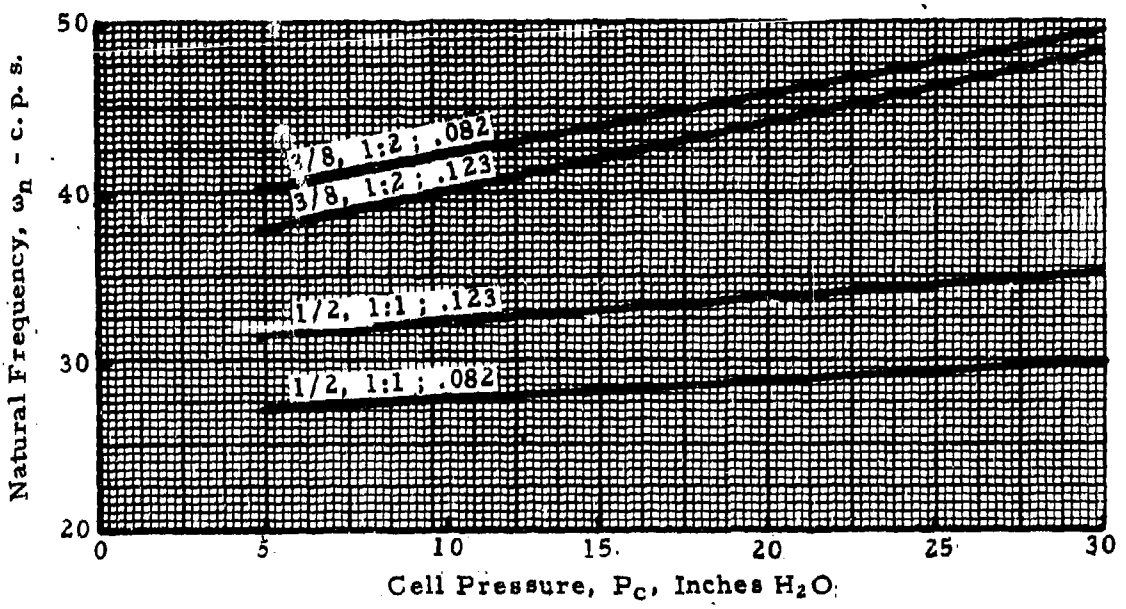

NOTE: $\frac{\delta_f}{r}$ is peak to peak amplitude, superimposed on basic $\frac{\delta_f}{r}$ values.

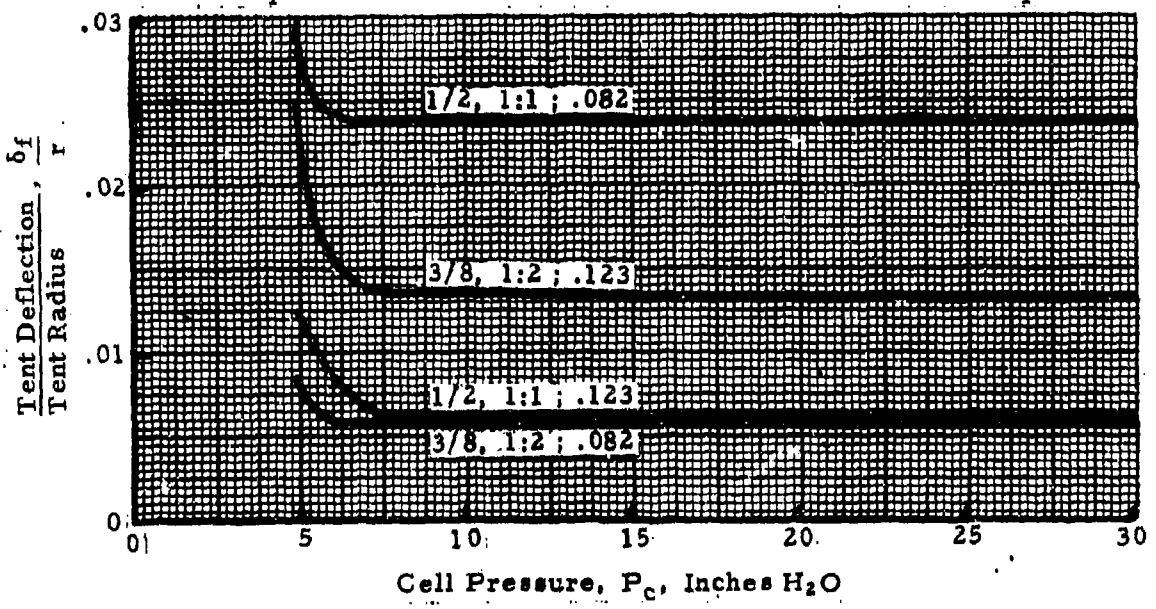

Figure 59. Tent Frequency and Amplitude of Vibration, Without Guy Lines Installed

TENT DYNAMICS
Guy Lines Installed

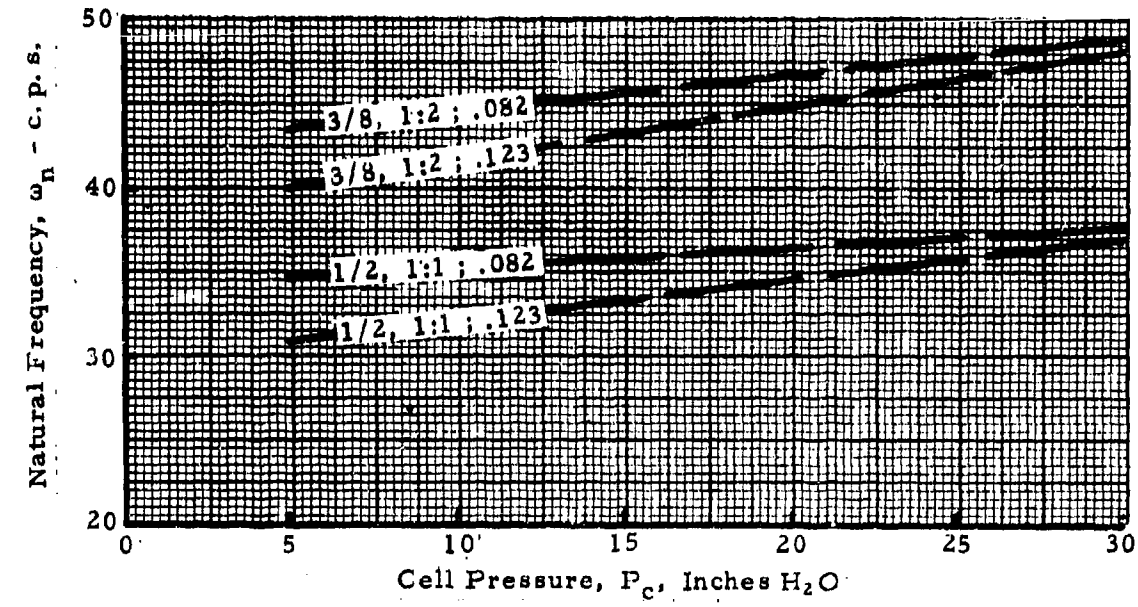

NOTE: $\frac{\delta f}{r}$ is peak to peak amplitude, superimposed on basic $\frac{\delta f}{r}$ values.

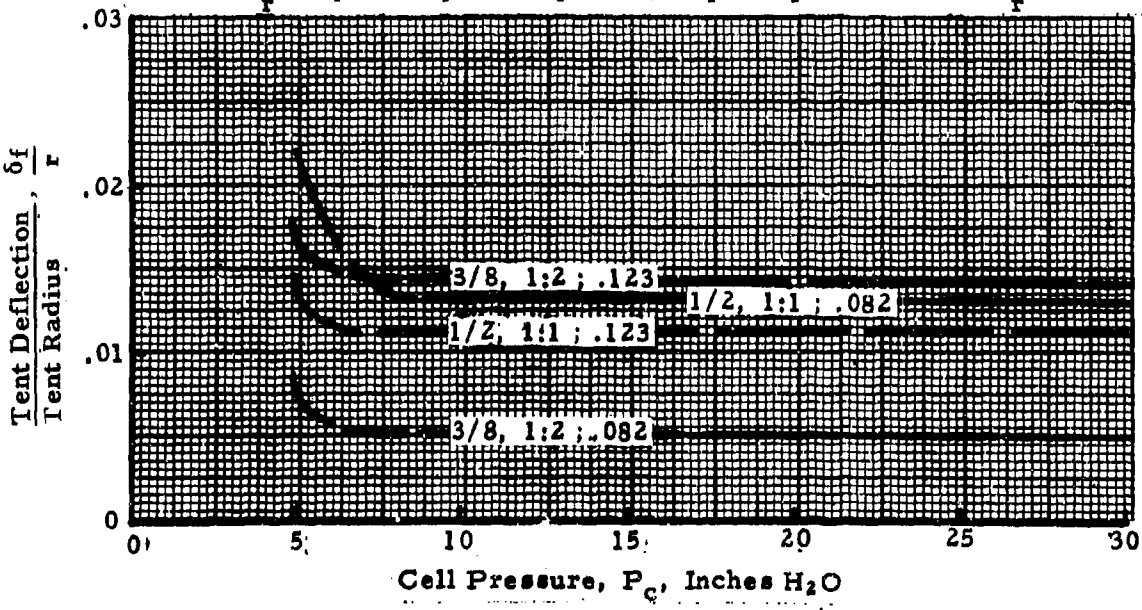

Figure 60. Tent Frequency and Amplitude of Vibration, Guy Lines Installed

TENT DYNAMICS

Cell Size .082

— — With Guy Lines Installed

——— Without Guy Lines Installed

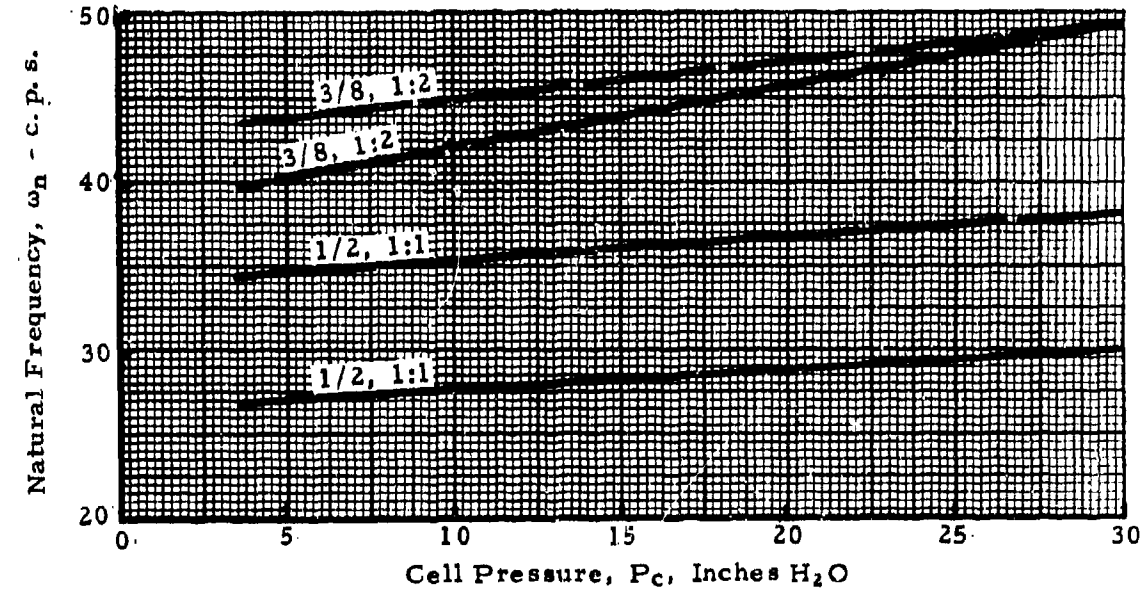

NOTE: $\frac{\delta_f}{r}$ is peak to peak amplitude, superimposed on basic $\frac{\delta_f}{r}$ values.

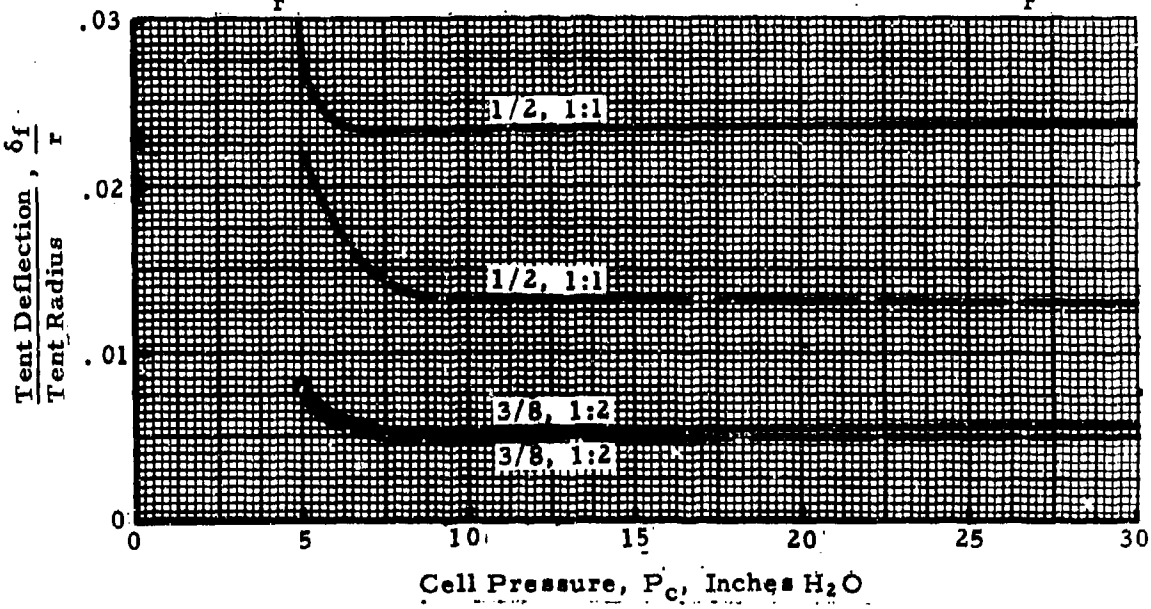

Figure 61, Tent Frequency and Amplitude of Vibration, Comparison of Guyed & Unguyed Conditions

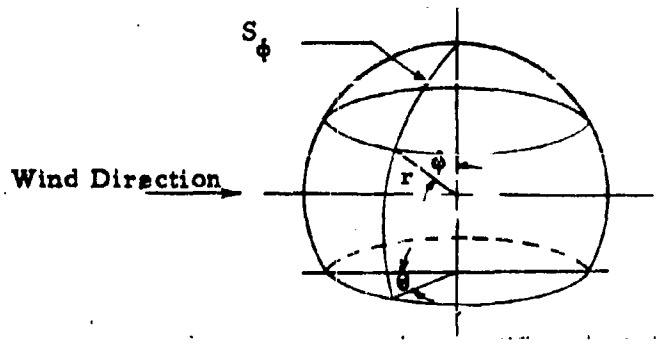

(a) Spherical Coordinates

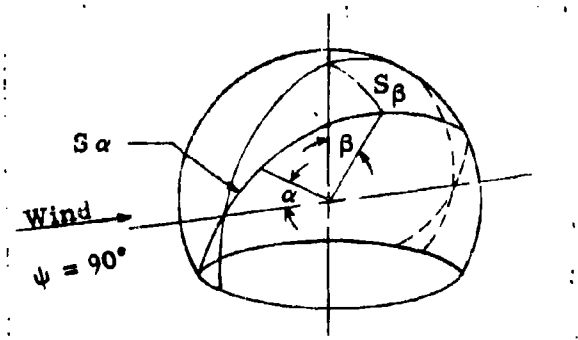

(b) Coordinates on Spherical Ends

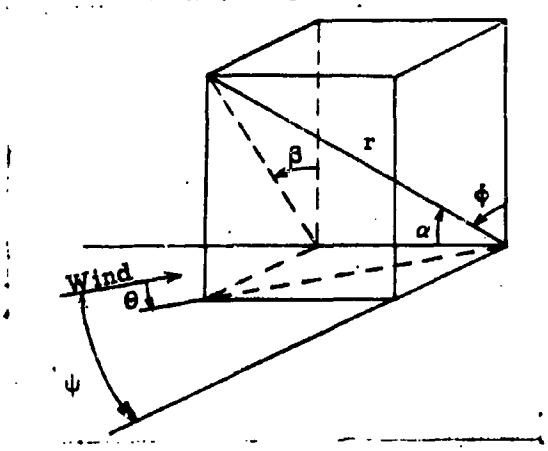

(c) Conversion from α,β to ϕ,θ Coordinates

Figure 62. Coordinate Systems Pertaining to Spherical Tents and Spherical Ends of Cylindrical Tents

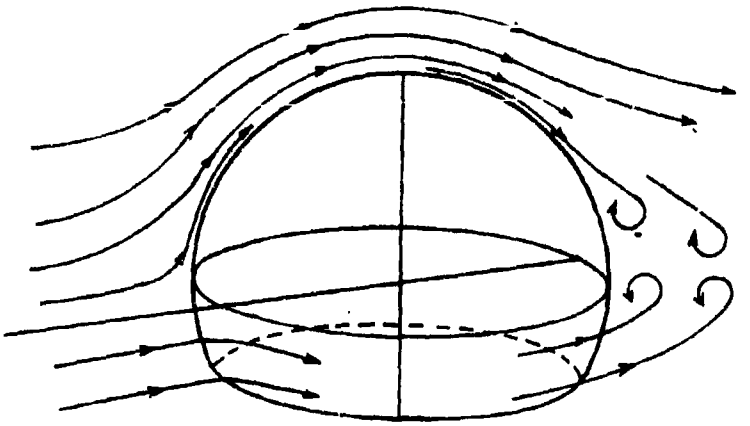

Typical Air Flow

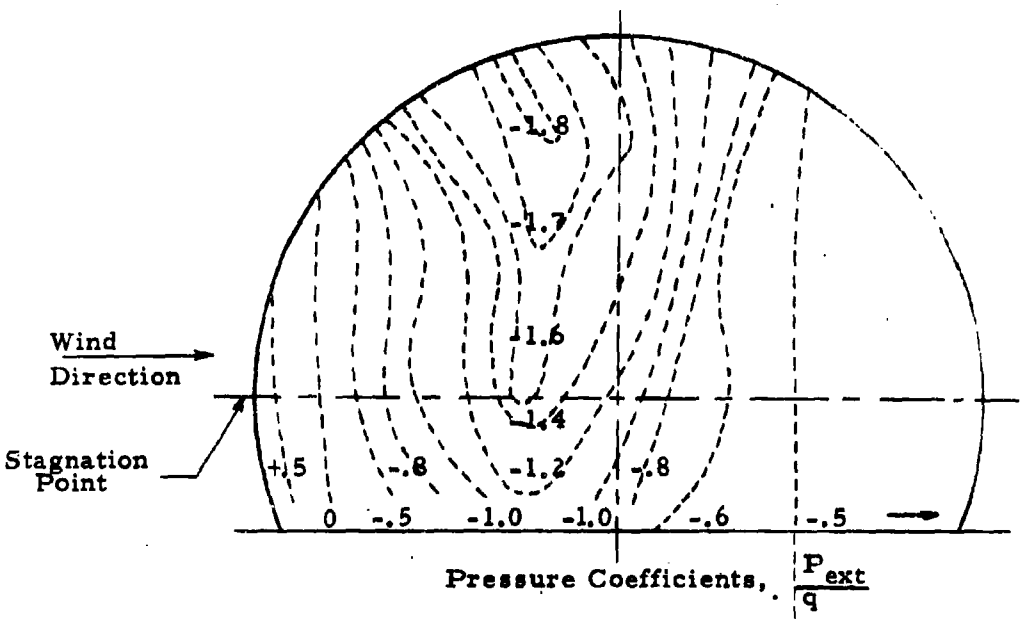

Figure 63. Typical Pressure Distribution on a Spherical Shell

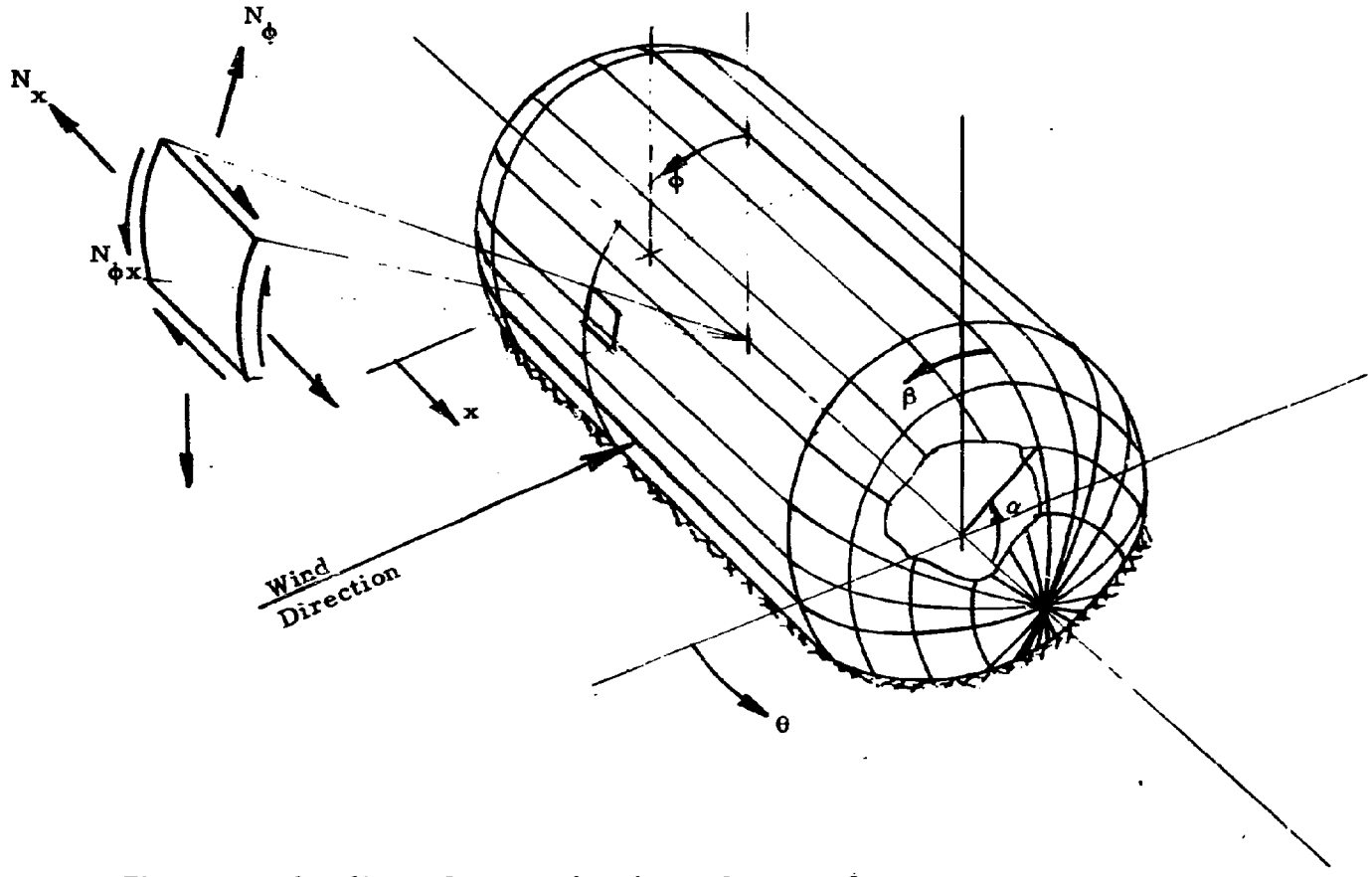

Figure 64. Coordinate System and Membrane Stresses for a Cylindrical Shell with Hemispherical Ends

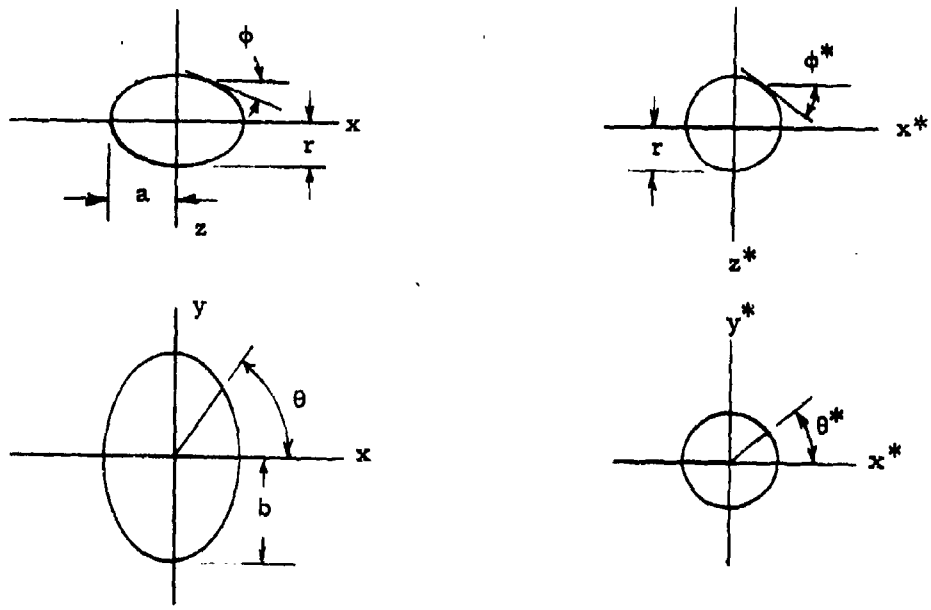

Ellipsoidal Shell, S

Spherical Shell, S*

Figure 65. Ellipsoidal and Spherical Coordinates

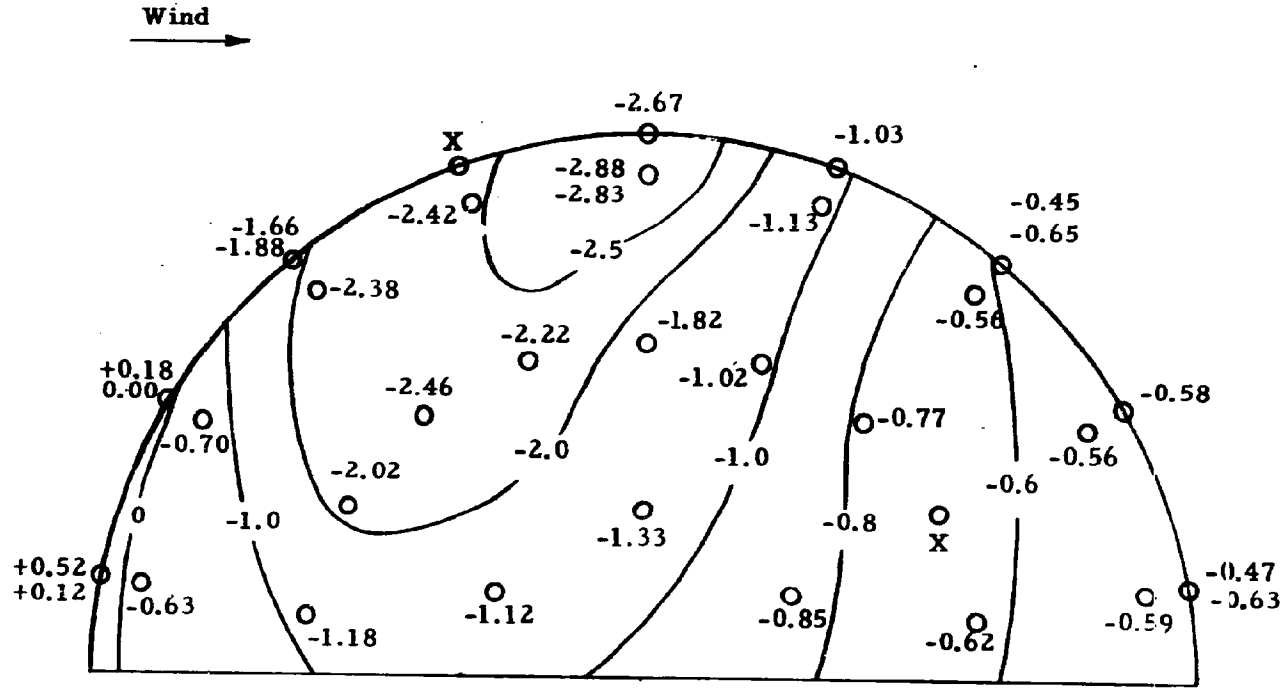

Figure 66. Experimental Pressure Distribution on Ellipsoidal End

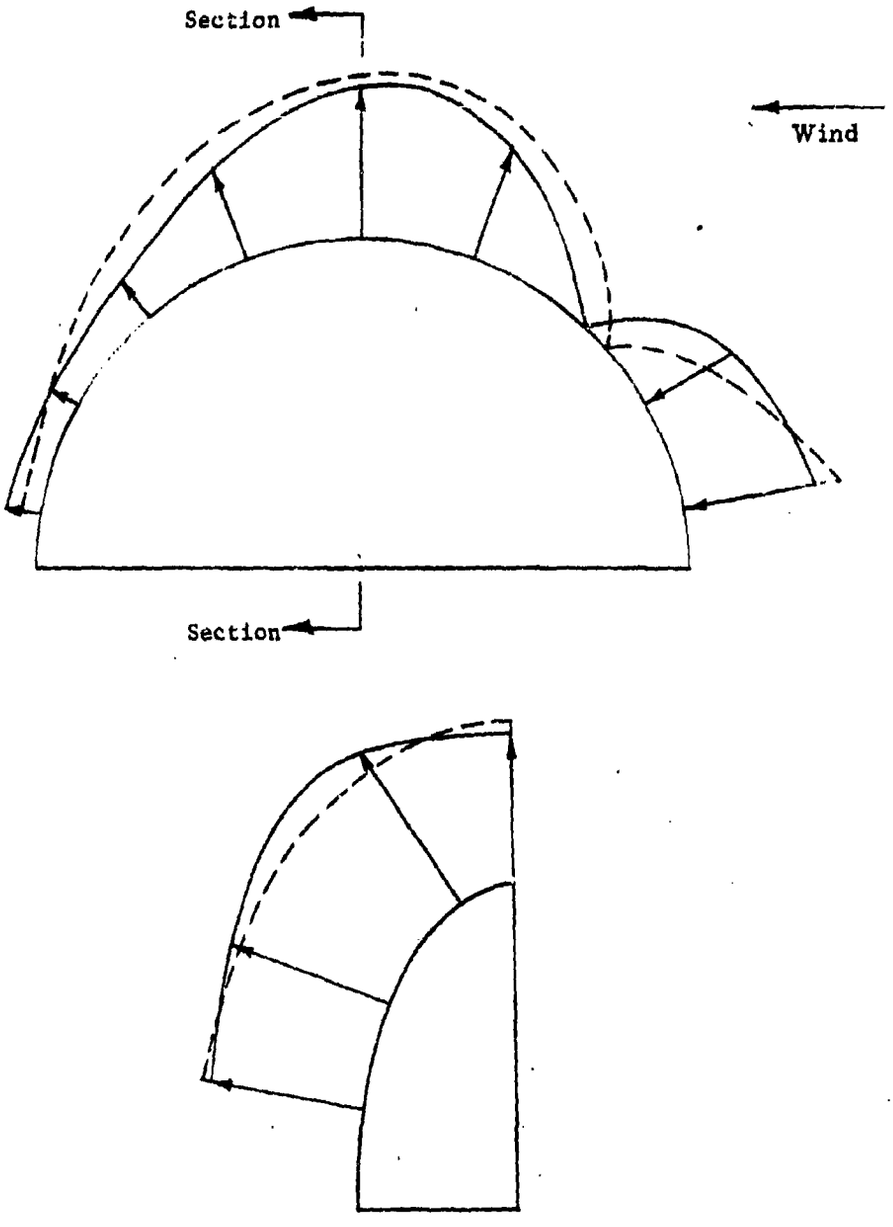

——— True Pressure Distribution

— — — Third Order Polynomial Curve Fit

Figure 67. Wind Load on Ellipsoidal End

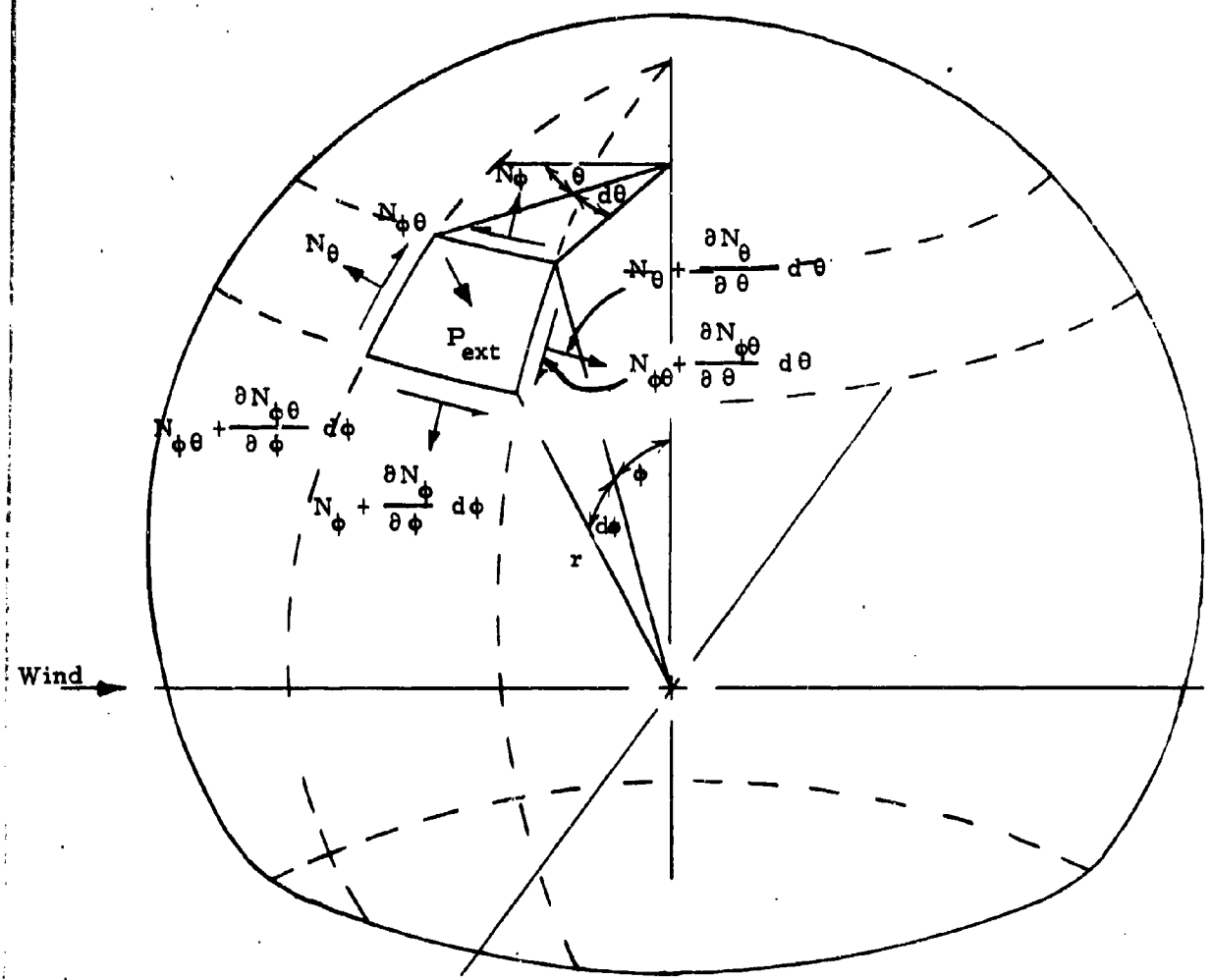

Figure 68. Coordinate System and Membrane Stresses for a Truncated Spherical Shell

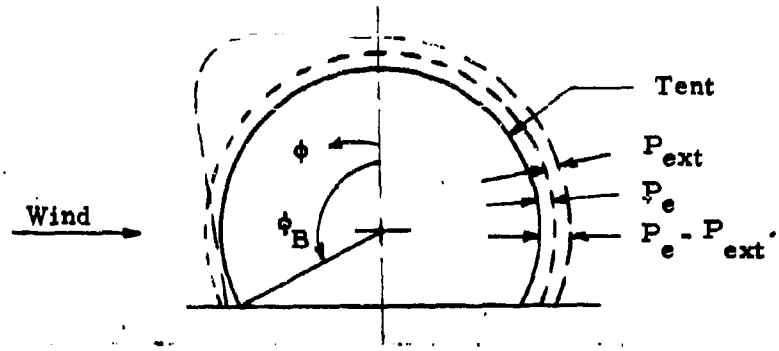

(a) Combined Radial Load

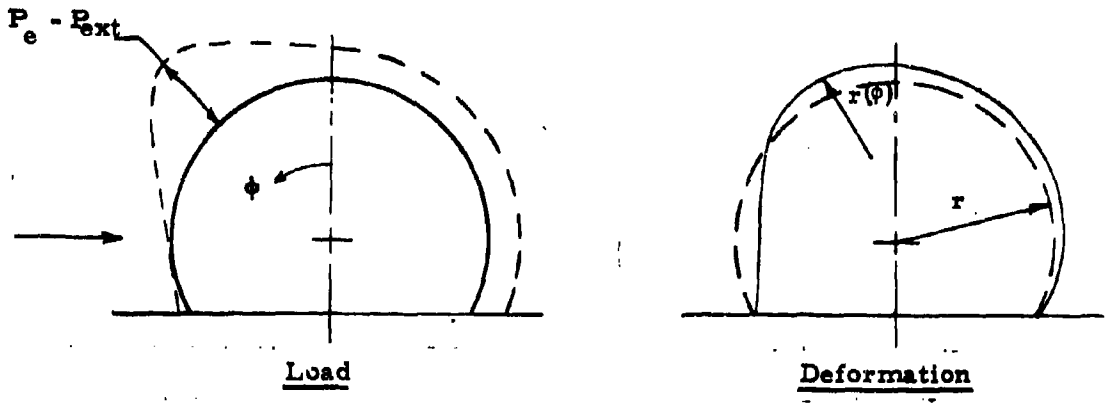

(b) Load and Deformation

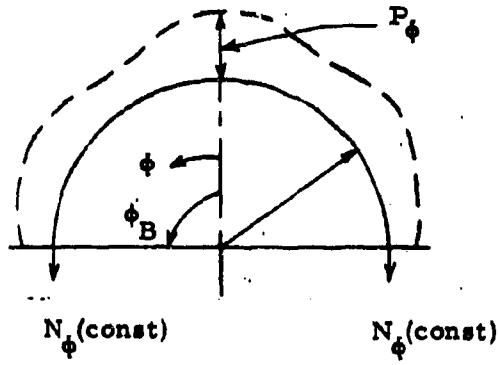

(c) Equilibrium

Figure 69. Loading and Deformation of Cylindrical Tent

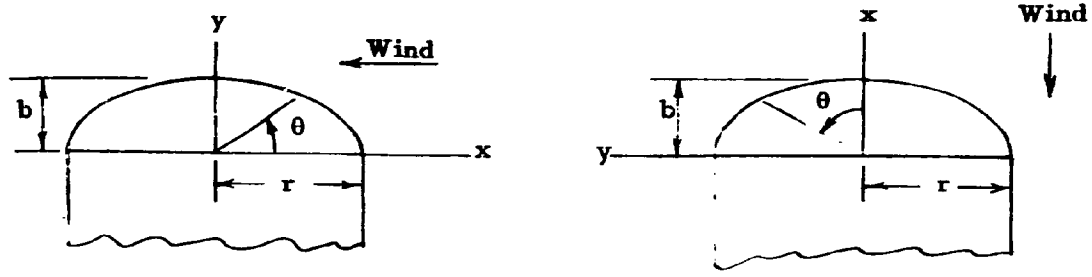

Broadside Wind

$\lambda_1 = 1, \quad \lambda_2 = b/r$

Head-on Wind

$\lambda_1 = b/r, \quad \lambda_2 = 1$

Figure 70. Variation of λ_1 and λ_2 with Wind Direction

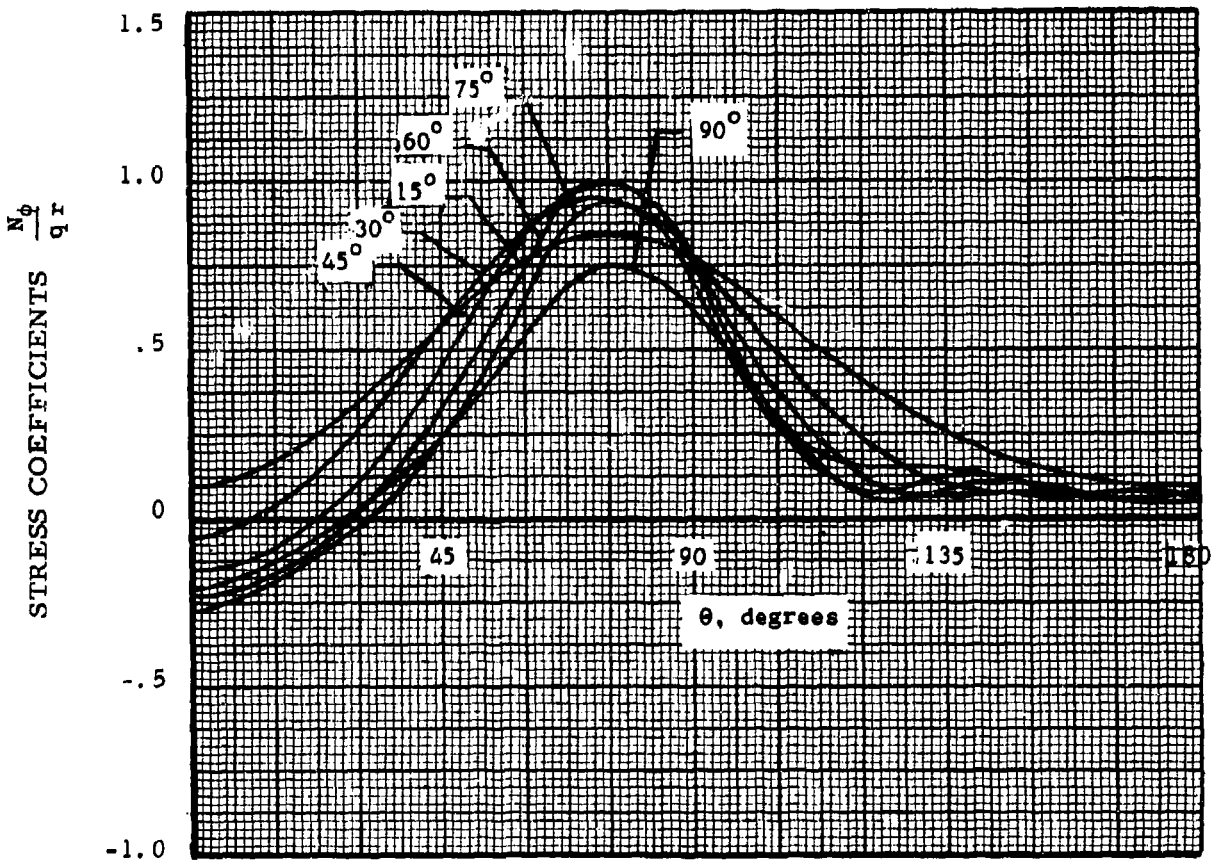

Figure 71. Typical Stress Coefficients, $\frac{N_\phi}{qr}$; Single-Wall Spheres, h/d = 1/2

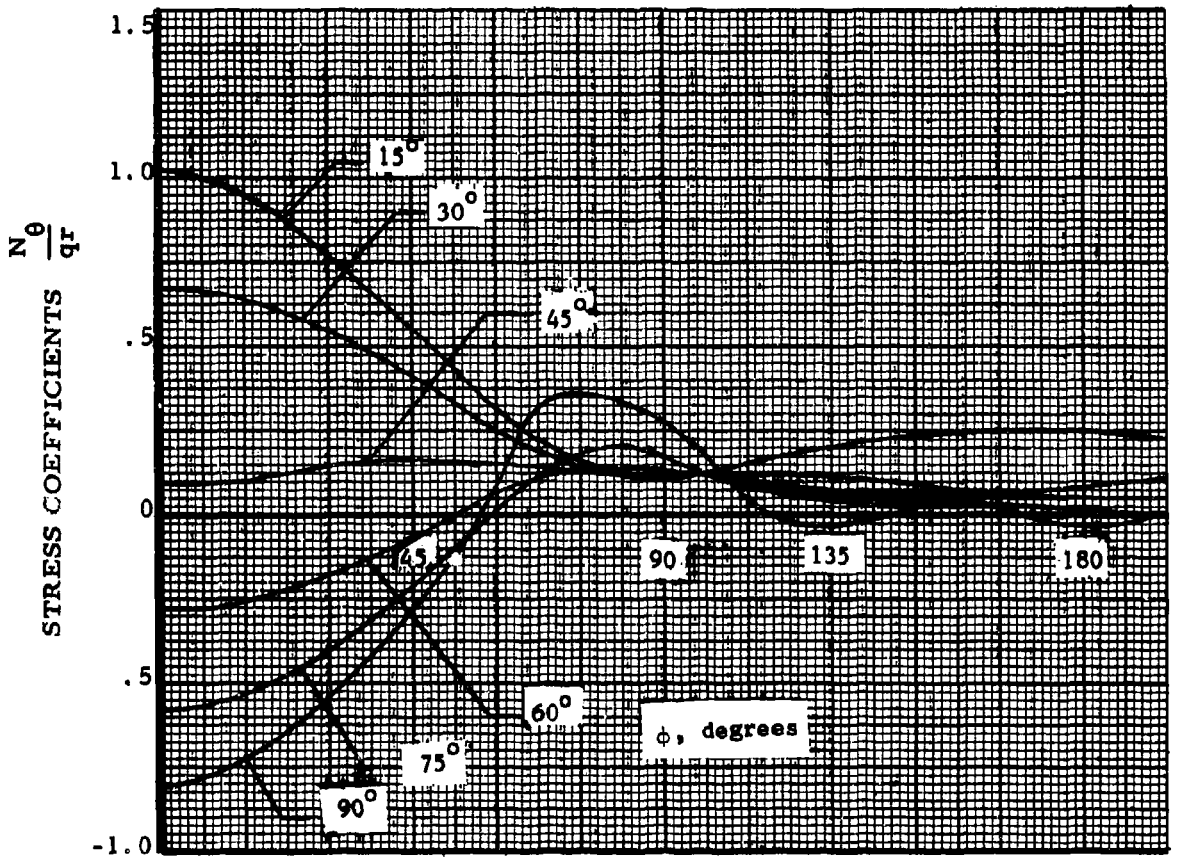

Figure 72. Typical Stress Coefficients, $\frac{N_\theta}{qr}$; Single-Wall Spheres, h/d = 1/2

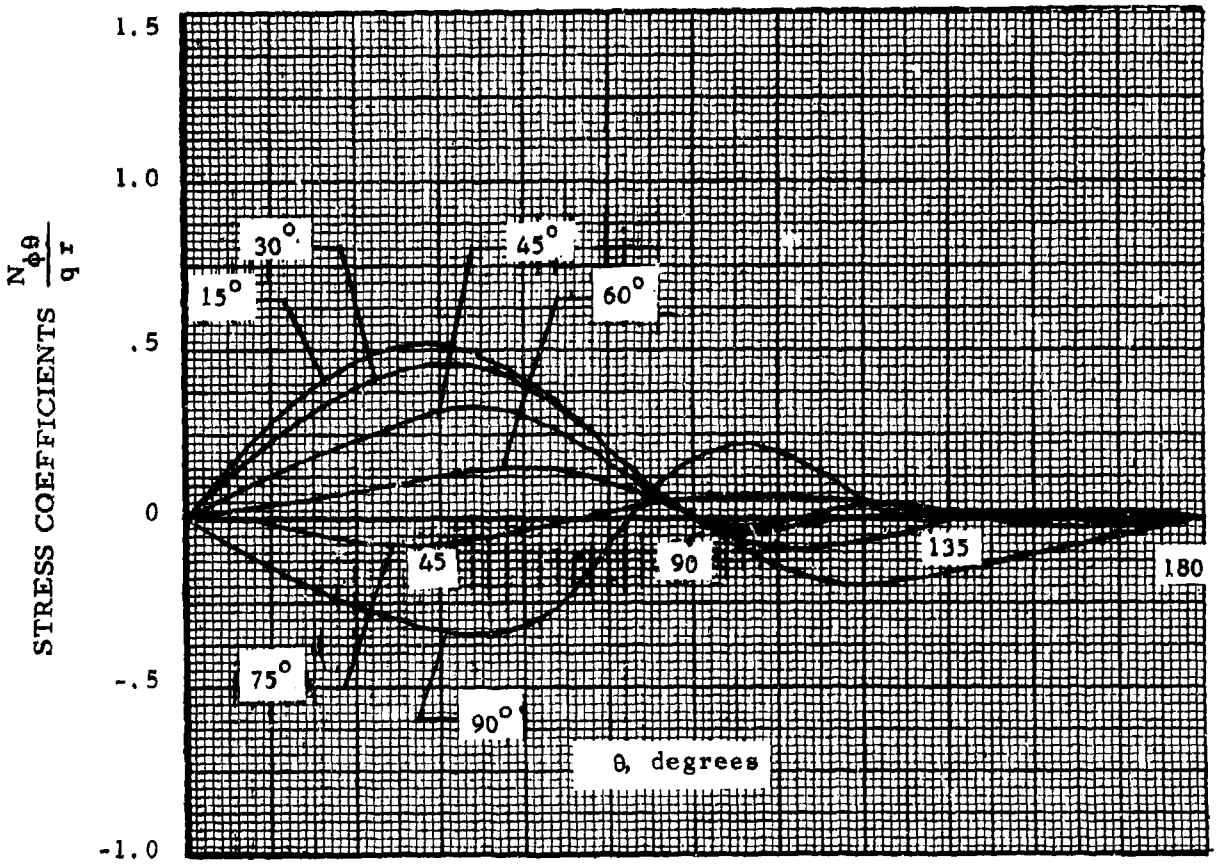

Figure 73. Typical Stress Coefficients, $\frac{N_{\phi\theta}}{qr}$; Single-Wall Spheres, h/d = 1/2

SINGLE-WALL SPHERES

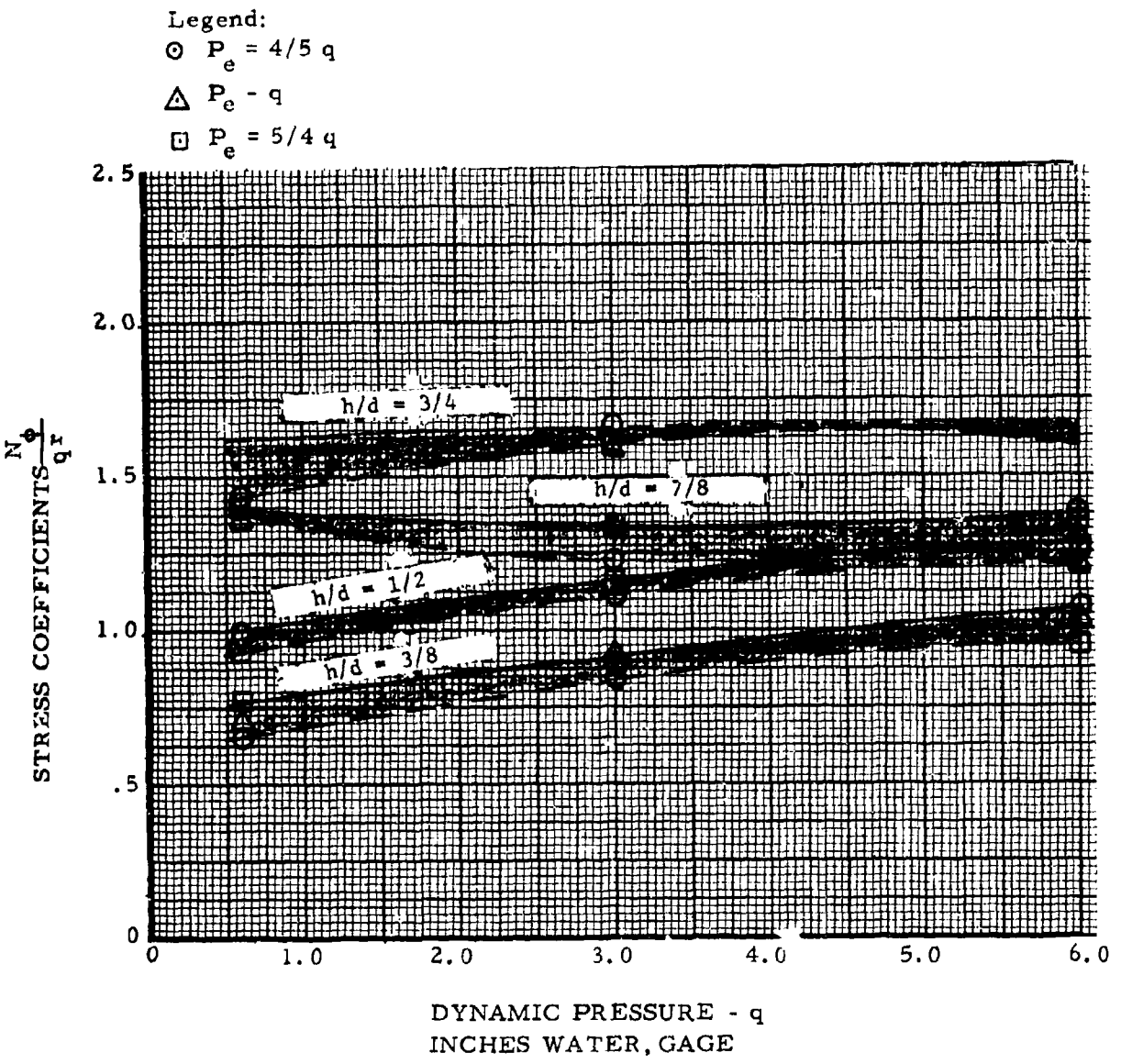

Figure 74. Calculated Peak Stress Coefficients, $\frac{N_\phi}{qr}$; Single-Wall Spheres

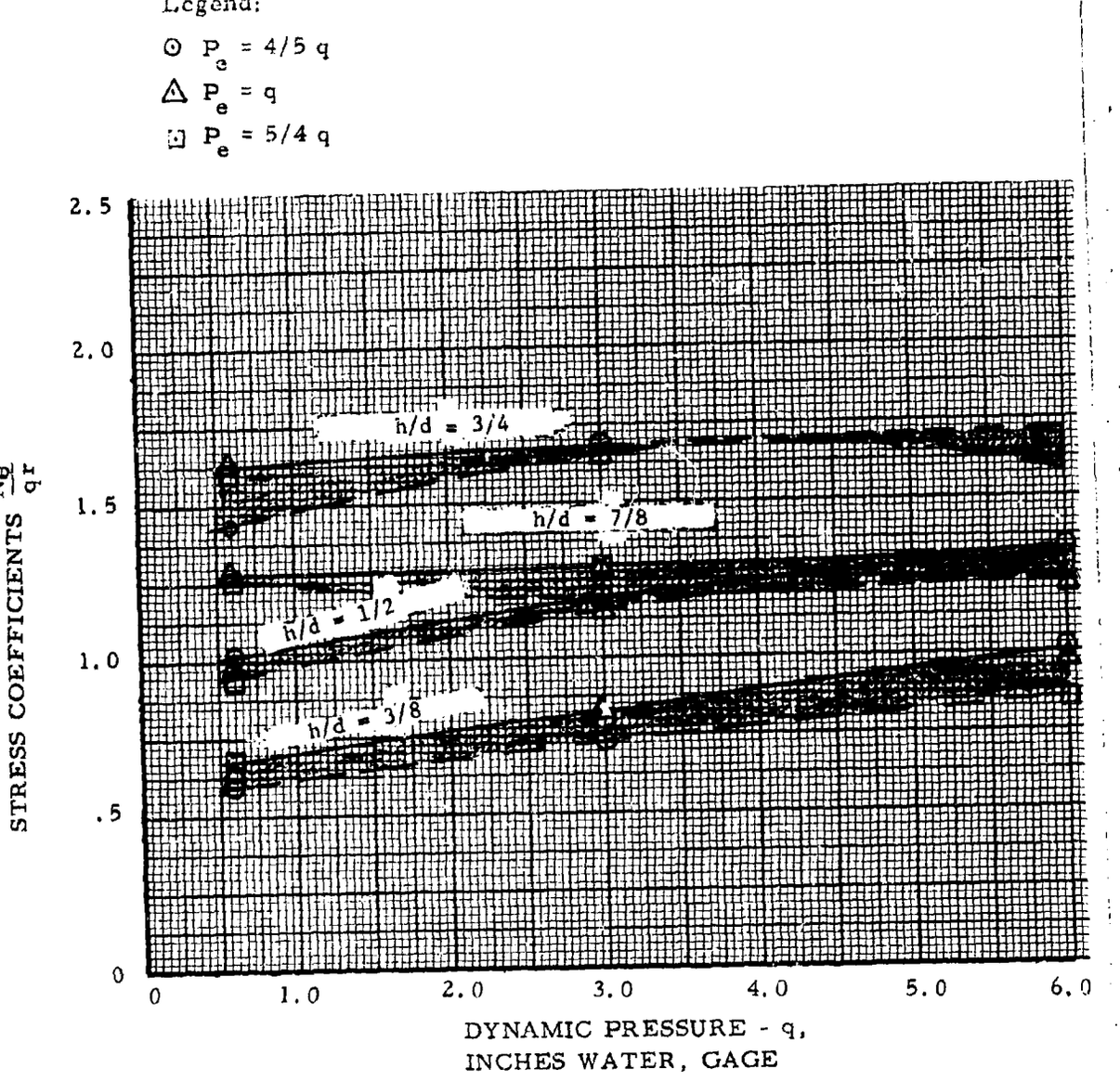

Figure 75. Calculated Peak Stress Coefficients, $\frac{N_\theta}{qr}$; Single-Wall Spheres

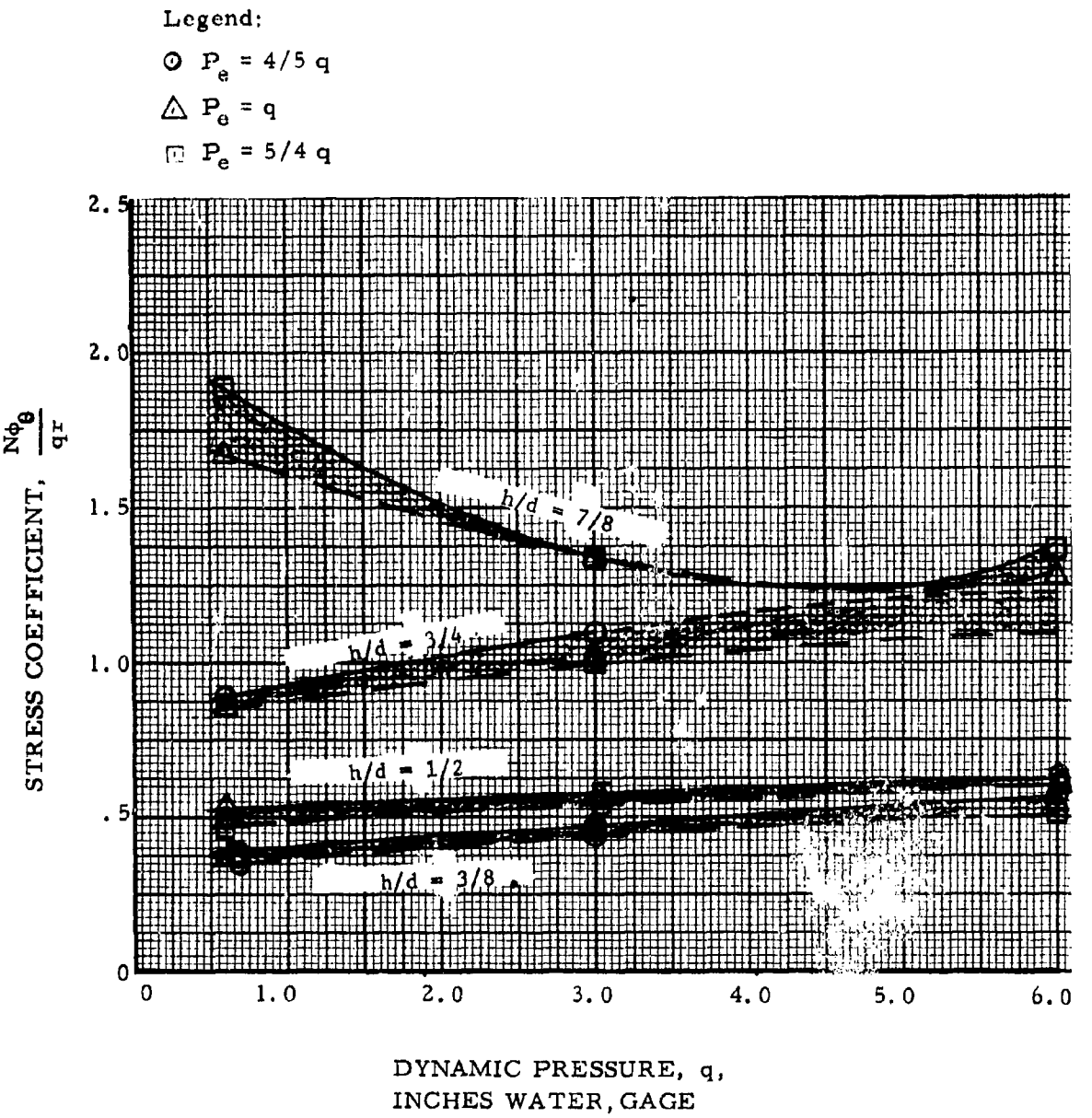

Figure 76. Calculated Peak Stress Coefficients, $\frac{N_{\phi\theta}}{qr}$; Single-Wall Spheres

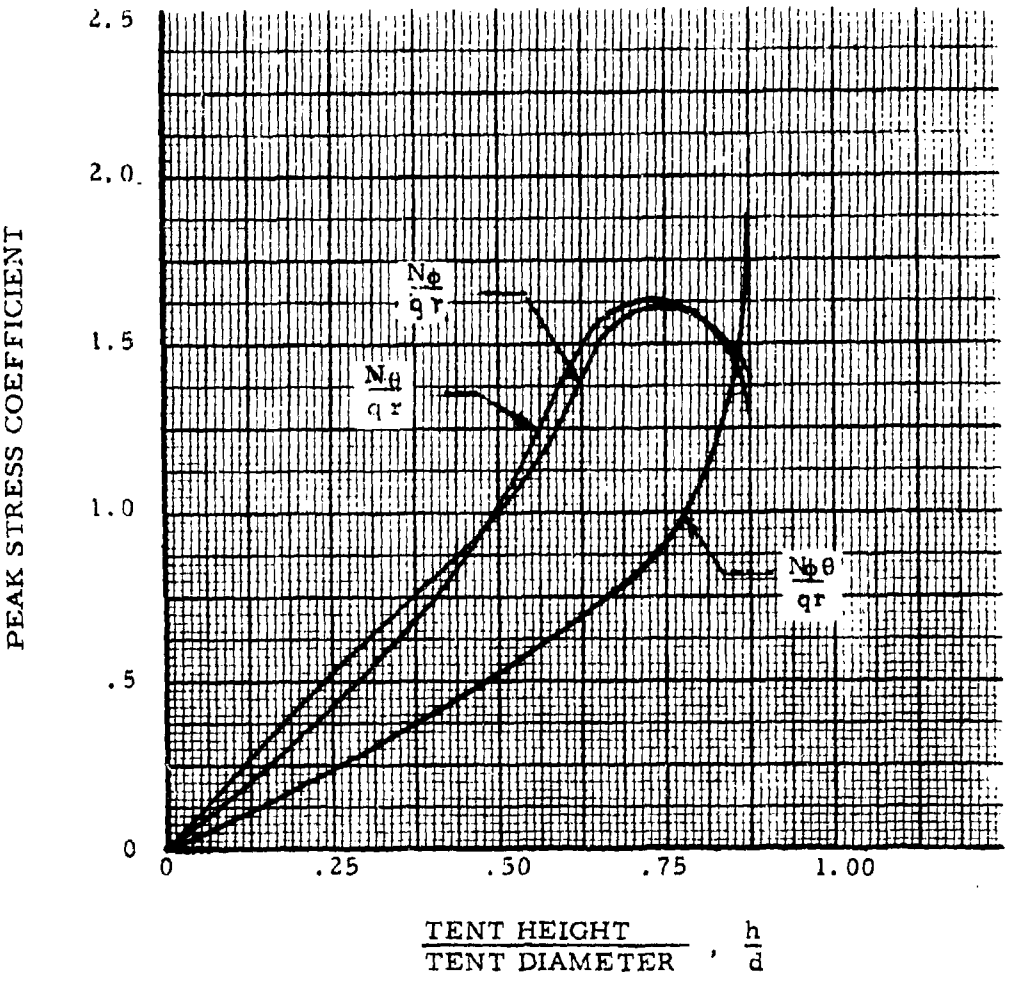

Figure 77. Variation of Peak Stress Coefficient with Shape at q = 0.6 Inches of Water Gage; Non Porous Single-Wall Spheres

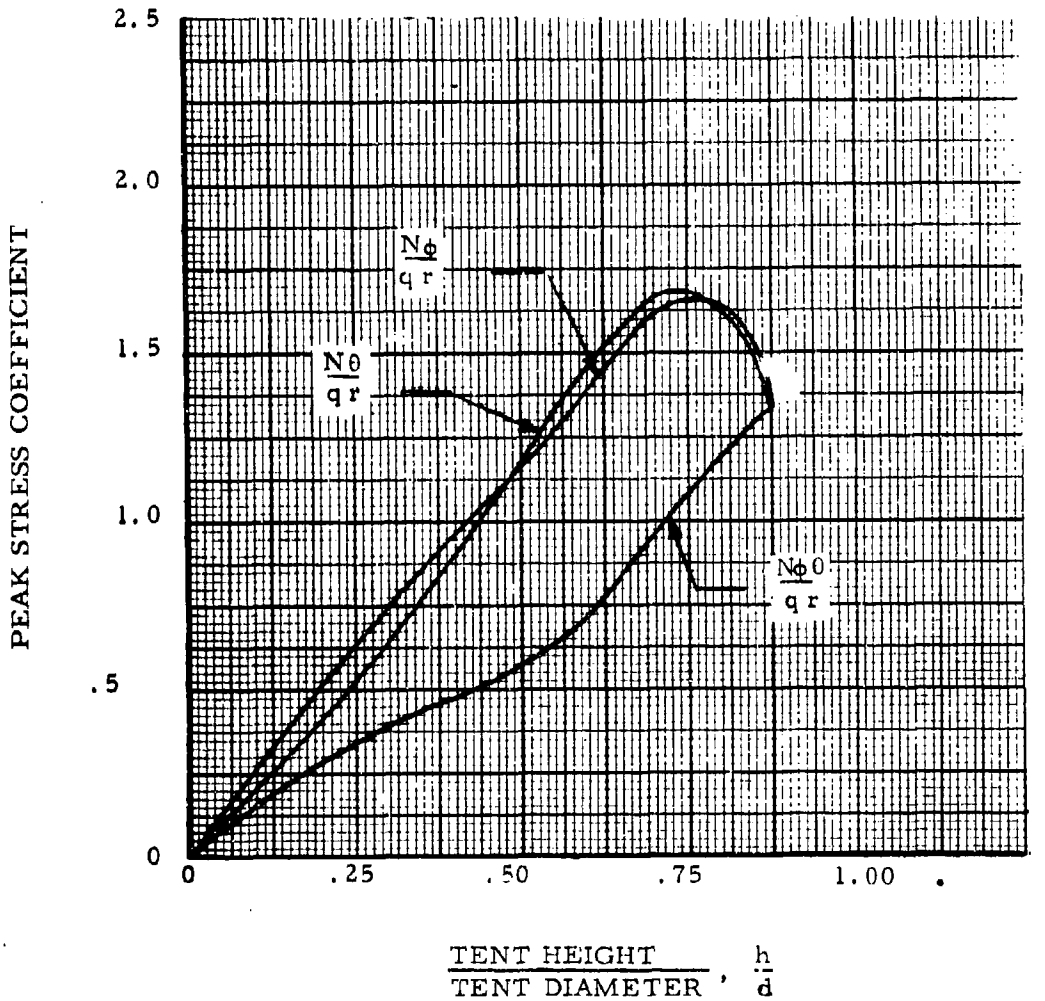

Figure 78. Variation of Peak Stress Coefficient with Shape at q = 3.0 Inches of Water Gage; Non-Porous Single-Wall Spheres

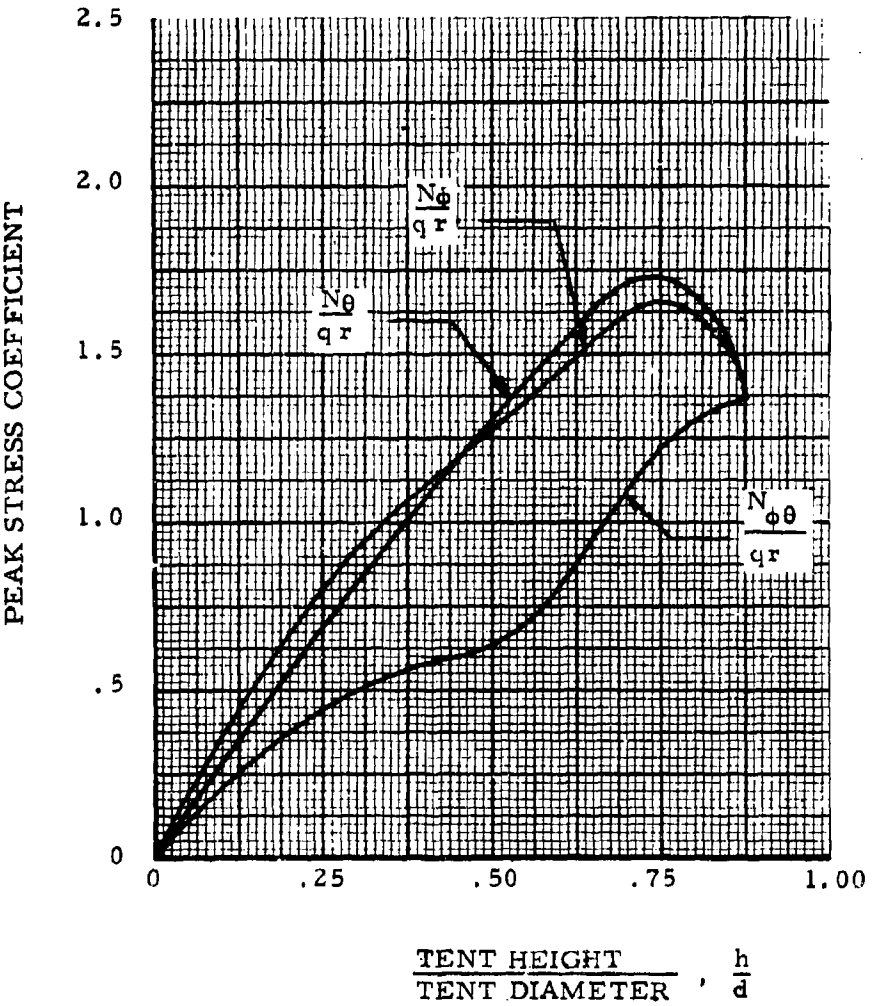

Figure 79. Variation of Peak Stress Coefficients with Shape at q = 6.0 Inches of Water Gage; Non-Porous Single-Wall Spheres

SINGLE-WALL SPHERES

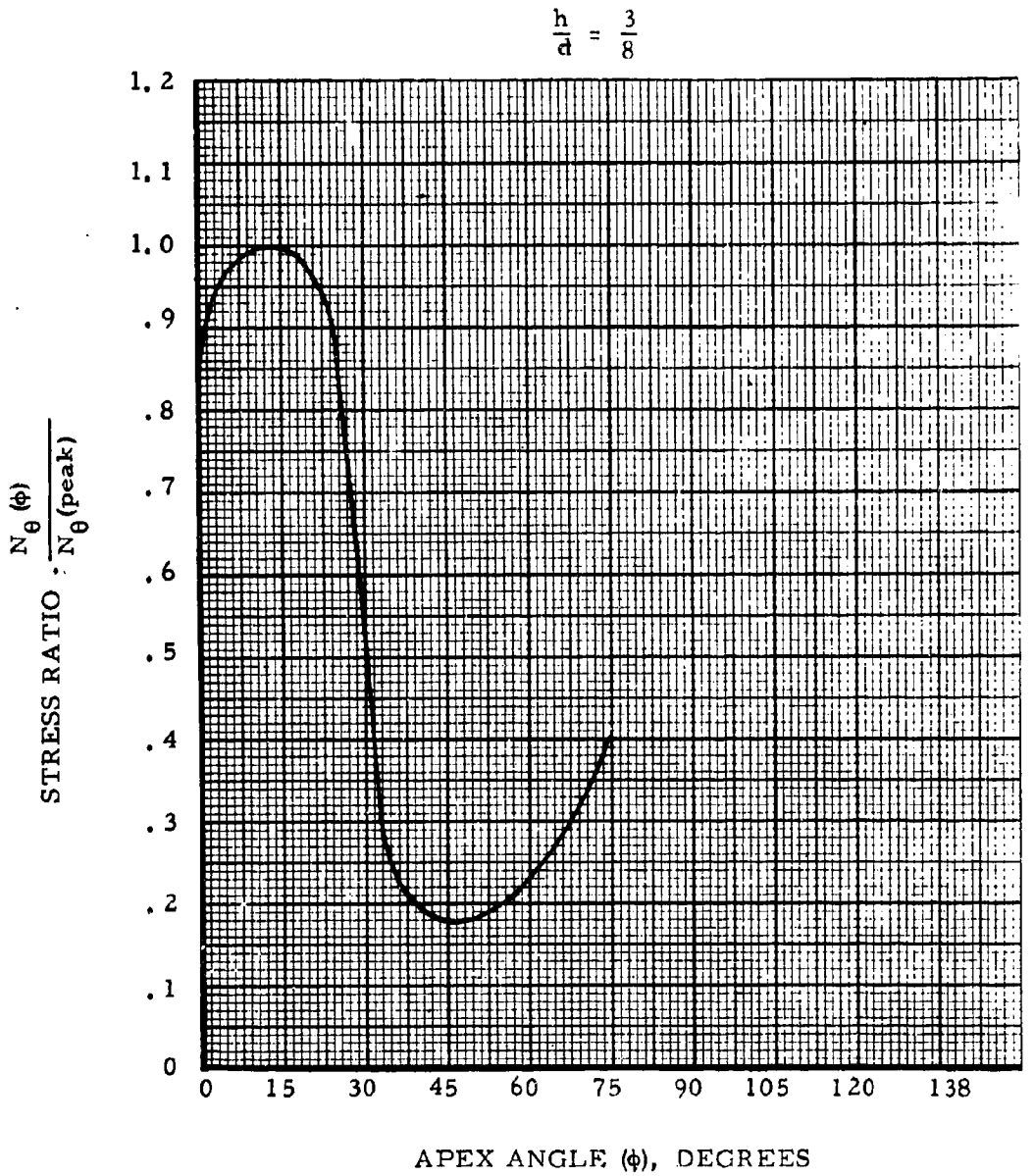

Figure 80. Stress Ratio, $\frac{N_\theta(\phi)}{N_\theta(\text{peak})}$ Vs. Apex Angle, ϕ; Single-Wall Spheres, h/d = 3/8

SINGLE-WALL SPHERES

$\frac{h}{d} = \frac{1}{2}$

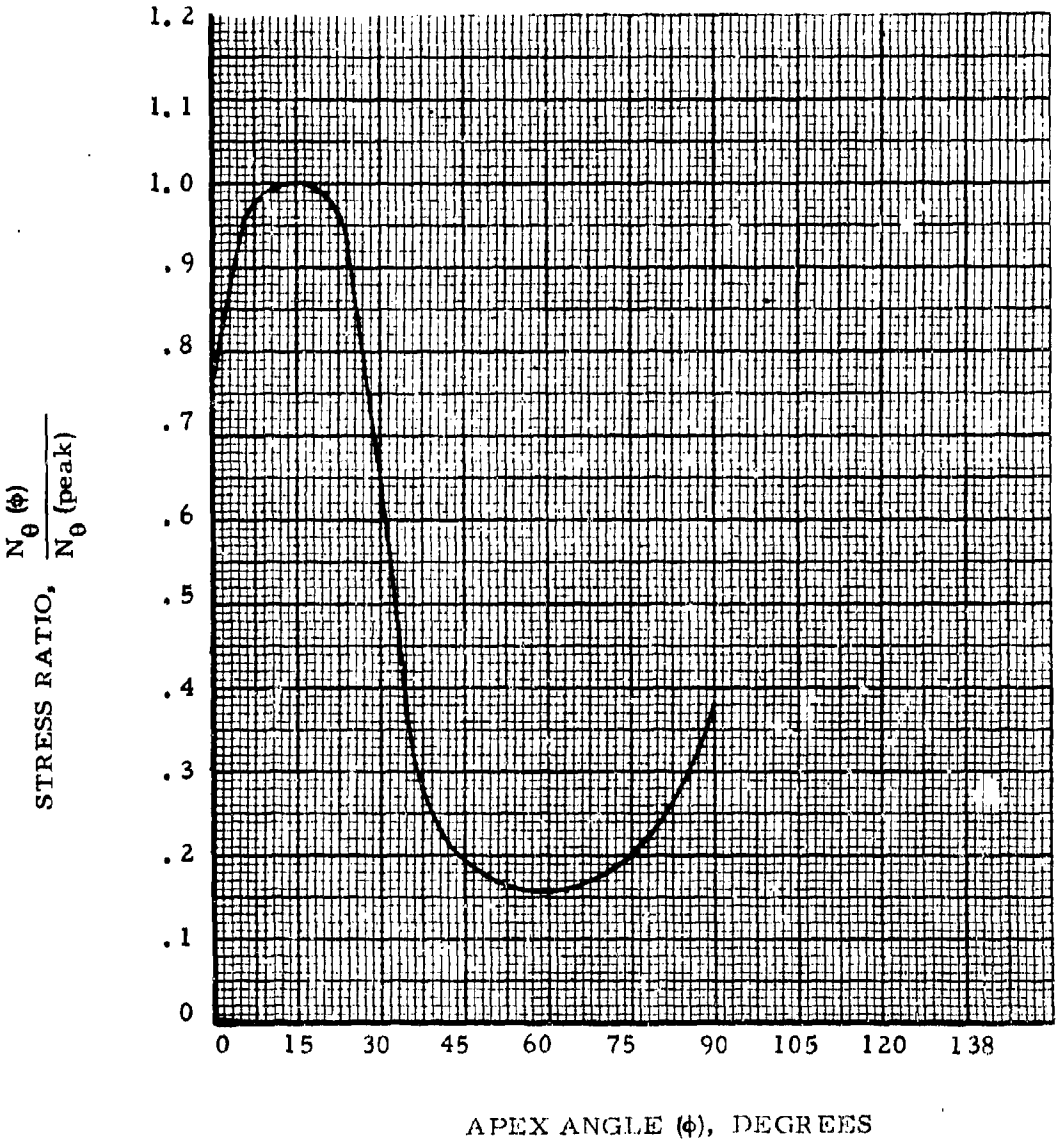

Figure 81. Stress Ratio, $\frac{N_\theta(\phi)}{N_\theta(\text{peak})}$ Vs. Apex Angle, ϕ; Single-Wall Spheres, h/d = 1/2

SINGLE-WALL SPHERES

$\frac{h}{d} = \frac{3}{4}$

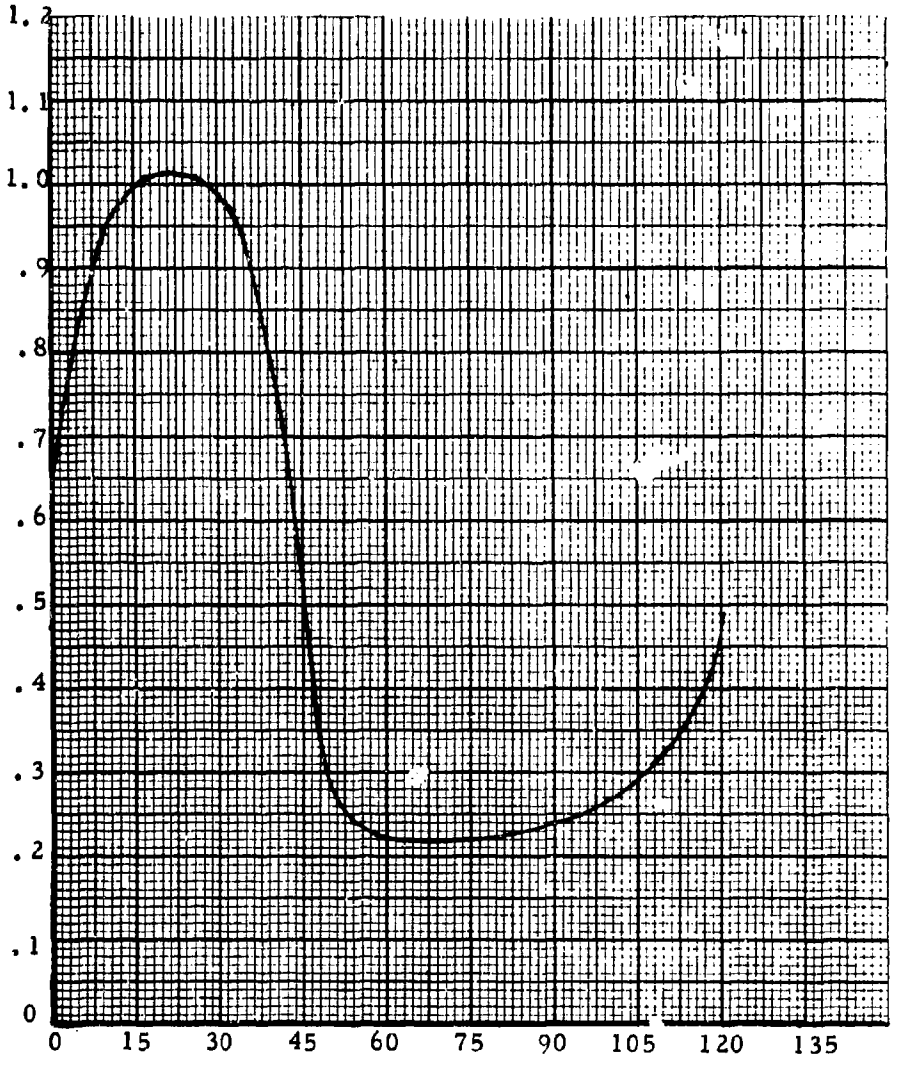

Figure 82. Stress Ratio, $\frac{N_\theta(\phi)}{N_\theta(peak)}$ Vs. Apex Angle, ϕ; Single-Wall Spheres, h/d = 3/4

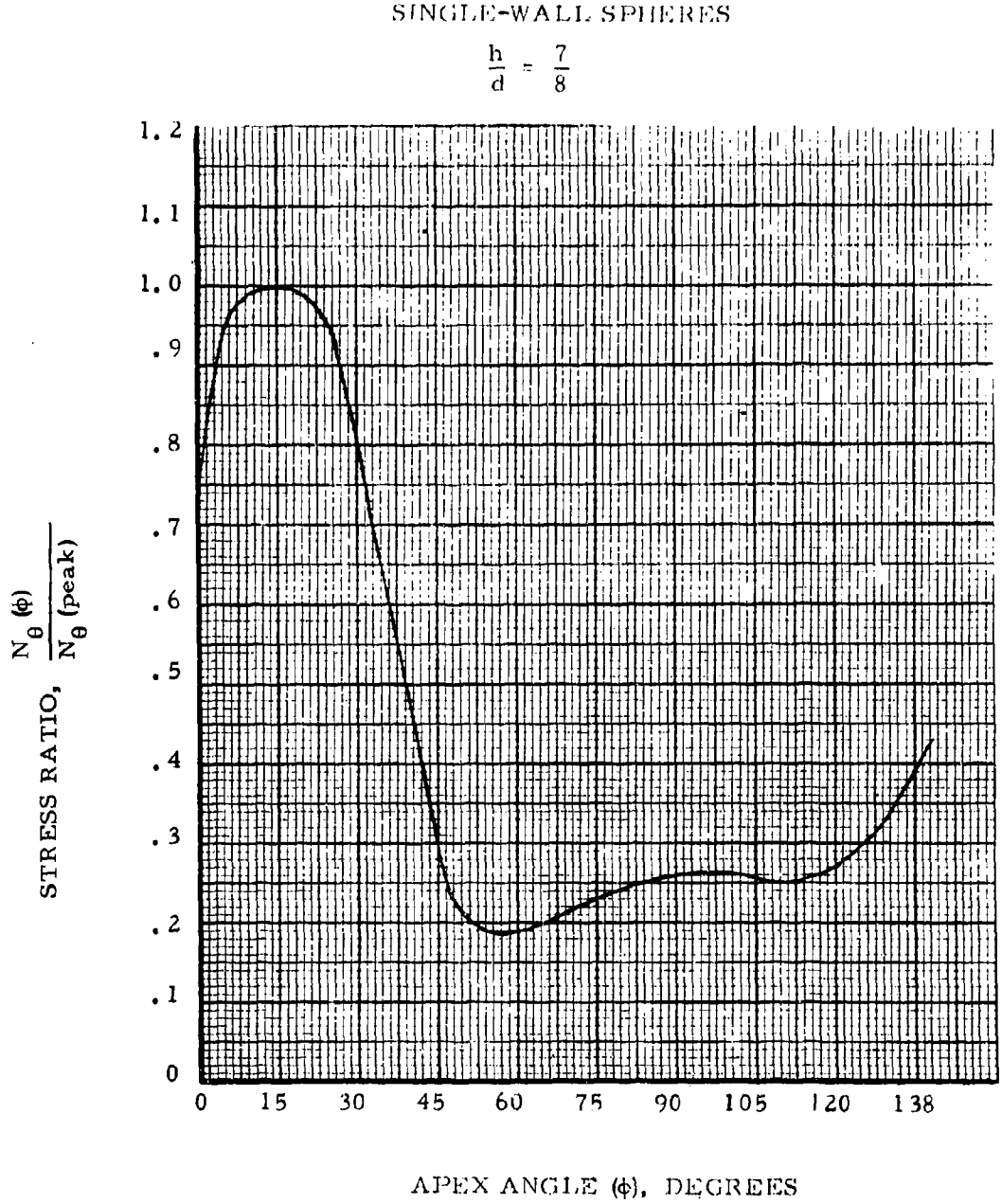

Figure 83. Stress Ratio, $\frac{N_\theta(\phi)}{N_\theta(\text{peak})}$ Vs. Apex Angle, ϕ; Single-Wall Spheres, h/d = 7/8

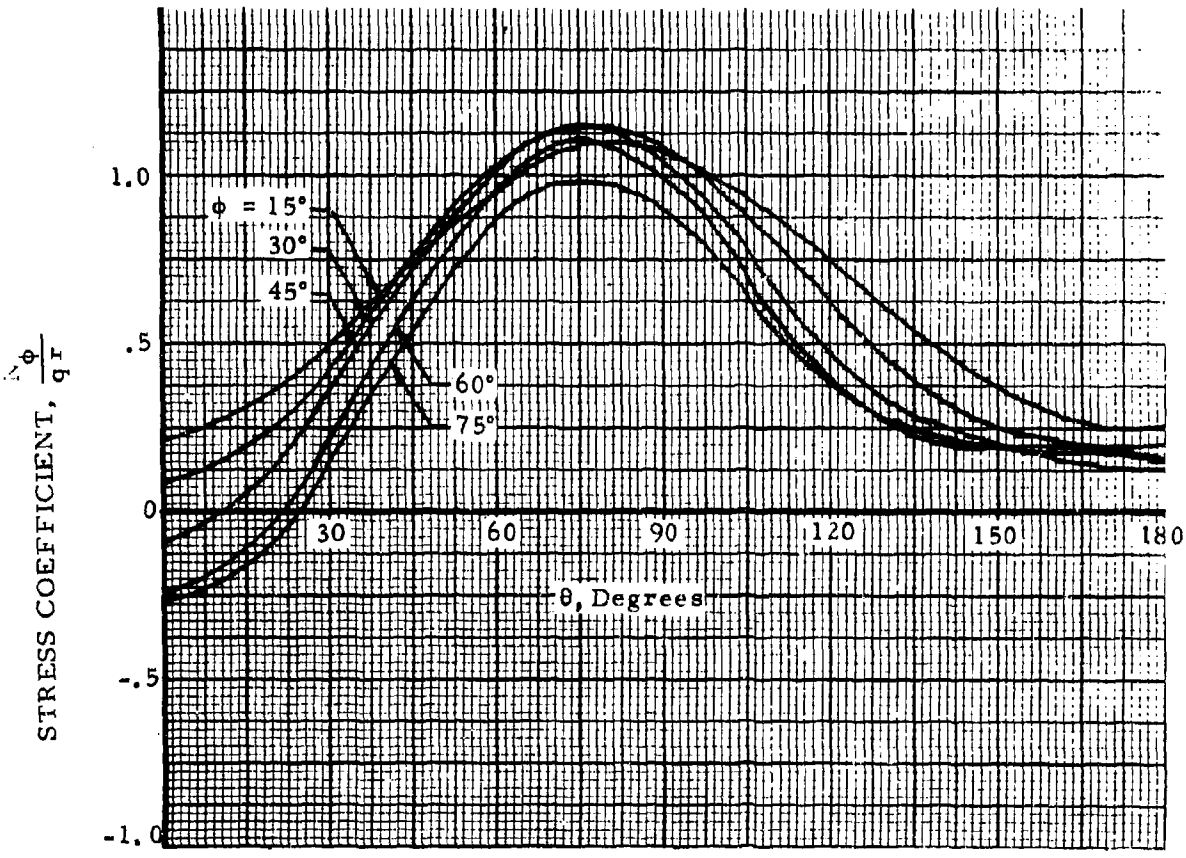

Figure 84. Typical Calculated Stress Coefficients, $\frac{N_\phi}{qr}$; Spherical Ends, h/d = 3/8, P_e = 4/5q, q = .6

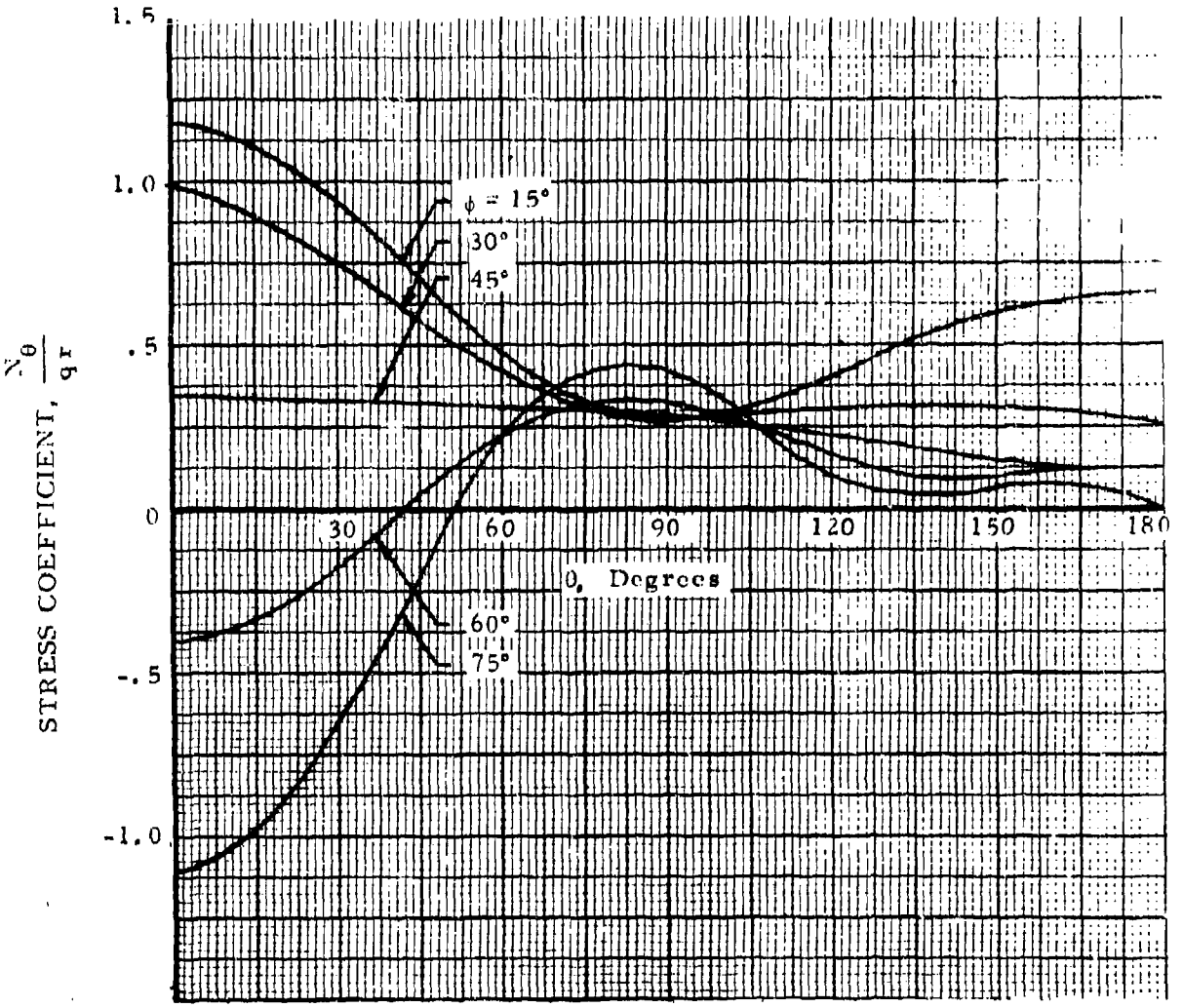

Figure 85. Typical Calculated Stress Coefficients, $\frac{N_\theta}{qr}$; Spherical Ends, h/d = 3/8, P_e = 4/5q, q = .6

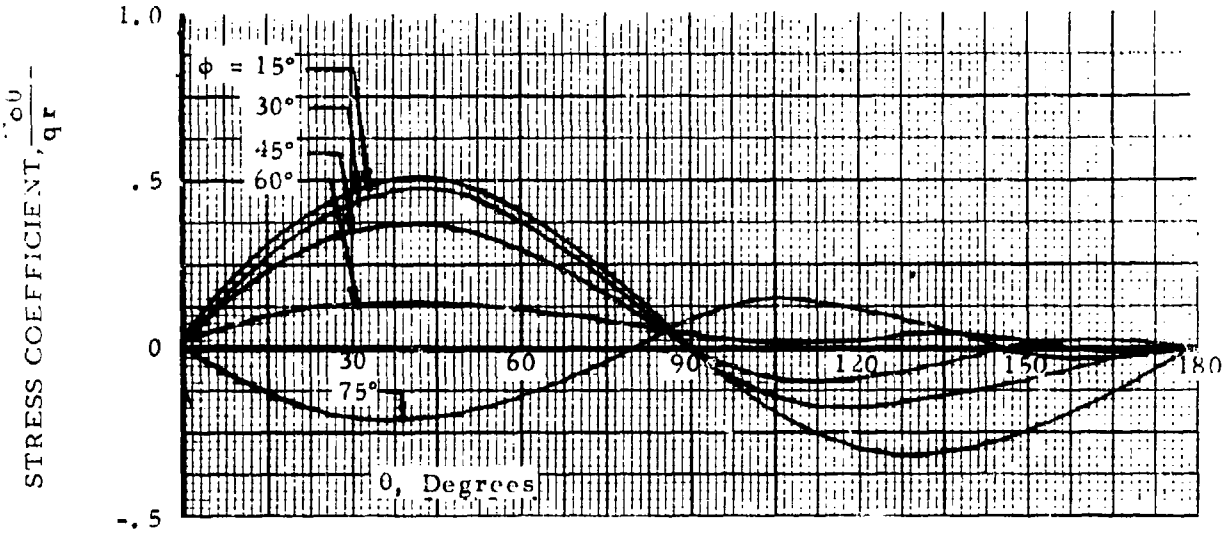

Figure 86. Typical Calculated Stress Coefficients, $\frac{N_\theta}{qr}$; Spherical Ends, h/d = 3/8, P_e = 4/5q, q = .6

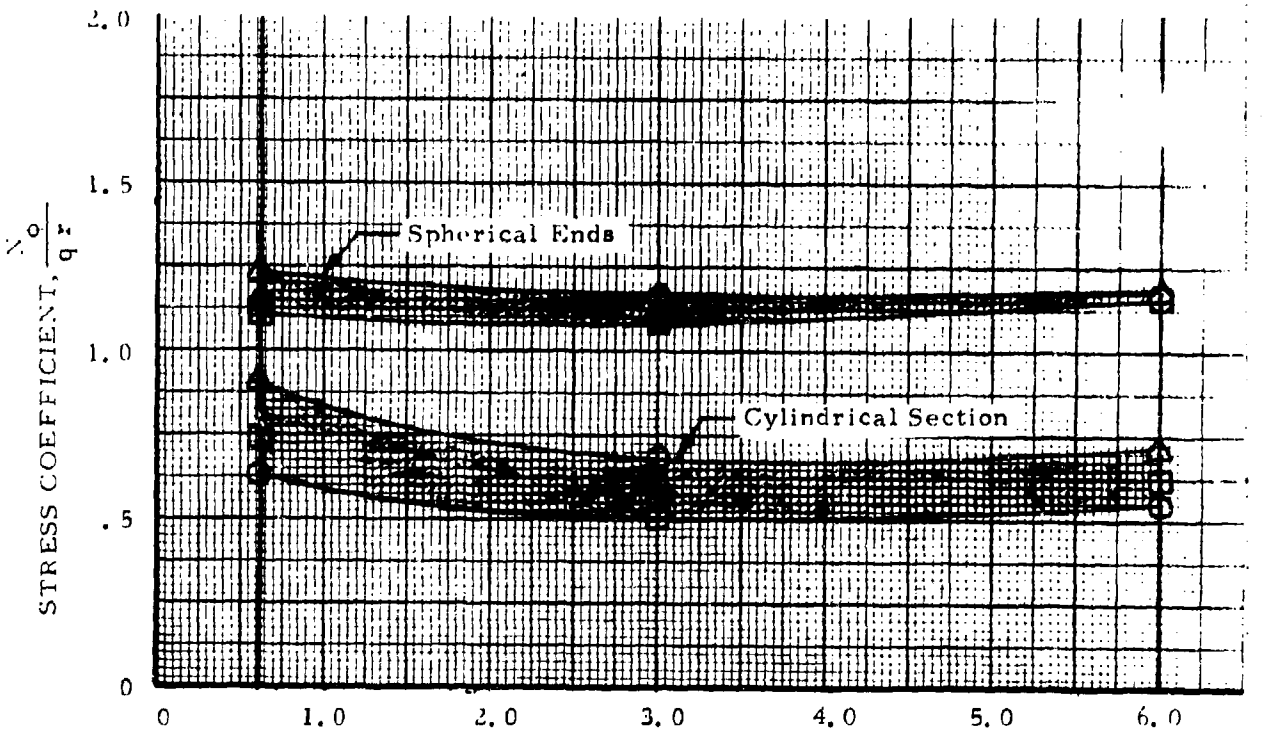

SYM	P_e
⊙	4/5 q
△	1 q
⊡	5/4 q

Figure 87. Array of Calculated Stress Coefficients, $\frac{N_\phi}{qr}$; Cylindrical Tents with Spherical Ends, W/ℓ_h = 1/2, h/d = 3/8

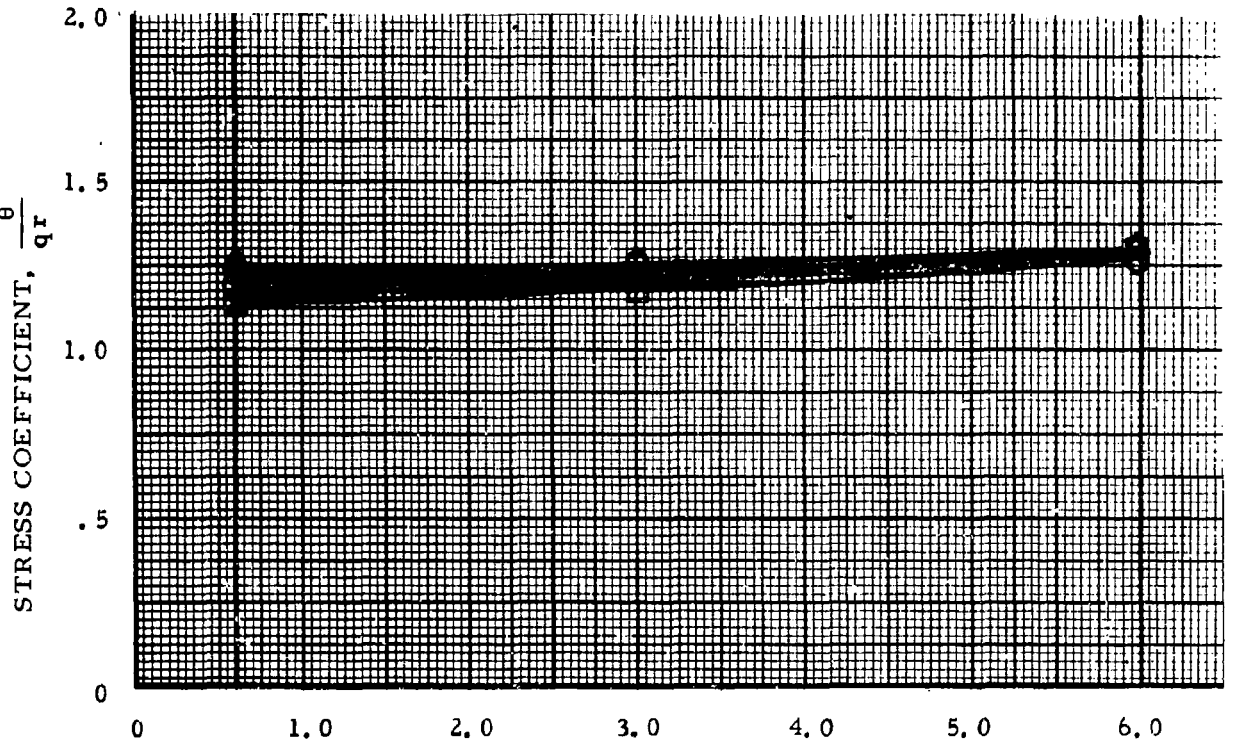

Figure 88. Array of Calculated Stress Coefficients, $\frac{N_\theta}{qr}$; Cylindrical Tents with Spherical Ends. $W/\ell_h = 1/2$, $h/d = 3/8$

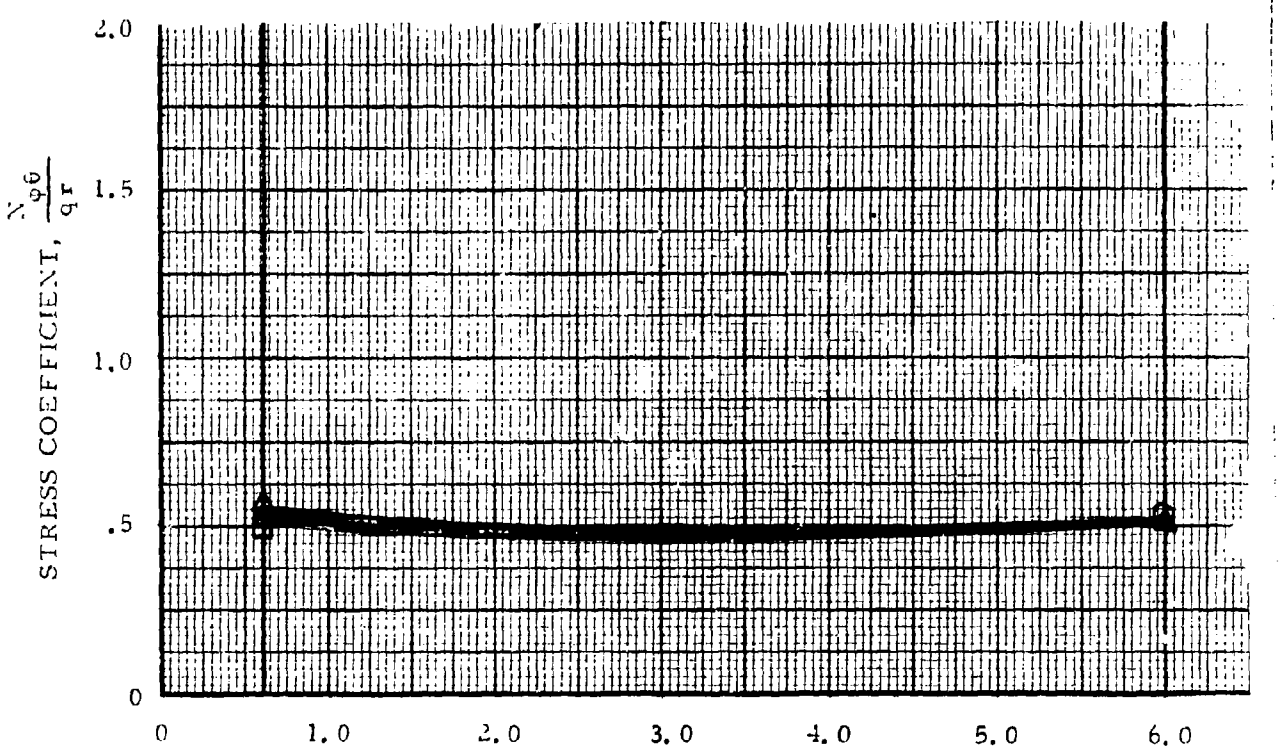

SYM	P_e
⊙	4/5 q
△	1 q
⊡	5/4 q

Figure 89. Array of Calculated Stress Coefficients, $\frac{N_{\phi\theta}}{qr}$; Cylindrical Tents with Spherical Ends, W/ℓ_h = 1/2, h/d = 3/8

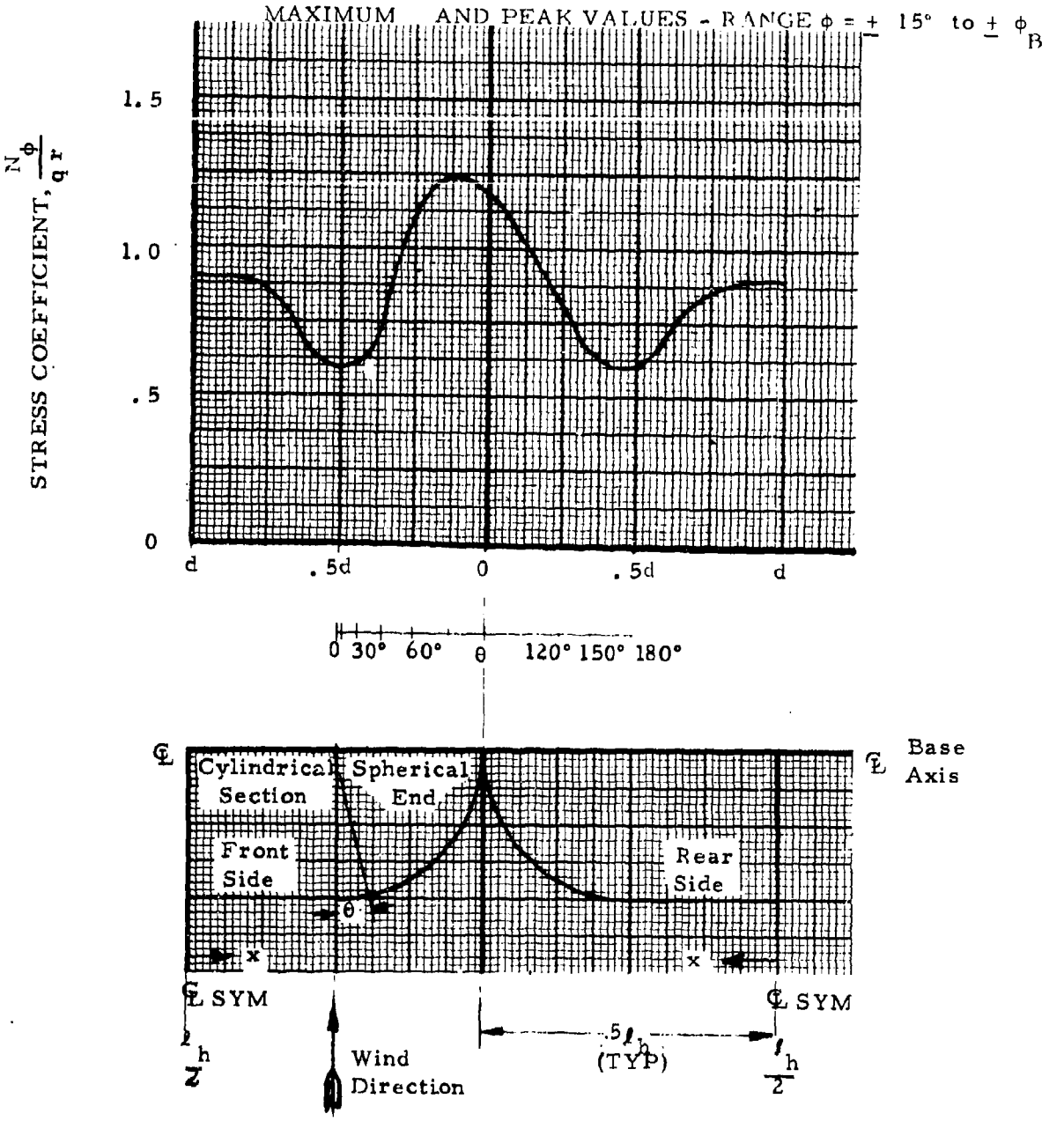

Figure 90. Typical Annular - Longitudinal Stress Coefficient, $\frac{N_\phi}{qr}$, Distribution; Cylindrical Tents with Spherical Ends, $W/\ell_h = 1/2$, $h/d = 3/8$

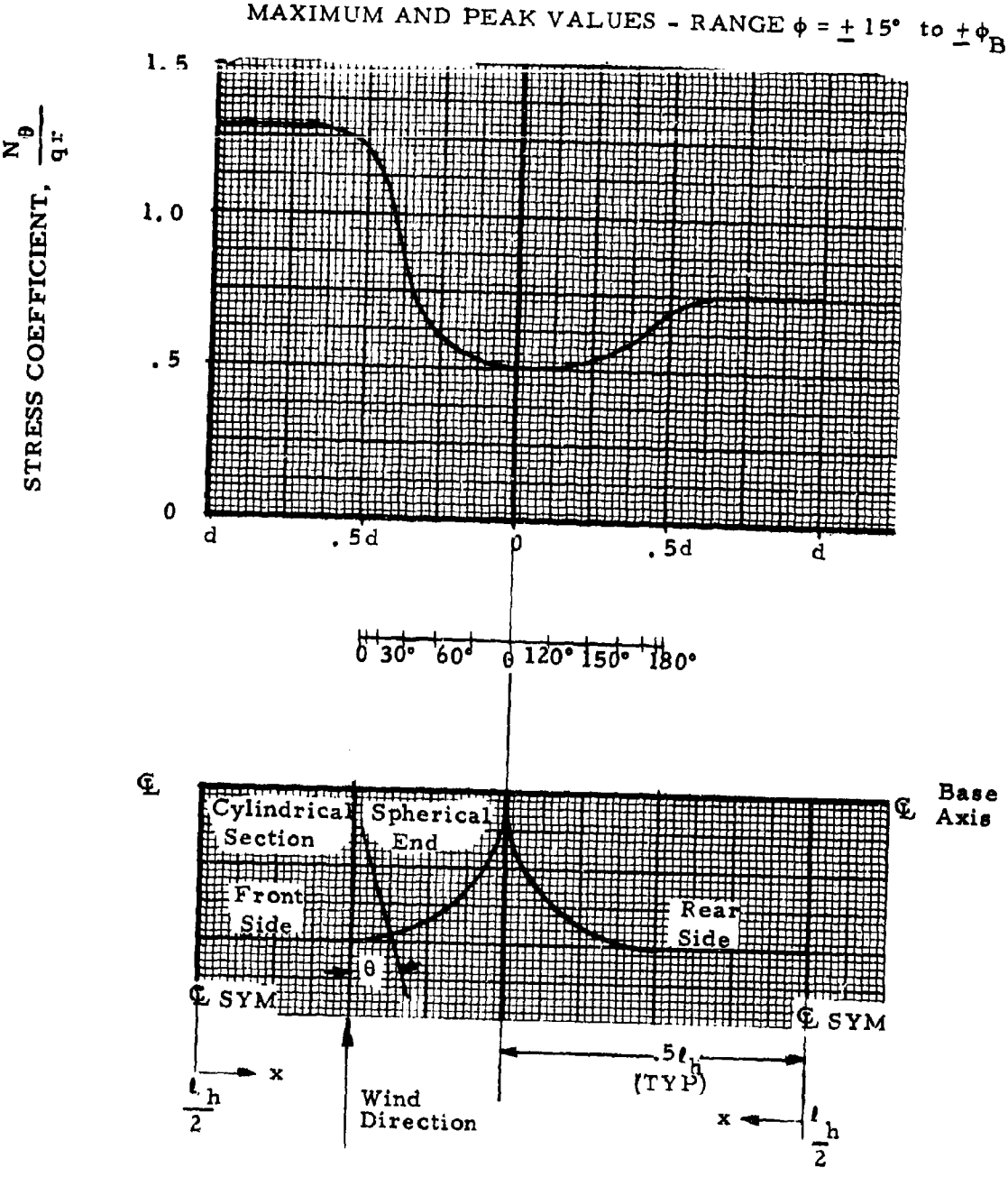

Figure 91. Typical Annular - Longitudinal Stress Coefficient, $\frac{N_\theta}{qr}$, Distribution; Cylindrical Tents with Spherical Ends, $W/\ell_h = 1/2$, $h/d = 3/8$

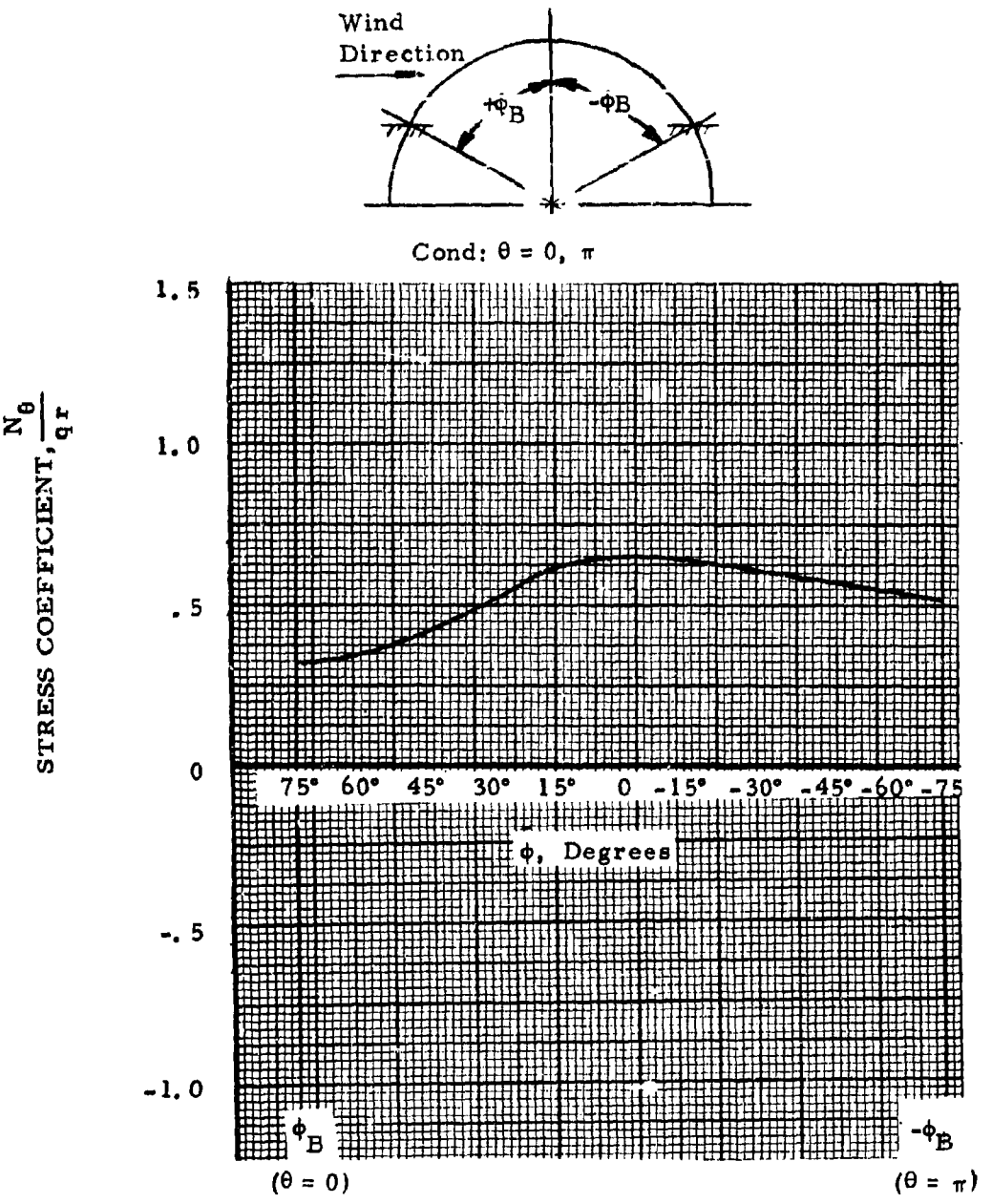

Figure 92. Typical Maximum Peripheral Stress Coefficient, $\frac{N_\theta}{qr}$, Distribution; Cylindrical - Spherical End Junction, $W/\ell_h = 1/2$, $h/d = 3/8$

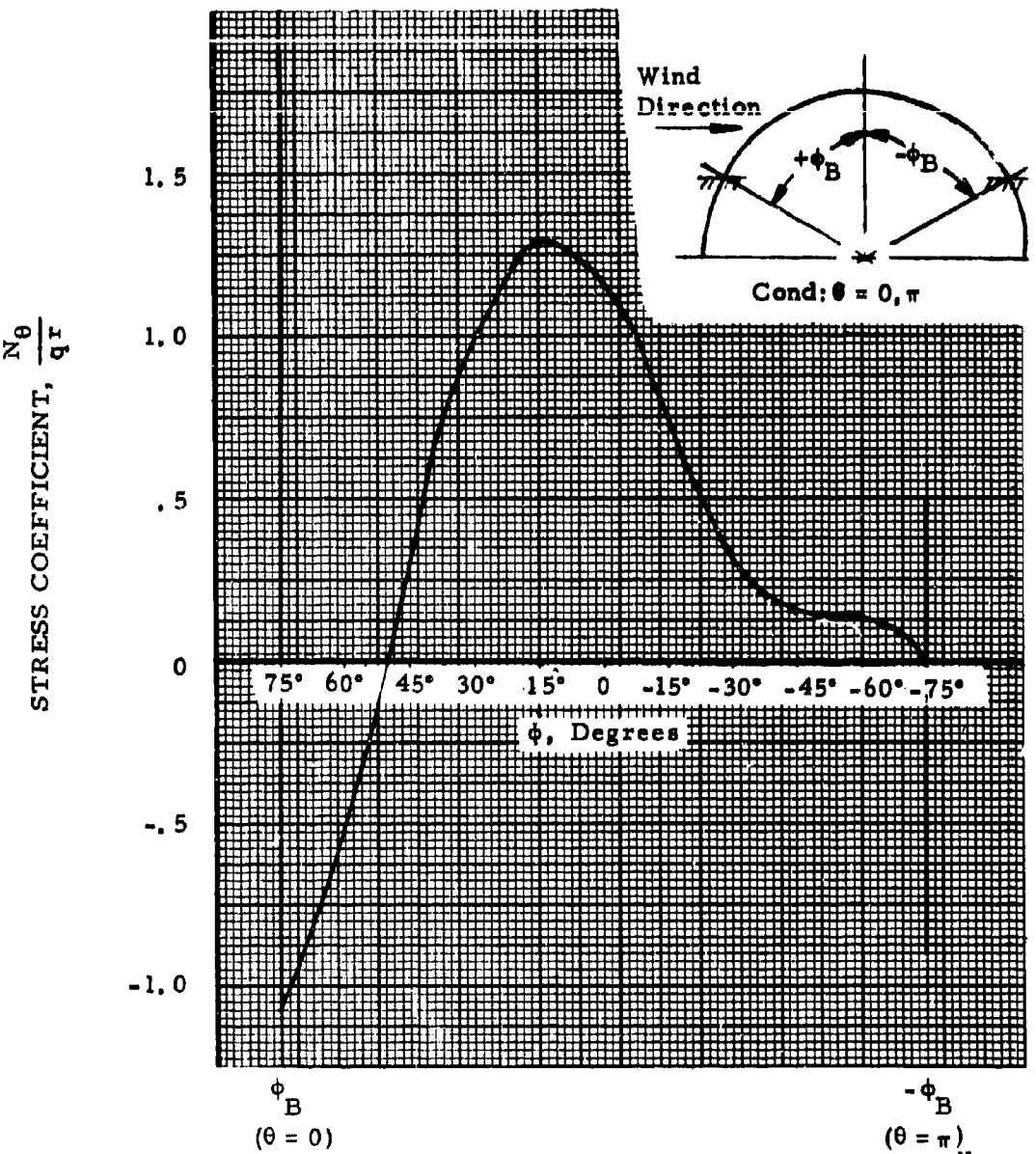

Figure 93. Typical Maximum Peripheral Stress Coefficient, $\frac{N_\theta}{qr}$, Distribution; Cylindrical - Spherical End Junction, $W/\ell_h = 1/2$, $h/d = 3/8$

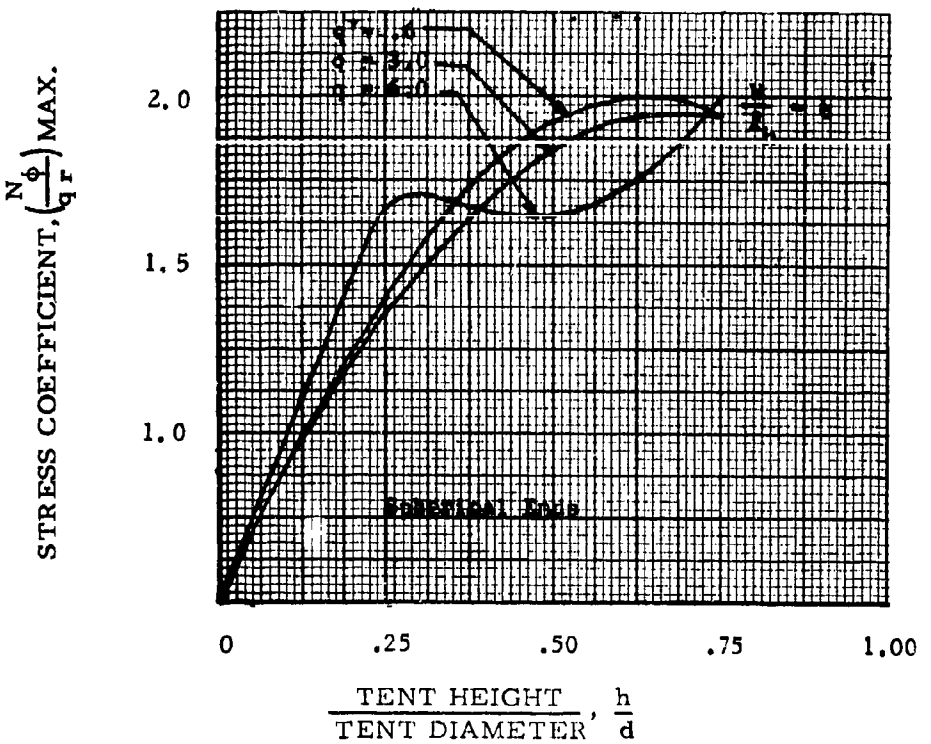

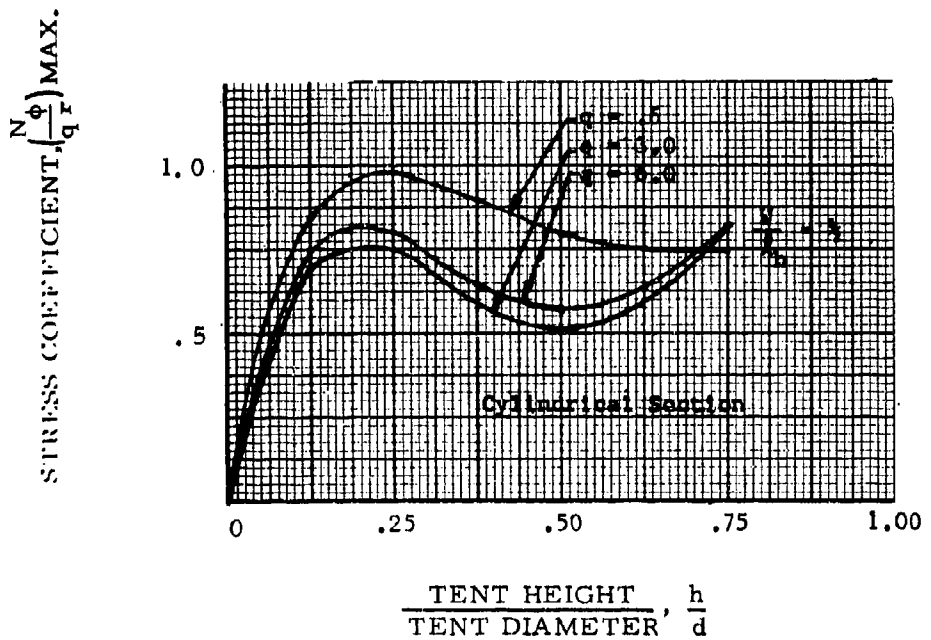

Figure 94. Maximum Design Stress Coefficient, $\frac{N_\phi}{qr}$, Specific Dynamic Pressure

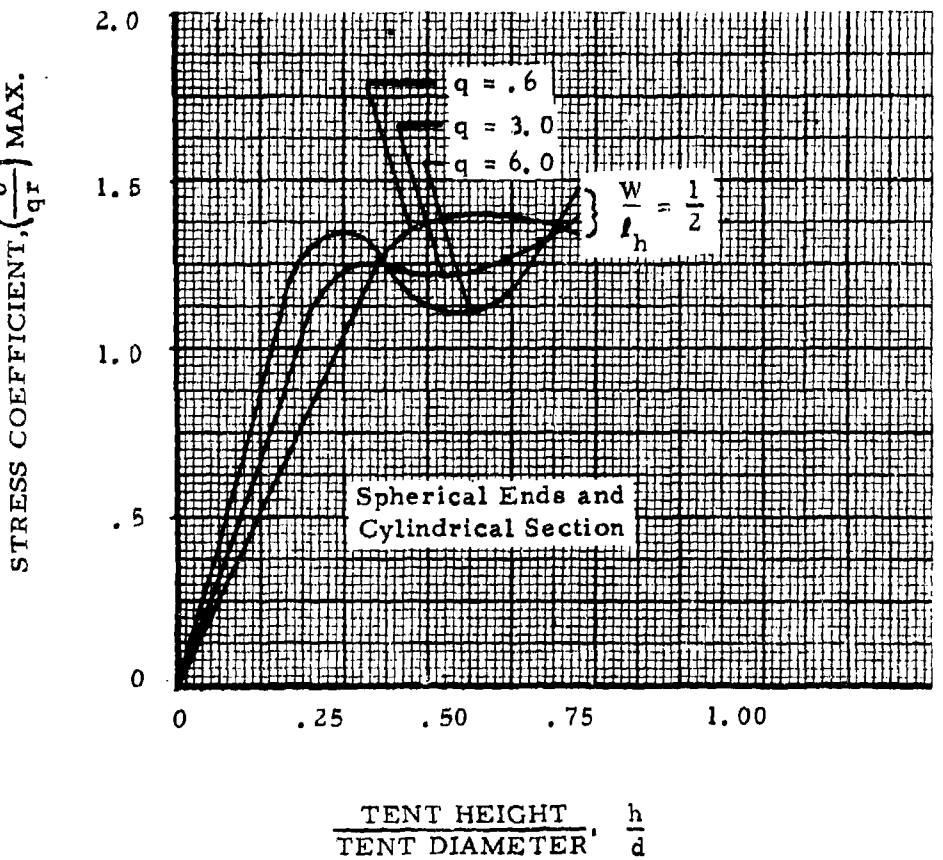

Figure 95. Maximum Design Stress Coefficient, $\frac{N_\theta}{qr}$, Specific Dynamic Pressure

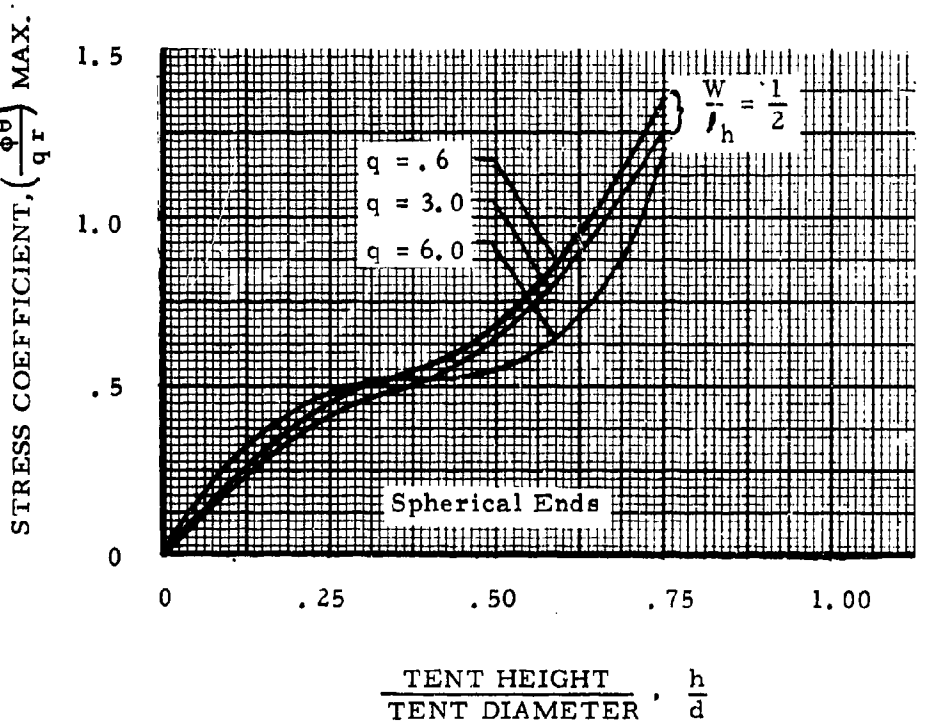

Figure 96. Maximum Design Stress Coefficient, $\frac{N_{\phi\theta}}{qr}$, Specific Dynamic Pressure

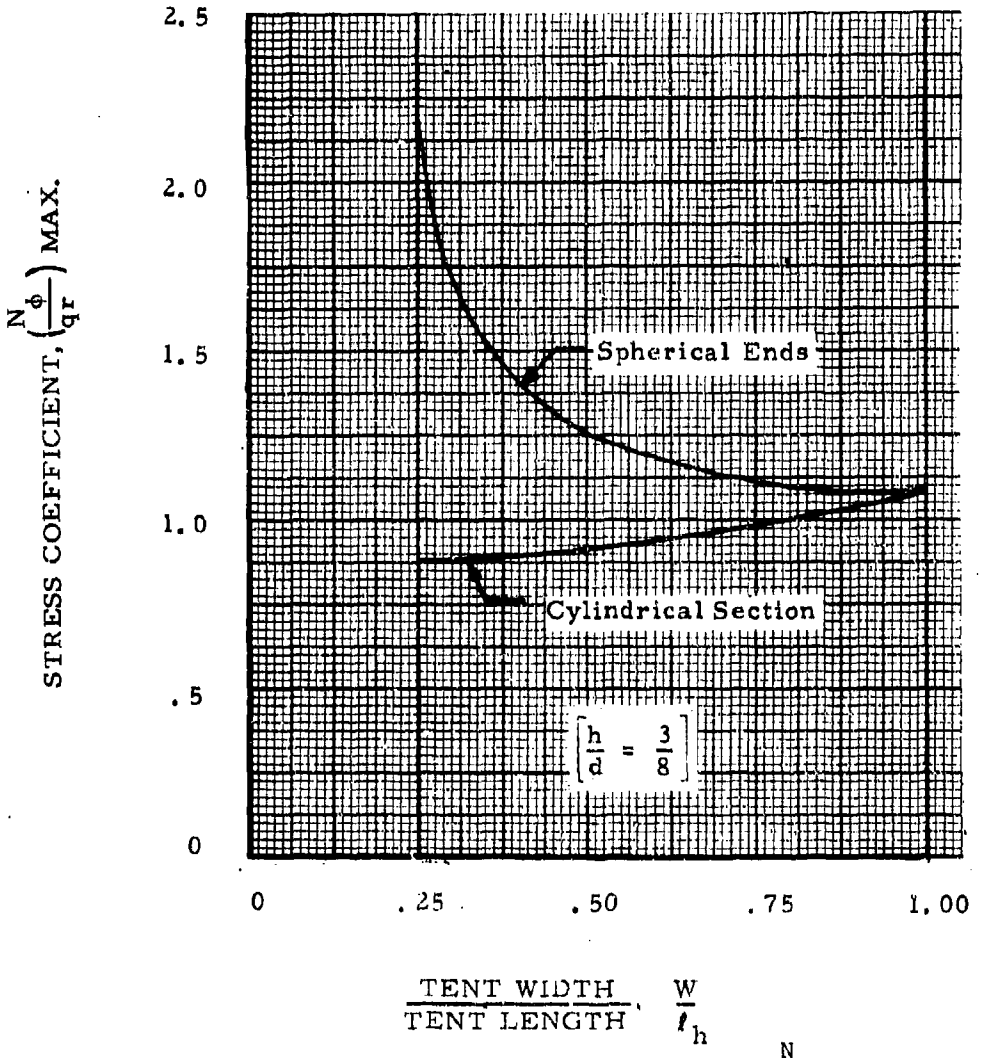

Figure 97. Maximum Design Stress Coefficient, $\frac{N_\phi}{qr}$, Dynamic Pressure Limit ($q = 6.0$) Constant $h/d - W/\ell_h$ Range ($W/\ell_h = .25$ to 1.00), $h/d = 3/8$

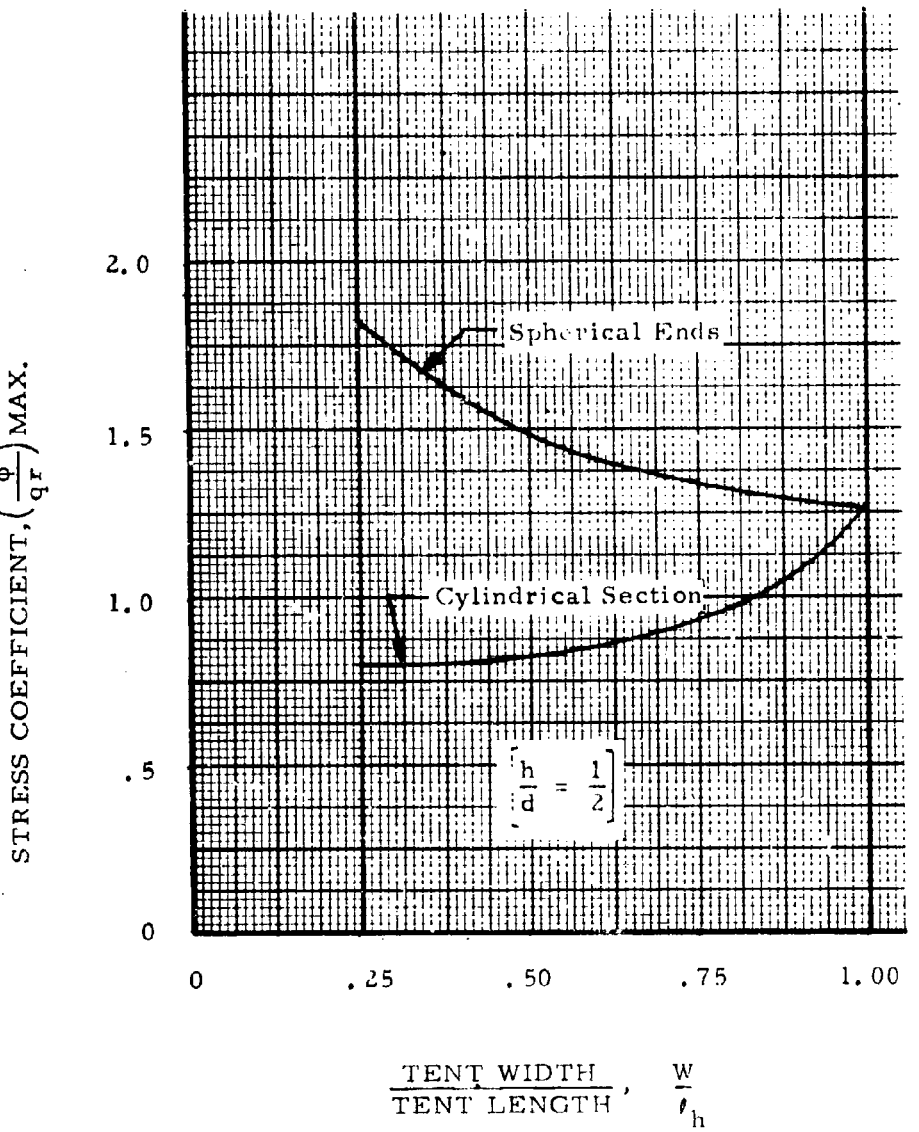

Figure 98. Maximum Design Stress Coefficient, $\frac{N_\phi}{qr}$, Dynamic Pressure Limit (q = 6.0) Constant h/d - W/ℓ_h Range (W/ℓ_h = .25 to 1.00), h/d = 1/2

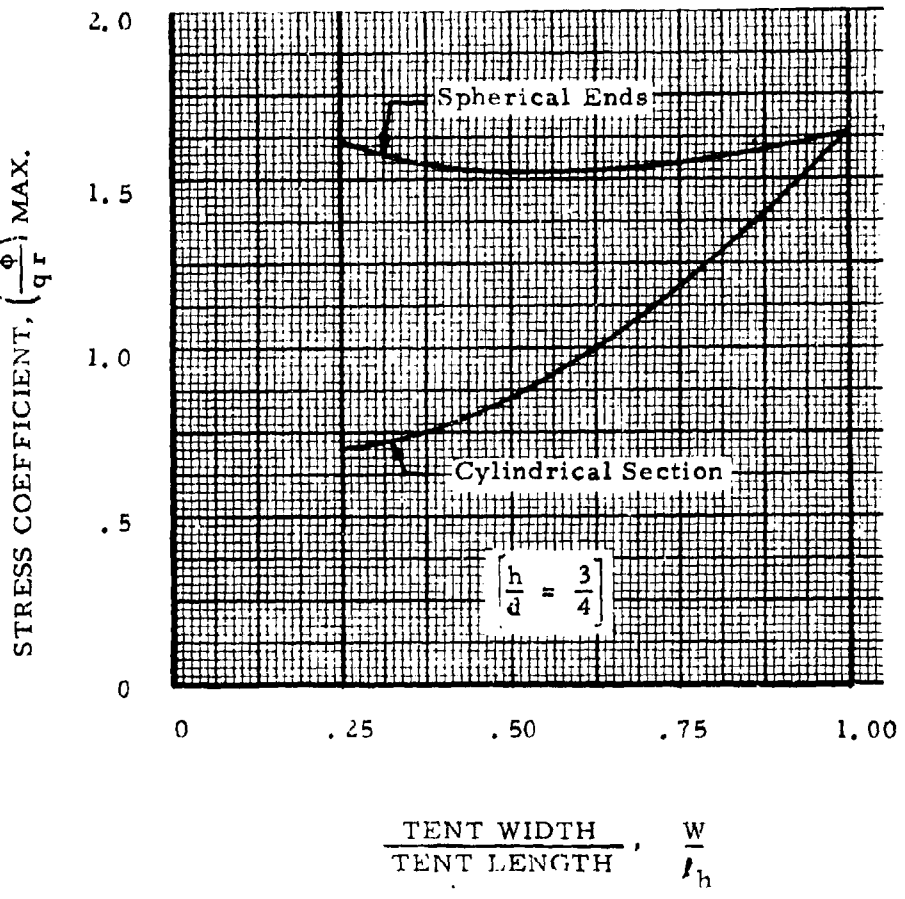

Figure 99. Maximum Design Stress Coefficient, $\frac{N_\phi}{qr}$, Dynamic Pressure Limit (q = 6.0) Constant h/d - W/ℓ_h Range (W/ℓ_h = .25 to 1.00), h/d = 3/4

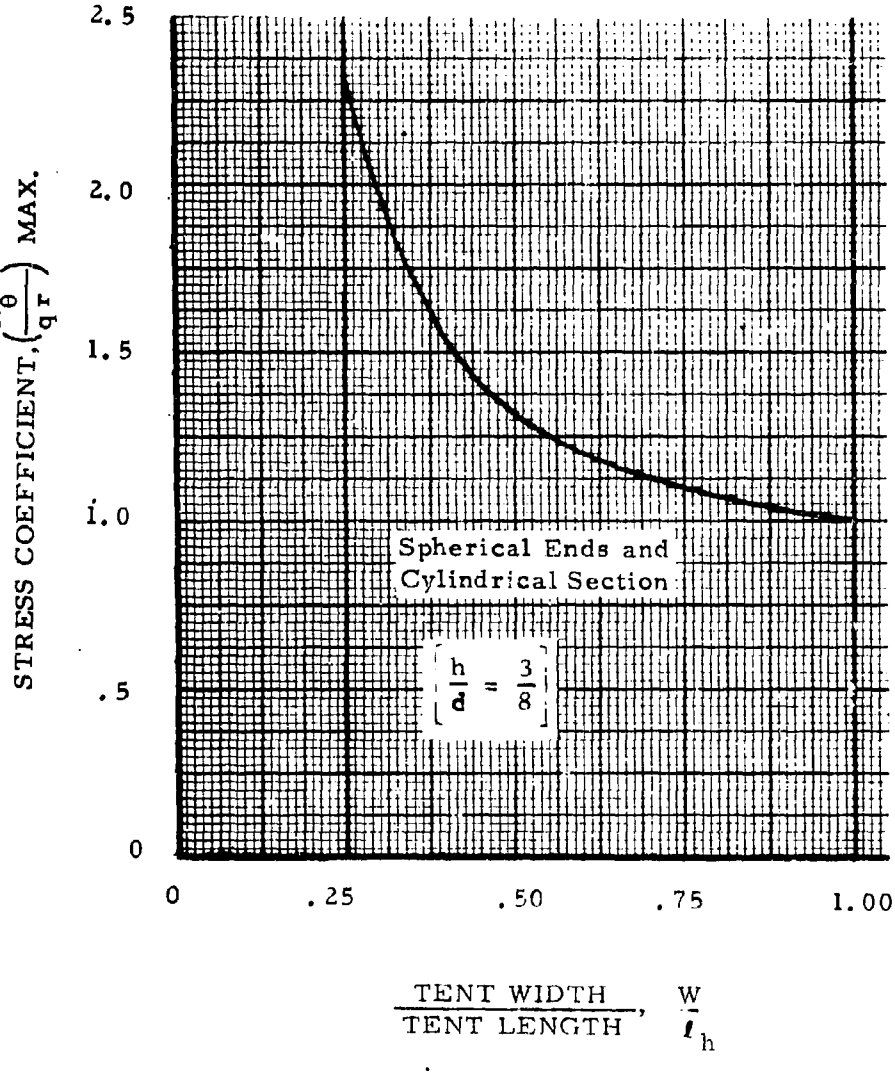

Figure 100. Maximum Design Stress Coefficient, $\frac{N_\theta}{qr}$, Dynamic Pressure Limit (q = 6.0) Constant h/d - W/ℓ_h Range (W/ℓ_h = .25 to 1.00), h/d = 3/8

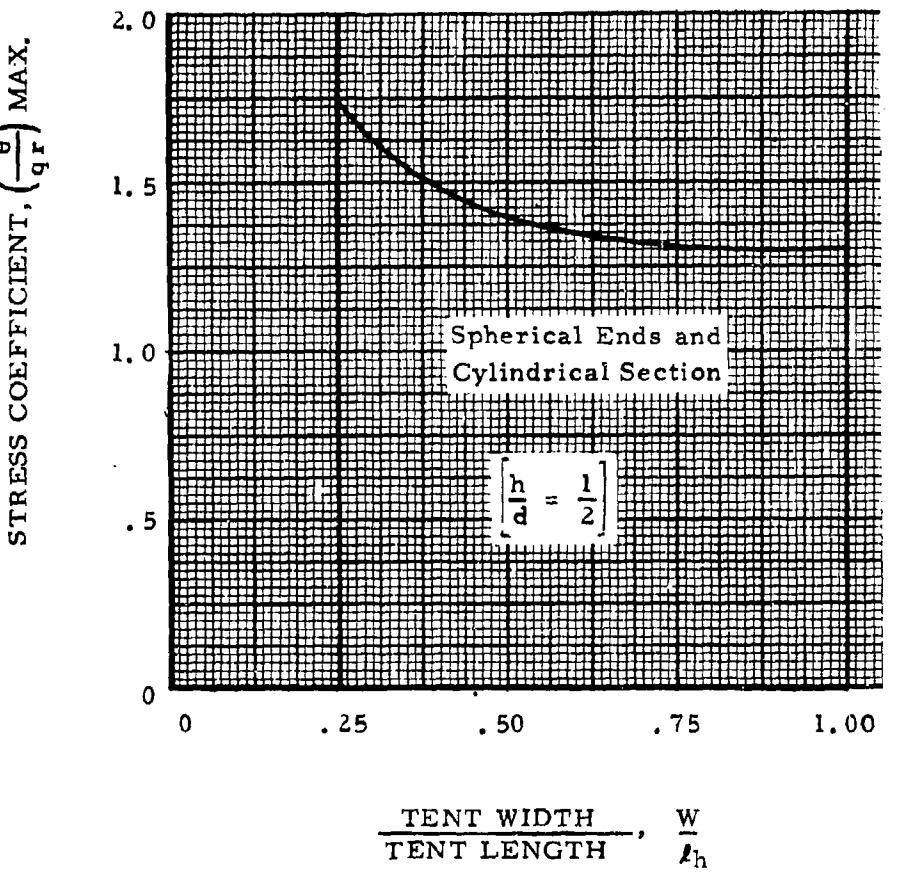

Figure 101. Maximum Design Stress Coefficient, $\frac{N_\theta}{qr}$, Dynamic Pressure Limit (q = 6.0) Constant h/d - W/ℓ_h Range (W/ℓ_h = .25 to 1.00), h/d = 1/2

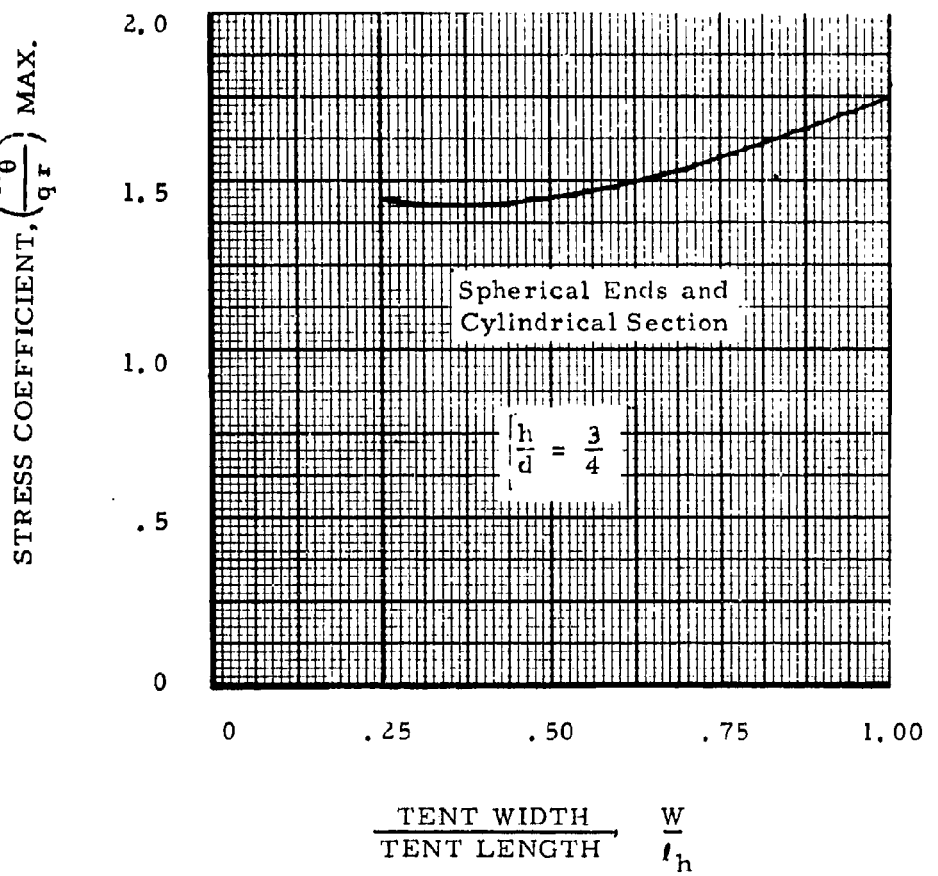

Figure 102. Maximum Design Stress Coefficient, $\frac{N_\theta}{qr}$, Dynamic Pressure Limit (q = 6.0) Constant h/d - W/ℓ_h Range (W/ℓ_h = .25 to 1.00), h/d = 3/4

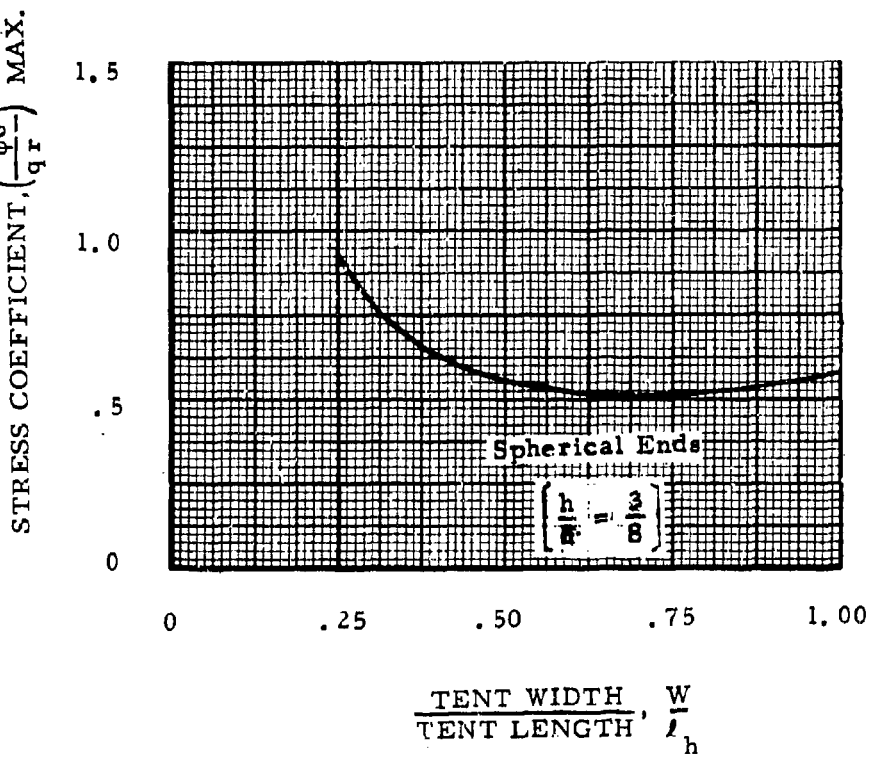

Figure 103. Maximum Design Stress Coefficient, $\frac{N_{\phi\theta}}{qr}$, Dynamic Pressure Limit (q = 6.0) Constant h/d - W/ℓ_h Range (W/ℓ_h = .25 to 1.00), h/d = 3/8

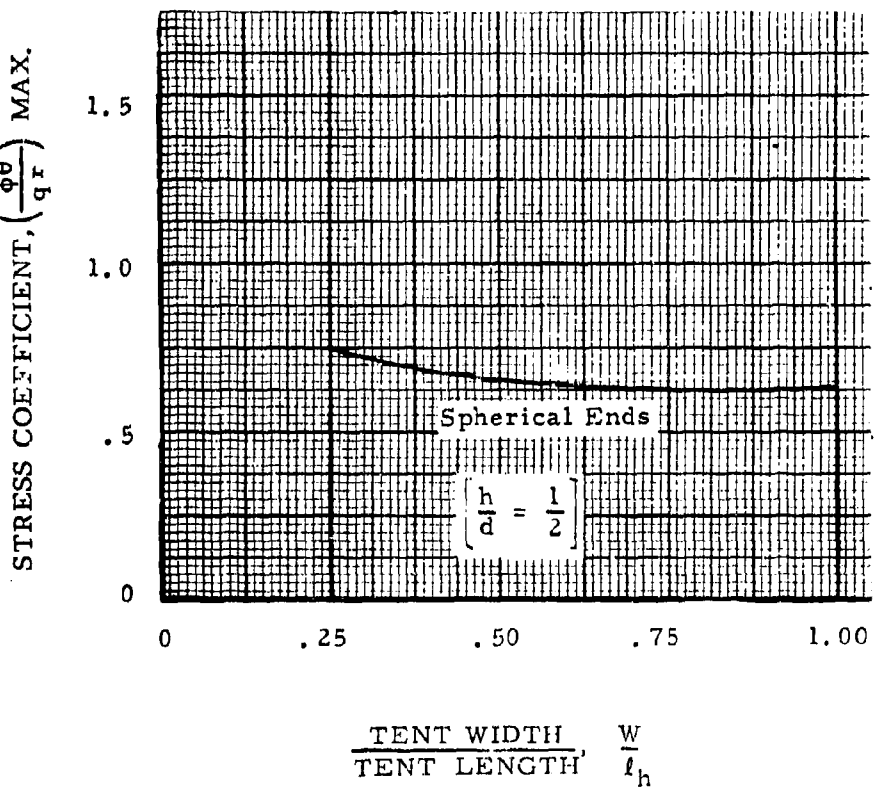

Figure 104. Maximum Design Stress Coefficient, $\frac{N_{\phi\theta}}{qr}$, Dynamic Pressure Limit (q = 6.0) Constant h/d - W/ℓ_h Range (W/ℓ_h = .25 to 1.00), h/d = 1/2

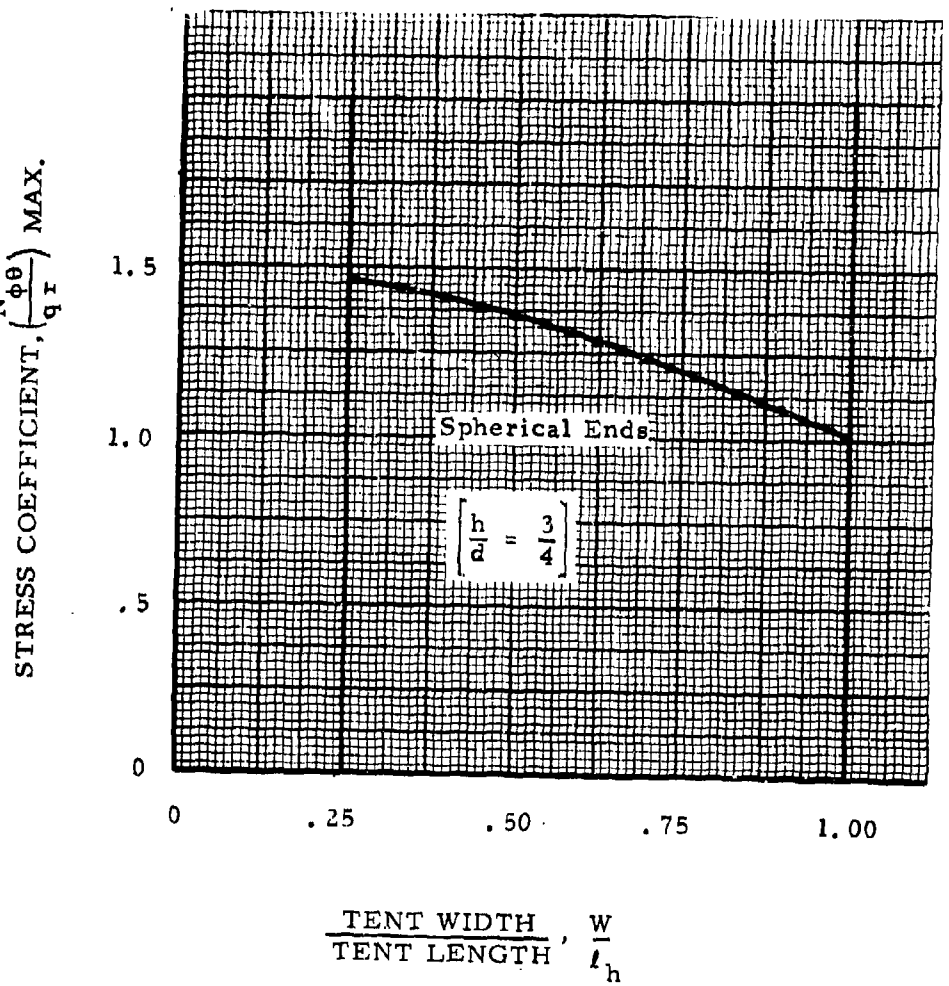

Figure 105. Maximum Design Stress Coefficient, $\frac{N_{\phi\theta}}{qr}$, Dynamic Pressure Limit (q = 6.0) Constant h/d - W/ℓ_h Range (W/ℓ_h = .25 to 1.00), h/d = 3/4

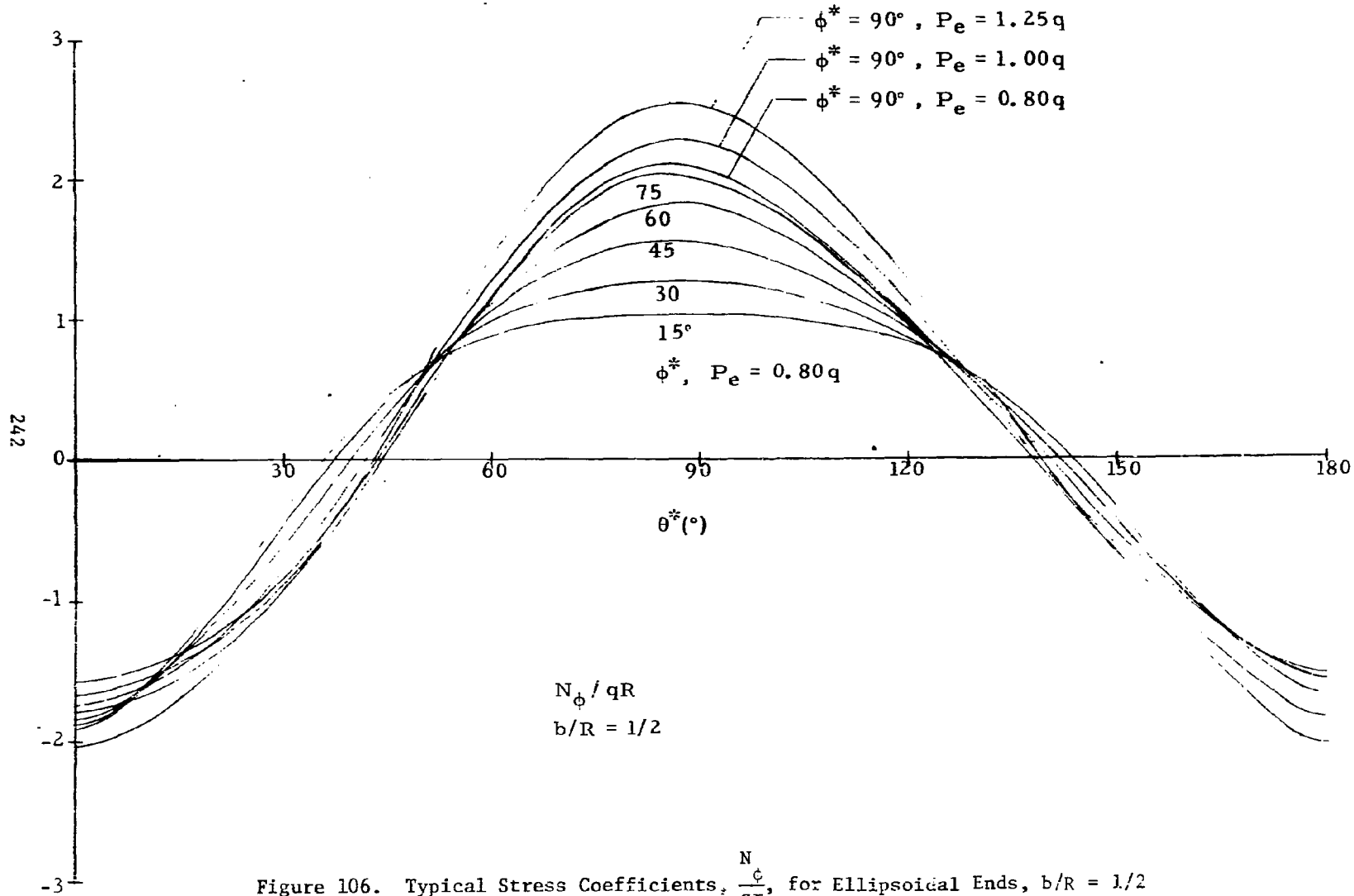

Figure 106. Typical Stress Coefficients, $\frac{N_\phi}{qr}$, for Ellipsoidal Ends, b/R = 1/2

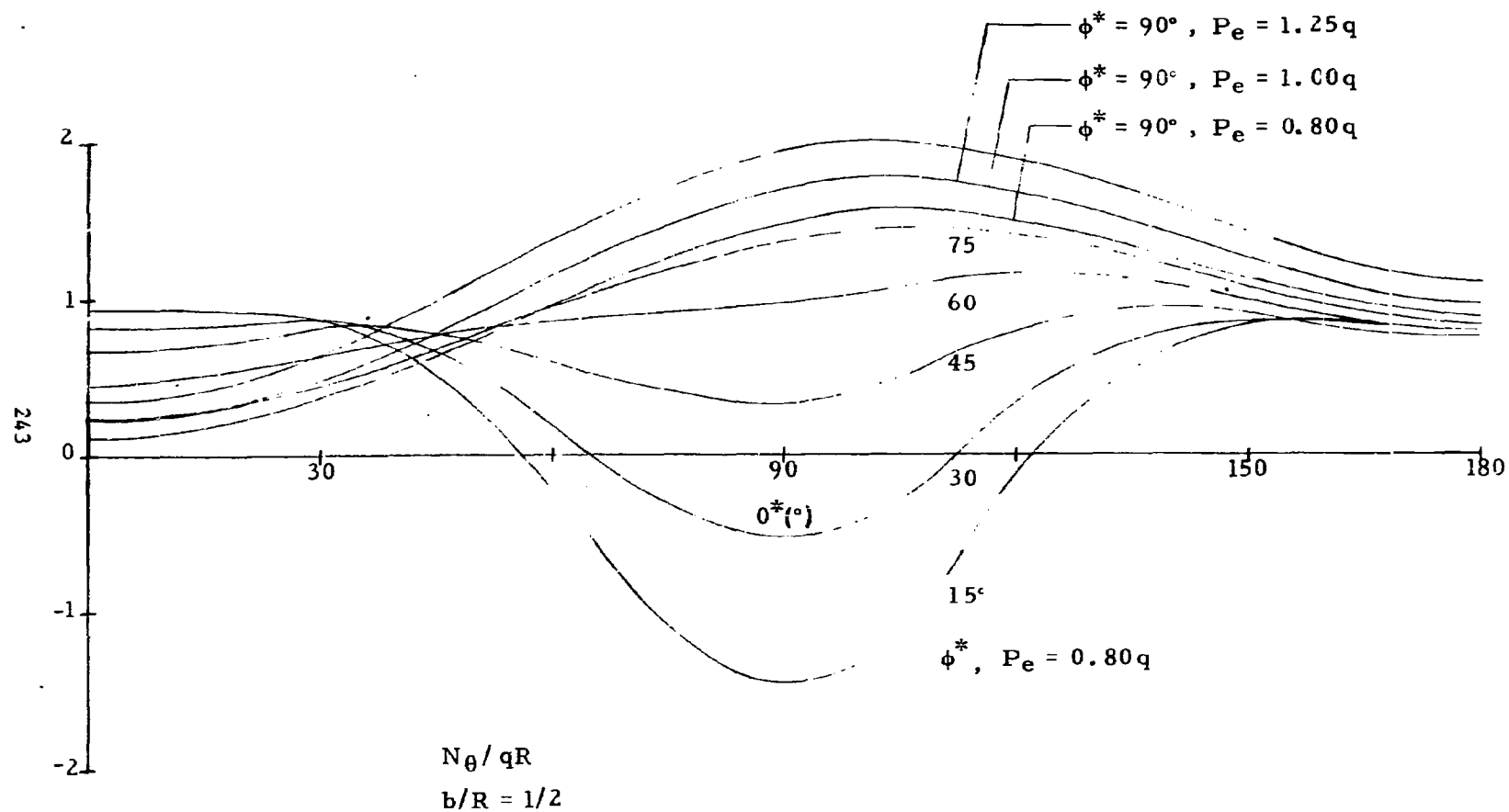

Figure 107. Typical Stress Coefficients, $\frac{N_\theta}{qr}$, for Ellipsoidal Ends, b/R = 1/2

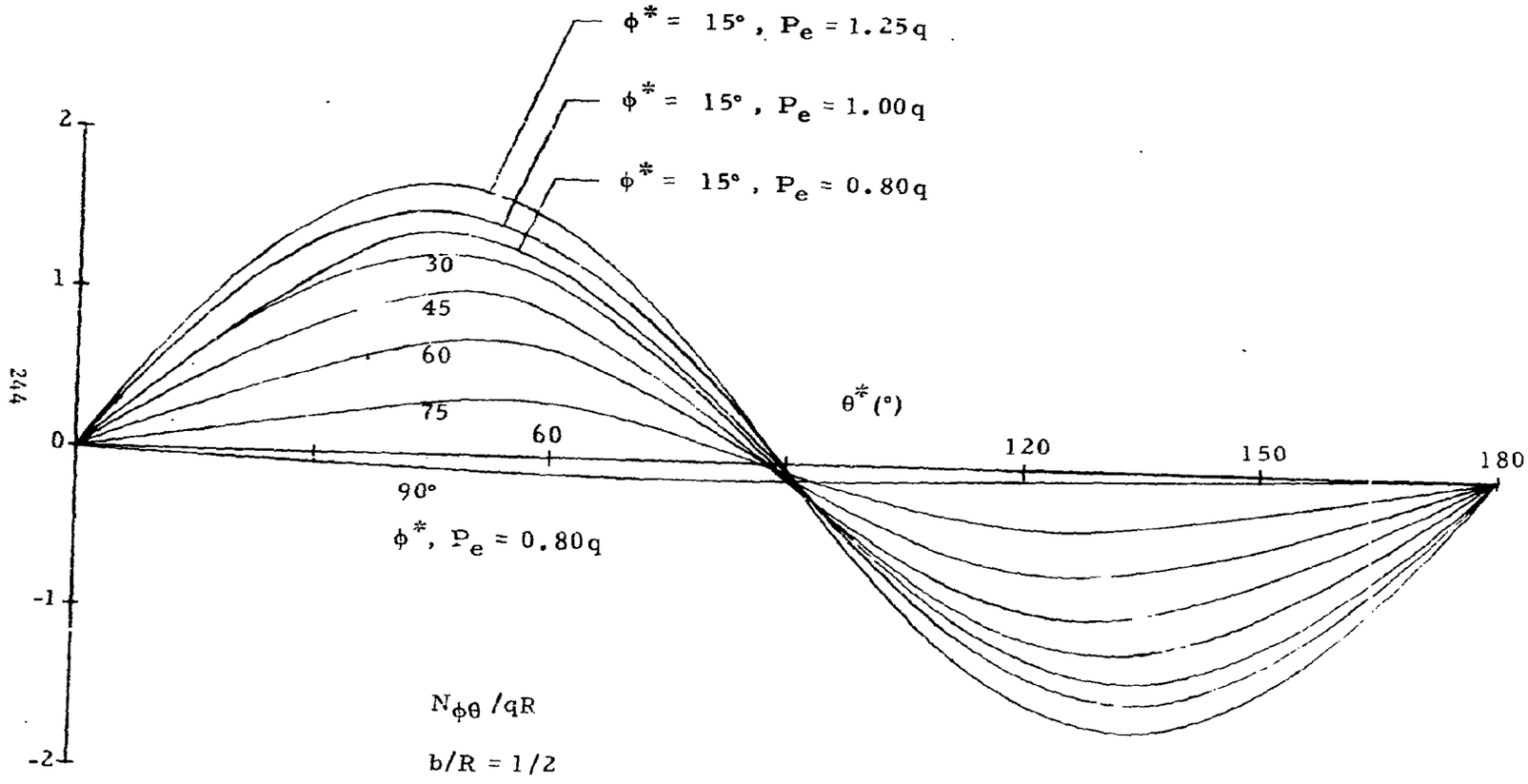

Figure 108. Typical Stress Coefficients, $\frac{N_{\phi\theta}}{qr}$, for Ellipsoidal Ends, b/R = 1/2

Basic Maximum Stress Coefficients for

h/d = 1/2

W/ℓ_h = 1/2

b/r = 1/2

P_e/q = 1

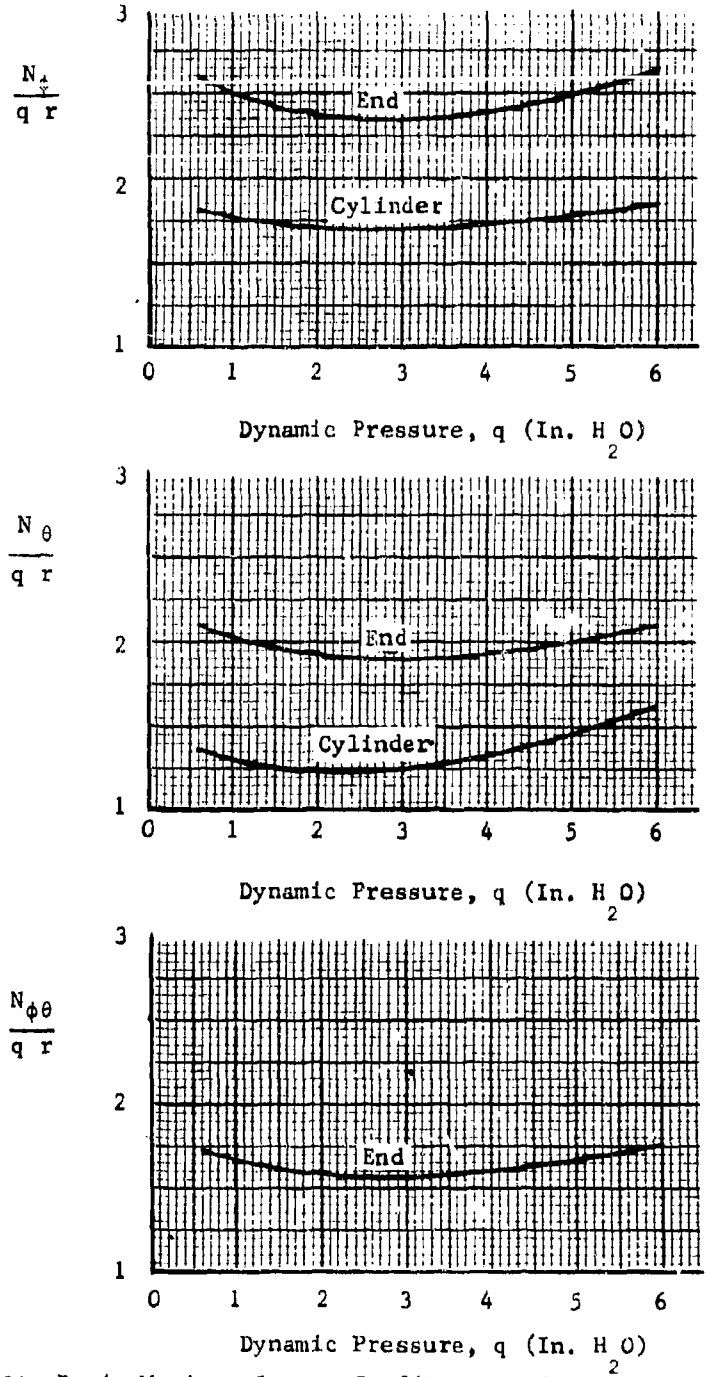

Figure 109. Basic Maximum Stress Coefficients for Cylindrical Tents with Ellpsoidal Ends, b/R = 1/2

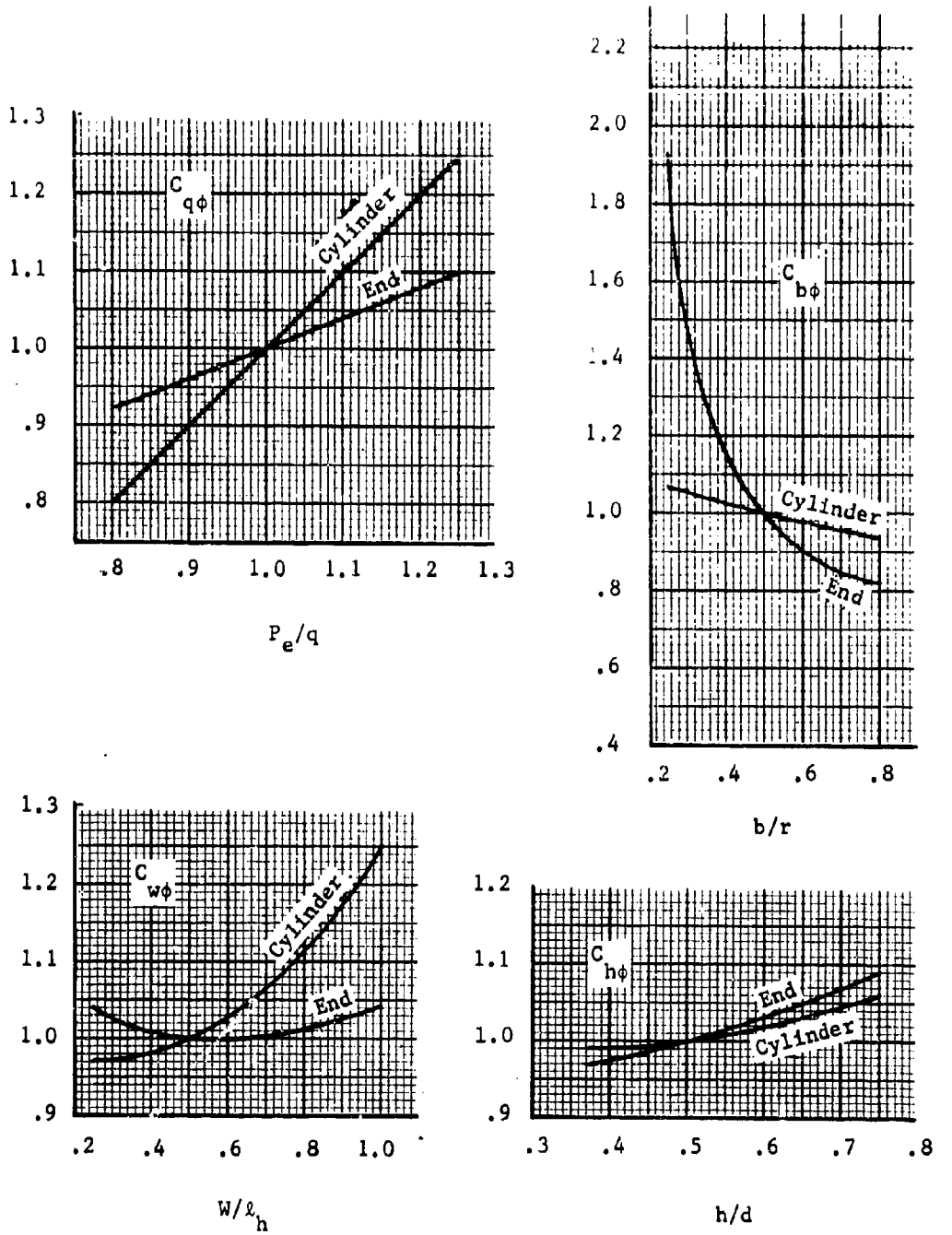

Figure 110. Correction Factors, (ϕ), for Cylindrical Tents with Ellipsoidal Ends

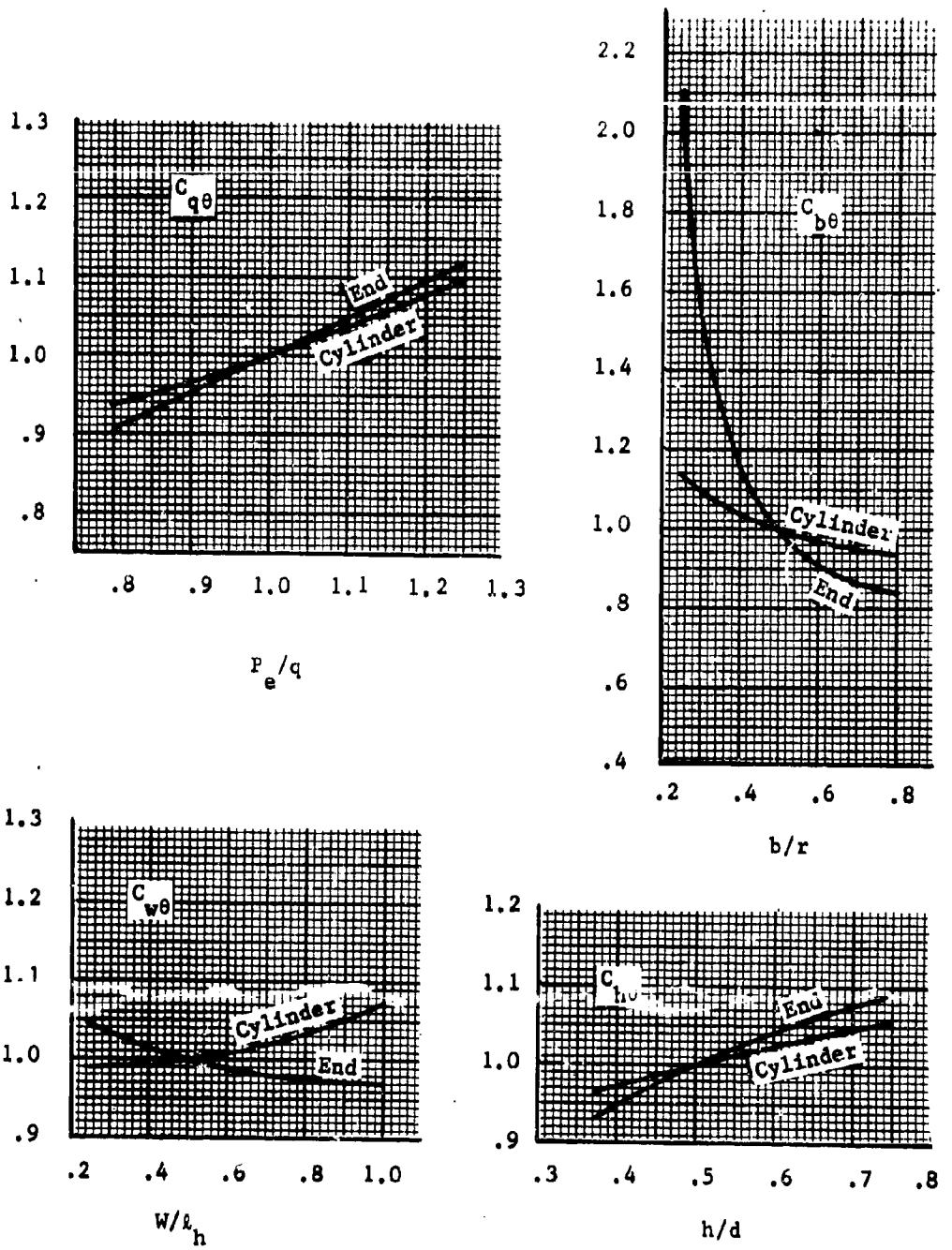

Figure 111. Correction Factors, (θ), for Cylindrical Tents with Ellipsoidal Ends

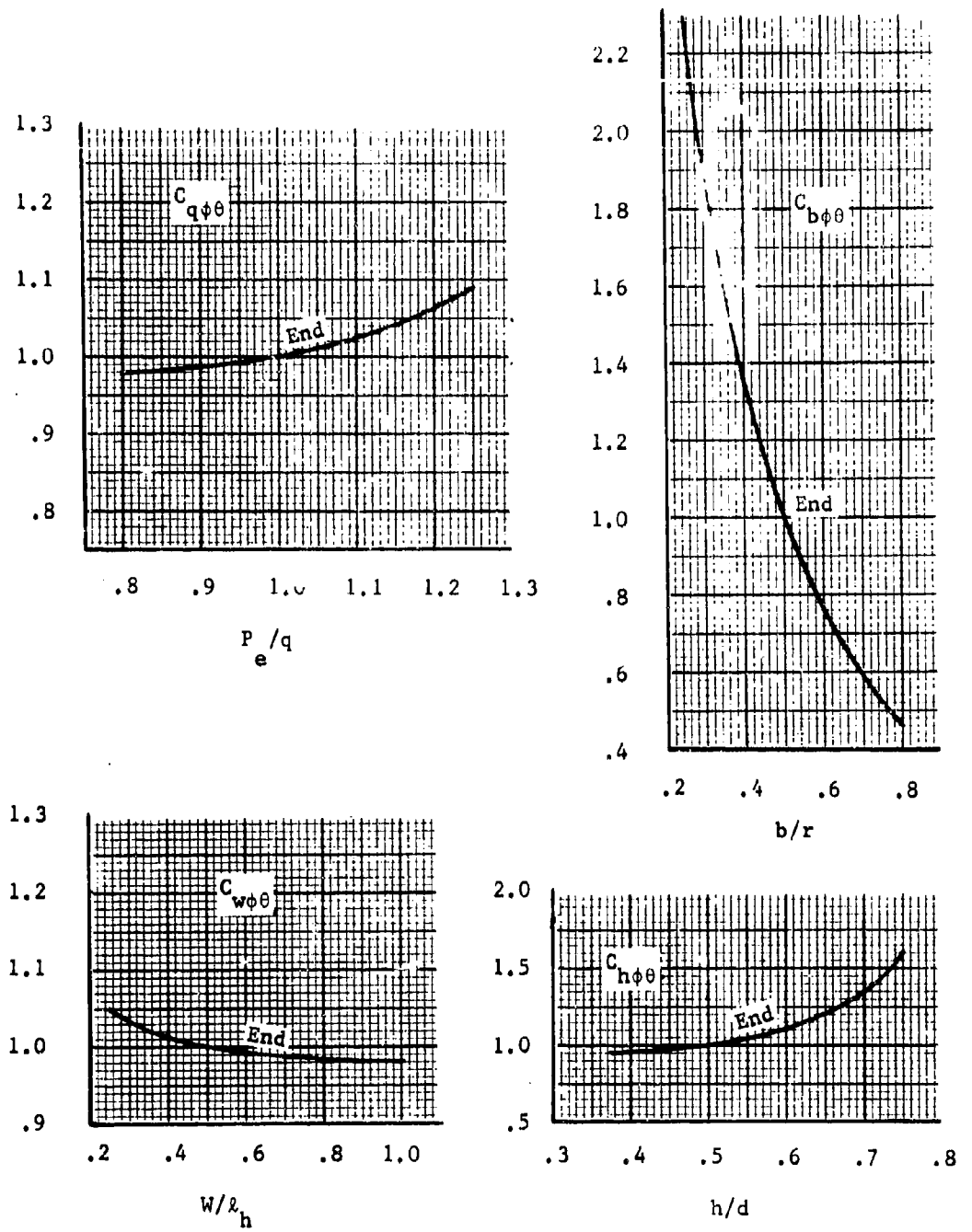

Figure 112. Correction Factors, ($\phi\theta$), for Cylindrical Tents with Ellipsoidal Ends

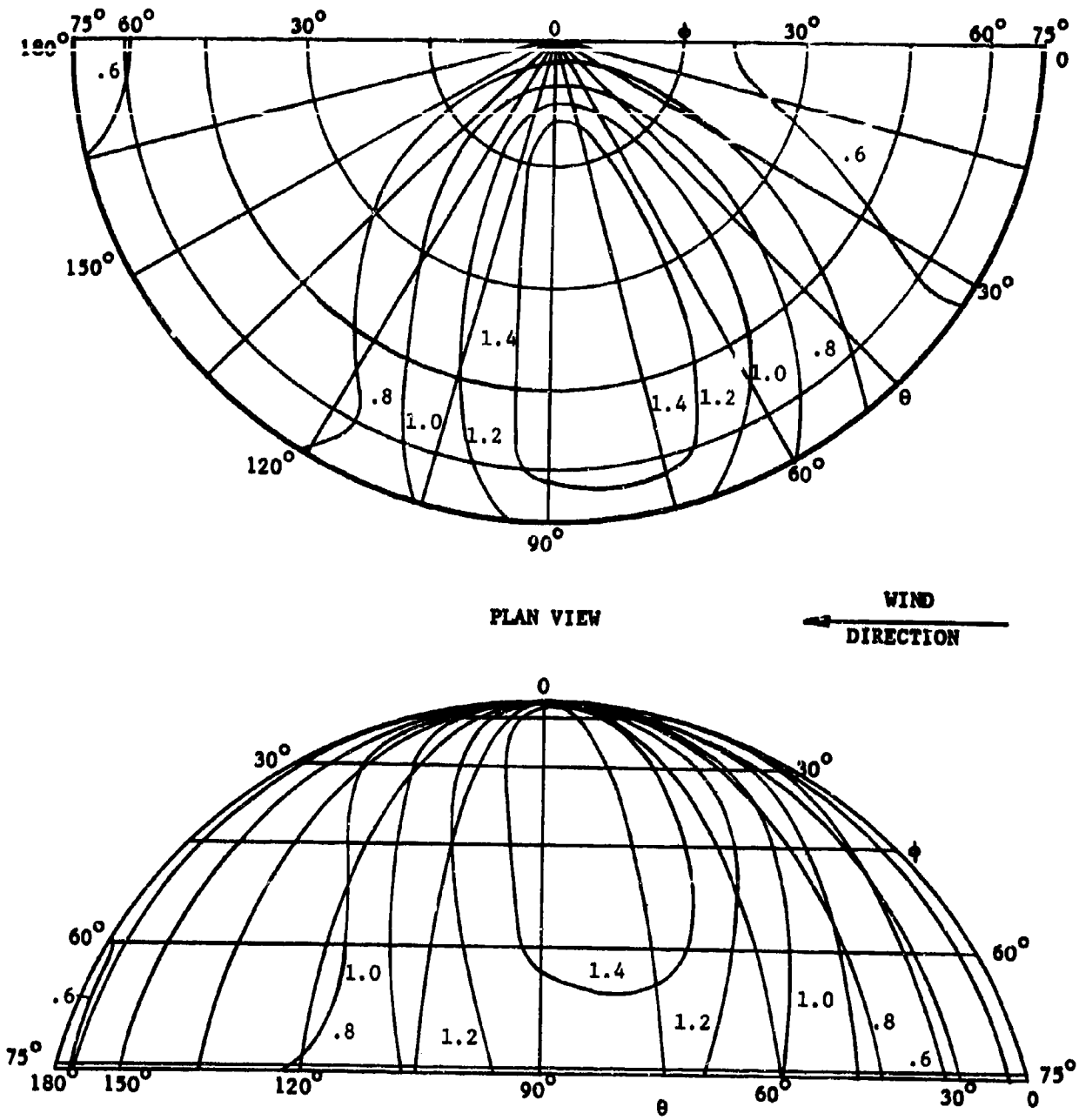

Figure 113. N_ϕ/qr for Spherical Tent (h/d = 3/8)

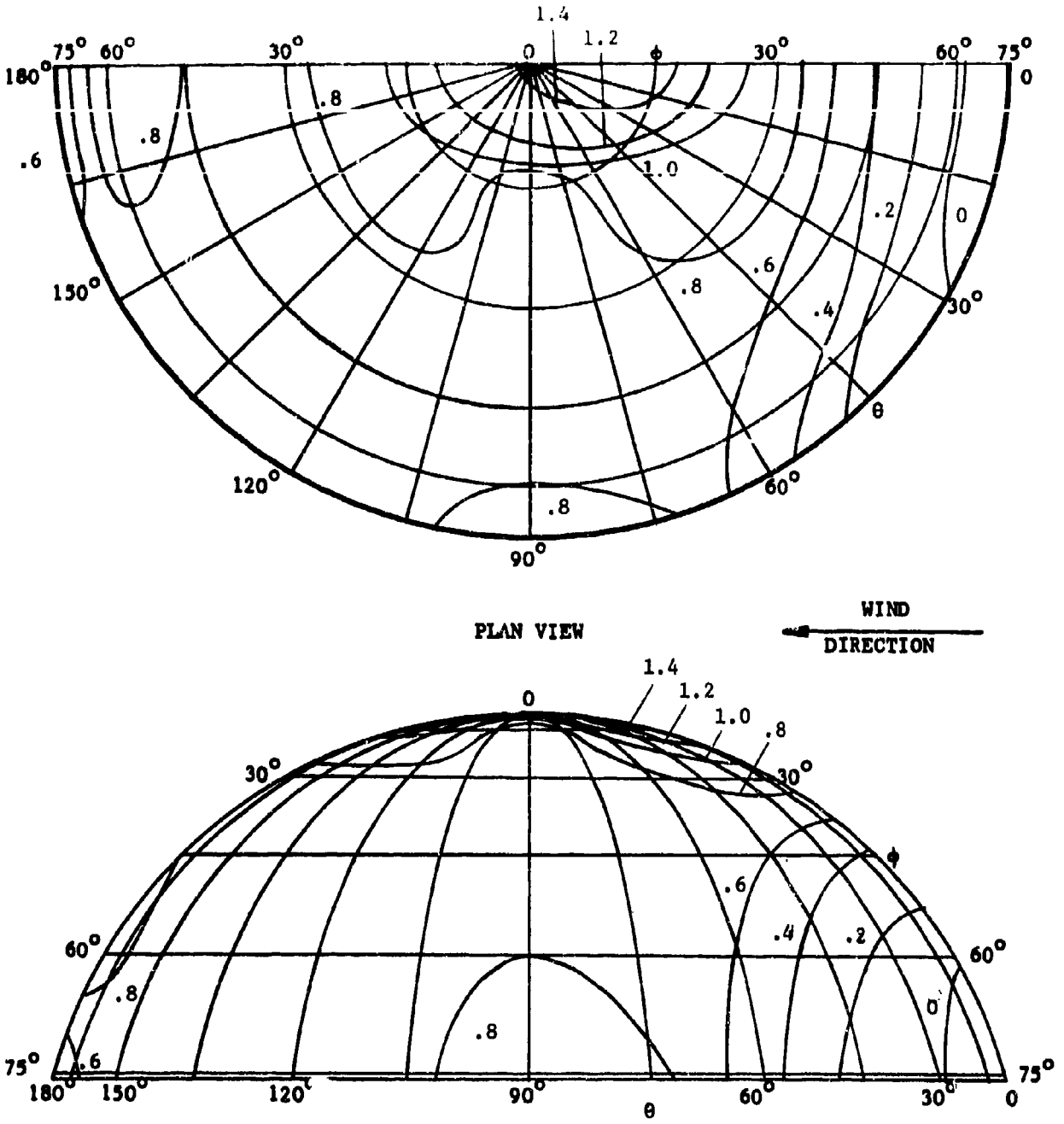

Figure 114. N_θ/qr for Spherical Tent (h/d = 3/8)

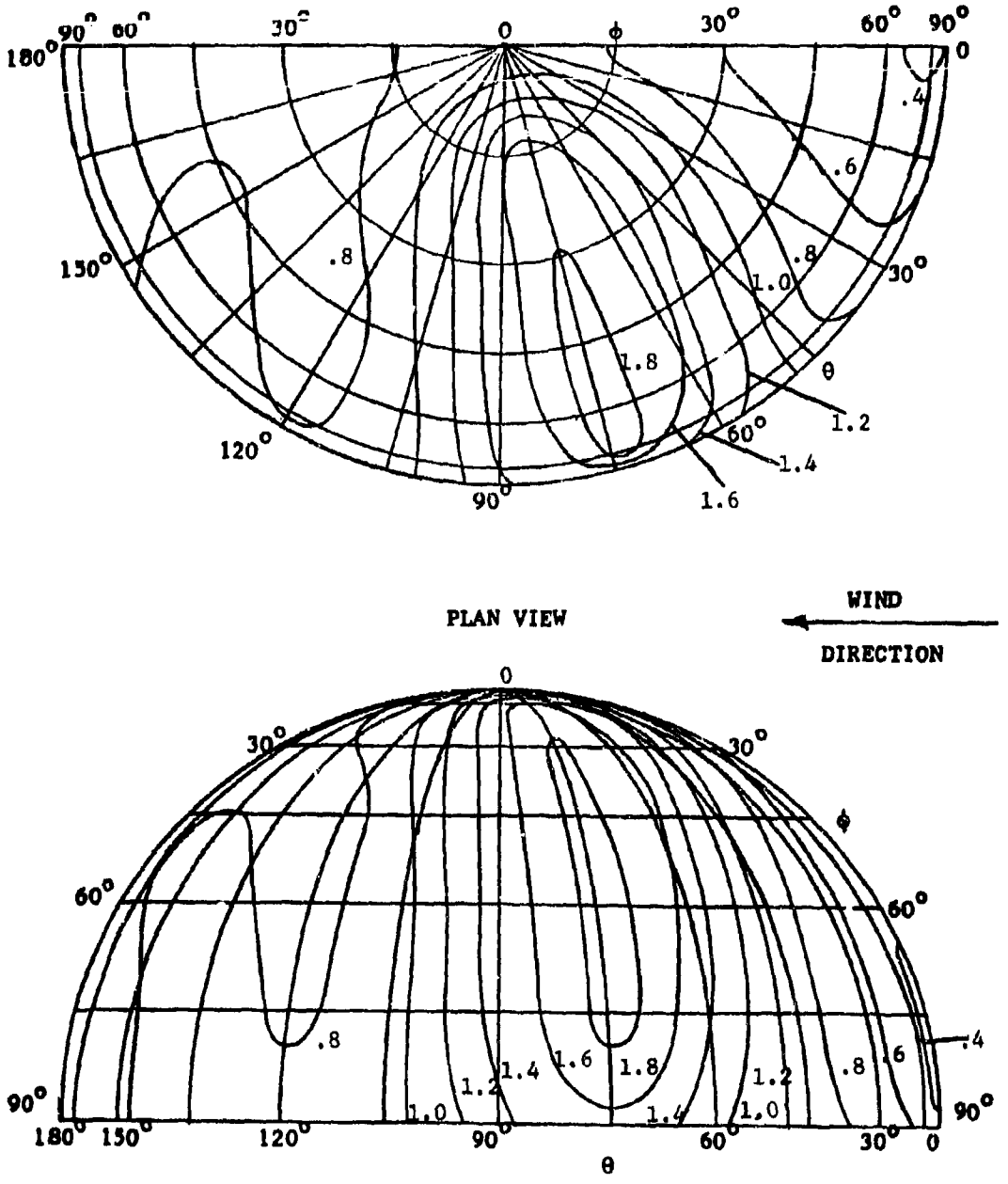

Figure 115. N_ϕ/qr for Spherical Tent (h/d = 1/2)

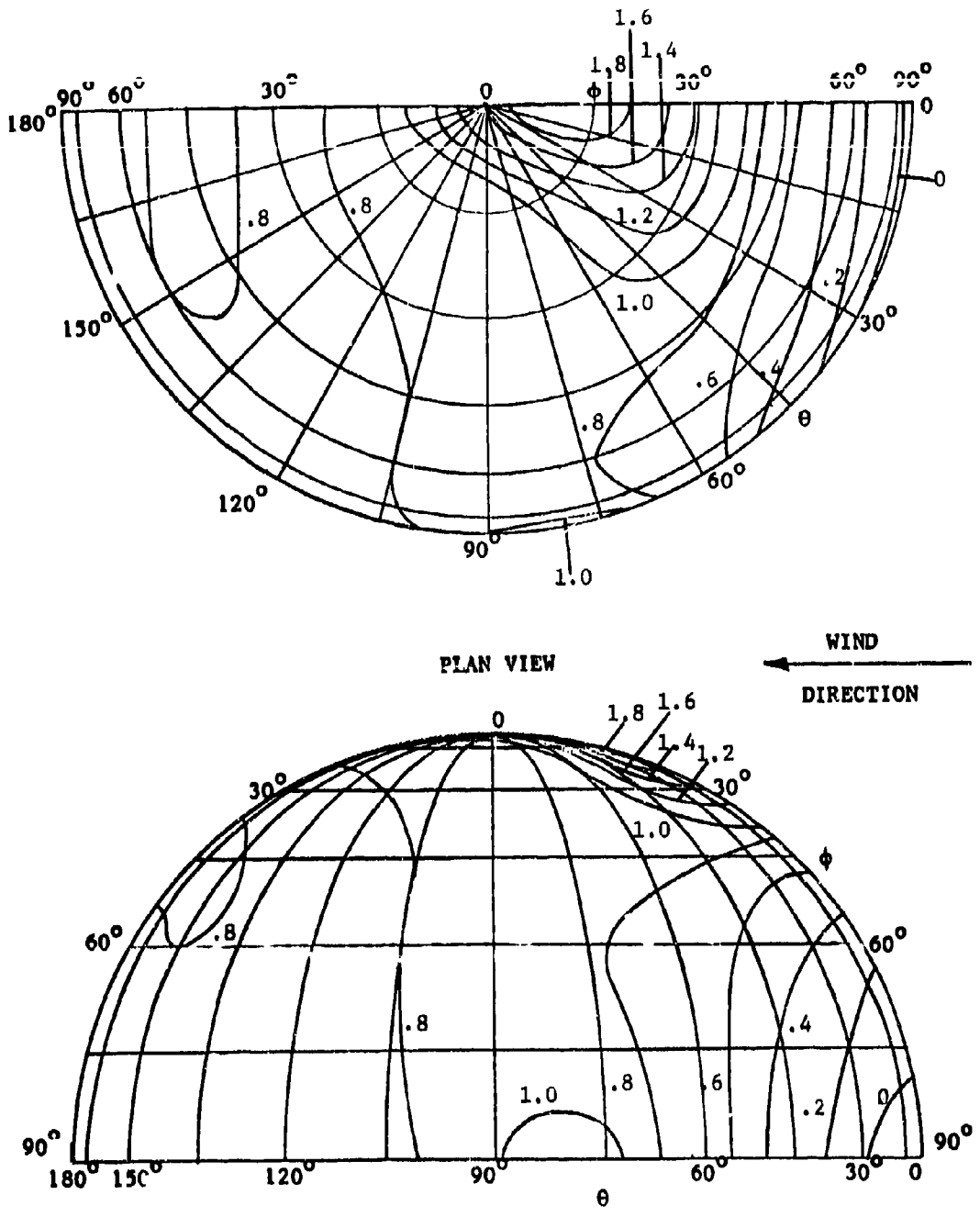

Figure 116. N_θ/qr for Spherical Tent (h/d = 1/2)

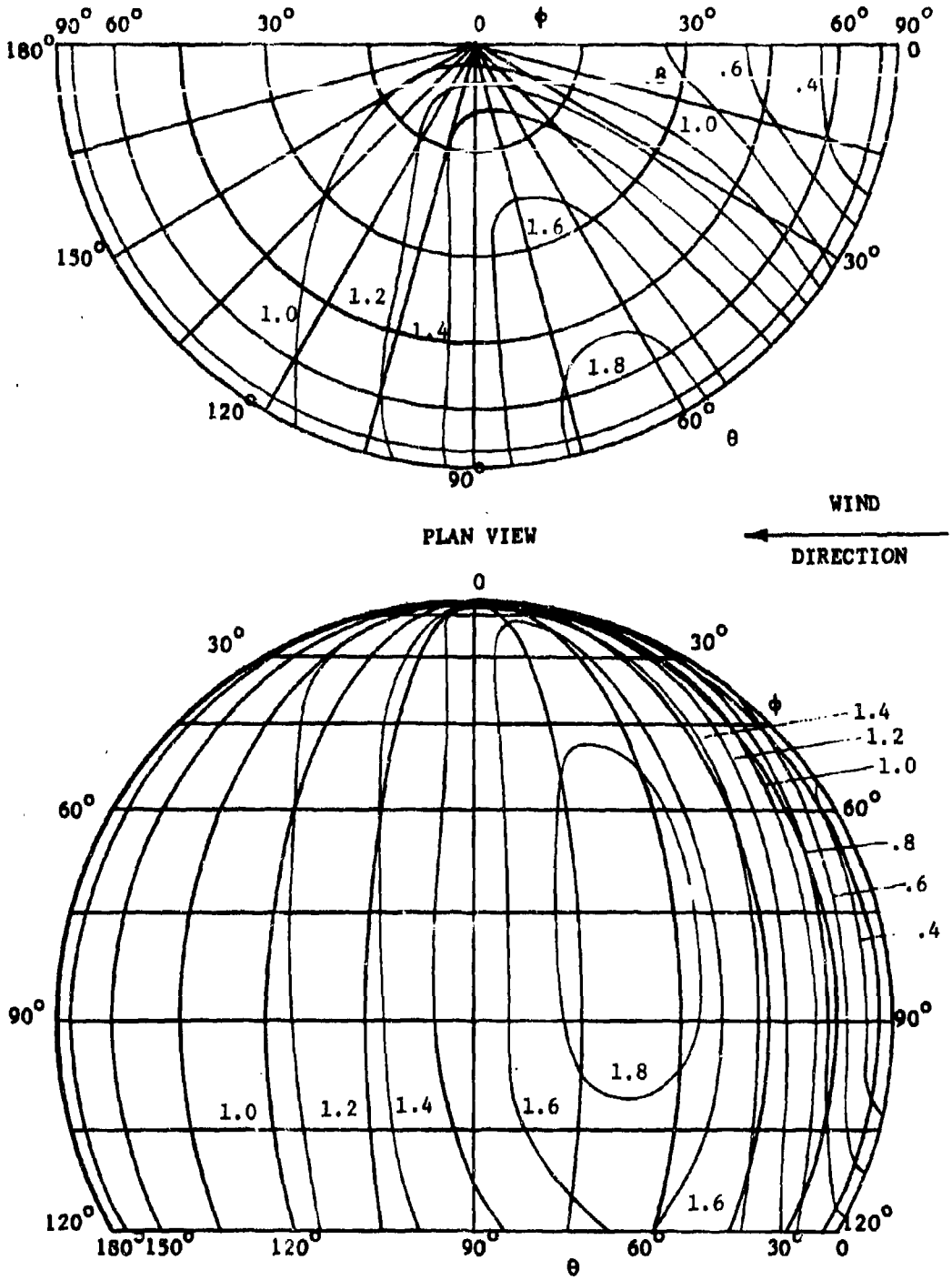

Figure 117. N_ϕ/qr for Spherical Tent (h/d = 3/4)

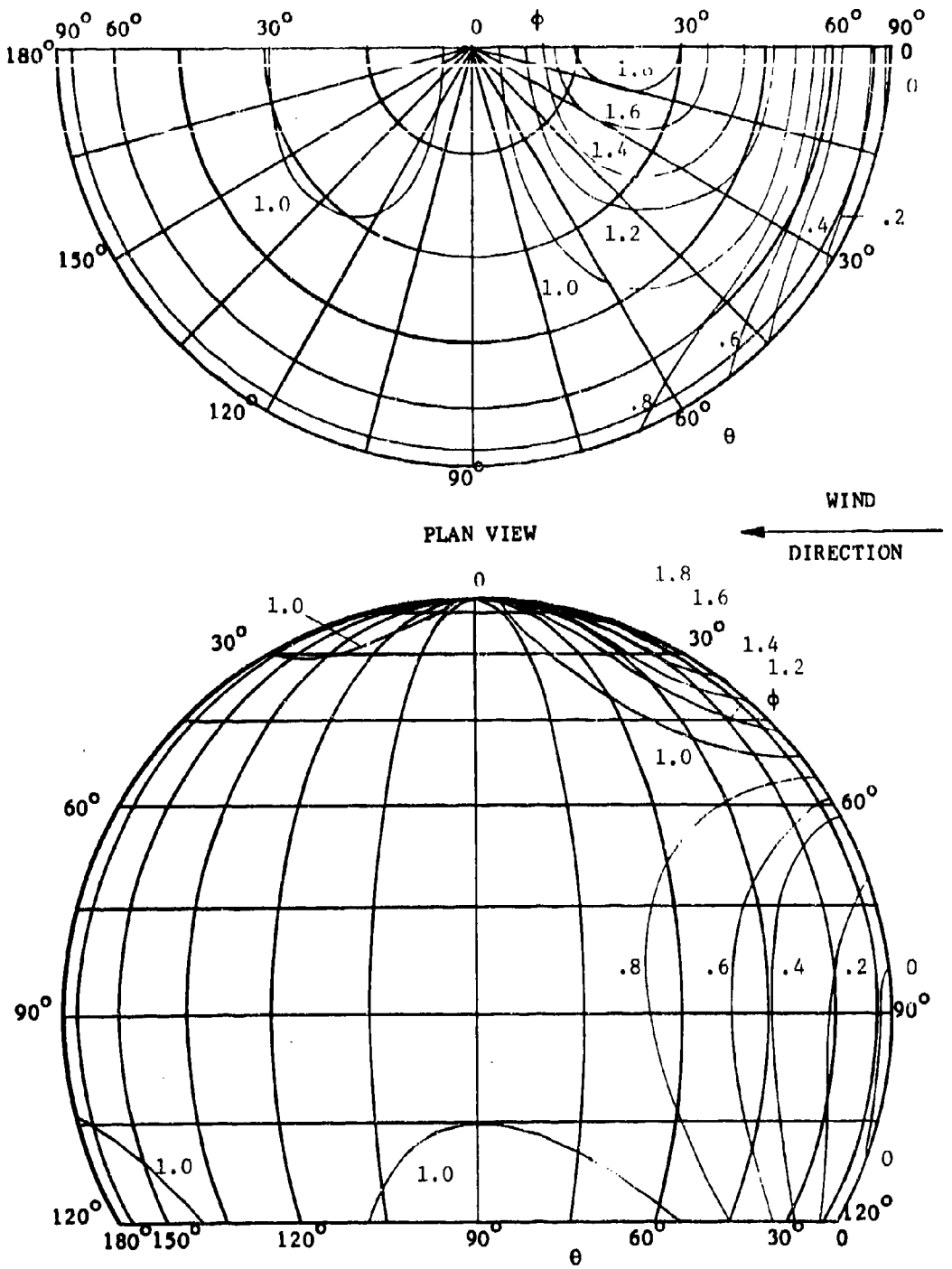

Figure 118. N_θ/qr for Spherical Tent (h/d = 3/4)

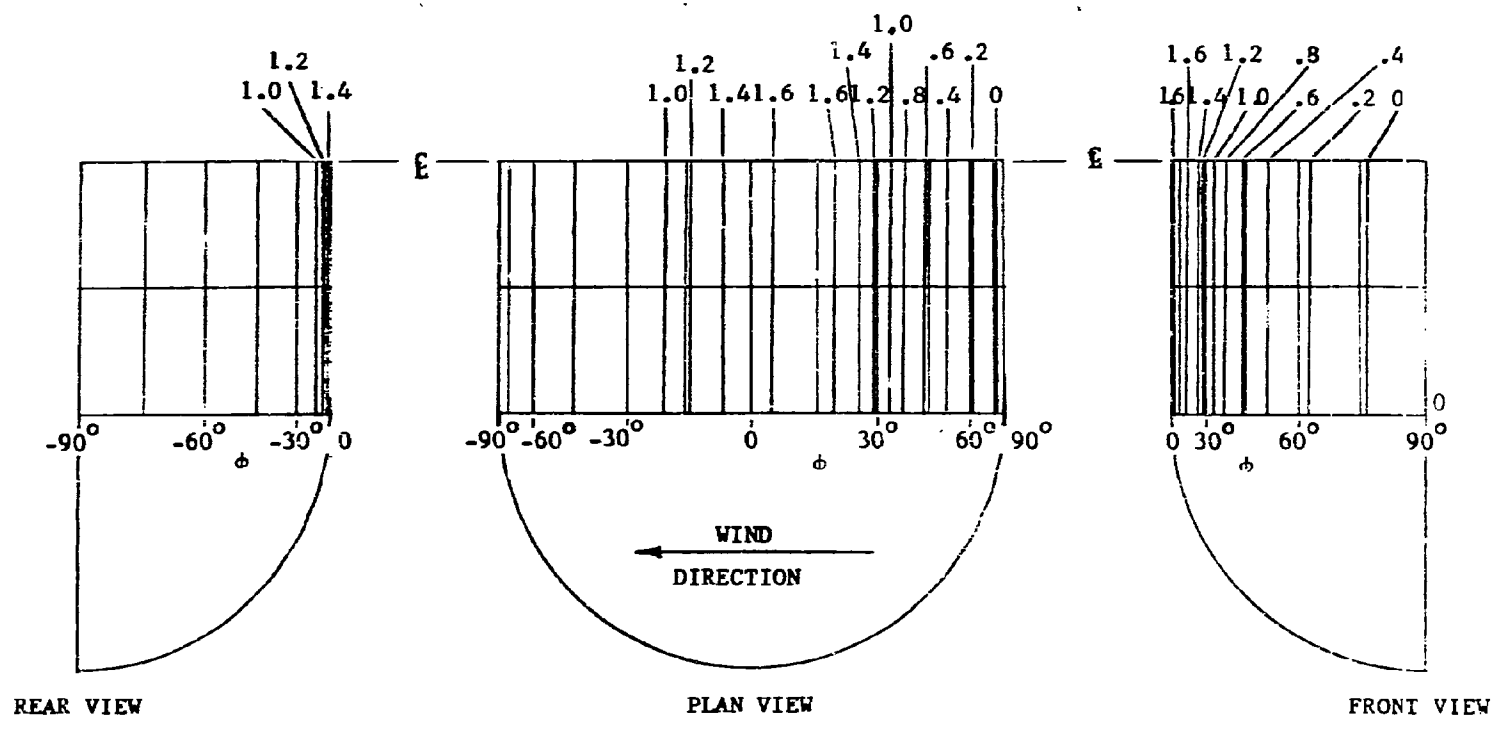

Figure 119. N_x/qr for Cylindrical Tent with Spherical Ends (l/ℓ_h = 1/2, h/d = 1/2)
N_ϕ/qr = 1.82 (constant)

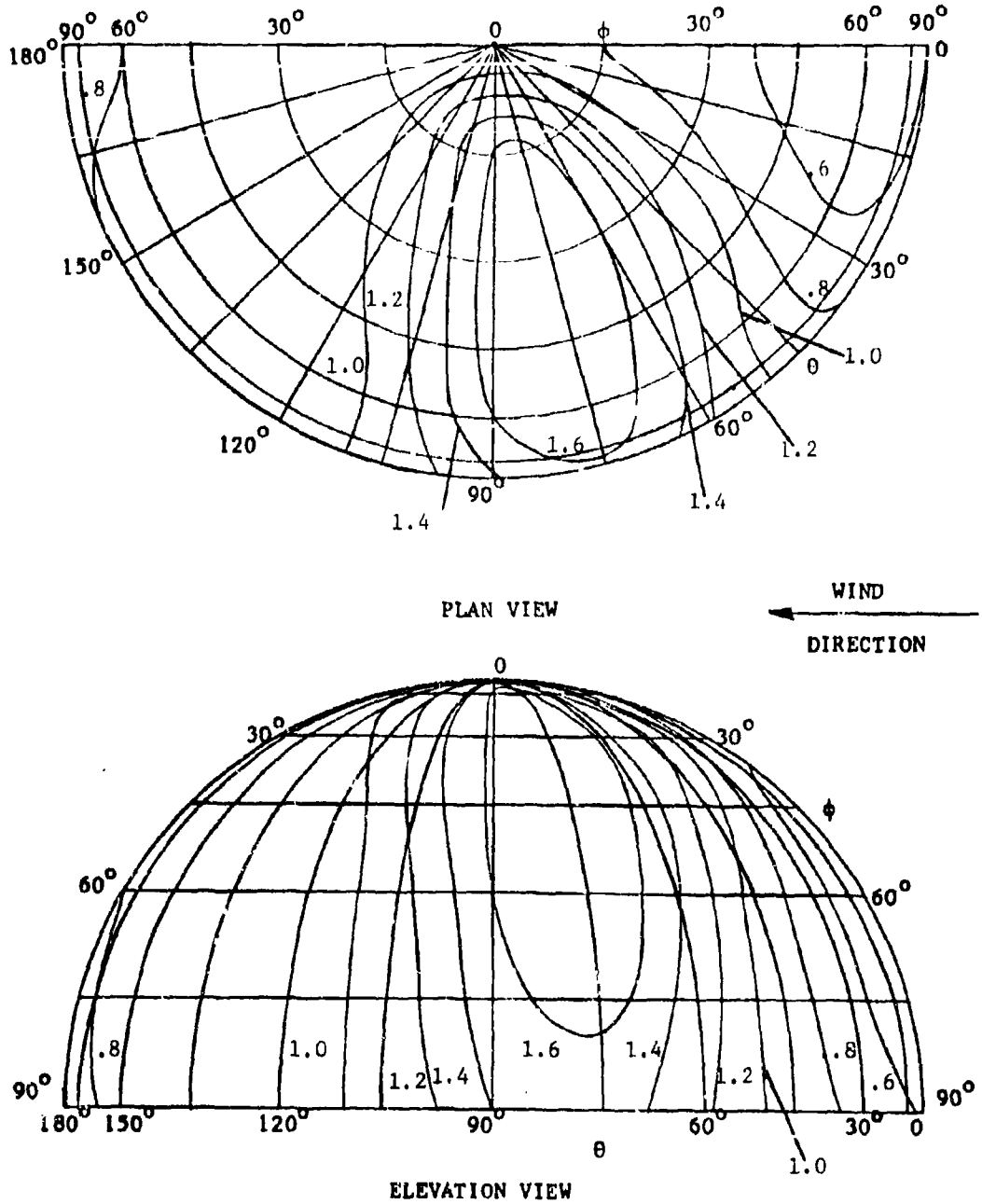

Figure 120. N_ϕ/qr for Spherical End of Cylindrical Tent (W/ℓ_h = 1/2, h/d = 1/2)

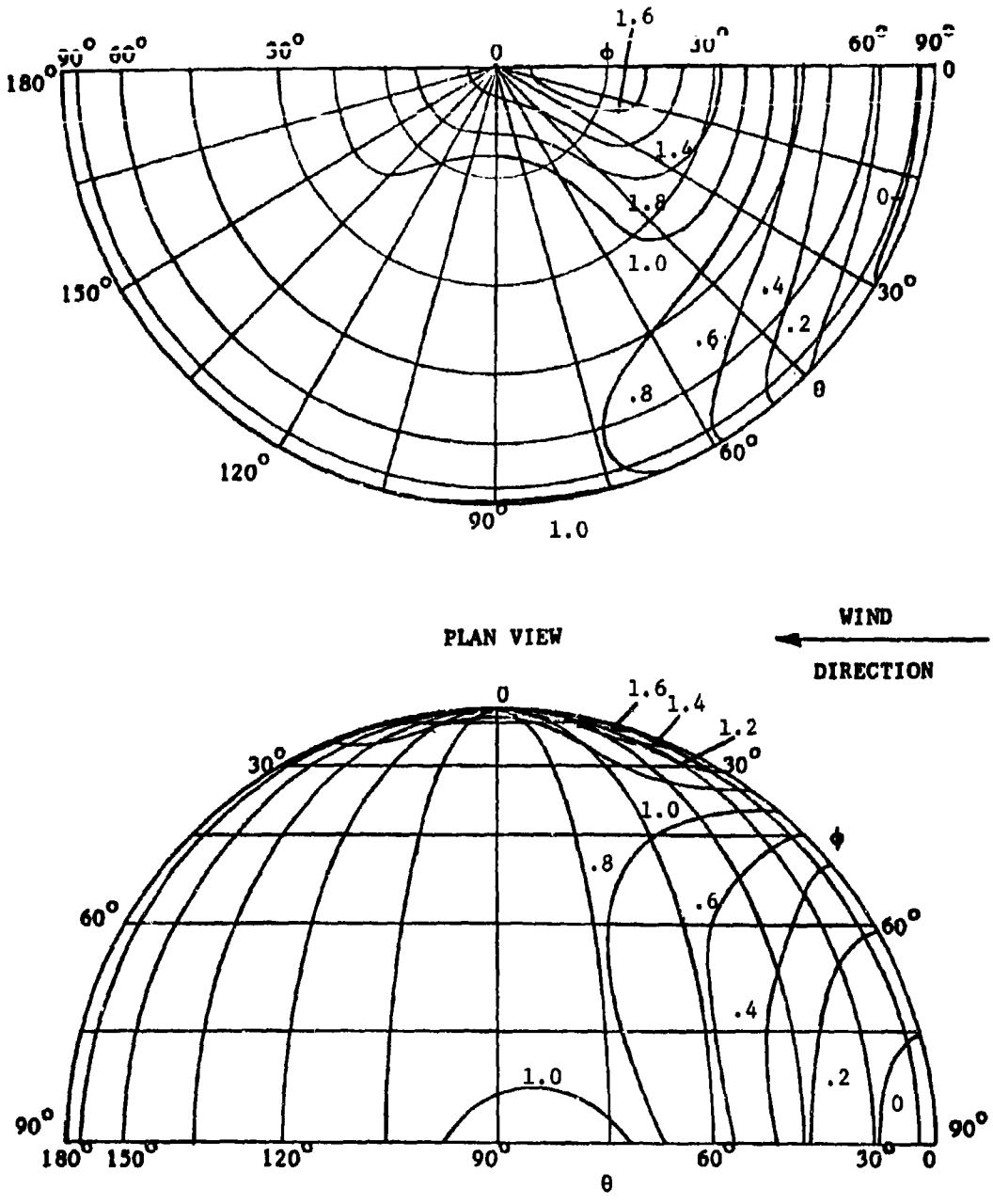

Figure 121. N_θ/qr for Spherical End of Cylindrical Tent (W/ℓ_h = 1/2, h/d = 1/2)

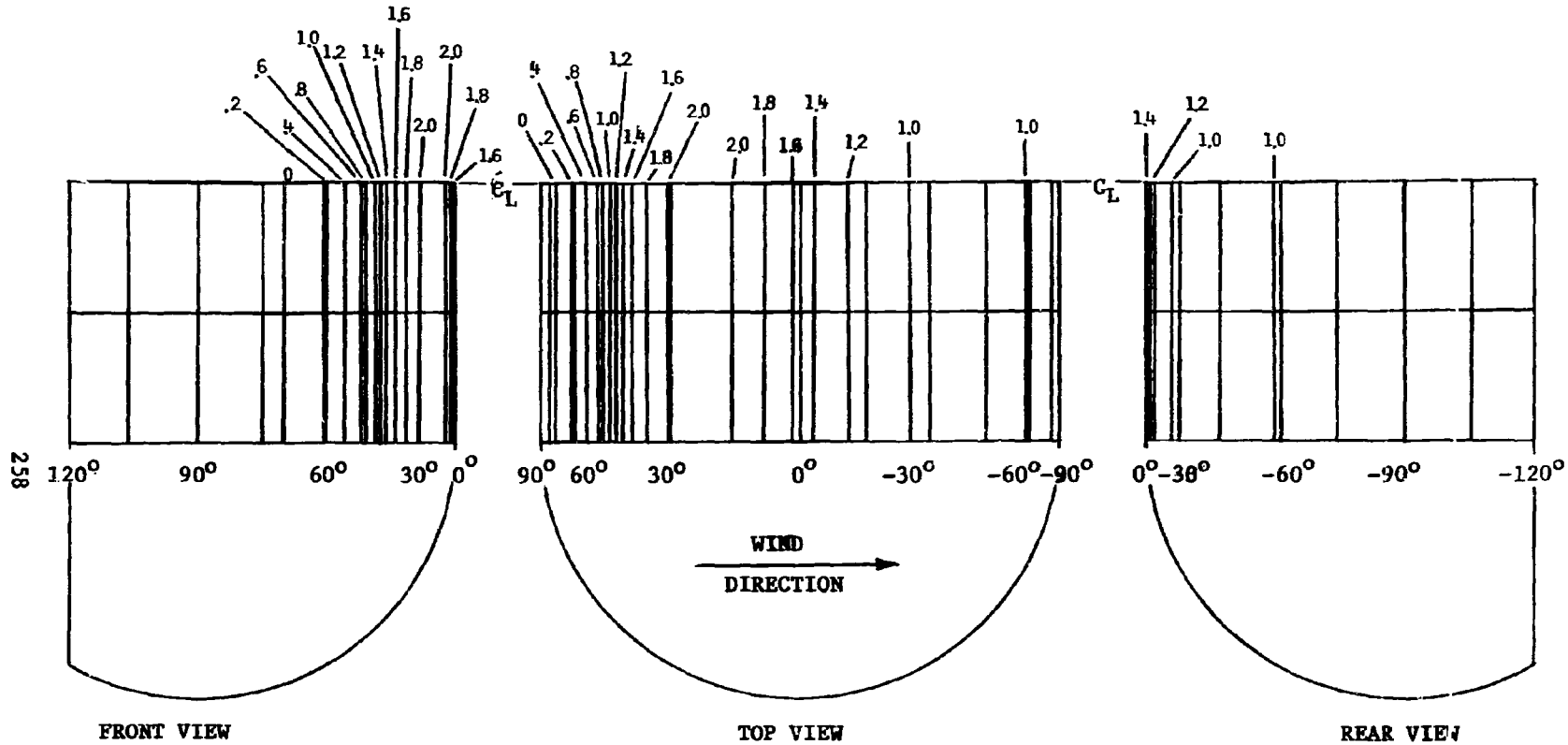

Figure 122. N_x/qr for Cylindrical Tent with Spherical Ends (W/ℓ_h = 1/2, h/d = 3/4)
N_ϕ/qr = 2.04 (constant)

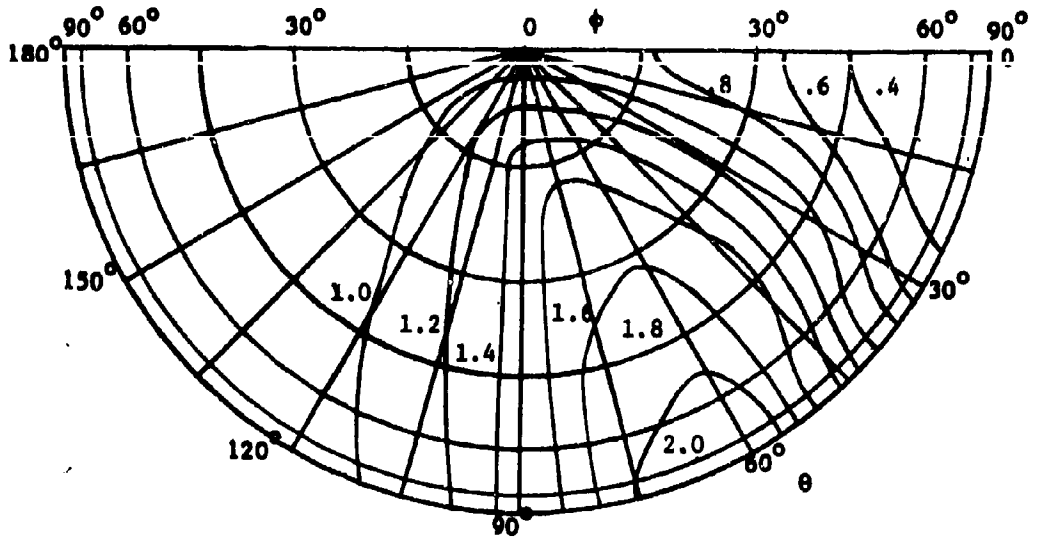

PLAN VIEW

WIND DIRECTION

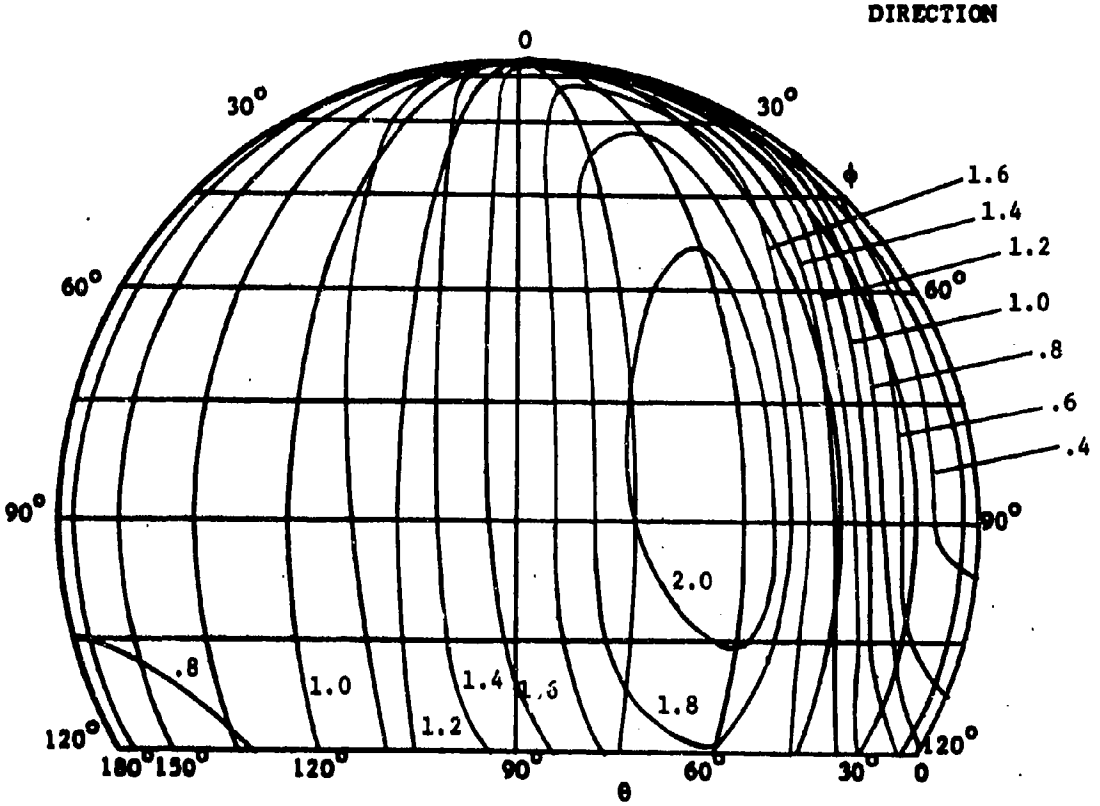

ELEVATION VIEW

Figure 123. N_ϕ/qr for Spherical Ends of Cylindrical Tent (W/ℓ_h = 1/2, h/d = 3/4)

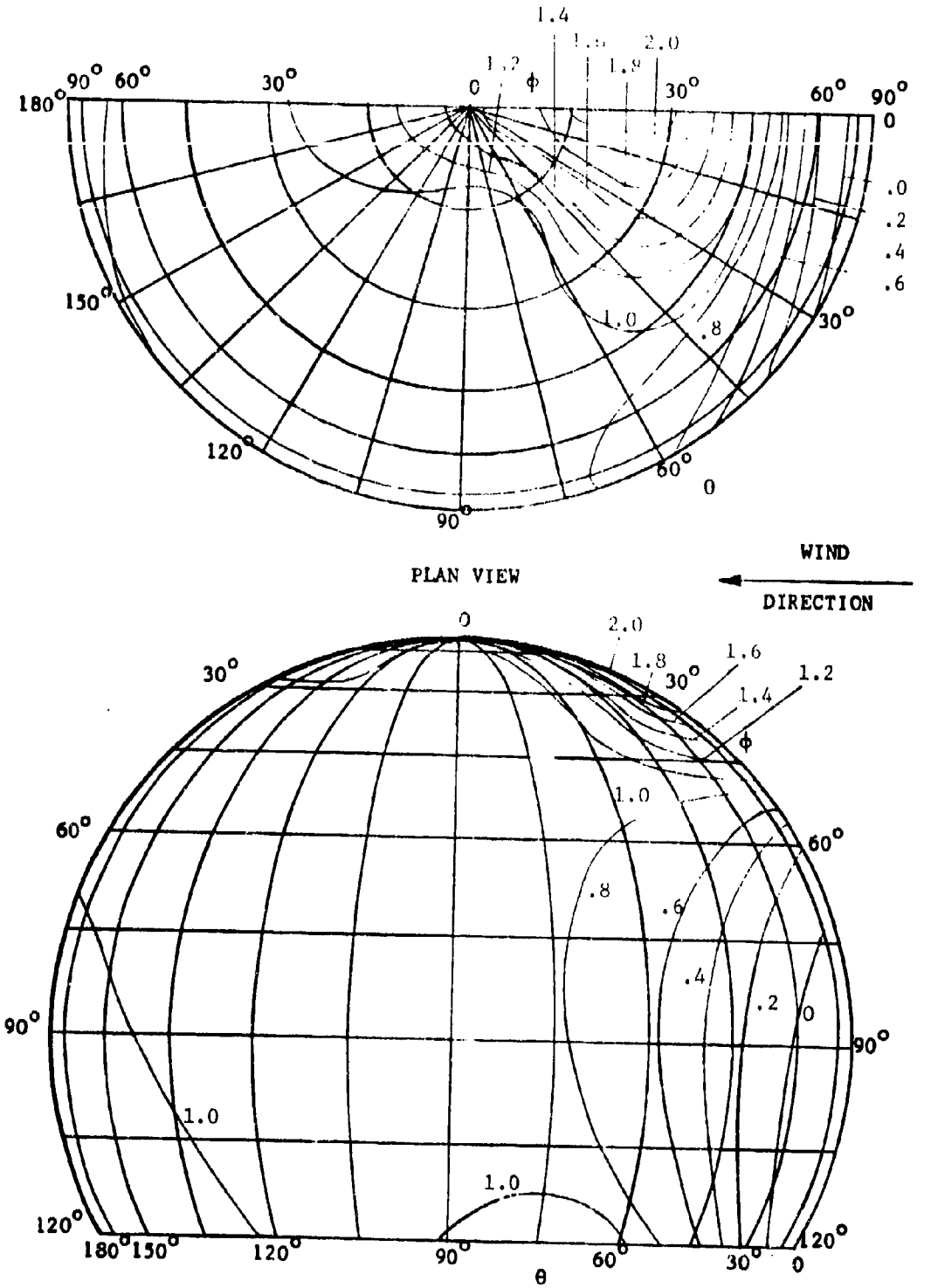

Figure 124. N_θ/qr for Spherical Ends of Cylindrical Tents ($W/\ell_h = 1/2$, $h/d = 3/4$)

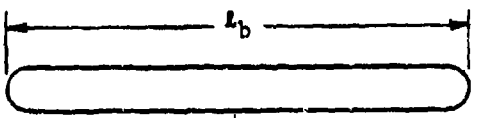

(a) Straight Test Beam

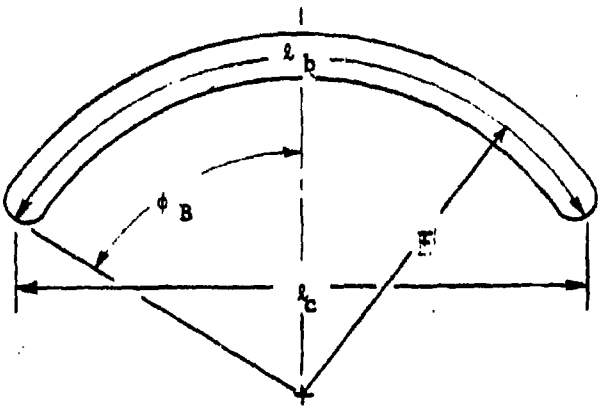

(b) Circular Test Beam

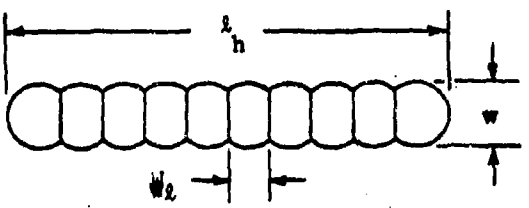

(c) Test Beam Cross-Section

Figure 125. Cellular Beam Test Model Geometry

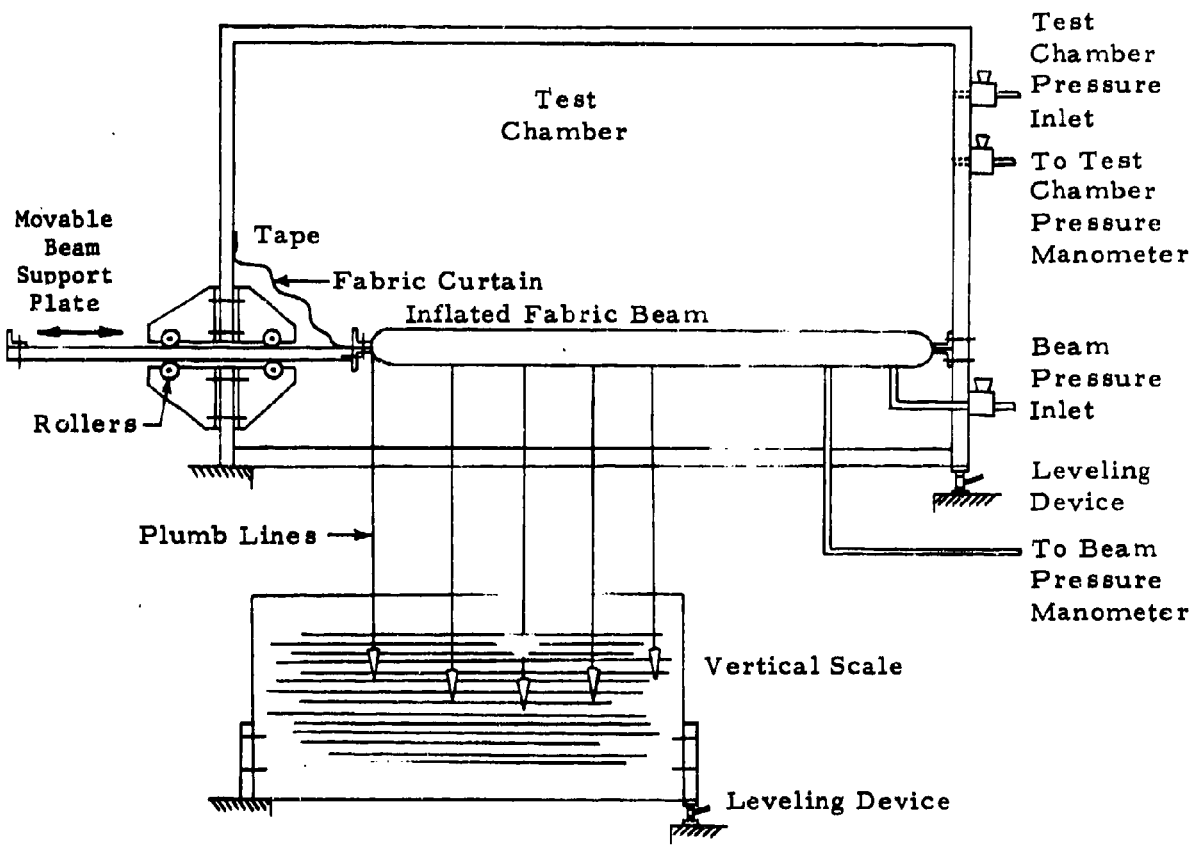

Figure 126. Test Fixture with Beam Installed

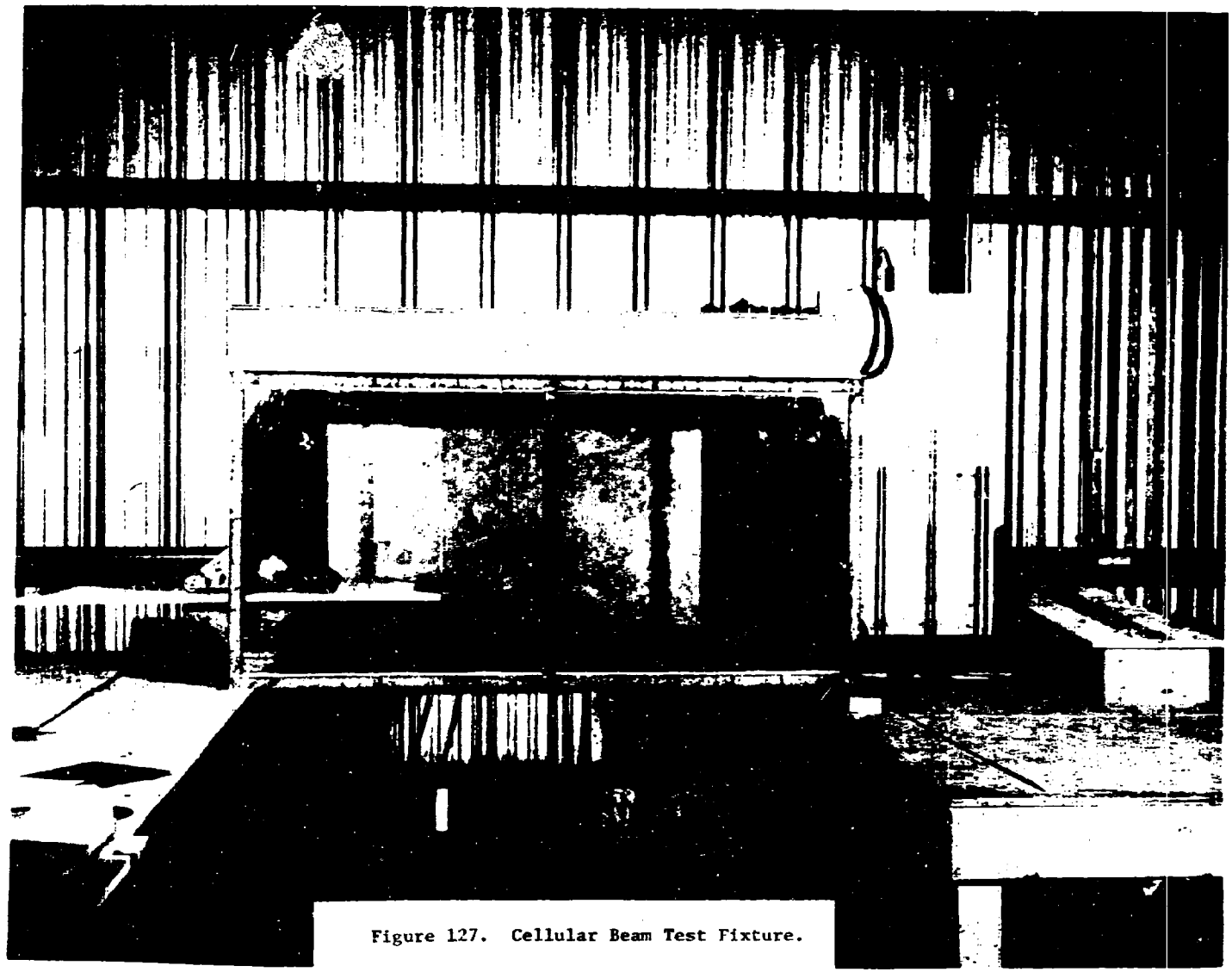

Figure 127. Cellular Beam Test Fixture.

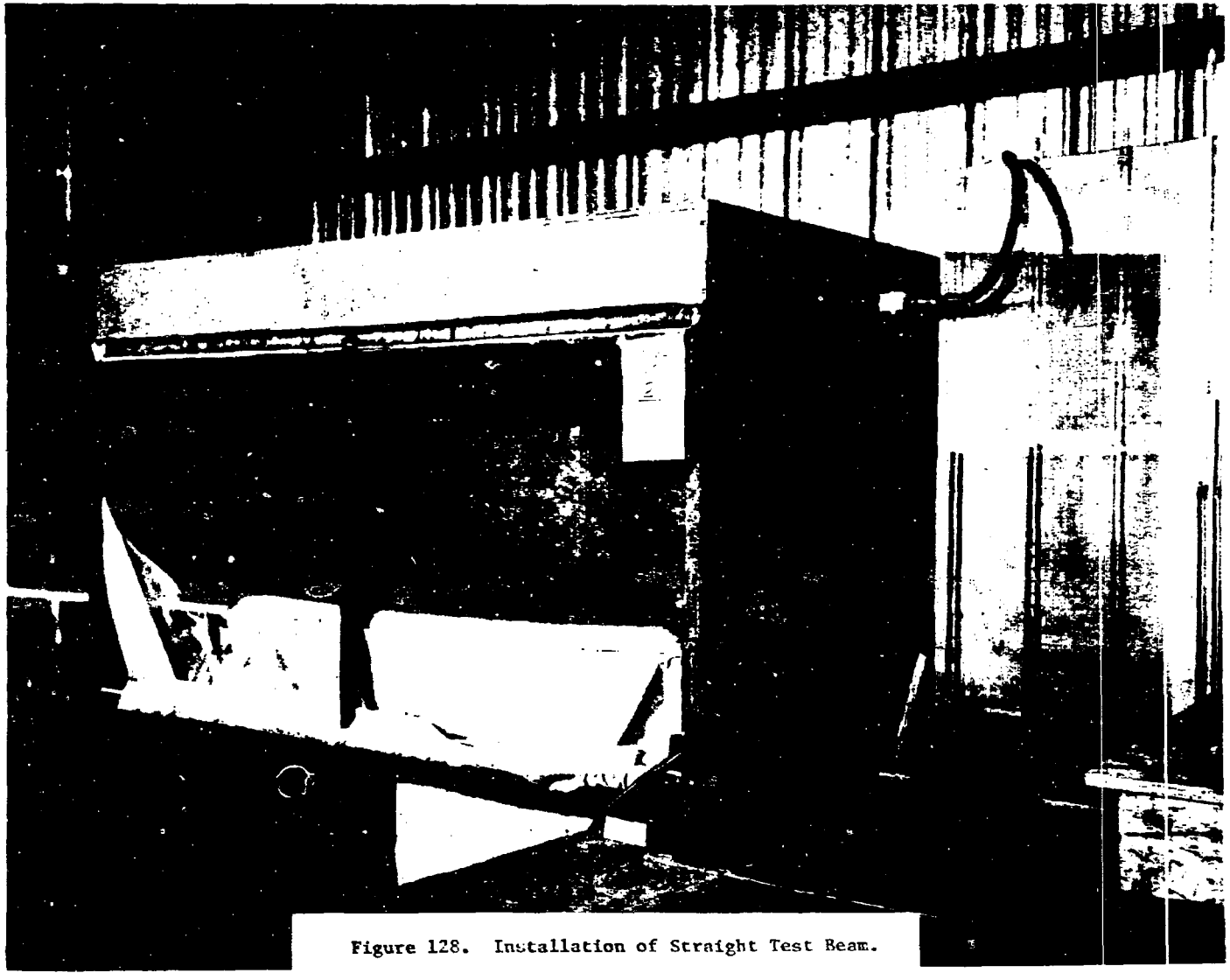

Figure 128. Installation of Straight Test Beam.

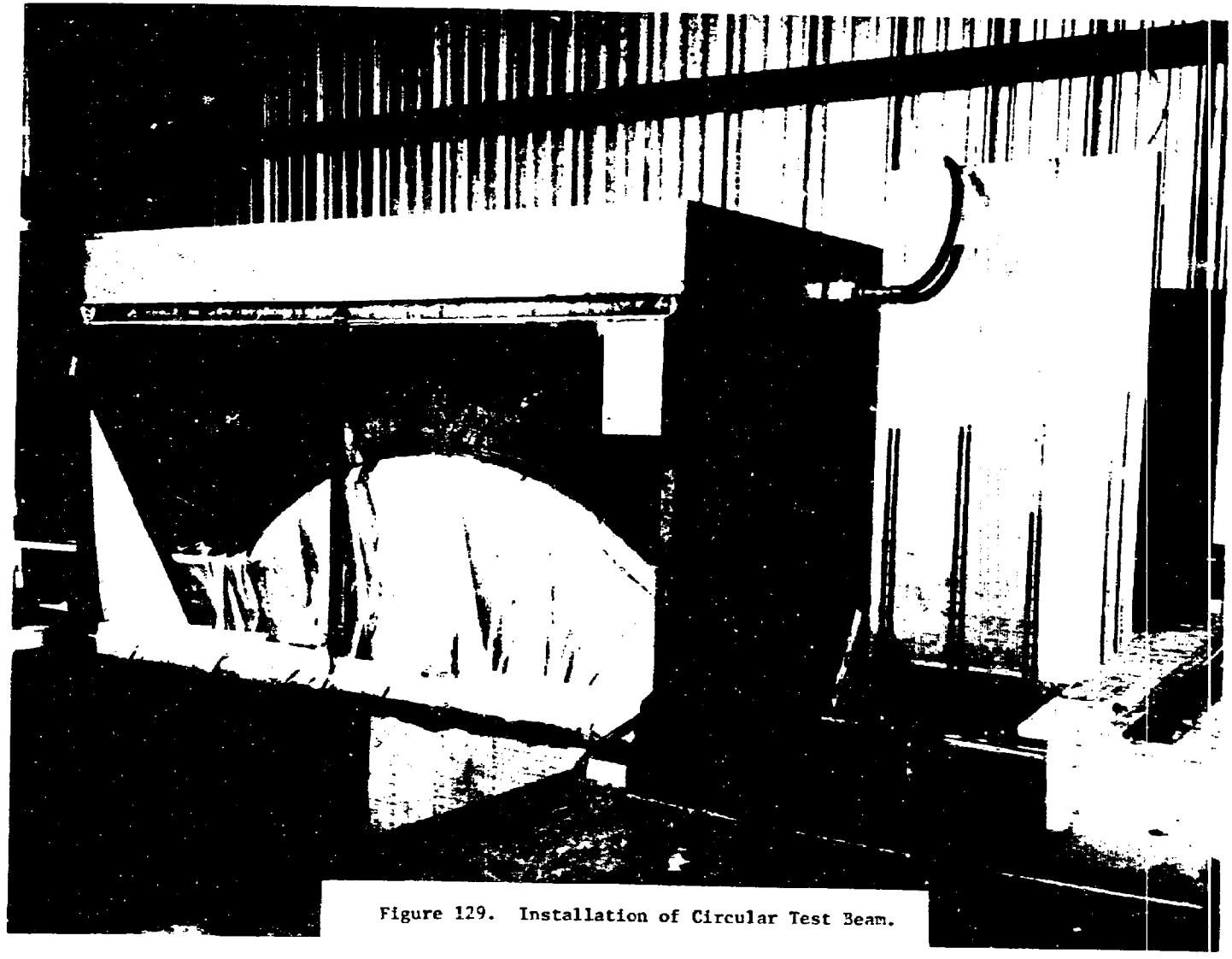

Figure 129. Installation of Circular Test Beam.

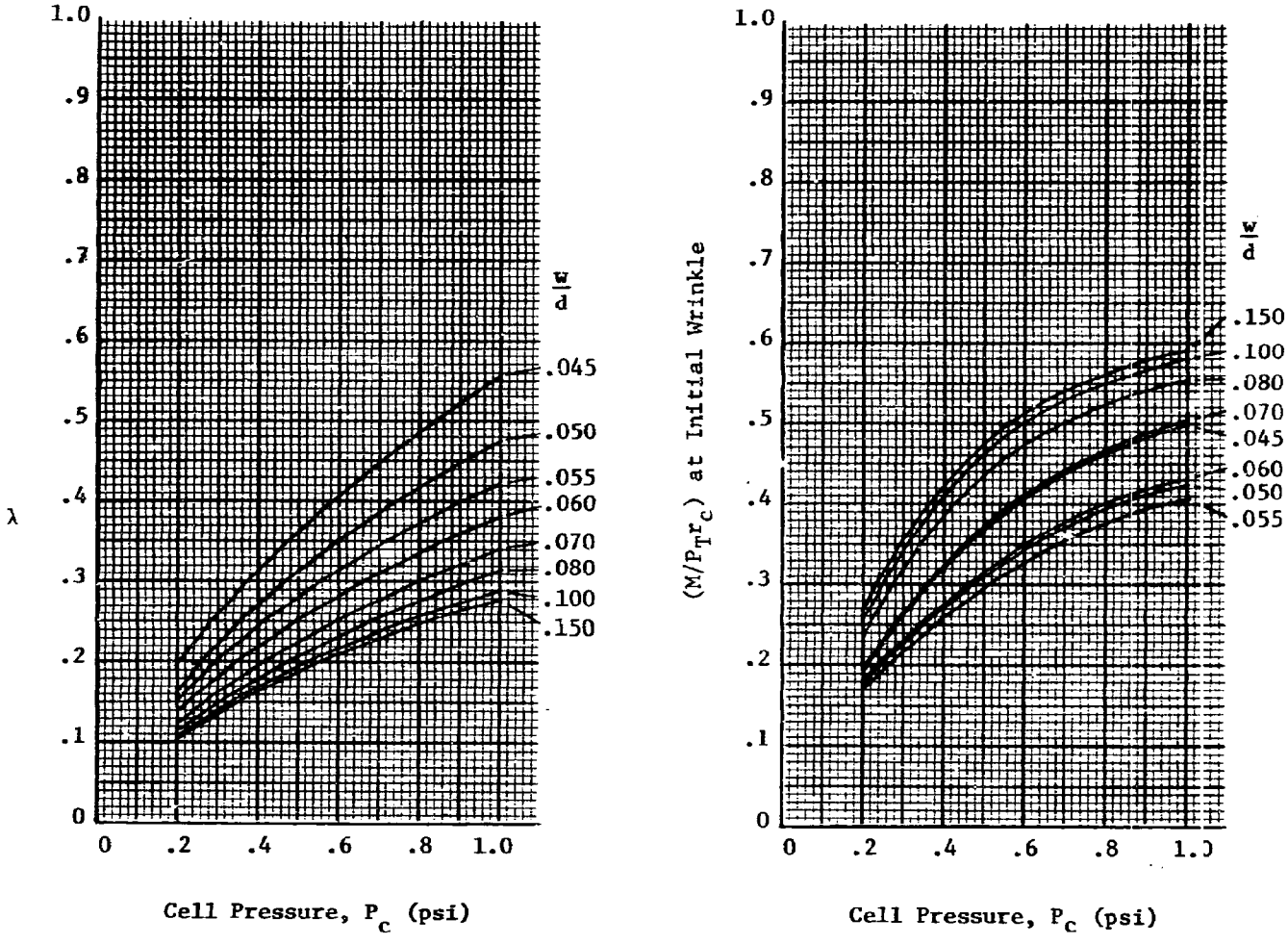

Figure 130. Empirical Relations (λ),$(M/P_T r_c)$ for Cellular Fabric Beams

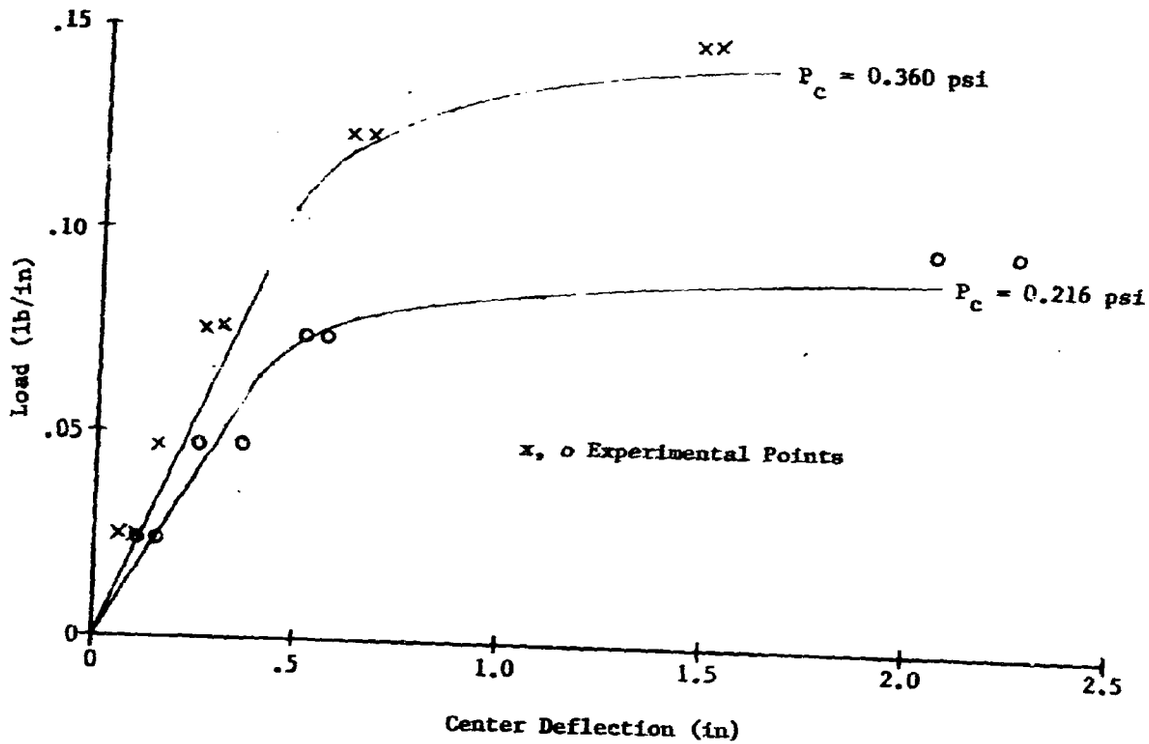

Figure 131. Deflection of Straight Test Beam
r_c = 1.500 in

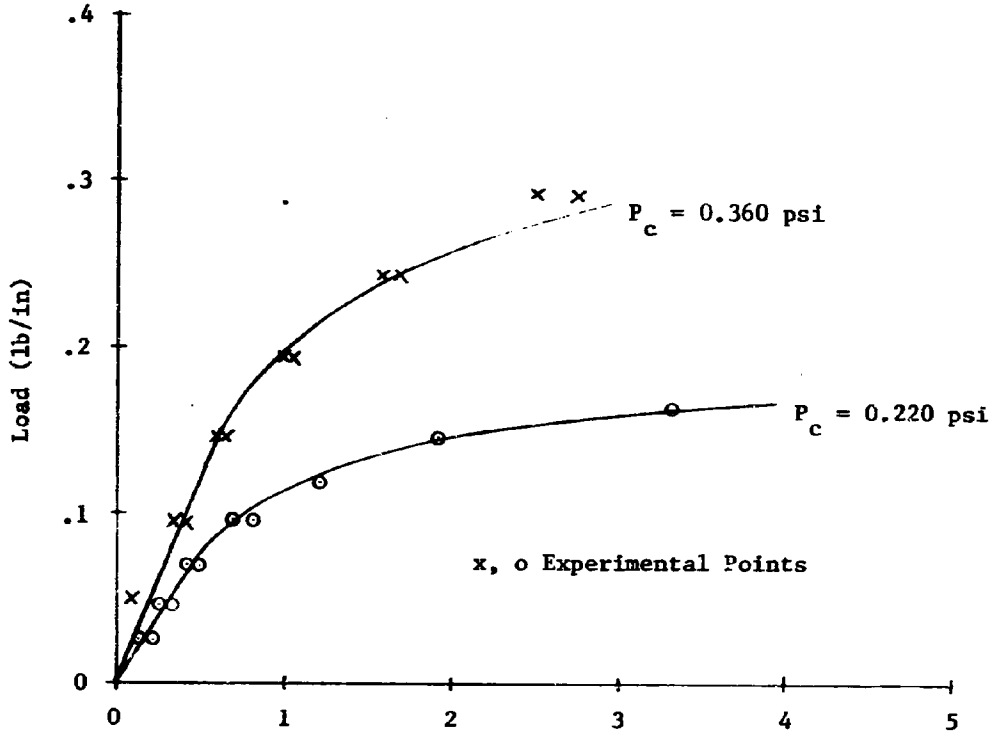

Figure 132. Deflection of Circular Test Beam
r_c = 1.875 in, r = 24.36 in

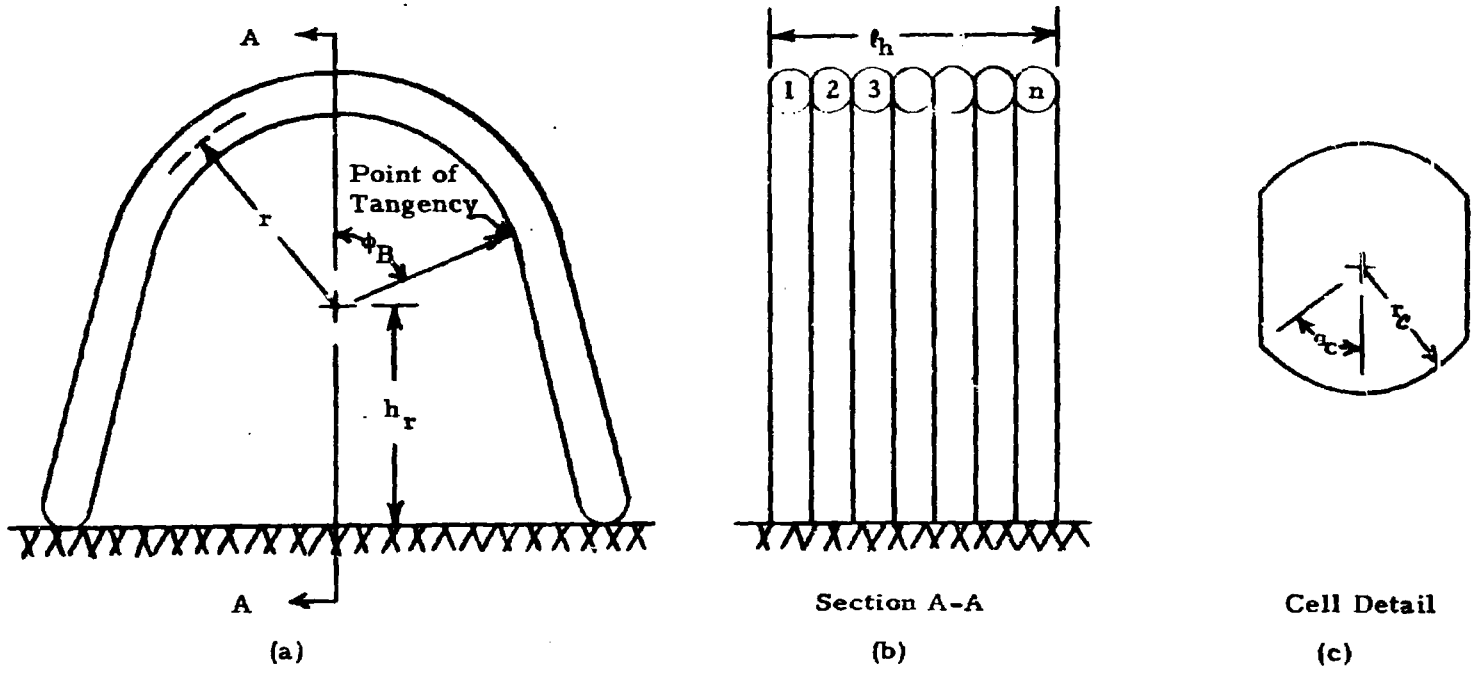

Figure 133. Tent Geometry, Double-Wall Tent

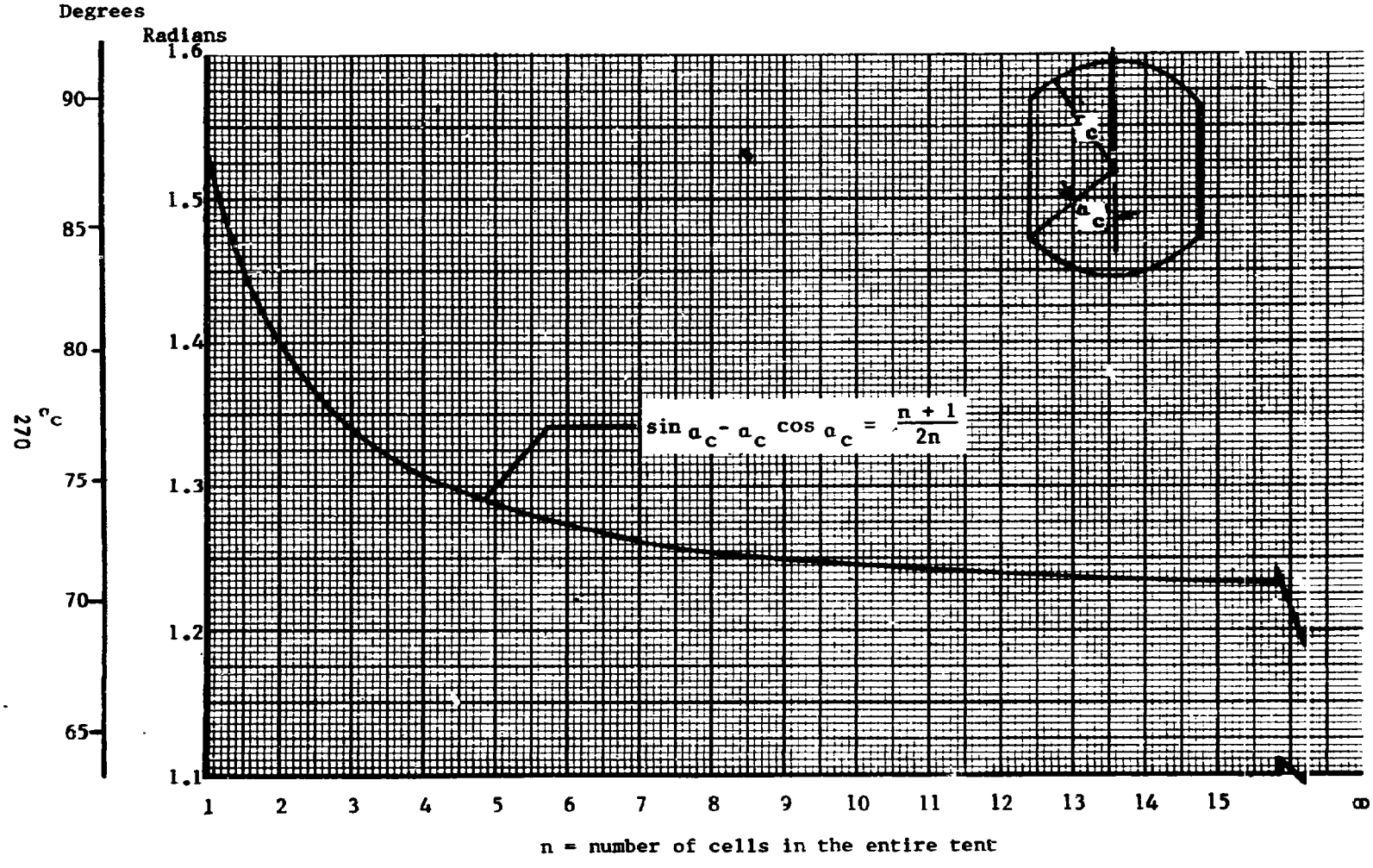

Figure 134. α_c-n Relationship for Maximum Volume to Weight Ratio; Double-Wall Tent

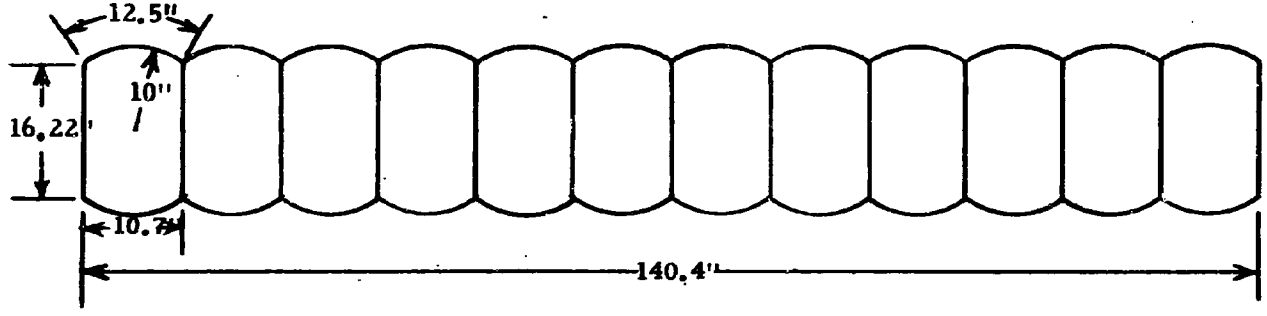

Cell Size, Tent # 1 Scale: 1/20

(a)

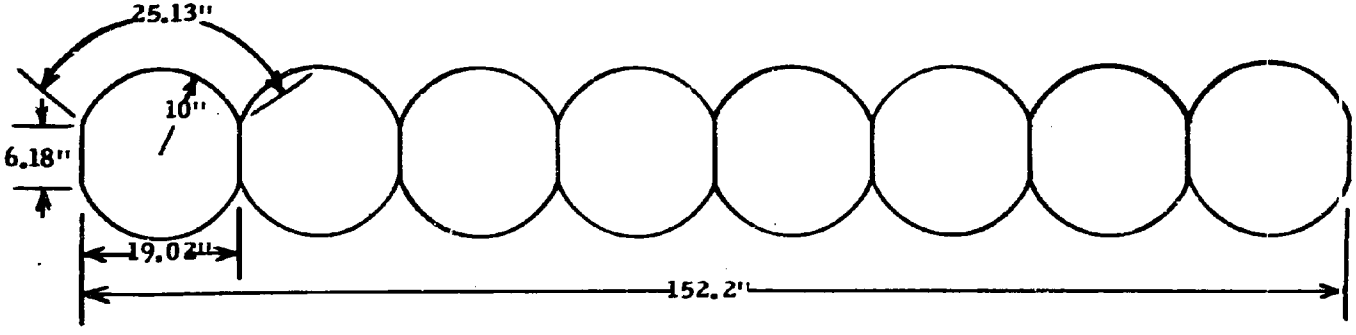

Cell Size, Tent # 2 Scale: 1/20

Figure 135. Relative Sizes of Tent Cells

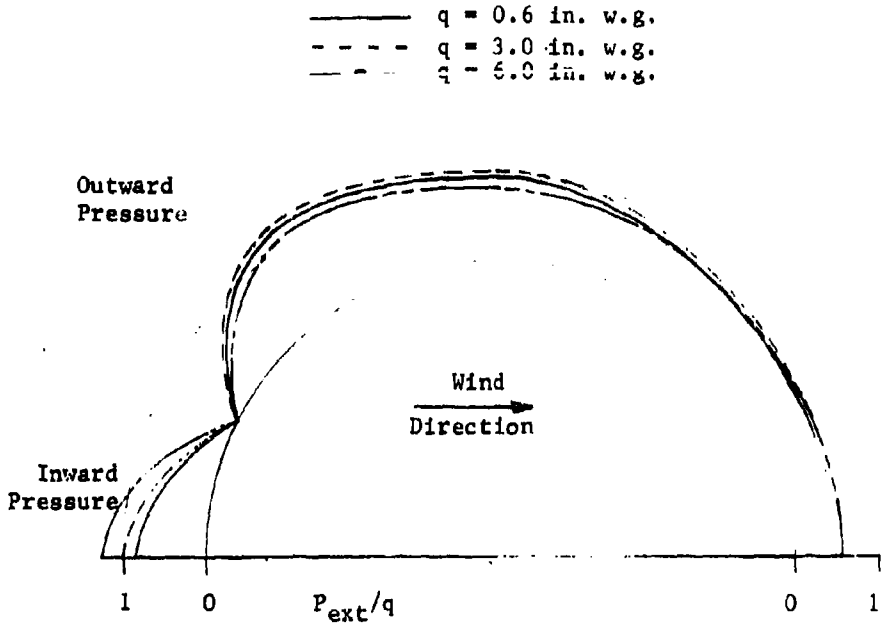

Figure 136. Pressure Distribution on Unguyed Double-Wall Tents (h/d = 1/2, W/ℓ_h = 1/2)

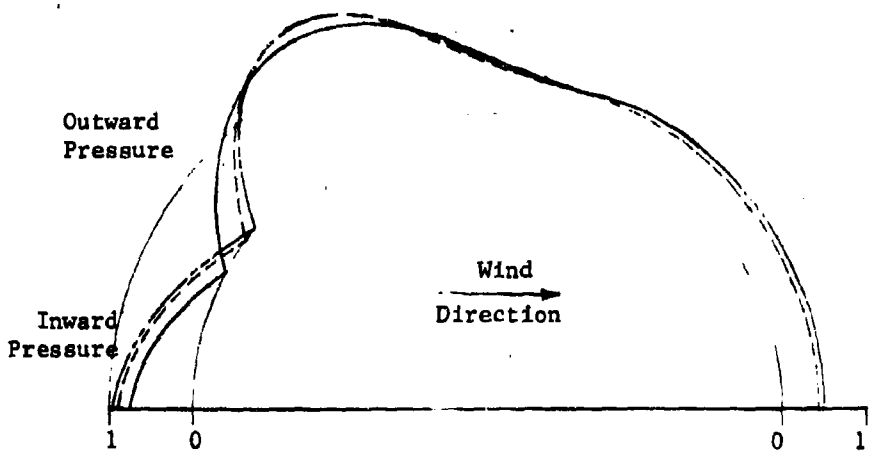

Figure 137. Pressure Distribution on Guyed Double-Wall Tents (h/d = 1/2, W/ℓ_h = 1/2)

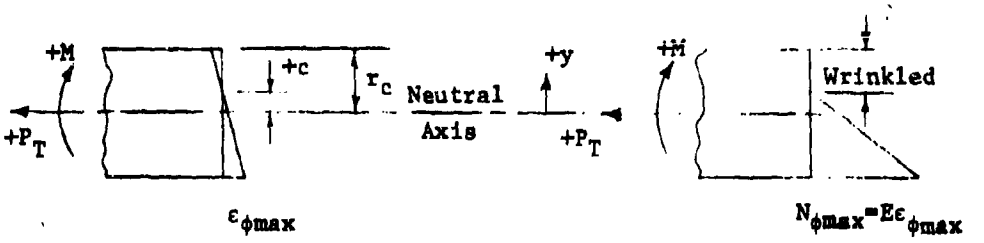

(a) Strain (b) Stress

Figure 138. Stress and Strain of Cellular Beam

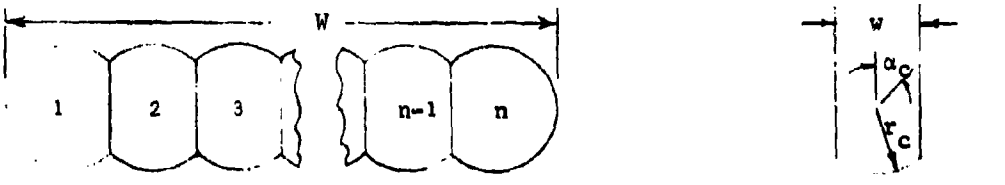

(a) Beam Cross Section (b) Cell Geometry

Figure 139. Cellular Beam Cross Section

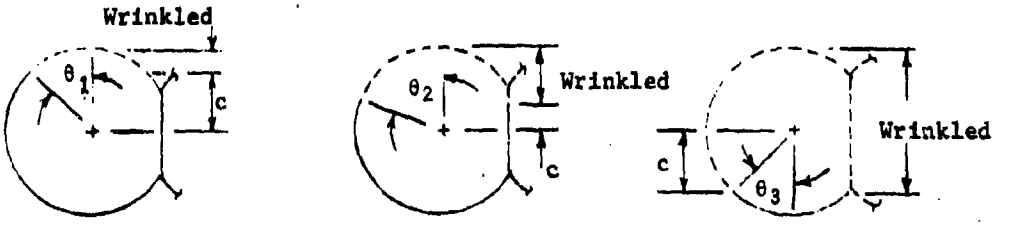

(a) Wrinkled into Upper Skin (b) Wrinkled into Web (c) Wrinkled into Lower Skin

Figure 140. Stages of Wrinkling of Cellular Beams

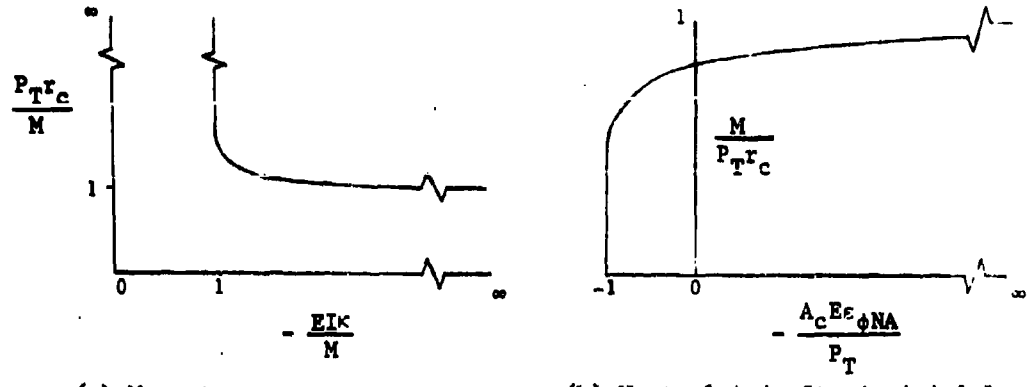

(a) Moment-Curvature (b) Neutral Axis Strain-Axial Load

Figure 141. Nonlinear Load-Strain Relations

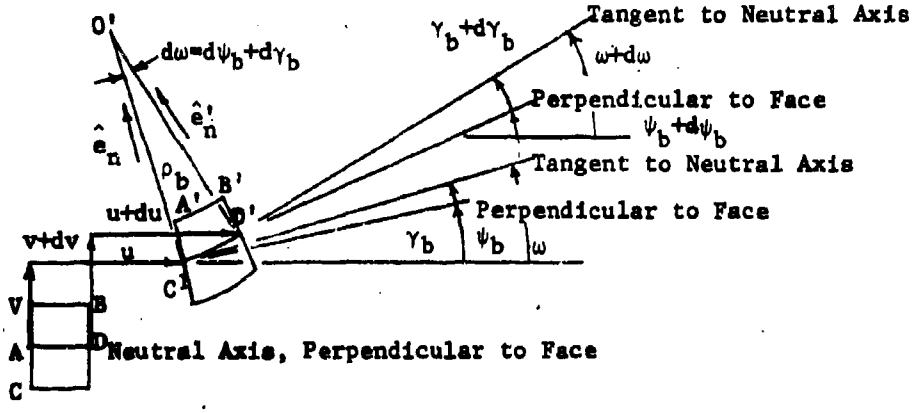

Figure 142. Deformation of Straight Beam Element

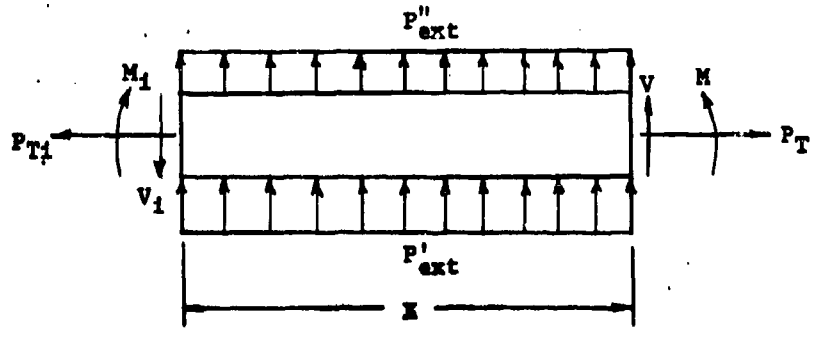

Figure 143. Equilibrium of Straight Beam

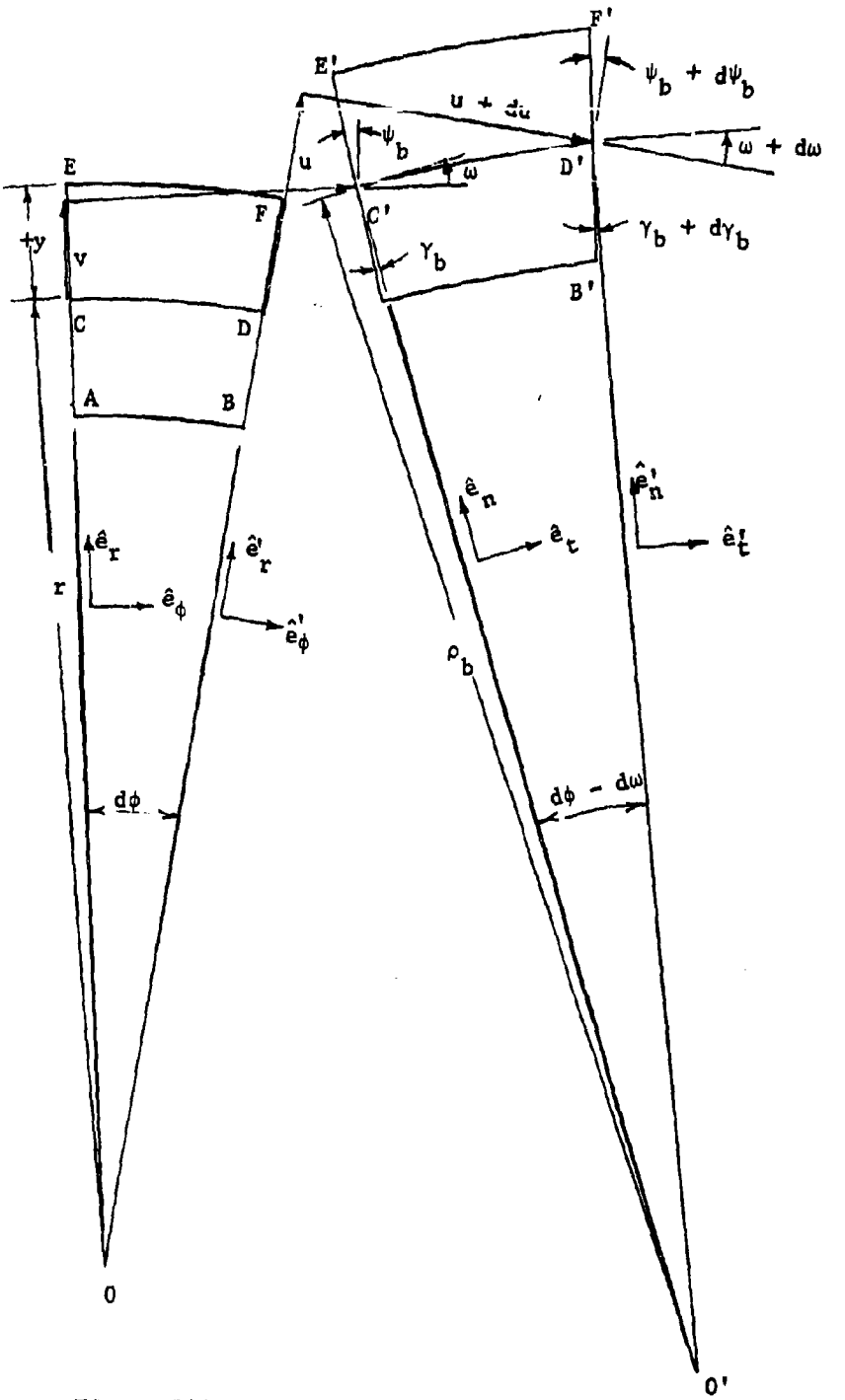

Figure 144. Deformation of Circular Beam Element

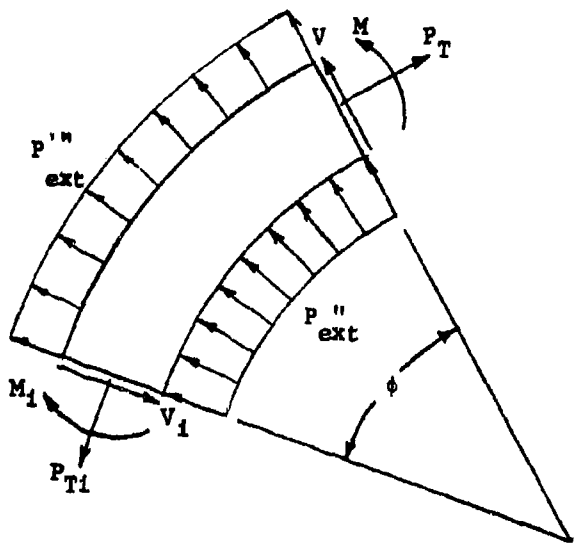

Figure 145. Equilibrium of Circular Beam Element

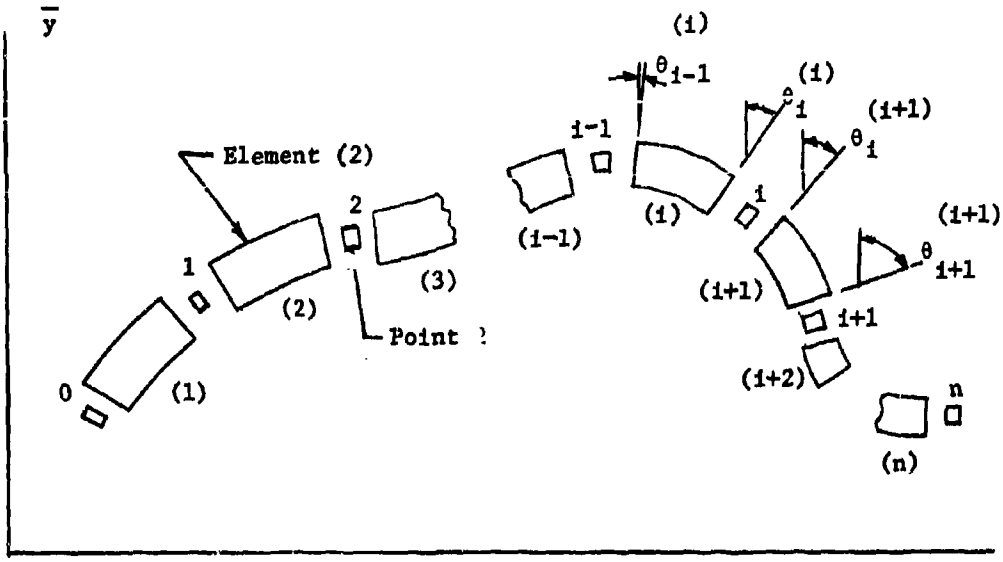

Figure 146. Finite Element Identification

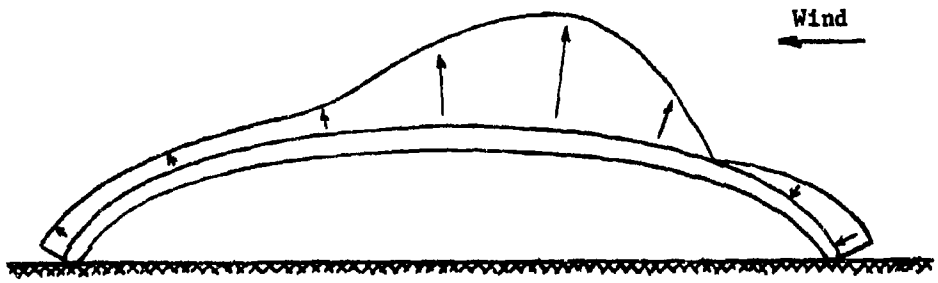

Figure 147. Wind Load on Double-Wall Tent

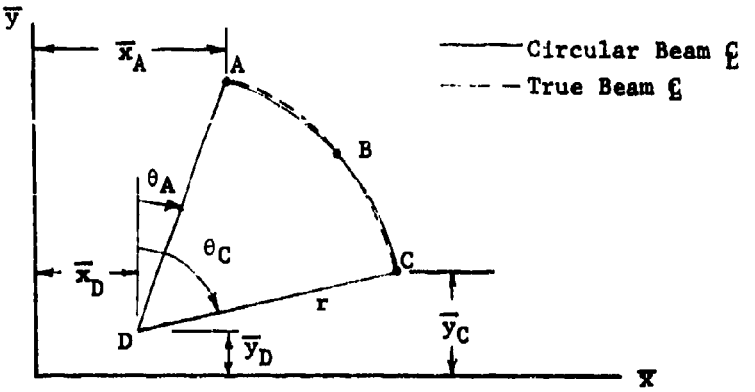

Figure 148. Beam Element Geometry

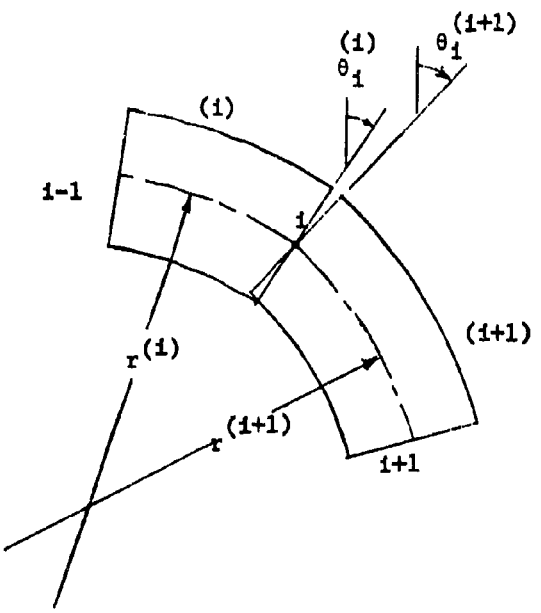

Figure 149. Mismatch of Finite Elements

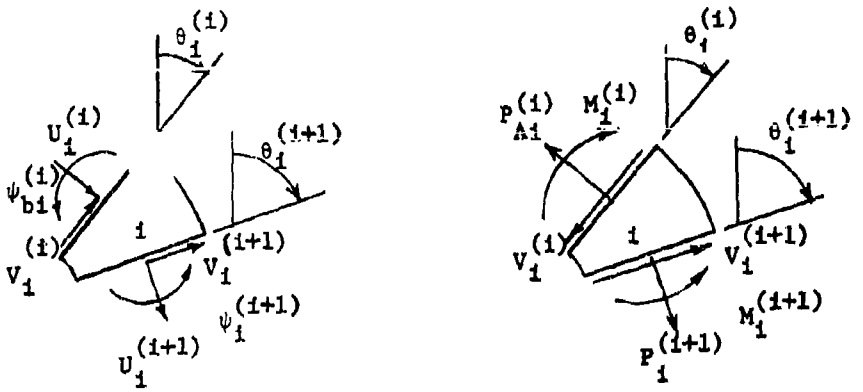

Figure 150. Point Geometry and Equilibrium

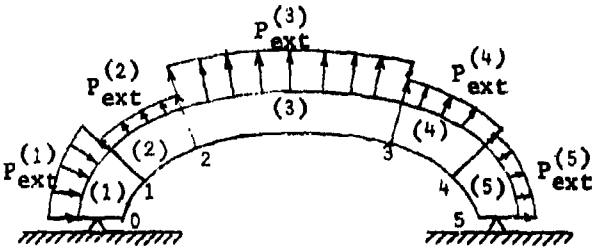

Figure 151. Five Element Beam

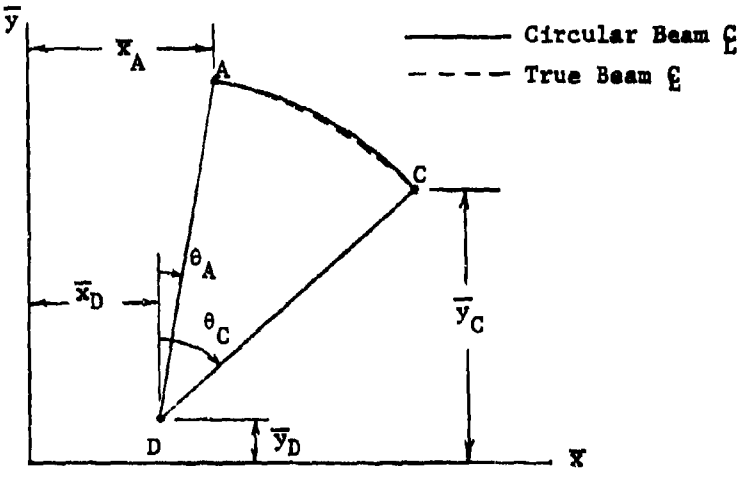

Figure 152. Beam Element Geometry

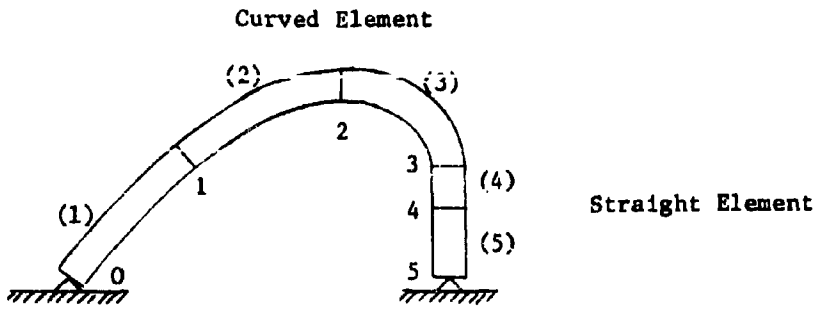

Figure 153. Tent with Straight and Curved Elements

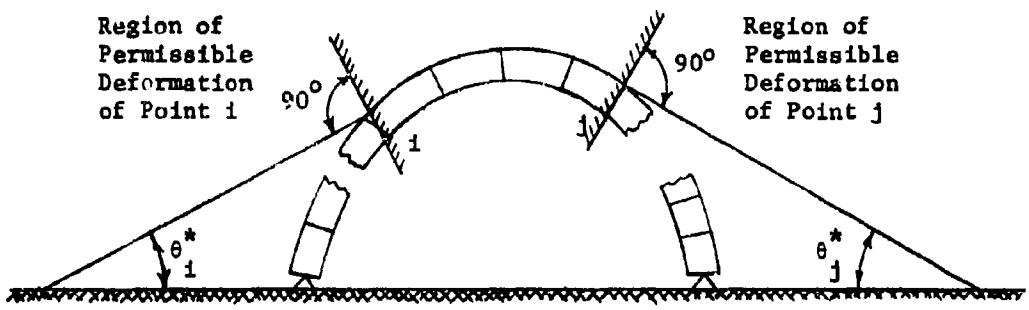

Figure 154. Deflection Condition at Guy Wires

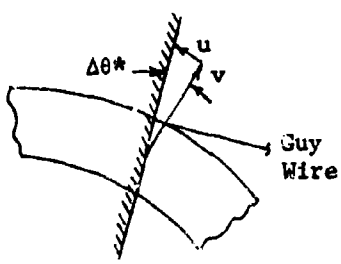

Figure 155. Deflection at Guy Wire

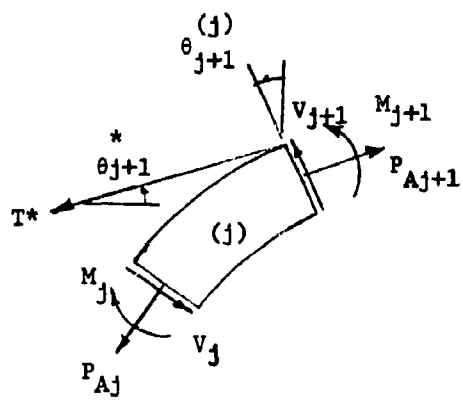

Figure 156. Equilibrium at Guy Wire

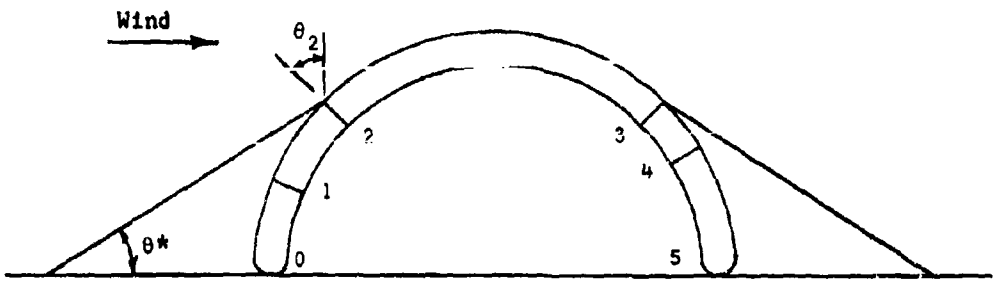

(a) One Guy

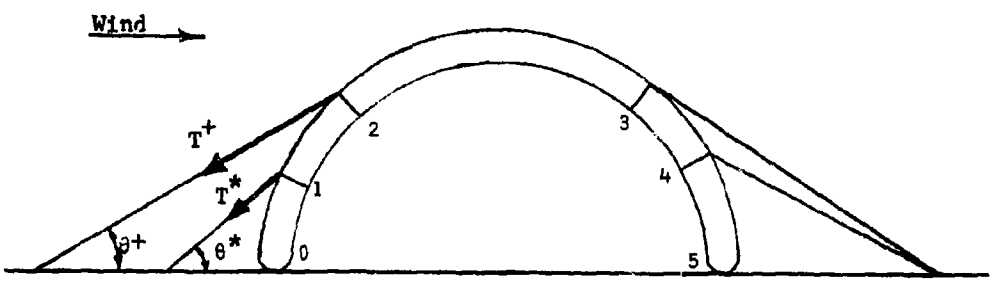

(b) Two Guys

Figure 157. Guyed Tents

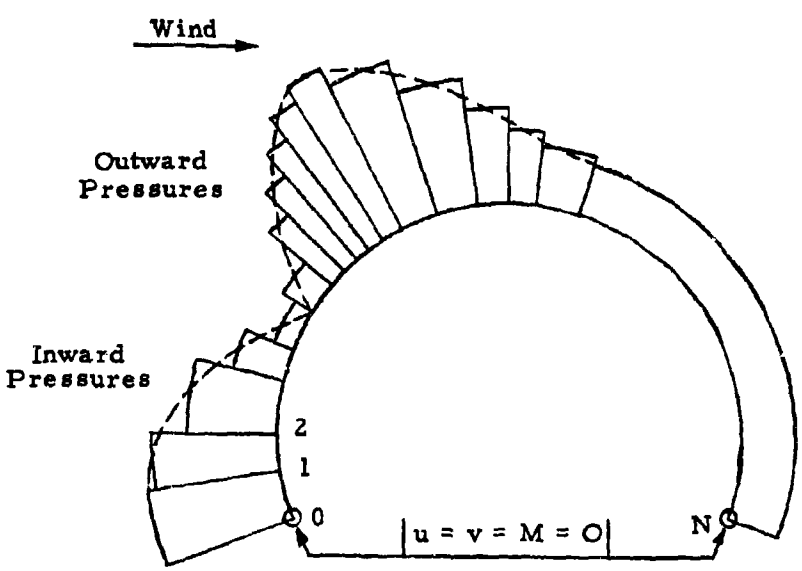

Figure 158. Loads and Boundary Conditions

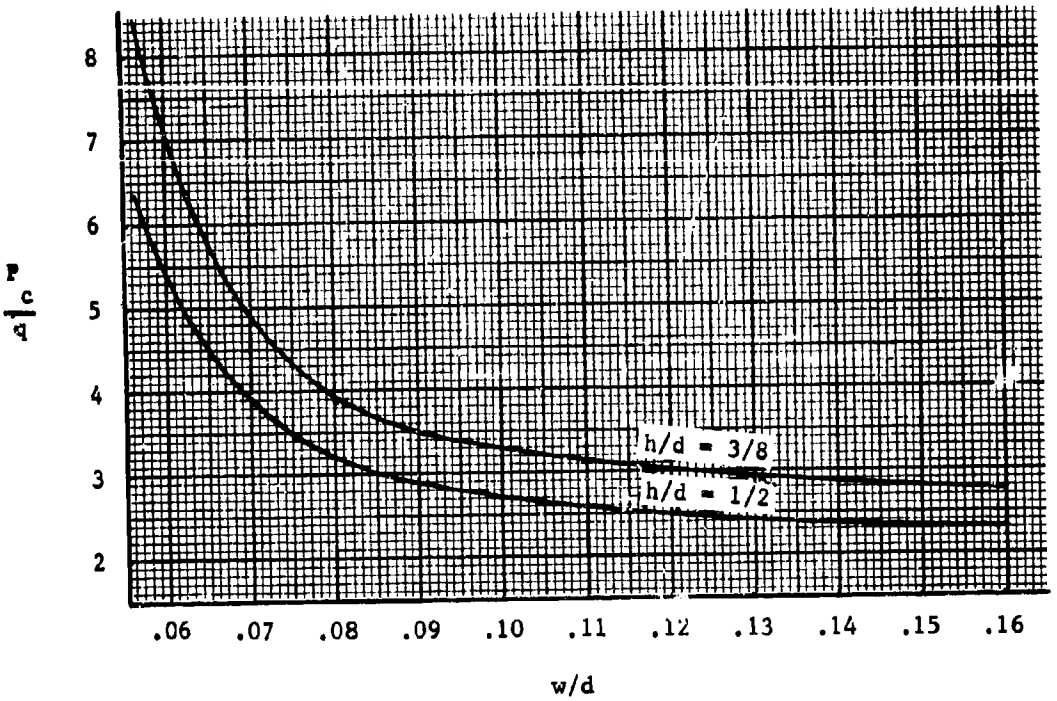

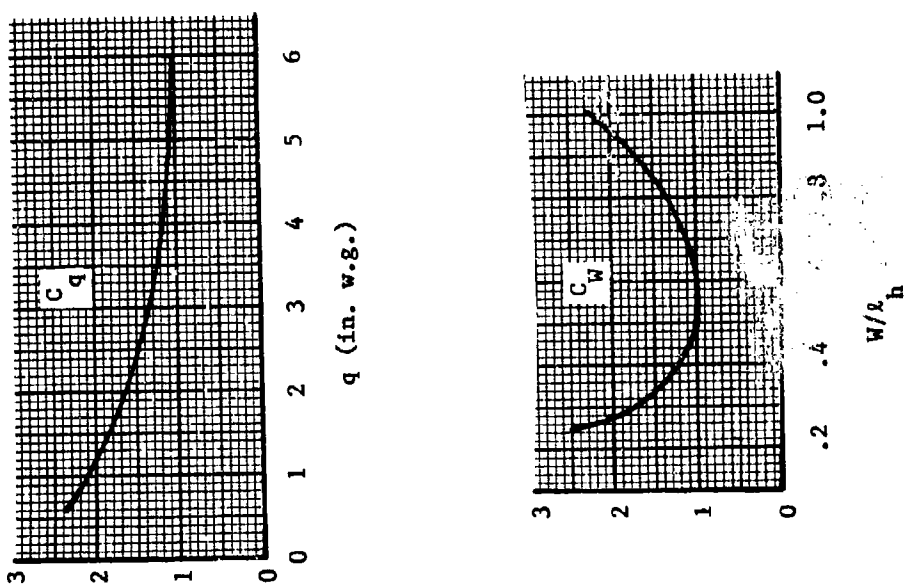

Figure 159. Double-Wall Tent Cell Pressure

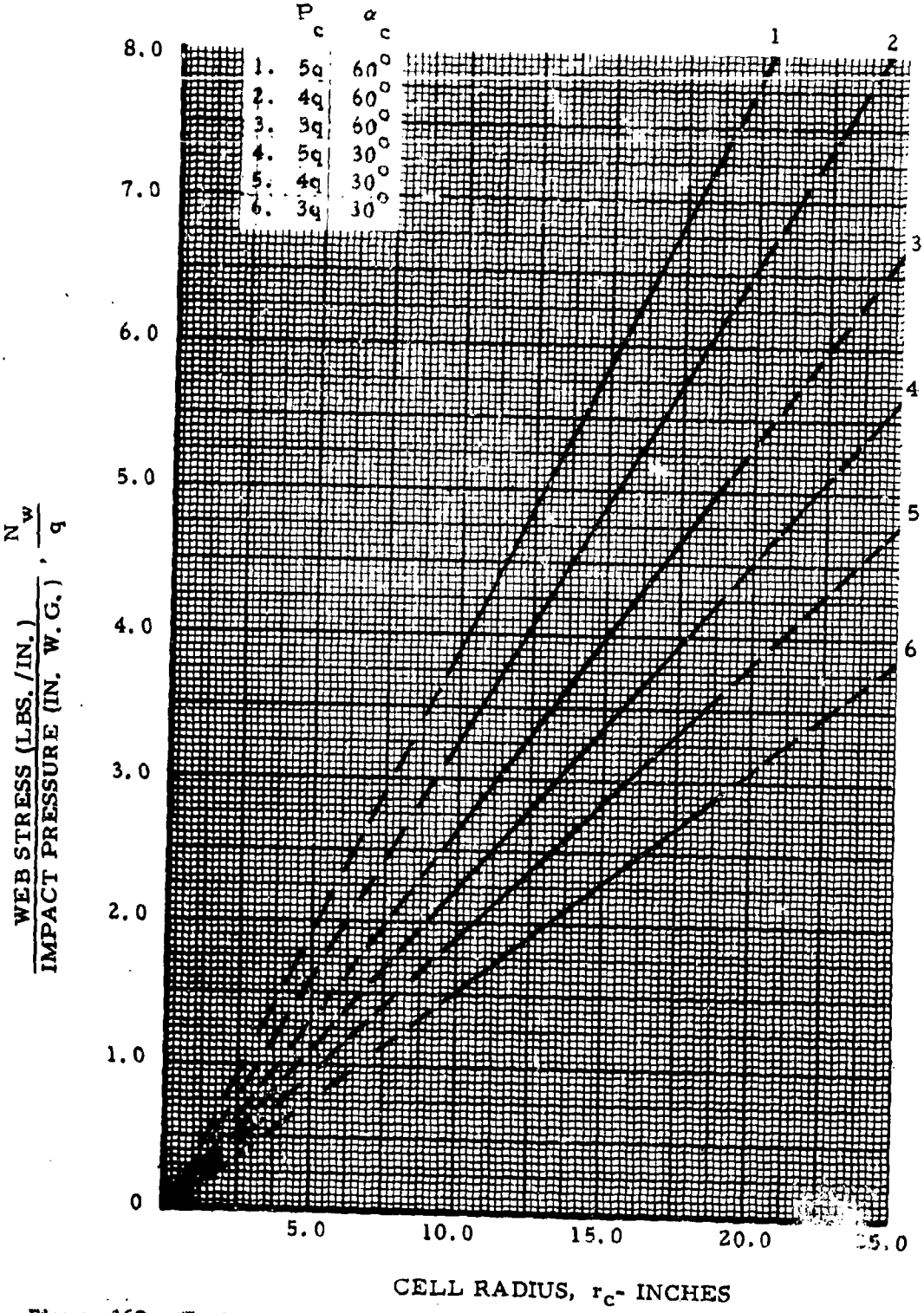

Figure 160. Variation of Ratio of Web Stress to Impact Pressure with Cell Radius; Double-Wall Cylinders

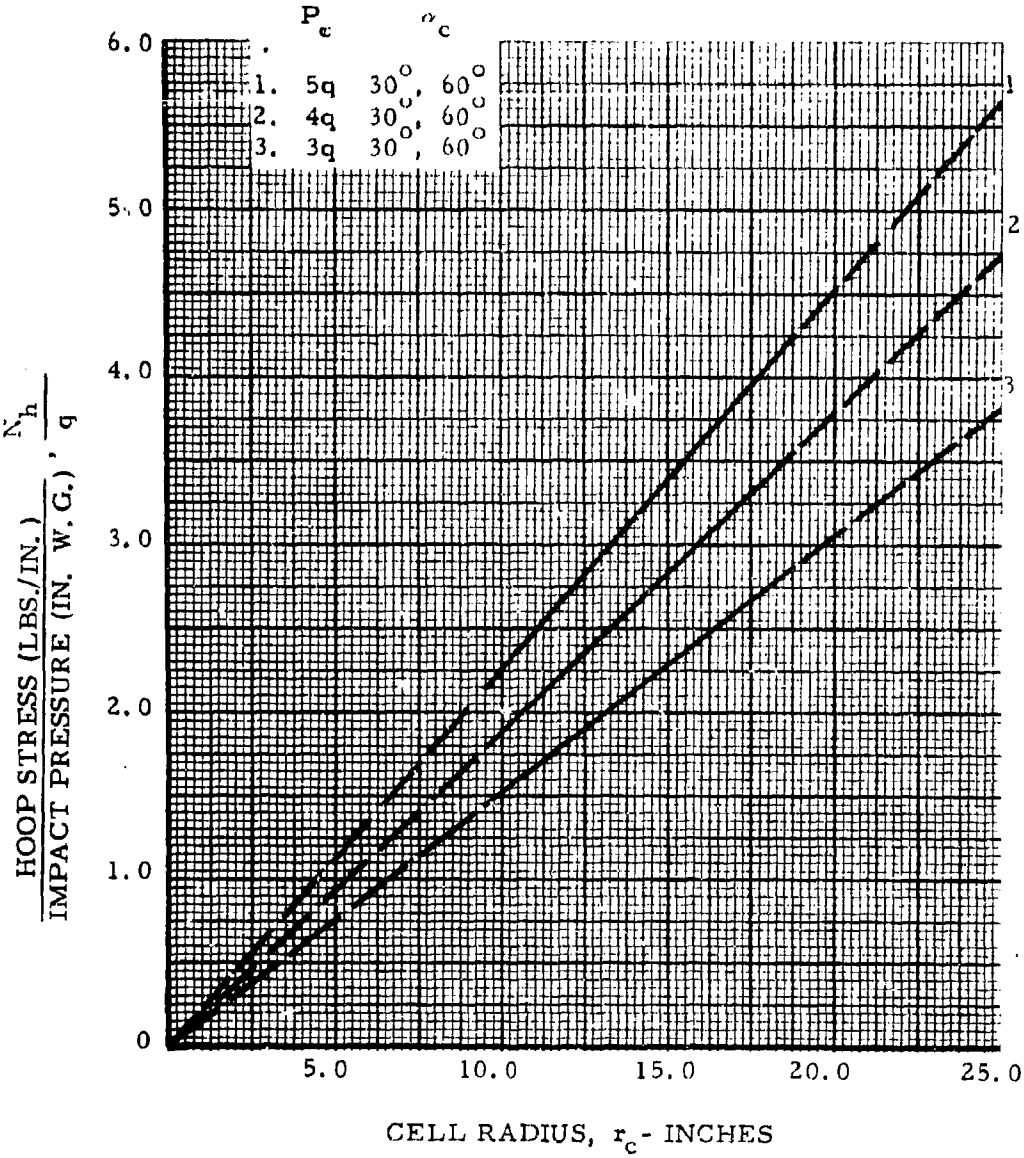

Figure 161. Variation of Ratio of Hoop Stress with Impact Pressure with Cell Radius; Double-Wall Cylinders

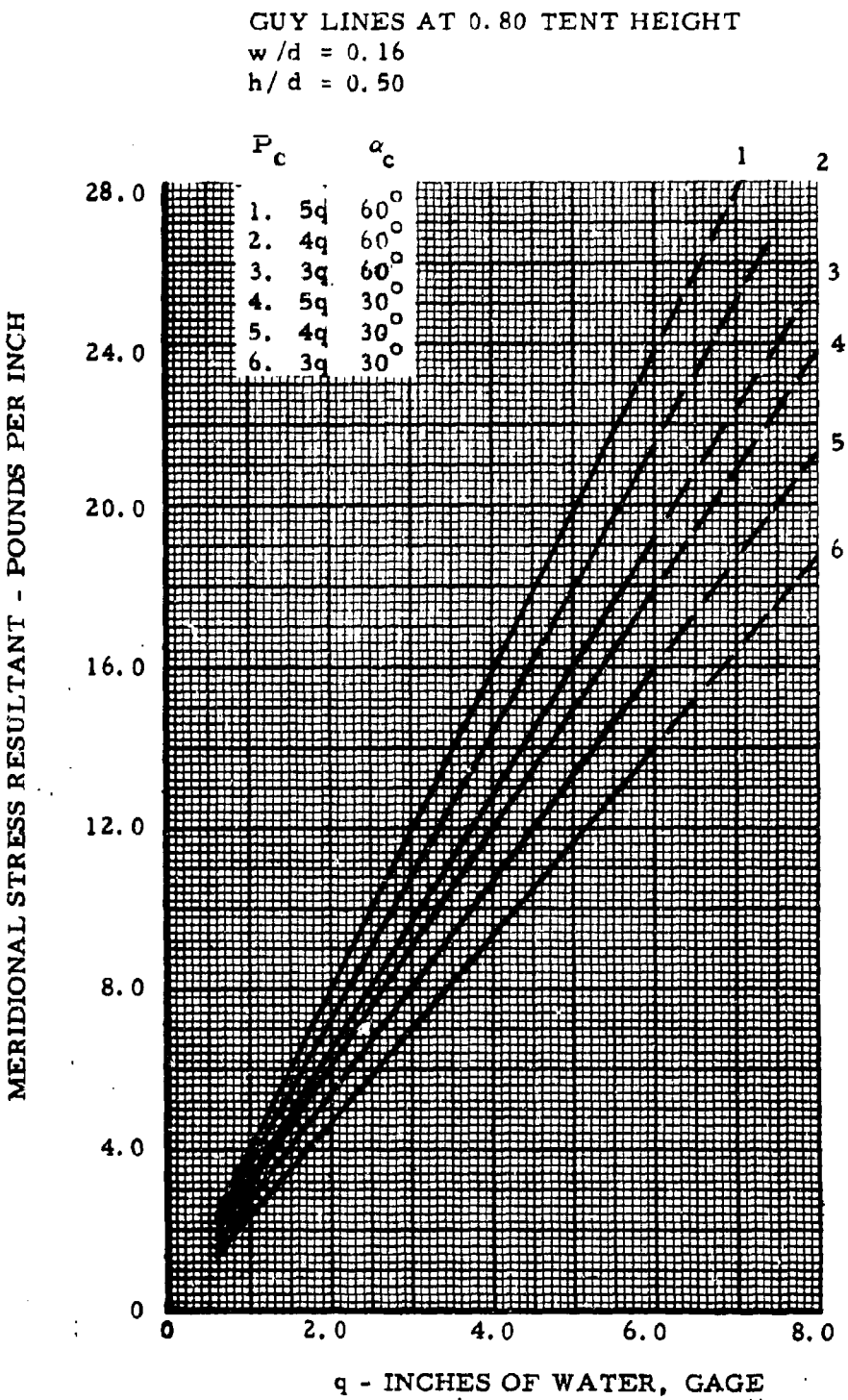

Figure 162. Variation of Meridional Stress Resultant with Impact Pressure, q; Double-Wall Cylinders, w/d = 0.16, h/d = .5

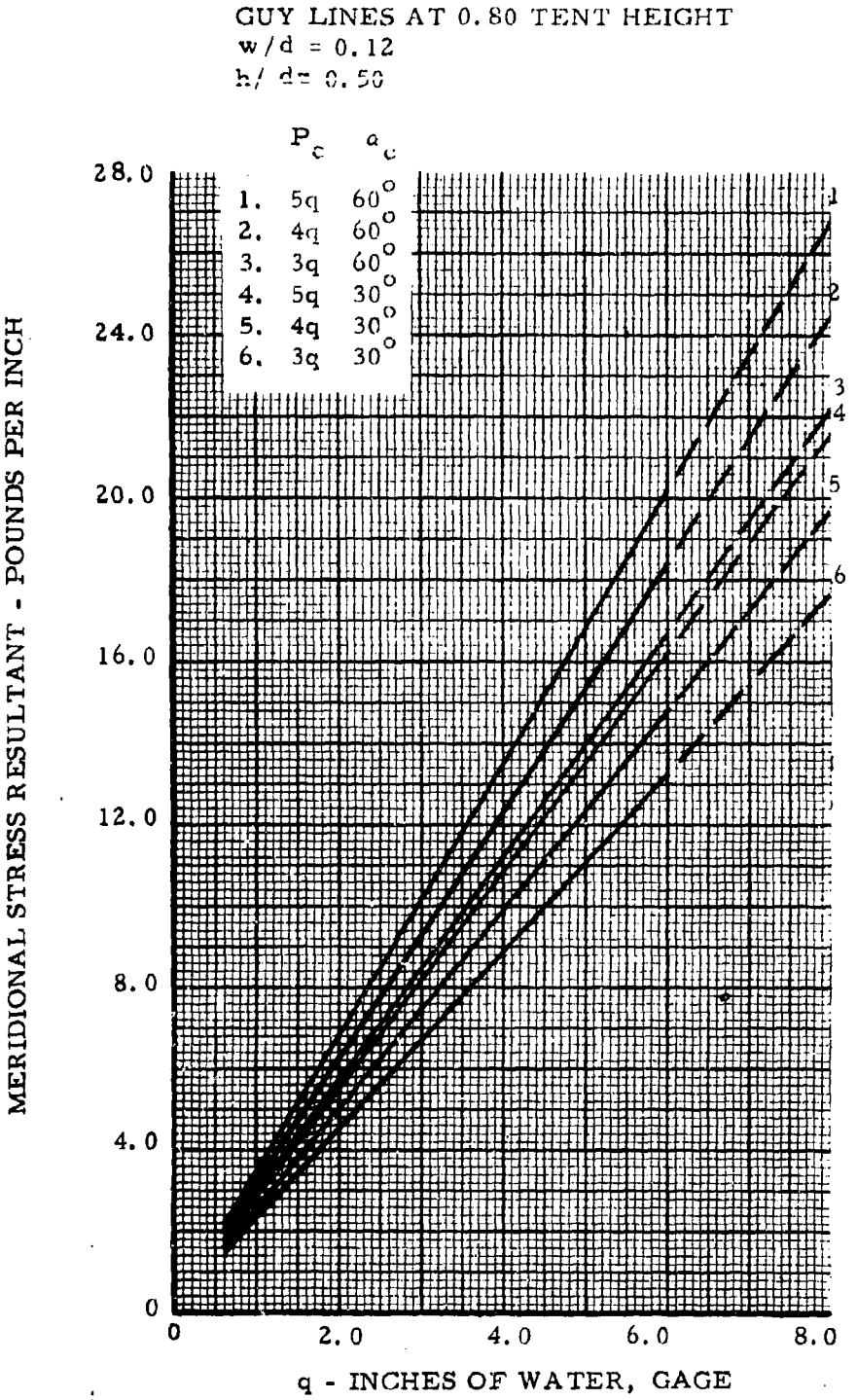

Figure 163. Variation of Meridional Stress Resultant with Impact Pressure, q; Double-Wall Cylinders, w/d = 0.12, h/d = .5

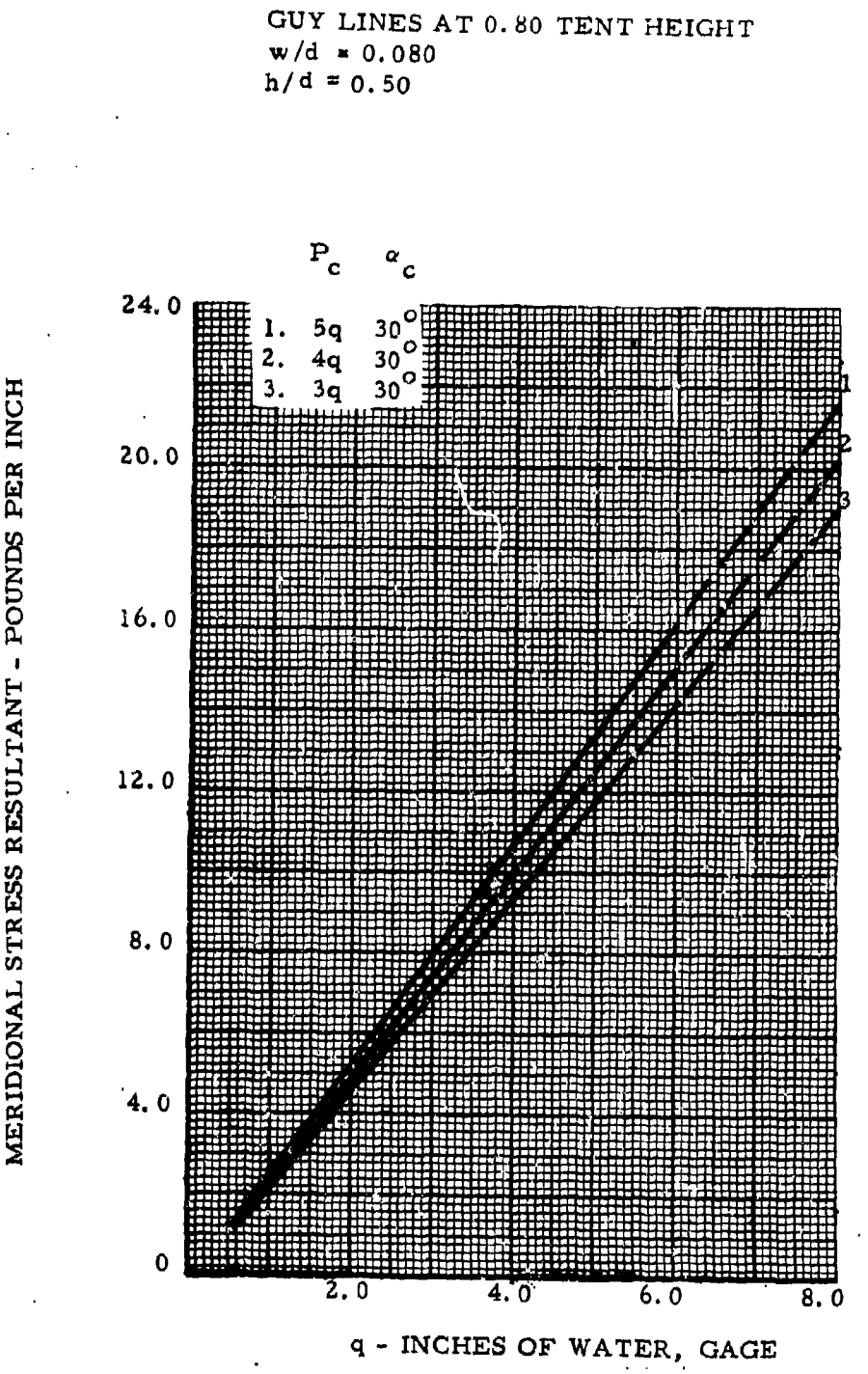

Figure 164. Variation of Meridional Stress Resultant with Impact Pressure, q; Double-Wall Cylinders, w/d = 0.08, h/d = .5

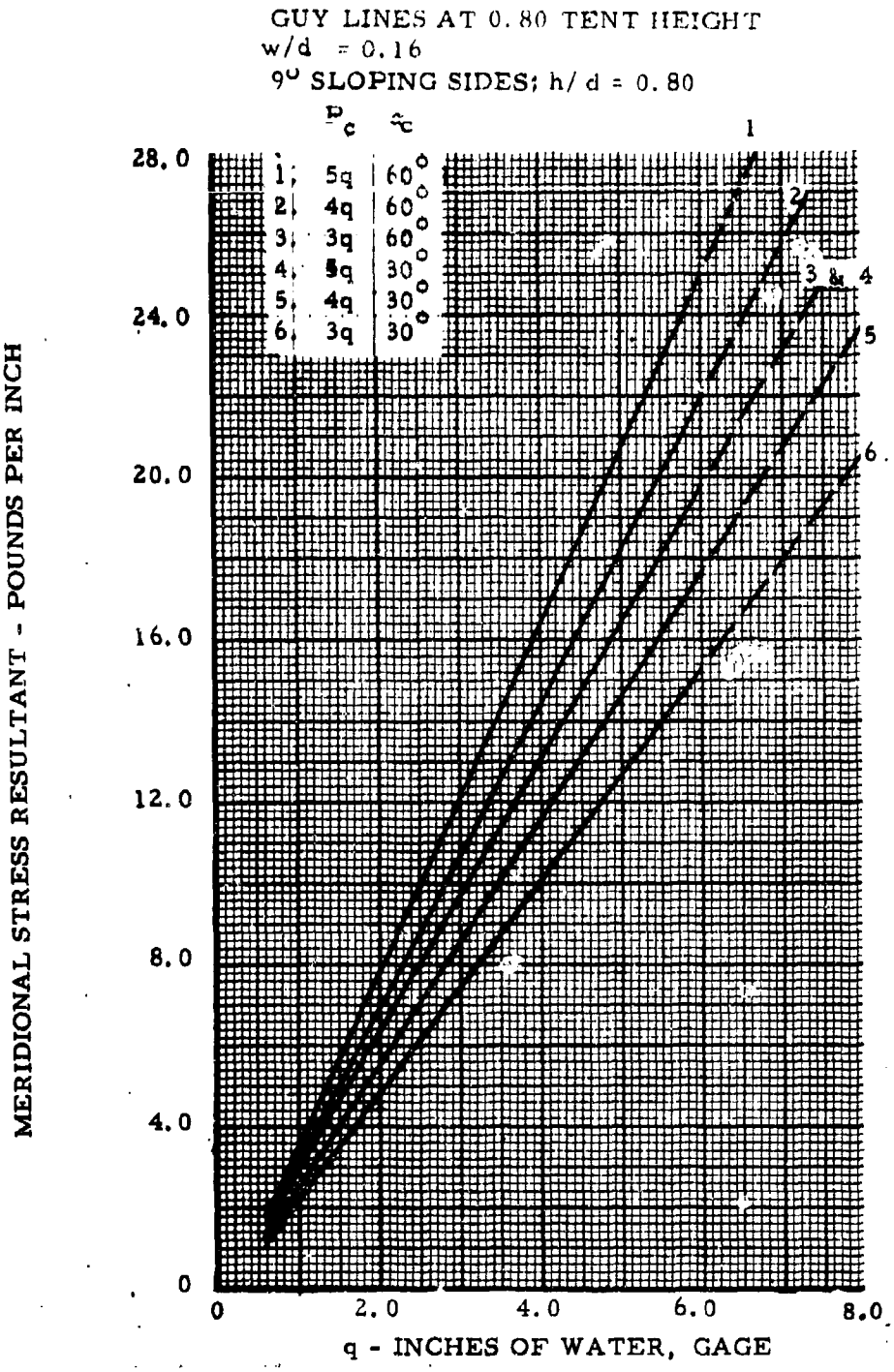

Figure 165. Variation of Meridional Stress Resultant with Impact Pressure, q; Double-Wall Cylinders, w/d = 0.16, 9° Sloping Sides, h/d = 0.8

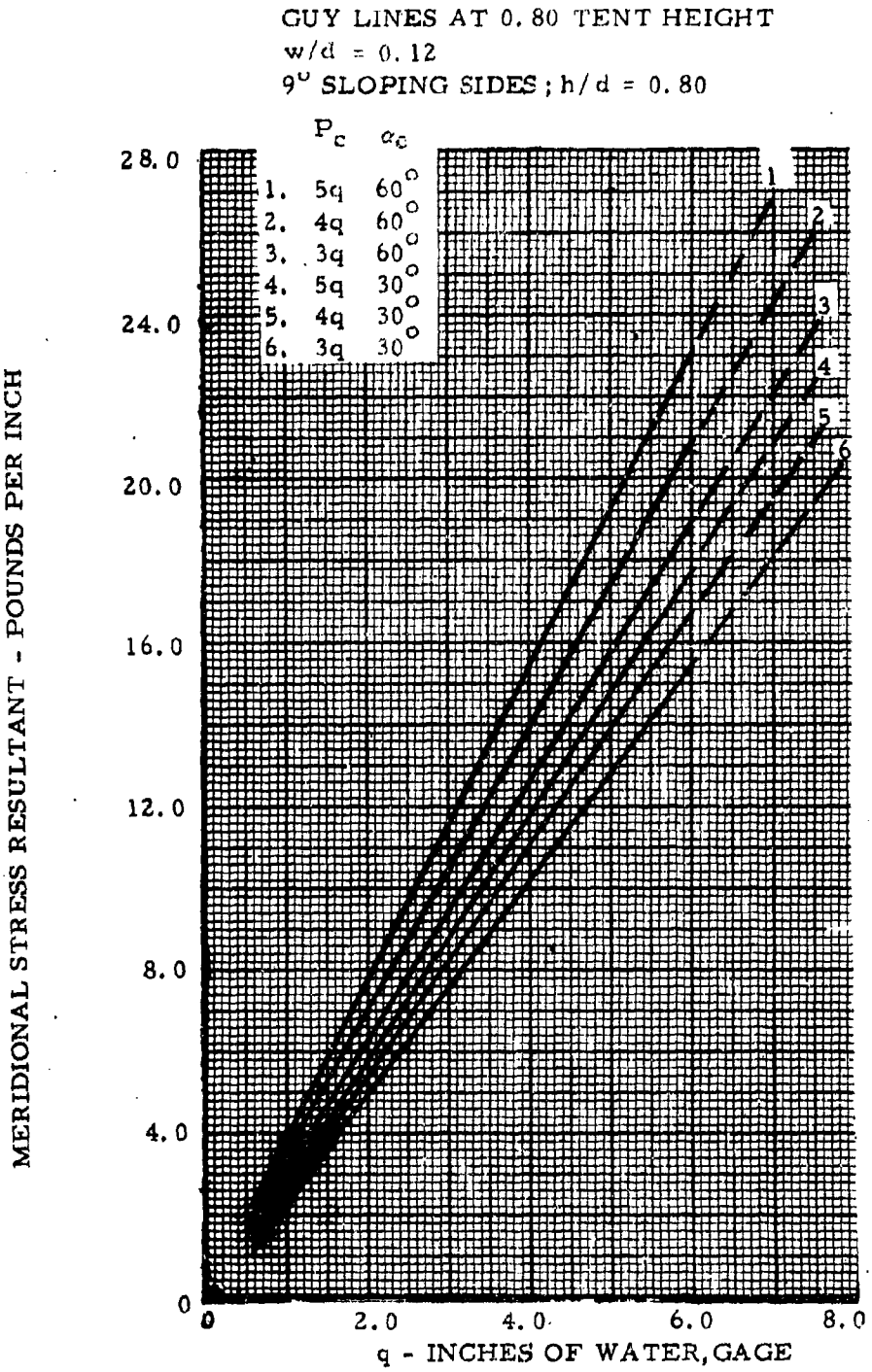

Figure 166. Variation of Meridional Stress Resultant with Impact Pressure, q; Double-Wall Cylinders, w/d = 0.12, 9° Sloping Sides, h/d = 0.8

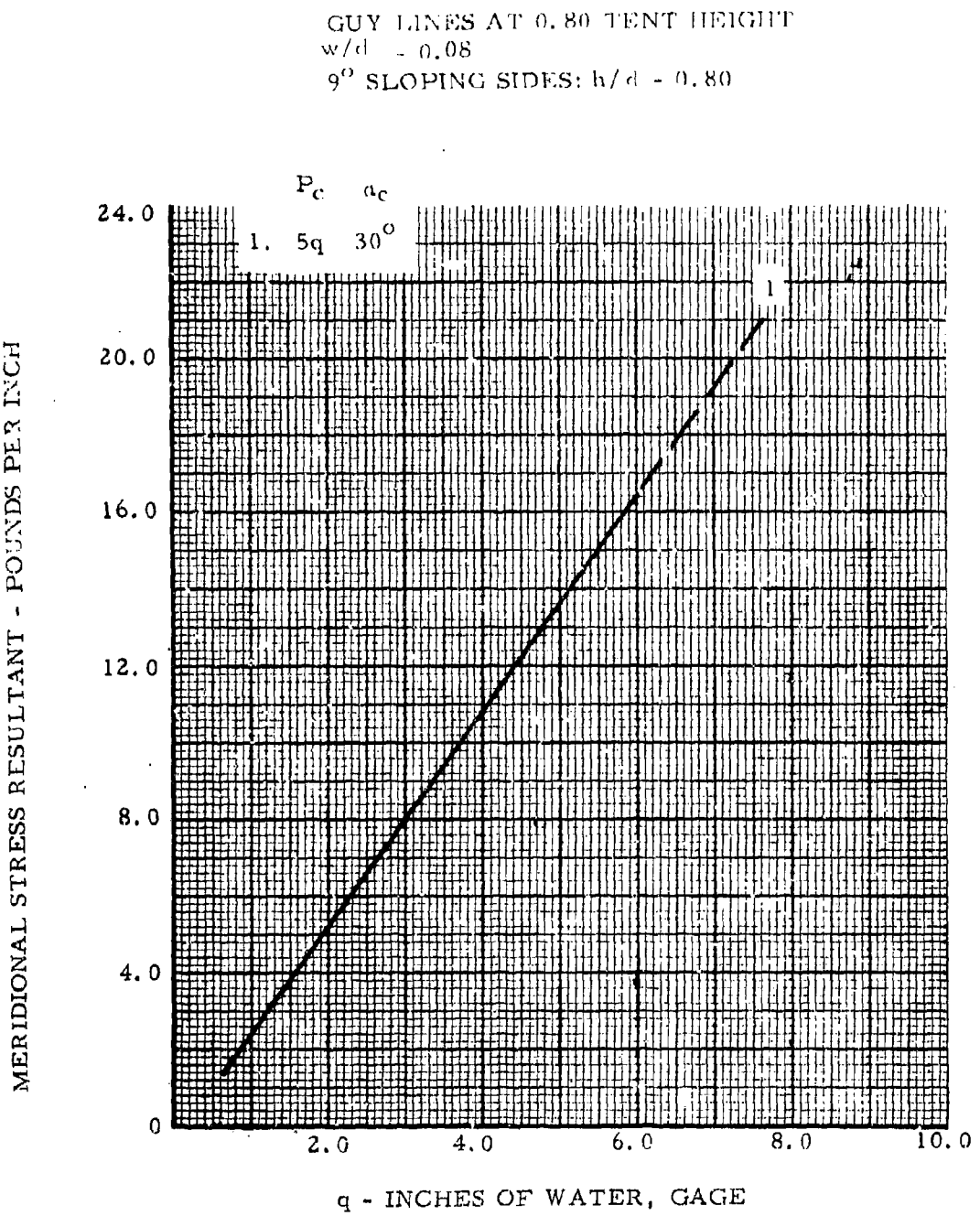

Figure 167. Variation of Meridional Stress Resultant with Impact Pressure, q; Double-Wall Cylinders, w/d = 0.08, 9° Sloping Sides, h/d = 0.8

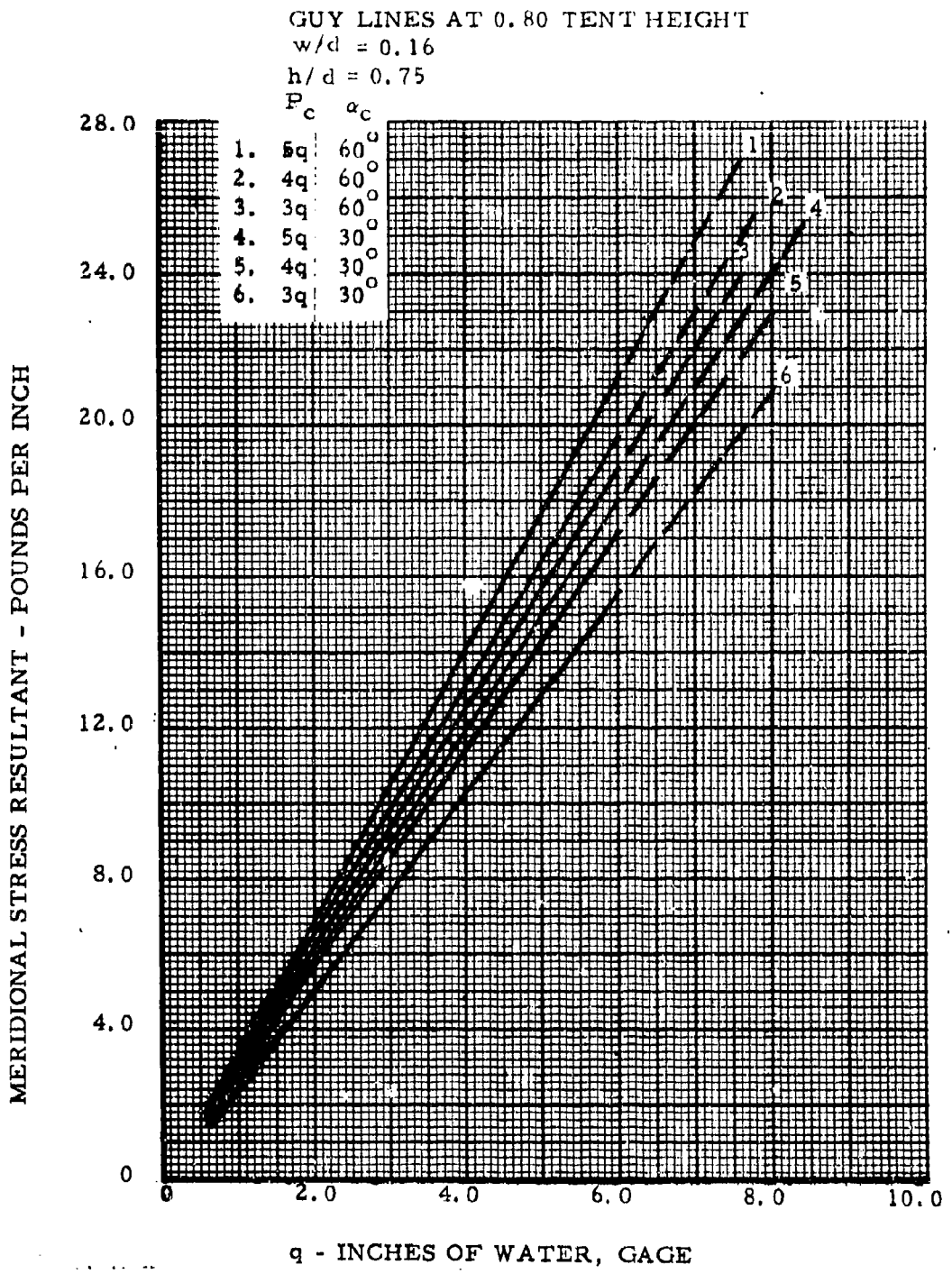

Figure 168. Variation of Meridional Stress Resultant with Impact Pressure, q; Double-Wall Cylinders, w/d = 0.16, h/d = 0.75

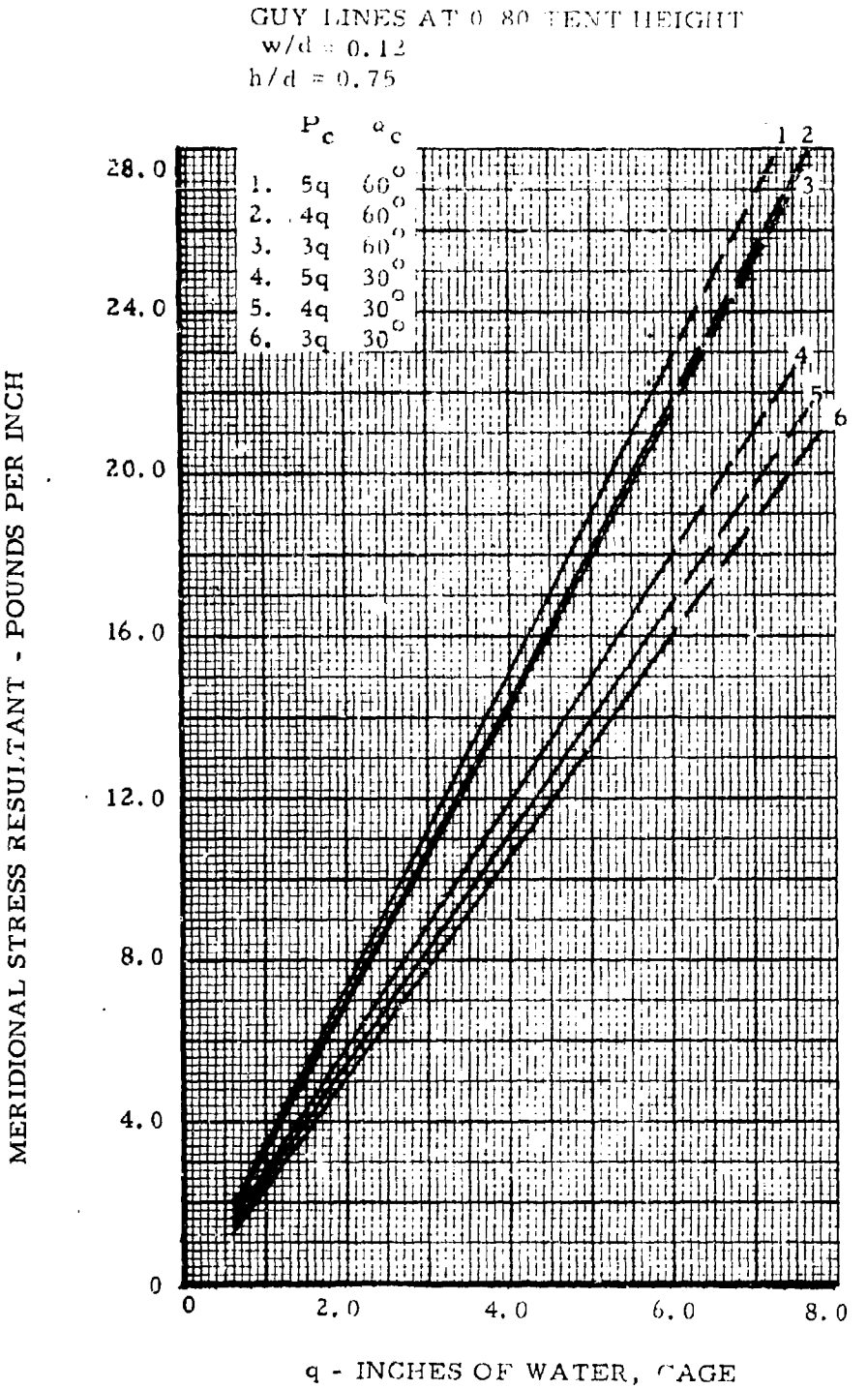

Figure 169. Variation of Meridional Stress Resultant with Impact Pressure, q; Double-Wall Cylinders, w/d = 0.12, h/d = 0.75

GUY LINES AT 0.80 TENT HEIGHT
w/d = 0.08
h/d - 0.75

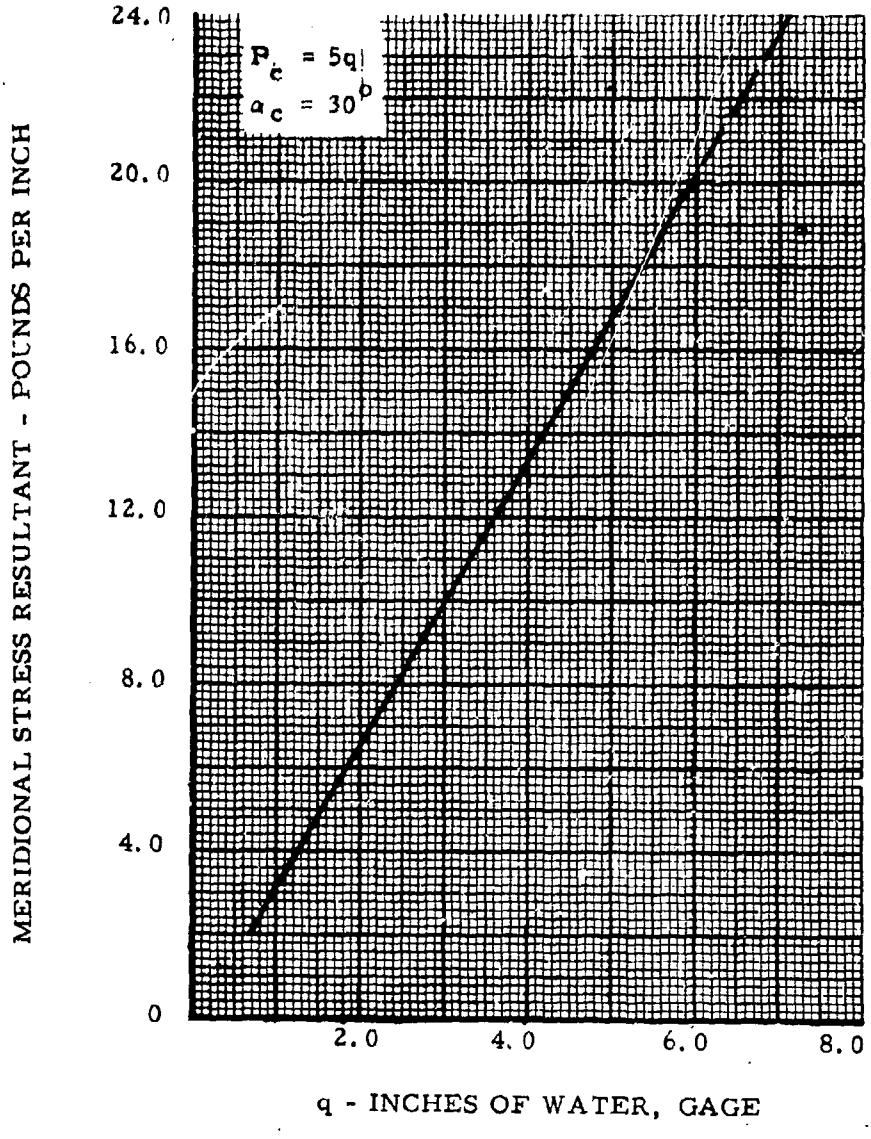

Figure 170. Variation of Meridional Stress Resultant with Impact Pressure, q; Double-Wall Cylinders, w/d = 0.08, h/d = 0.75

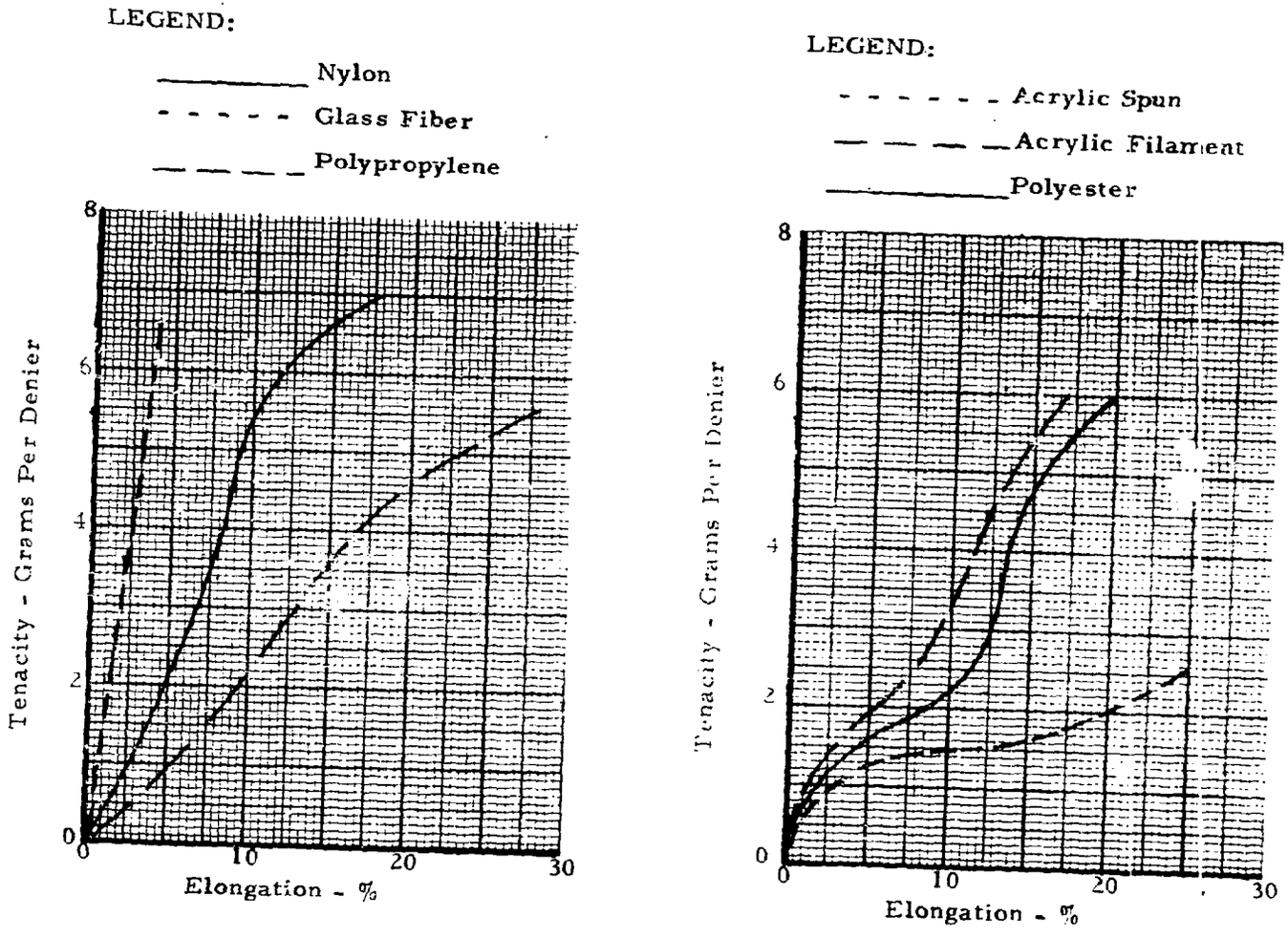

Figure 171. Tenacity vs. Elongation Diagram of Fiber.

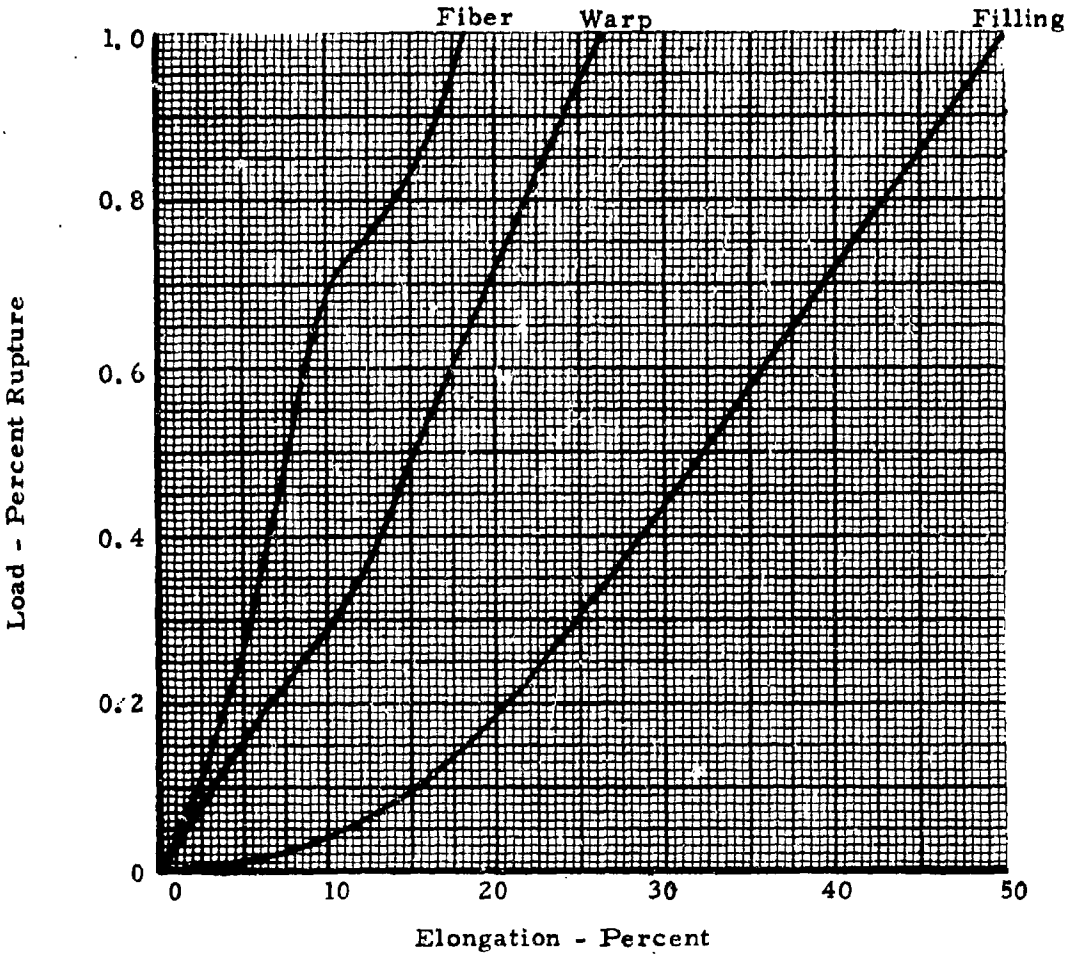

Figure 172. Load - Elongation Diagram of Fiber and Plain Weave Fabric; Nylon

POLYESTER

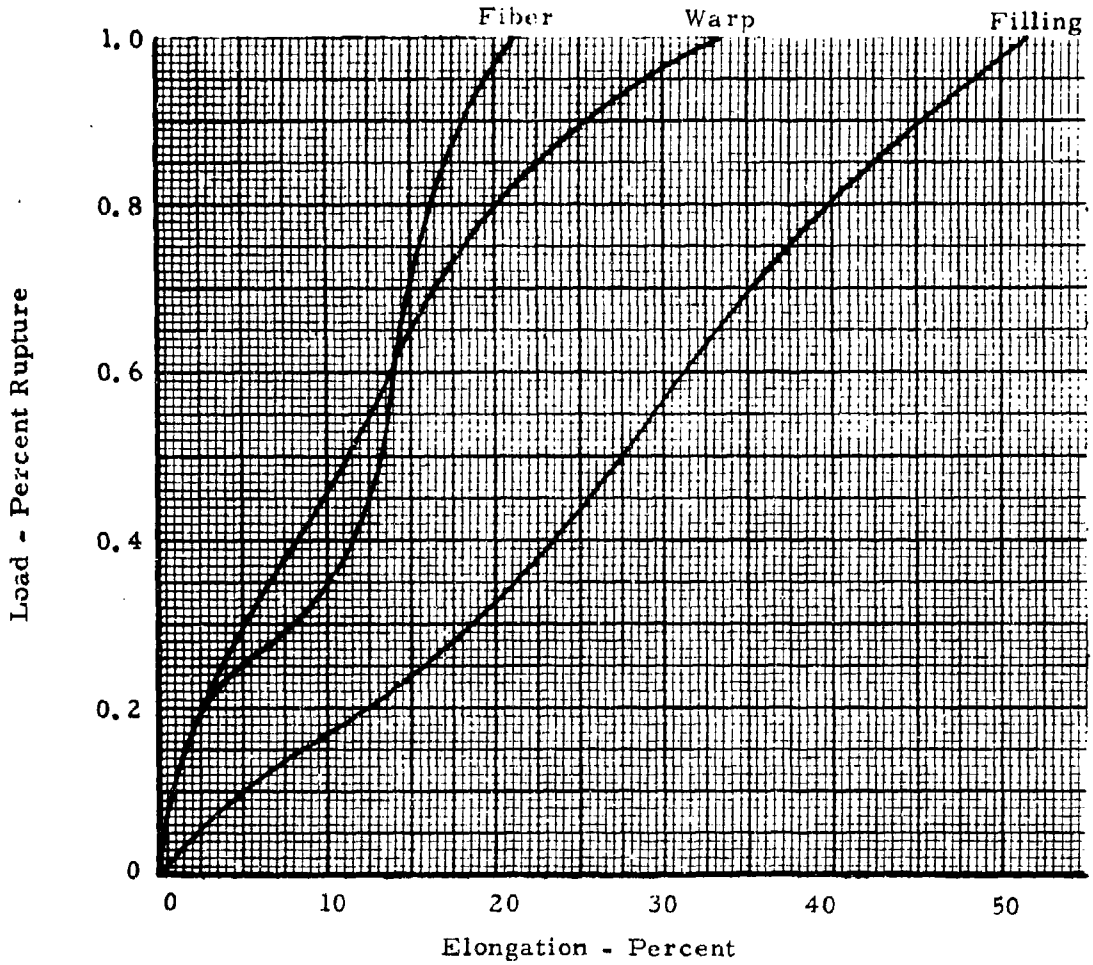

Figure 173. Load - Elongation Diagram of Fiber and Plain Weave Fabric; Polyester

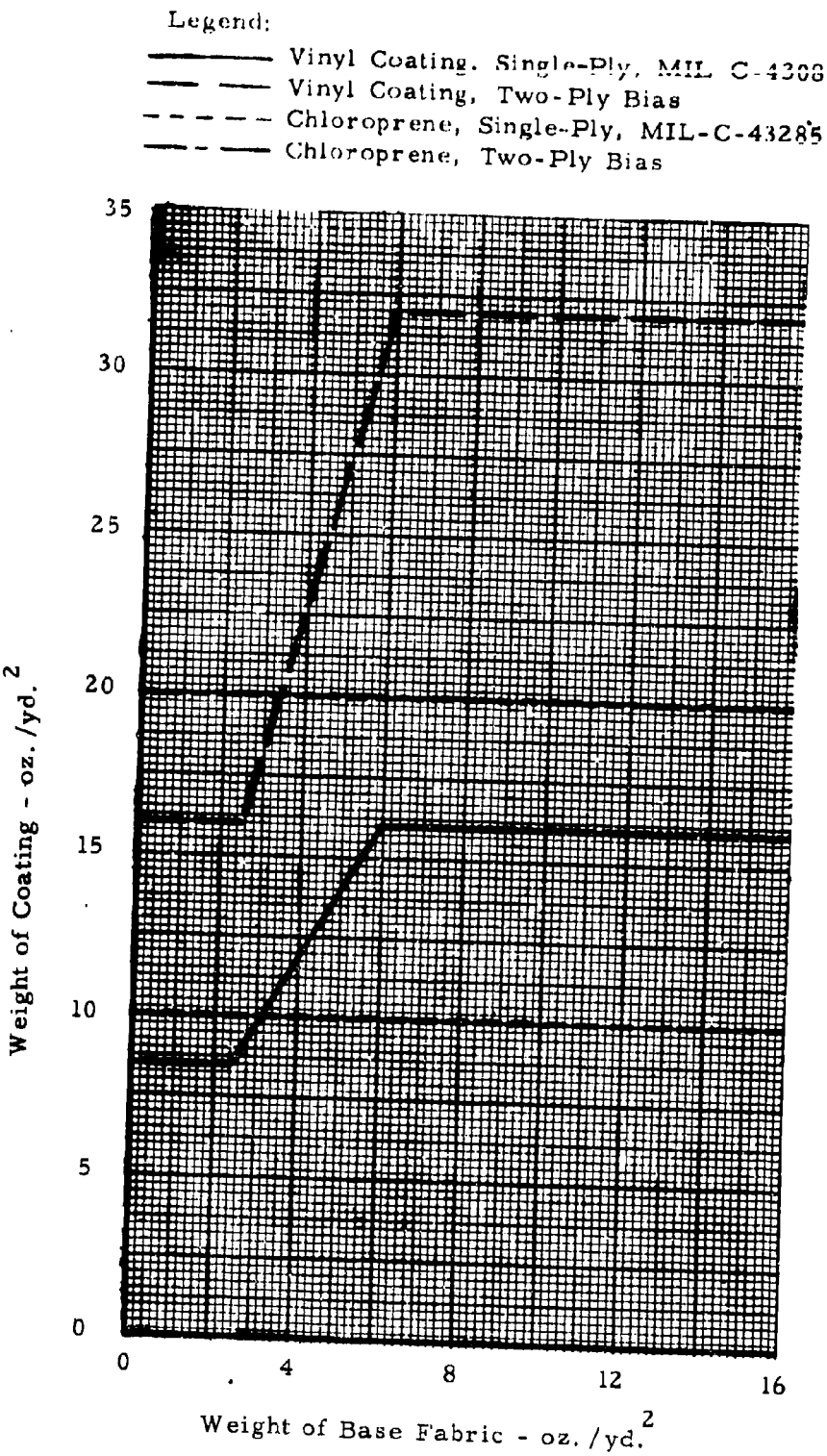

Figure 174. Weight of Coating For Single-And Two-Ply Coated Fabric

13. ABSTRACT (cont'd)

Tests were conducted at stabilized wind speeds up to 110 miles per hour in the Virginia Polytechnic Institute's six-foot by six-foot stability tunnel. In the analytical phase, test data were used to develop fabric stress and aerodynamic coefficient data variation with tent parameters.

Results of the wind tunnel investigations and stress analyses have been incorporated and include comprehensive, practical design data suitable for engineering reliable, stable, single- and double-wall, air-supported shelters. Data, in general, are presented in nondimensional coefficient form, and, therefore, are applicable to full-scale shelters within the range of the parameters investigated. Design information is presented as charts and tables on shelter aerodynamic force and moment coefficients, anchor and guy line coefficients, structural deflection, vibration, and material stresses.

UNCLASSIFIED
Security Classification

DOCUMENT CONTROL DATA - R & D

(Security classification of title, body of abstract and indexing annotation must be entered when the overall report is classified)

1. ORIGINATING ACTIVITY (Corporate author)	2a. REPORT SECURITY CLASSIFICATION
Hayes International Corporation Birmingham, Alabama	Unclassified 2b. GROUP

3. REPORT TITLE

Wind Tunnel Tests and Analyses for Ground-Mounted, Air-Supported Structures (Revised)

4. DESCRIPTIVE NOTES (Type of report and inclusive dates)

Research report - July 1963 - May 1968

5. AUTHOR(S) (First name, middle initial, last name)

A. E. Dietz, R. B. Proffitt, R. S. Chabot, and E. L. Moak, Hayes International Corporation, and C. J. Monego, U. S. Army Natick Laboratories.

6. REPORT DATE	7a. TOTAL NO. OF PAGES	7b. NO. OF REFS
July 1969	297	28

8a. CONTRACT OR GRANT NO.	9a. ORIGINATOR'S REPORT NUMBER(S)
DA19-129-AMC-953(N)	
b. PROJECT NO. 1M62410D503	
c.	9b. OTHER REPORT NO(S) (Any other numbers that may be assigned this report) 70-7-GP
d.	

10. DISTRIBUTION STATEMENT

This document has been approved for public release and sale, its distribution is unlimited.

11. SUPPLEMENTARY NOTES	12. SPONSORING MILITARY ACTIVITY
supersedes U. S. Army NLABS TR 67-36-ME, Wind Tunnel Tests and Analyses for Ground Mounted Air-Supported Structures, Oct 66	U. S. Army Natick Laboratories Natick, Massachusetts 01760

13. ABSTRACT

The objective of this program is to provide tentage information based on wind tunnel test data that can be applied either to the evaluation and improvement of existing ground-mounted, air-supported tents or to the design of such future structures.

The program consisted of two study, test and analytical investigation phases, the first from July 1963 to October 1966, and the second from May 1966 to May 1968. This second report is a revised and expanded edition of a prior study entitled "Wind Tunnel Tests and Analysis of Ground Mounted Air Supported Structures". During the study phase a review was made on pertinent literature on experimental techniques, data and analyses applicable to determining maximum aerodynamic force and stresses in fabric structures.

The first wind tunnel investigation consisted of detailed investigations of basic single-wall tent configurations constructed of porous and nonporous fabrics and double-wall tents. The tent configurations tested included shelter shapes such as spheres, cylinders with spherical ends, and cylinders with flat ends. This study was made to expand the scope of the report to include data on cylindrical shelters with elliptical ends, the bending stiffness of an inflated beam, vibration characteristics of single-wall and double-wall shelters, the effect of wind skirts on the ground anchors, and a study of factors to improve the stability of double-wall shelters.

(see continuation sheet attached)

DD FORM 1 NOV 68 1473 REPLACES DD FORM 1473, 1 JAN 64, WHICH IS OBSOLETE FOR ARMY USE.

UNCLASSIFIED
Security Classification

14. KEY WORDS	LINK A		LINK B		LINK C	
	ROLE	WT	ROLE	WT	ROLE	WT
Testing	8					
Inflatable structures	8, 9		4			
Tents	8, 9		4			
Air-supported	0					
Wind tunnels	10					
Armed Forces equipment	4		4			
Evaluation			8			
Physical properties			9			
Flexibility			9			
Low-temperature			0			
Dielectric constant			9			
Weight			6, 9			
Tensile properties			7, 9			
Fabrics			9			
Fibers			9			